Low-temperature NO_x-hydrocarbon interactions at elevated pressure probed with synchrotron double imaging photoelectron photoion coincidence spectroscopy

zur Erlangung des akademischen Grades
DOKTOR DER INGENIEURWISSENSCHAFTEN (Dr.-Ing.)
der Fakultät für Maschinenbau der Universität Paderborn

genehmigte
DISSERTATION

von
Martin Höner
aus Duisburg

Tag des Kolloquiums: 18.12.2023
Referent: Prof. Dr. Tina Kasper
Koreferent: Prof. Dr. Christof Schulz

Abstract/Kurzfassung

The research objective of this work was to understand the interactions of hydrocarbon fuels with oxides of nitrogen at elevated pressures. To achieve the objective, conditions of methane doped with NO were probed with synchrotron double imaging photoelectron photoion coincidence spectroscopy in a newly developed reactor experiment. Specifically, the target molecule was intermediately formed nitrous acid. Despite recent theoretical reaction rates pointing in the opposite direction, no HNO_2 intermediate was found. It was shown that the intermediate should have been detectable since its cation is bound. In contrast, the *cis*-HONO isomer was found to dissociate upon ionization at energies close to its adiabatic threshold. This circumstance makes the detection of this isomer unattainable with photoionization methods. It was found that the *trans*-HONO isomer is produced in quantities above the detection threshold. A steep decline of the transition intensities at higher photon energies in the threshold photoelectron spectrum pointed towards dissociative ionization, which was confirmed by electronic structure methods.

Ziel dieser Forschungsarbeit war es die Reaktionen zwischen Kohlenwasserstoffen und Stickoxiden in Verbrennungsprozessen unter erhöhtem Druck zu untersuchen. Dazu wurden Reaktionsgemische von Methan mit NO mithilfe von bildgebender Photoionen-Photoelektronen Koinzidenz Spektroskopie untersucht. Besonderes Augenmerk wurde auf die salpetrige Säure gelegt. In den Experimenten war kein HNO_2 detektierbar obwohl theoretische Reaktionsgeschwindigkeiten auf das Gegenteil hindeuten. Es wurde gezeigt, dass HNO_2 detektierbar sein sollte, da das Kation nahe der Ionisationsenergie keine Dissoziation unterläuft. Im Gegensatz dazu wurde festgestellt, dass das *cis*-HONO Isomer bei der Ionisierung bei Energien nahe seiner adiabatischen Schwelle dissoziiert. Dieser Umstand macht den Nachweis dieser Spezies mit Photoionisationsmethoden unmöglich. Ebenfalls wurde nachgewiesen, dass das *trans*-HONO Isomer in ausreichenden Konzentrationen entsteht, um detektiert zu werden. Ein steiler Abfall der Übergangsintensitäten bei höheren Photonenenergien im Schwellenphotoelektronenspektrum deutet jedoch auf dissoziative Ionisation hin, was durch den Einsatz von Elektronenstrukturmethoden bewiesen wurde.

Publications

Journal publications as first author with peer-review

Nitrous acid in high-pressure oxidation of CH_4 doped with nitric oxide: Challenges in the isomer-selective detection and quantification of an elusive intermediate
Hoener, M., Kasper, T.
Combustion and Flame, 2022, 243, 112096

Threshold photoionization shows no sign of nitryl hydride in methane oxidation with nitric oxide
Hoener, M., Bodi, A., Hemberger, P., Endres, T., Kasper, T.
Physical Chemistry Chemical Physics, 2021, 23(2), pp. 1265–1272

A pressurized flow reactor combustion experiment interfaced with synchrotron double imaging photoelectron photoion coincidence spectroscopy
Hoener, M., Kaczmarek, D., Bierkandt, T., Bodi, A., Hemberger, P., Kasper, T.
Review of Scientific Instruments, 2020, 91(4), 045115

Journal publications as co-author with peer-review

A combustion chemistry study of tetramethylethylene in a laminar premixed low-pressure hydrogen flame
Bierkandt, T., Hemberger, P., Oßwald, P., Gaiser, N., **Hoener, M.**, Krüger, D., Kasper, T., Köhler, M.
Proceedings of the Combustion Institute, 2023, 39(2), pp. 1699–1708

Activation effect of ozone and DME on the partial oxidation of natural gas surrogates and validation of pressure-dependent ozone decomposition
Kaczmarek, D., Bierkandt, T., Rudolph, C., Grimm, S., Shaqiri, S., **Höner, M.,** Gaiser, N., Atakan, B., Köhler, M., Hemberger, P., Kasper, T.
Applications in Energy and Combustion Science, 2023, 13, 100107

Observation of low-temperature chemistry products in laminar premixed low-pressure flames by molecular-beam mass spectrometry
Bierkandt, T., Oßwald, P., Gaiser, N., Krüger, D., Köhler, **M., Hoener,** M., Shaqiri, S., Kaczmarek, D., Karakaya, Y., Hemberger, P., Kasper, T.
International Journal of Chemical Kinetics, 2021, 53(10), pp. 1063–1081

Experimental flat flame study of monoterpenes: Insights into the combustion kinetics of α-pinene, β-pinene, and myrcene
Bierkandt, T., **Hoener, M.**, Gaiser, N., Hansen, N., Köhler, M., Kasper, T.
Proceedings of the Combustion Institute, 2021, 38(2), pp. 2431–2440

Conferences

Pollutant formation in energy conversion processes
Höner, M., Bierkandt, T., Shaqiri, S., Kaczmarek, D., Kluge, S., Köhler, M., Oßwald, P., Hemberger, P., and Kasper, T.
Molecular Physics and Physical Chemistry with Advanced Photon Sources
739. WE-Heraeus-Seminar (2022)

Optimiertes Design eines Plug-Flow Reaktors zur Durchführung von Verbrennungsexperimenten
Liaw, J.C., Höner, M., Kasper, T.
Thermodynamik-Kolloquium 2019, Universität Duisburg, Germany (2019)

Photoelektronen-Photoionen Koinzidenz Spektrometrie in Hochdruckreaktorexperimenten mit NO dotierten mageren und fetten Methangemischen
Höner, M., Kaczmarek, D., Osswald, P., Kasper, T.
29. Deutscher Flammentag, Bochum, Germany (2019)

A Novel Instrument Platform for the Investigation of Particle Formation from the Gas Phase
Kasper, T., Höner, M., Papanastasiou, D., Lekkas, A., Kounadis, D., Orfanopoulos, J.
67th American Society of Mass Spectrometry Conference, Atlanta, GA, USA (2019)

Study of the Influence of Nitric Oxide Addition on Lean Partial Oxidation of Methane
Höner, M., Kasper, T.
37. International Symposium on Combustion, Dublin, Ireland (2018)

Lean Partial Oxidation of Methane in the Presence of Nitrogen Monoxide as a Model for Exhaust Gas Recirculation
Höner, M., Kaczmarek, D., Kasper, T.
66th American Society of Mass Spectrometry Conference, San Diego, Ca, USA (2018)

Molecular-beam Mass Spectrometric and Numerical Investigation of the Intrusive Flame Sampling Effect on Premixed Low-Pressure Flame Structure
Karakaya, Y., Deng, L., Wlokas, I., Höner, M., Kasper, T.
65th American Society of Mass Spectrometry Conference, Indianapolis, In, USA (2017).

An integrated overall system model for model-based development | Ein integriertes Gesamtsystemmodell für die modellbasierte Entwicklung
Hooshmand, Y., Höner, M., Danjou, S., Köhler, P.
DFX 2016: Proceedings of the 27th Symposium Design for X, 2016, pp. 243–254

Index

Figures

Index of abbreviations

CRF-PEPICO	combustion reactions followed by double imaging photo ion photoelectron coincidence spectroscopy
EI-ToF-MBMS	electron ionization time-of-flight molecular beam mass spectrometry
i^2PEPICO	double-imaging photoelectron photoion coincidence spectroscopy
ms-TPES	mass selective photoelectron spectrum
NOx	oxides of nitrogen (i.e., NO, NO_2, N_2O)
PES	potential energy surface
ROI	region of interest
TPE	threshold photoelectrons
TPES	threshold photoelectron spectrum
a, b, c, …	stochiometric coefficients
A, B, C, …	reactants
A	pre-exponential factor
c	disturbance factor
C_A	concentration of A (mol/m^3)

D_i	mass discrimination for species i
E_A	activation energy of reactant A
F_A	injected molar feed rate of reactant A (mol/s)
FKT	sampling function
k	rate constant
$k^{(f)}$	forward reaction rate constant
$k^{(r)}$	reverse reaction rate constant
$k_{j/k}$	calibration factor for species j and k
m/z	mass to charge ratio
n	amount of substance
Q	constant flow rate
r_A	rate of reaction for reactant A
R	ideal gas constant (J mol^{-1} K^{-1})
S_i	signal intensity for species i
t	time (s)
T	Temperature (K)

T_{inj}	injection temperature of the sampled gas (K)
T^b	temperature dependence of the pre-exponential factor
v_0	velocity at the reactor entrance (ms^{-1})
V	volume (m^3)
X_A	fraction of reactant A that is converted
x_i	mol fraction of species i
α_i	signal loss factor for species i
σ_i	photoionization cross section of species i
τ	residence time
0	index for reactor entrance
f	index for reactor exit
i	species index
ref	index for reference species

1 Introduction

Combustion plays an important role in energy systems and still most energy is converted by combustion both to produce electricity and heat as well as mechanical energy in transport (British Petroleum, 2023). Hence, understanding combustion processes is still important in the present and will be important for the future (Kohse-Höinghaus, 2023).

The current energy crisis that unfolded starting in mid-2022 in Europe shows that fossil fuels and, hence, combustion still play a significant role in the energy mix providing power to western (and all other) societies. Europe's dependence on Russian fossil fuel imports (Li *et al.*, 2023) made the European economy susceptible to the shock introduced by the changing geopolitical situation (Mišík and Nosko, 2023). In short, the whole energy crisis unfolding in Europe and elsewhere is also a fossil fuel crisis and shows the importance of fossil energy sources. The primary energy provided by fossil fuels is mainly (i.e., very close to 100 %) converted by combustion. Coal is converted in thermal power plants, while gas is converted to thermal energy in households, to generate electricity, and industrial process heating. Oil is the primary source of energy for transport, in every mode (i.e., land-bound, sea-bound and air-bound).

To conclude, it can be stated that combustion-based power is still in high demand and increasing power consumption can, in the short run, only be addressed by fossil power generation. This circumstance is clearly visible in emerging economies like China, which constantly increase their fossil fuel consumption and expand their fossil power conversion (Ahmed, Shuai and Ahmed, 2023).

In the present work several reaction conditions of methane doped with nitric oxide were investigated. The objective was to gain understanding of the interactions of oxides of nitrogen (NO_x) with low temperature combustion reactions at elevated pressures. Such conditions can be found when NO_x are directly introduced into fresh combustible mixtures or through decomposition of NO_x forming chemicals in a combustion mixture. To perform the experiments a reactor set up coupled to synchrotron double imaging photoelectron photoion spectroscopy was devised. Research in NO_x interactions is important to mitigate the emission of oxides of nitrogen and enable clean combustion. In the course of the work performed for this thesis new insights into the energetics and kinetics of nitric acid were gained. These findings can help

improve the understanding not only of combustion processes, but also of basic chemistry and in specialized fields like atmospheric chemistry and even astrochemistry.

2 Nitrogen chemistry

2.1 The role of nitrogen chemistry in combustion

Nitrogen chemistry plays a significant role in most practical combustion processes, since, almost always, air is used as the oxidizer. Air is comprised of ca. 78 % nitrogen, 21 % oxygen and some trace gases, of which most is argon. When temperatures are sufficiently high, oxygen reacts directly with nitrogen to form NO (Lissianski, Zamansky and Gardiner, 2000 pp. 126-128). But, also, the complex radical pool formed upon hydrocarbon combustion can interact with the nitrogen contained in air and produce NO (Lissianski, Zamansky and Gardiner, 2000 pp. 126-128; Glarborg *et al.*, 2018). Another source of nitrogen to interact in combustion processes can be nitrogen containing fuels such as NH_3 (Valera-Medina *et al.*, 2018) or simple wood and organically derived fuels such as coal. Especially in biomass combustion, significant amounts of bound nitrogen interact in combustion processes to release oxides of nitrogen (Kohse-Höinghaus *et al.*, 2010). Another source of nitrogen interacting in combustion processes are nitrogen releasing agents that are used as fuel additives such as cetane enhancers (Ickes, Bohac and Assanis, 2009). This large array of nitrogen interactions encountered in combustion shows the significance of understanding nitrogen chemistry in hot chemically reacting systems.

Oxides of nitrogen are the most important nitrogenized species to interact in combustion. For many reaction networks, the origin is the simplest oxide of nitrogen NO. Further oxidized, it forms NO_2, which is highly reactive and has a strong radical character (Fuller and Goldsmith, 2019). Another important role is played by N_2O in combustion nitrogen chemistry (Tomeczek and Gradoń, 2003). Oxides of nitrogen also play a significant role in the reactivity of combustion mixtures. NO has been shown to have both inhibiting as well as sensitizing effects on combustion reactions (Rasmussen, Rasmussen and Glarborg, 2008; Zhang *et al.*, 2021). HONO, the focus of this work, is formed by the reaction of NO_2 with hydrogen (among other reactions) and dissociates mainly to form NO and OH. This process recycles the nitrous oxide, while providing the reactive OH radical to interact in further reactions, e.g., in ignition if NO_x is present in the combustible mixture (Chai and Goldsmith, 2017; Hoener and Kasper, 2022).

2.2 NO_x formation mechanisms

To understand the intricacies of nitrogen interactions in combustion, it is first necessary to understand the basis on which nitrogen chemistry takes place in reacting hydrocarbon systems. Several mechanisms are known which produce reactive nitrogen compounds in low and high temperature combustion. In the following sections the different basic pathways of formation of nitrogen compounds in combustion will be presented. The classification follows that of (Lissianski, Zamansky and Gardiner, 2000, pp. 126-128) and includes:

- The Zeldovich NO formation mechanism (Thermal NO)
- The Fenimore NO formation mechanism (Prompt NO)
- The N_2O formation pathway
- The fuel NO formation pathway
- The NNH mechanism

Since the classification provided by Lissianski et al. some advances have been made in the understanding of formation pathways and updated knowledge will be included in this section.

2.2.1 The Zeldovich NO formation mechanism

The production of NO by the Zeldovich or thermal NO mechanism progresses via direct reactions of the nitrogen contained in the combustible gas mixture (e.g., if air is used as the oxidizer). The original mechanism proposed by Zeldovich only considers the direct reaction of nitrogen with oxygen as shown in R1 and R2 (Zeldovich, 1946).

$$N + O_2 = NO + O \qquad (R1)$$

$$O + N_2 = NO + N \qquad (R2)$$

Deviating from and in addition to the reactions proposed by Zeldovich, Lissanksi et al. state that radical reactions also play a role in thermal NO formation (Lissianski, Zamansky and Gardiner, 2000, p. 126) as shown in R3.

$$N + OH = NO + H \qquad (R3)$$

In a recycling step, a reaction with H occurs producing more OH to further interact in the reaction to form NO as shown in R4.

$$H + O_2 = OH + O \qquad (R4)$$

Thermal NO is mostly formed in the regions of highest temperatures and radical activity (Lissianski, Zamansky and Gardiner, 2000, pp. 126-127). High combustion temperatures are required for thermal NO formation because of the high activation energies of the rate limiting reactions for this process (Maligne, Cessou and Stepowski, 2009). R1 occurs at a reaction rate of $k = 1.8 \cdot 10^{14} \exp(318\ kJ \cdot mol^{-1}/RT)$ with a very high activation energy of 318 kJ/mol (Warnatz, Maas and Dibble, 2006, p. 260). Oxygen radicals attack the N-N bond in the N_2 atom at sufficiently high temperatures and the reaction is very temperature sensitive (Lissianski, Zamansky and Gardiner, 2000, pp. 126-127) and the strong triple bond of molecular nitrogen results in the high activation energy. In technical combustion systems thermal NO formation, thus, occurs at high temperatures such as the temperatures encountered in the Diesel process and represents the main formation pathway for NO_x in this particular process (Verbiezen *et al.*, 2007; Maligne, Cessou and Stepowski, 2009). Of course, other processes with sufficiently high temperatures also led to the formation of thermal NO, and hence a strategy for the reduction of thermal NO_x emissions is to lower the combustion temperature (Liu *et al.*, 2017).

2.2.2 The Fenimore NO formation mechanism

The Fenimore or prompt NO mechanism attempts to describe the rapid formation of NO in the flame front, where insufficiently high temperatures are encountered for the production of thermal NO (Lissianski, Zamansky and Gardiner, 2000, p. 127; Glarborg *et al.*, 2018). To produce NO, the strong triple bond in molecular nitrogen must be broken, which can thermally only occur at sufficiently high temperatures. The Fenimore mechanism circumvents the activation energy requirement through attack of the nitrogen bond by CH radicals, which are present in high concentration in the flame front (Lissianski, Zamansky and Gardiner, 2000, p. 127). The CH radicals react with N_2 to form HCN and N as shown in R5.

$$CH + N_2 = HCN + N \qquad (R5)$$

NO formation proceeds through R1 and R3 (Lissianski, Zamansky and Gardiner, 2000, p. 127). The elementary reaction R5, however, does not convey the true nature of the reaction of

nitrogen with the CH radical, since the reaction is spin forbidden (Harvey, 2007). The CH radical has a doublet ground state, atomic nitrogen a quartet ground state, while the stable HCN and N_2 are singlet species (Harvey, 2007). Hence, the reaction proceeds via intermediate steps. It has been proposed that it involves the formation of the internally excited (Moskaleva and Lin, 2000) intermediate HCN_2 (Berman and Lin, 1983). Similarly, and more recently Harvey proposed a formation route via HCN_2 with a subsequent stabilization of the quartet state and a resulting break of the N-N bond, leading to HCN + N (Harvey, 2007). Spin forbidden processes are unfavorable with respect to spin allowed processes at higher temperatures (Harvey, 2007) and other theoretical work presents a different, spin-allowed path to the formation of NO from the promptly formed N (Moskaleva and Lin, 2000). The reaction proceeds by the formation of NCN and H from CH reacting with N_2 as stated in R6.

$$CH + N_2 = NCN + H \qquad (R6)$$

This reaction has successfully been implemented in a reaction mechanisms, was successfully validated and can now be considered state of the art (Klippenstein *et al.*, 2018). It has to be noted, however, that Berman et al. propose that the HCN_2 may still play a role in the NCN mechanism (Berman *et al.*, 2007).

The different mechanisms explaining the formation of prompt NO and the ongoing discussion show that nitrogen chemistry in combustion is a field of active research with some knowledge gaps that still have to be filled.

2.2.3 The N_2O formation pathway

In a reaction similar to the thermal NO route, atomic oxygen can attack the molecular nitrogen in a reaction with an additional collider (M) to form N_2O (Warnatz, Maas and Dibble, 2006, p. 265) as shown in R7.

$$N_2 + O + (M) = N_2O + (M) \qquad (R7)$$

Direct decomposition of N_2O plays a secondary role, since it is a spin forbidden process (Karabeyoglu *et al.*, 2008). To decompose, N_2O can react with atomic oxygen to form NO as stated in R8.

$$N_2O + O = NO + NO \qquad (R8)$$

Moreover, the reaction of N_2O with atomic hydrogen as stated in R9 and R10 plays a significant role in the decomposition of N_2O as recently reported reaction rates validated against flame speed measurements for this process show (Janzer *et al.*, 2022).

$$N_2O + H = N_2 + OH \qquad (R9)$$

$$N_2O + H = NH + NO \qquad (R10)$$

While R10 contributes to the formation of NO_x, R9 does not and acts as a sink for N_2O without creating NO in the process. Obviously, R9 may interact with thermal NO formation through the OH radical according to R3. Subsequently, OH radical formation leads to further fuel destruction.

2.2.4 The fuel NO formation pathway

When fuels containing nitrogenous compounds are combusted, fuel nitrogen (Warnatz, Maas and Dibble, 2006, pp. 265-267) can be converted into NO via intermediate steps (Warnatz, Maas and Dibble, 2006, pp. 265-267; Glarborg *et al.*, 2018). Conversion mainly takes place via the initial formation of ammonia and HCN (Lissianski, Zamansky and Gardiner, p. 128, 2000; Lucassen *et al.*, 2011). Lucassen et al. found significant concentrations of both HCN and NH_3 at similar heights above burner in laminar premixed combustion (Lucassen *et al.*, 2009). In this case, HCN had a concentration an order of magnitude higher than NH_3, hinting at HCN playing a significant role as a combustion intermediate in the formation of fuel NO_x. Generally speaking, fuel-bound nitrogen has a significant contribution to NO_x emissions in biomass combustion (Kohse-Höinghaus *et al.*, 2010) and when (former) organic matter is involved such as e.g. in the combustion of lignite (Wang *et al.*, 2012).

Since ammonia formation is a key kinetics path to fuel NO, the same reactions play a significant role in ammonia combustion, as ammonia is a nitrogen-containing fuel. Ammonia combustion has recently been broadly studied as a route to carbon free combustion processes (Valera-Medina *et al.*, 2018). It is proposed that the combustion of ammonia in practical combustion systems, like gas turbines is feasible (Okafor *et al.*, 2019). The conversion of ammonia into NO, however, poses significant challenges for NO_x emission control in such processes. The NO concentration in the exhaust gas stream of NH_3 combustion processes can reach very high concentrations of, e.g., 1000 ppm (Okafor *et al.*, 2019). NO_x control is paramount for such

conversion processes to be feasible and acceptable in a regulated environment (Okafor *et al.*, 2019).

2.2.5 The NNH mechanism

The NNH mechanism acts in a similar manner to the N_2O mechanism, however in this case a direct addition of hydrogen to nitrogen takes place according to R11 (Glarborg *et al.*, 2018). This mechanism creates a significant portion of the NO formed during combustion and requires the participation of both O and H radicals in a subsequent reaction to form NO and NH as shown in R12 (Lissianski, Zamansky and Gardiner, 2000, p. 128).

$$N_2 + H + (M) = NNH + (M) \qquad (R11)$$

$$O + NNH = NO + NH \qquad (R12)$$

2.3 NO doped low-temperature hydrocarbon conversion

In this work the influence of NO on low-temperature combustion interactions was investigated (Hoener *et al.*, 2020, 2021; Hoener and Kasper, 2022). To investigate the interactions of NO with the reaction network, the oxidation of methane doped with NO was investigated for three different conditions in a plug-flow reactor (Hoener and Kasper, 2022). The processes took place at an elevated pressure of 6 bar and were probed with synchrotron double imaging photoelectron photoion spectroscopy (i^2PEPICO) (Hoener *et al.*, 2021). The reactions in the reactor occurred at relatively modest temperatures between 473.15 K and 973.15 K (Hoener and Kasper, 2022). In practical combustion systems such interactions of NO_x and the remaining reactant mixture can take place when NO_x is introduced to the reactive mixture prior to ignition, e.g., in exhaust gas recirculation (Knyazkov *et al.*, 2009).

NO has been shown to have both sensitizing and inhibiting effects on combustion (Zhang *et al.*, 2021). Slow reacting hydrocarbons such as methane show a sensitization by the addition of NO to the reactant stream (Song *et al.*, 2019). For high dopant concentrations of NO recent combustion mechanisms show some disagreement with the measurement for the reaction onset temperature so further investigation of these conditions may be warranted (Hoener and Kasper, 2022). In fact, a recent uptick of research in the interaction of NO in low-temperature

chemistry could be observed, e.g., (Marrodán *et al.*, 2018, 2019; Gossler *et al.*, 2021; Yuan *et al.*, 2021; Zhang *et al.*, 2021). In this thesis the interactions of NO_x in low-temperature combustion were probed with a focus on the formation and decomposition of nitrous acid intermediates (Hoener *et al.*, 2020, 2021; Hoener and Kasper, 2022).

2.4 Nitrous acid intermediates in combustion processes

Nitrous acid (HONO/HNO_2) represents an important intermediate in low temperature combustion kinetics involving reactive nitrogen species, such as NO_x. Many HONO conformations theoretically exist. Asatryan et al. identified several isomers using *ab-initio* methodology (Asatryan, Bozelli and Simmie, 2007), which are not proposed to exist in combustion. In combustion reaction networks, only the rather stable HNO_2, *trans*-HONO and *cis*-HONO isomers are encountered (Fuller and Goldsmith, 2019).

In the NO_2 molecule, all atoms act as radical sites, which gives this species a very strong radical character (Fuller and Goldsmith, 2019). The radical nature allows NO_2 to rapidly interact with its reaction partners even at low temperatures as encountered in atmospheric chemistry or in compressed fuel/oxidizer mixtures prior to ignition. All HONO isomers are formed by the reaction of hydrogen with NO_2. The direction and location of addition of the hydrogen atom to the NO_2 molecule dictates which of the three nitrous acid isomers are formed (Chai and Goldsmith, 2017), as is shown in Figure 1.

The reactions shown in Figure 1 can also occur if no hydrogen is present and Figure 1 shows only the most rudimentary direct reaction with atomic hydrogen to form nitrous acid. In real world reaction networks if no H is present, hydrogen can be directly abstracted from hydrogen-containing species due to the very active properties of NO_2. In combustion, these reactions are mainly direct abstraction reactions from the hydrocarbon fuel and hydrogen-containing radicals and intermediates.

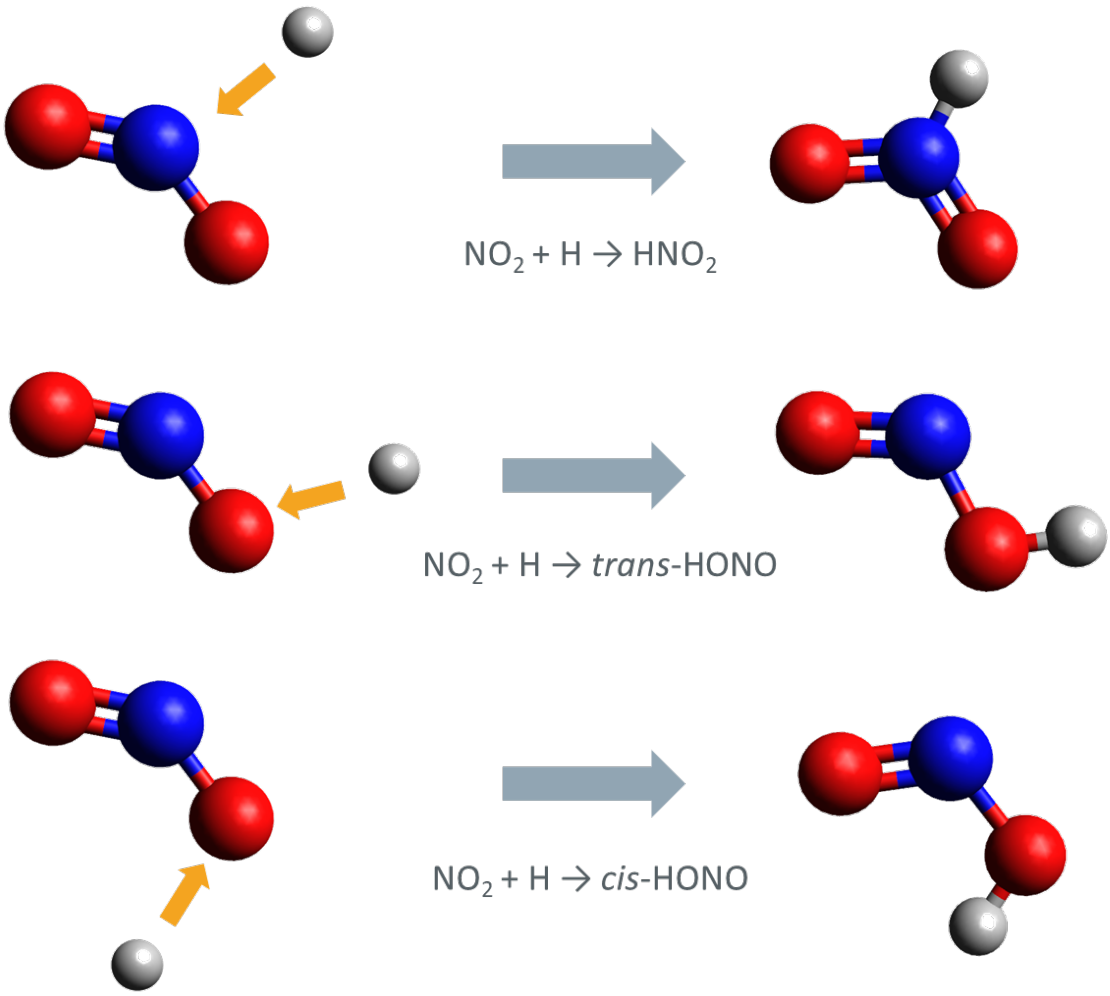

Figure 1: Formation of the three different nitrous acid isomers formed in combustion reactions (Chai and Goldsmith, 2017) by hydrogen addition to NO_2 at different positions in the NO_2 molecule and from different directions.

Of high significance for this work are the abstraction reactions from CH_4 acting as the hydrocarbon fuel, as shown in reactions R13, R14 and R15, since these reactions were investigated in published work leading up to this thesis (Hoener *et al.*, 2021; Hoener and Kasper, 2022).

$$CH_4 + NO_2 = CH_3 + \textit{trans}\text{-HONO} \qquad \text{(R13)}$$

$$CH_4 + NO_2 = CH_3 + \textit{cis}\text{-HONO} \qquad \text{(R14)}$$

$$CH_4 + NO_2 = CH_3 + HNO_2 \qquad \text{(R15)}$$

These reactions can take place in any hydrogen containing fuel prior to, during, and after initiation of combustion. In a more general form, the reactions of hydrocarbons with NO_2 to form

nitrous acid isomers can be written as R16, R17 and R18. In these reactions, R denotes some residual hydrocarbon moiety or H (Chai and Goldsmith, 2017).

$$RH+NO_2 = R + \textit{trans}\text{-}HONO \qquad (R16)$$

$$RH+NO_2 = R + \textit{cis}\text{-}HONO \qquad (R17)$$

$$RH+NO_2 = CH_3 + HNO_2 \qquad (R18)$$

R16, R17 and R18 are the initiating reactions that can take place at low temperature in the presence of NO_2 and, hence, they may be at play in ignition chemistry.

At higher temperatures, reactions with HNO to form HONO dominate according to R19 (Hoener and Kasper, 2022).

$$NO_2 + HNO = NO + HONO \qquad (R19)$$

In practical combustion processes, NO_2 must either be introduced into the reactive mixture or be formed prior to combustion for the reactions with fuel to take place. Introduction into the reactants can be found, e.g., in exhaust gas recirculation. In such processes, a fraction of the exhaust gases of a combustion process is recirculated into the combustion chamber (Chai and Goldsmith, 2017). These processes will by design introduce NO_x into the combustible mixture prior to ignition. There, they are mixed with the fresh charge in the case of internal combustion engines or with fresh combustible mixtures in other cases. Reburning of the exhaust gases reduces the NO_x fraction of the gas (Knyazkov *et al.*, 2009). This is an important process by which ignition of the combustible mixture can be influenced. The nitrogenized species, mainly NO and NO_2, can interact with the un-combusted mixture and in the low-temperature combustion regime, even during the initial stages of ignition. Low temperatures are advantageous for the formation of high concentrations of NO_2 (Hoener *et al.*, 2021). The radical character of NO_2 then enables direct interaction with the fuel to form the nitrous acid intermediates. In turn, these intermediates decompose to form NO and OH according to R20. OH on the other hand can play a significant role in both ignition and later-stage combustion interactions.

$$HONO = OH + NO \qquad (R20)$$

HNO_2 was thought to mainly undergo isomerization to HONO and then to decompose. Recent theoretical reaction rates suggest that HNO_2 primarily undergoes unimolecular decomposition, completely bypassing the isomerization route to directly form OH and NO (Chen, Fuller

and Goldsmith, 2019; Hoener and Kasper, 2022). It was found in the present work that the assumptions suggested by the recent reaction rates by Chen et al. are not in good agreement with the measurements. No distinct HNO_2 signal was found in photoionization experiments despite the reaction rates suggesting otherwise (Hoener *et al.*, 2021).

Also, for combustion kinetics modeling both HONO (i.e., *trans* and *cis*) isomers are generally lumped into one species, while HNO_2 is often treated as a separate species, which is deemed generally acceptable (Fuller and Goldsmith, 2019). In the present work it was found, that the photoionization properties of *cis*-HONO do not allow the use of popular photoionization methods for its detection (Hoener *et al.*, 2021; Hoener and Kasper, 2022). Hence, it was concluded in the present work that, a separate treatment of both isomers in combustion models may be advantageous (Hoener and Kasper, 2022). Separate treatment of the HONO isomers would enable a direct comparison of measurements of the solely detectable *trans*-HONO isomer to simulation results. This approach would also enable the theoretical determination of isomer branching fractions.

3 Methods and Principles

3.1 Chemical kinetics

The progress of chemical reactions can be described by rate laws. The reaction rate for a species a is dependent on several different parameters and conditions like the concentration of species, temperature, etc. (Eq. 1) (Missen, Mims and Saville, 1999, p. 5).

$$r_A = r_A(\text{concentration}, \text{temperature}, \dots) \quad \text{Eq. 1}$$

The rate law with rate constant k expresses the consumption of species to form other species according to Eq. 2 (Warnatz, Maas and Dibble, 2006, p. 73).

$$A + B + C + \dots \xrightarrow{k} D + E + F + \dots \quad \text{Eq. 2}$$

For the consumption of species A this becomes Eq. 3 (Warnatz, Maas and Dibble, 2006, p. 73).

$$\frac{d[A]}{dt} = -k \cdot [A]^a \cdot [B]^b \cdot [C]^c \dots \quad \text{Eq. 3}$$

The exponents a, b and c describe the reaction orders for the species A, B and C, while k is the temperature-dependent rate coefficient of the reaction. The reaction order describes the relationship between the concentration of species in the mixture and the rate of the reaction.

Oftentimes reactions will not proceed to full consumption of the educts and an equilibrium between educts and products is achieved, as the forward and reverse rates of the reaction equalize (Theodore, 2012, p. 73).The dependence in Eq. 1 can then be expressed as in Eq. 4 (Warnatz, Maas and Dibble, 2006, p. 75), where the index f denotes the forward rate and r the reverse rate.

$$k^{(f)} \cdot [A]^a \cdot [B]^b \cdot [C]^c \cdot \dots = k^{(r)} \cdot\cdot [D]^d \cdot [E]^e \cdot [F]^f \cdot \dots \quad \text{Eq. 4}$$

In reaction modeling, elementary reactions are used (Bierkandt, 2018, p. 15). They have distinct advantages like a constant reaction order, which can be determined by the molecularity of the reaction (Warnatz, Maas and Dibble, 2006, p. 76).

The isomerization or dissociation of a molecule is described by the unimolecular reaction as shown in Eq. 5. (Warnatz, Maas and Dibble, 2006, pp. 75-77).

$$\mathrm{A} \rightarrow \text{products} \quad (\mathrm{Eq.}\,5)$$

This reaction has a first-order time behavior (i.e., a doubling of the concentration causes a doubling of the reaction rate) (Warnatz, Maas and Dibble, 2006, p. 76). This reaction is of importance for the present work. Both the isomerization behavior and the unimolecular decomposition of HONO was investigated with respect to the theoretical rate laws for this species in light of the experimental observation (Hoener *et al.*, 2021; Hoener and Kasper, 2022).

Second-order reactions have the form expressed in Eq. 6 and Eq. 7 and are also called bimolecular, since two molecules are involved in the reaction (Warnatz, Maas and Dibble, 2006. p. 76).

$$\mathrm{A} + \mathrm{B} \rightarrow \text{products} \quad (\mathrm{Eq.}\,6)$$

$$\mathrm{A} + \mathrm{A} \rightarrow \text{products} \quad (\mathrm{Eq.}\,7)$$

The rate law of these reactions is of second order, meaning a doubling of the concentration of the reactants involved causes the rate to quadruple (Warnatz, Maas and Dibble, 2006, p.76).

Eq. 8, Eq. 9 and Eq. 10 show trimolecular reactions. These reactions are of third order and have a third-order reaction rate law (Warnatz, Maas and Dibble, 2006, p. 76). In the gas phase, third-order reactions are less likely than lower order reactions.

$$\mathrm{A} + \mathrm{B} + \mathrm{C} \rightarrow \text{products} \quad (\mathrm{Eq.}\,8)$$

$$\mathrm{A} + \mathrm{A} + \mathrm{B} \rightarrow \text{products} \quad (\mathrm{Eq.}\,9)$$

$$\mathrm{A} + \mathrm{A} + \mathrm{A} \rightarrow \text{products} \quad (\mathrm{Eq.}\,10)$$

The temperature dependence of a reaction is described by the Arrhenius, it describes the dependence of ($-r_A$) on the temperature law (Warnatz, Maas and Dibble, 2006, p. 79).The Arrhenius law is expressed in Eq. 11.

$$k_A = A \cdot e^{-\frac{E_A}{RT}} \quad (\mathrm{Eq.}\,11)$$

In Eq. 11, the activation energy of the reaction is denoted E_A. This value is the energy barrier that has to be overcome to initiate the reaction between the species (Warnatz, Maas and Dibble, 2006, p. 79). A is the preexponential factor, R the ideal gas constant and T is the temperature at which the reaction takes place.

Mechanistic modeling of combustion uses a set of elementary reactions (*vide supra*). The Arrhenius law is used in the modified version stated in Eq. 12, which takes into account the temperature dependence of the pre-exponential factor (Warnatz, Maas and Dibble, 2006, p. 79), to calculate the reaction velocity.

$$k_A = A \cdot T^b \cdot e^{-\frac{E_A}{RT}} \quad (\text{Eq. } 12)$$

Additionally, thermodynamic data is required, such as the enthalpy, entropy and heat capacity as functions of temperature. The data is stored in a polynomial format, i.e., by polynomial coefficients. The thermodynamic data is then interpolated for the given temperature by use of NASA polynomials, whose history, form and use are exhaustively discussed by McBride et al. (McBride, Zehe and Gordon, 2002).

3.2 The plug-flow reactor

The plug-flow reactor approaches ideal flow and reaction conditions for chemical kinetics experiments (Levenspiel, 1999, pp. 90-91; Theodore, 2012, p. 210). It allows for a single flow filament to model the flow inside the reactor using a one-dimensional assumption. Typically, such a reactor is realized as a heated and pressurized pipe. If plug flow is approached, the fluid has no radial temperature, concentration, or velocity gradients across the reactor volume (Theodore, 2012, pp. 209-210). Figure 2 shows the plug-flow velocity distribution in comparison to a viscid laminar flow with a boundary layer along a reactor volume (Theodore, 2012, p. 212).

Axially, no transport between differential flow elements is assumed and the flow is completely unmixed along the reactor (Theodore, 2012, pp. 209-210). A flow element (and all species contained in that element) thus will experience a residence time according to the flow velocity, as the plug of gas moves along the reactor (Theodore, 2012, p. 211). Furthermore, since there is no axial diffusion, the species will only interact withing that flow element. In practice,

for the simulation using reaction mechanisms, this means that no transport data is required for plug-flow reactor simulations.

Figure 2: Comparison of a laminar flow velocity profile with a plug-flow velocity profile according to (Theodore, 2012, p.212).

For the experiment used in this work, it has to be noted, that there is a temperature dependence of the residence time, since the volume flow injected into the reactor was held constant for all temperatures along a temperature ramp (Hoener *et al.*, 2020).

To develop the governing performance equations for a plug-flow reactor one has to consider the flows of educts and products across the boundaries of the reactor as shown in Figure 3.

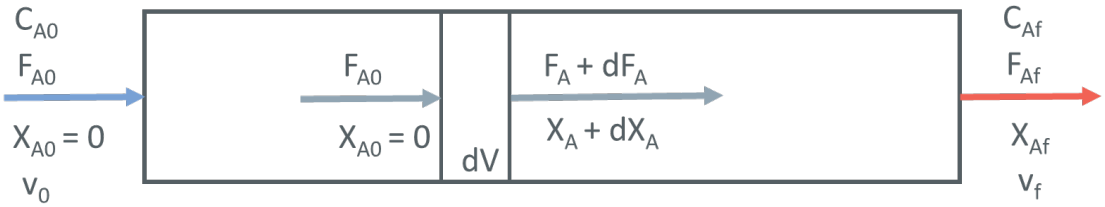

Figure 3: Conditions across the boundaries of the plug-flow reactor and through a volume element in the reaction volume of the reactor according to (Levenspiel, 1999, p. 101).

Levenspiel develops the plug-flow reactor performance equations for a volume element dV (Figure 3), as the composition of the fluid in the reactor varies across its length. Here C_A is the concentration of a species A, F_A is the injected molar flow rate of A, X_A is the conversion ratio of A, v_0 is the flow velocity at the inlet. Subscripts 0 denotes the inlet while subscript f denotes the outlet (Levenspiel, 1999, p. 101).

Eq. 1 expresses the balance of materials across the reactor (Levenspiel, 1999, p. 101).

$$input = output + disappearance\ by\ reaction\ (Eq. 13)$$

With F_A being the input of reactant A in moles/time, $F_A + dF_A$ being the output with the same unit and the disappearance of reactant A being $(-r_A)dV$ in moles/time Eq. 14 can be obtained. Combining Eq. 13 with Eq. 14 and noting Eq. 15 yields Eq. 16 (Levenspiel, 1999, p. 101).

$$F_A = (F_A + dF_A) + (-r_A)dV \quad (Eq. 14)$$

$$dF_A = d[(F_{A0}(1 - X_A)] = -F_{A0}dX_A \quad (Eq. 15)$$

$$F_{A0}dX_A = (-r_A)dV \quad (Eq. 16)$$

Integration yields the plug-flow performance equation (Eq. 17) (Levenspiel, 1999, p. 102)

$$\tau = \frac{V}{v_0} = \frac{VC_{A0}}{F_{A0}} = C_{A0}\int_0^{X_Af}\frac{dX_A}{-r_A} \quad (Eq. 17)$$

where τ is the residence time. Theodore expresses the equation for a constant flow rate Q across the inlet boundary of the reactor, in terms of the concentration of A and the reaction rate r_A in the more intuitive form shown in Eq. 18 (Theodore, 2012, p. 215).

$$\tau = \frac{V}{Q} = \int\frac{dC_A}{r_A} = C_{A0}\int\frac{dX_A}{-r_A} \quad (Eq. 18)$$

It is important to note that the plug-flow equations interrelate the rate of reaction, the extent of the reaction, the reactor volume, and the feed rate (Levenspiel, 1999, p. 103). If three quantities are known the fourth can be obtained (Levenspiel, 1999, p. 103). Hence, the plug-flow experiment can be used to find reaction rates or to compare measurements to known reaction rates. If a more complex chemically reacting mixture is present in the reactor, the chemical source term is a set of linked differential equations, which must be solved numerically (Theodore, 2012, p. 228). In the present work the plug-flow experiment was used to compare theoretically obtained reaction rates and the expected concentrations and molecular lifetimes to the ones observed in the experiment (Hoener *et al.*, 2021). This led to new insight into the kinetics of the reactions of HNO_2 and HONO.

3.3 Synchrotron vacuum ultra-violet radiation (VUV)

The experiments performed in this work used single-photon in single-electron out photoionization events for the ionization of species (Hemberger *et al.*, 2020). The ionization was achieved with tunable monochromatic synchrotron vacuum ultraviolet light. The advantage of using a synchrotron light source is the high light intensity while providing broad-spectrum light that can be filtered and monochromated down to a very narrow photon energy. This narrow photon energy can then be used to ionize all species in a rarified gas phase that have ionization energies below the selected photon energy. Ionization of species with ionization thresholds below the set photon energy are achieved while leaving all species with higher ionization energies in the neutral state. When used in mass spectrometry experiments the ionization energy yields a secondary selection criterion to distinguish isobaric (i.e., same nominal mass) species by their photon energies (Taatjes *et al.*, 2008). This property of the ionization method is extremely favorable when complex mixtures of species are encountered in a sample, such as in the complex species pool produced by chemically reacting flows in combustion experiments.

The broad-spectrum synchrotron radiation is produced by high-velocity electrons that experience some form of acceleration. The electrons are contained in a circular ultra-high vacuum tube and are focused and guided by magnetic fields. The electrons are typically released from an electron gun and accelerated in a linear accelerator (Willmott, 2011, p. 53). In the booster ring electrical fields are used to accelerate the electrons to near light speed before they enter the larger storage ring (Willmott, 2011, p. 53). Modern synchrotrons have long beam lifetimes and the lost electrons in the storage ring are replaced (i.e., a mode that is called top-up operation) by the injection system (Willmott, 2011, p. 53). This way the electron beam exists at a (near) constant beam current and velocity allowing for a constant photon flux and extremely high light intensity of the produced photons. Modern synchrotron facilities are designed specifically to produce synchrotron light that contains all wavelengths of the electromagnetic spectrum. The light energies range from deep infrared, over visible light and ultraviolet components to soft, hard and ultra hard x-rays (Willmott, 2011, p. 6). Some of those wavelengths can be produced by other light sources, e.g., lasers. Those sources, however, usually either provide lower intensity or non-tunable light in a narrow spectrum. Synchrotron light sources provide brilliant high intensity light. Either by design of the light producing device in the

electron beam path and/or filtering and monochromating facilities, the light becomes tunable and narrow spectrum (Johnson *et al.*, 2009; Willmott, 2011, p. 7).

The light is produced by insertion devices (Willmott, 2011, pp. 86-87), of which several general types exist, or by bending magnets. As the name suggests, bending magnets bend the electron beam contained in the ultra-high vacuum pipe, according to the Lorentz law. A magnetic field perpendicular to the velocity vector of the electron beam forces the electrons into a circular path, similar to what can be observed in a Teltron tube. Since the electrons have to go around the synchrotron, such bending magnets are required for the operation of any synchrotron. They are required not just to produce synchrotron radiation, but also to allow the electrons not to hit the wall of the pipe. In fact, the modern synchrotron is not a perfectly circular facility, but the electrons travel along straight pipe segments, to then be bent by bending magnets into the next straight segment (Willmott, 2011, p. 7). Bending magnets produce a broad spectrum, but lower intensity light. To obtain higher intensities, wigglers and undulators are inserted into the beam path (Willmott, 2011, pp. 86-97). These devices force the electron beam on a sinusoidal path using alternating magnetic fields. While the wiggler uses lower intensity fields and forces the electron beam on a lower acceleration path, the undulator forces the electrons into tighter bends along the sinusoidal path. Hence, the wiggler produces a broader light spectrum, than the undulator which produces a very bright peak in a narrow band of photon energies (Willmott, 2011, p. 6).

The light provided to the CRF-PEPICO (Combustion Reactions Followed by Photoelectron Photoion Coincidence Spectroscopy) endstation (Sztáray *et al.*, 2017) is produced by a bending magnet (Johnson *et al.*, 2009), yielding broad spectrum light. For the experiment, only the VUV spectrum between ca. 6 eV and 20 eV of photon energies is required and all other frequencies need to be excluded from the experiment. Furthermore, to ionize species in the beam interaction zone of the spectrometer (*vide infra*), only a narrow band of photon energies (in fact, one single photon energy would be preferrable, but can hardly be achieved technically) is desirable. To achieve this narrow photon energy band, all photons of other energies produced by the bending magnet must be discarded and the desirable photons must be guided to the experimental chamber.

These functions are achieved by the beam line (Johnson *et al.*, 2009). In the case of vacuum ultraviolet light, as the name suggests, the beam line has to be evacuated to very high vacuum,

since the desired VUV light will be absorbed, e.g., by water and oxygen molecules, depending on the photon energy. The beamline guides the light from the bending magnet tangentially inside the biological shielding provided by the encasing of the synchrotron storage ring.

The beamline accepts the light from the bending magnet through two slits in vertical and horizontal direction that can be used to adjust the photon flux (Johnson *et al.*, 2009). The desired light is deflected across several mirrors, that let harder radiation (i.e., x-rays) pass through. The hard radiation in the beam path is absorbed by an x-ray blocker before the desired spectrum leaves the synchrotron radiation shielding (Johnson *et al.*, 2009). After leaving the shielding, the radiation passes through a monochromating device that uses blazed and laminar gratings that can be set at an angle (Bodi *et al.*, 2012). By changing the incident angle of light (i.e., by tilting the grating), the photon energy of the reflected light beam is selected. The light is then guided through the evacuated tube, passing a secondary focusing mirror chamber to arrive at the rare-gas filter (Johnson *et al.*, 2009). The monochromator may let some undesirable higher harmonics pass through at lower intensities. These higher harmonics would severely disturb the ionization experiments, by creating ionization events at those higher harmonic energies. Hence, selective ionization by the narrow band light would not be possible. To reduce the intensity of those higher harmonics, the light beam is passed through an absorbing gas or gas mixture at higher pressure than the beam line (Johnson *et al.*, 2009). Since there is no known optical material to allow transmission of a large portion of the VUV wavelengths (i.e., above ca. 10.3 eV), continuity between the higher-pressure chamber of the rare-gas filter and the low-pressure beam line tube must be achieved (Johnson *et al.*, 2009). This is done by flowing a filtering gas into a metal tube that is open on both ends and differentially pumping the ends of the pressurized tube to achieve a steep drop in pressure of the filtering gas and preventing the gas from entering the beam line (Johnson *et al.*, 2009). Magnesium fluoride (MgF_2) allows passage of VUV photons below ca. 10.3 eV, and hence for these energies, a MgF_2 window that can be inserted into the beam path by a manual mechanical stage can be used as a filtering device (Hoener *et al.*, 2020). Above this photon energy, MgF_2 is opaque to VUV radiation and does not allow higher harmonics to pass through.

In conclusion of this chapter, it can be stated that the synchrotron coupled with the beam line facility delivers tunable, monochromatic light for the selective VUV ionization of species. The method enabled an energy selective and species-specific probing of the combustion species encountered in the experiments that led to this work and provided indispensable information

about the energetics and ionization properties of the HONO intermediate (Hoener *et al.*, 2021; Hoener and Kasper, 2022).

3.4 Molecular-beam sampling

Injection of gaseous samples into the ionization region of the spectrometer for the reactor experiments is performed using the molecular-beam sampling technique. This technique uses a nozzle skimmer arrangement to draw a gas sample form the reacting flow, expand the gas beam and inject the sample into the high-vacuum ionization region of the spectrometer (Hansen *et al.*, 2009; Hoener *et al.*, 2020). The arrangement used in the experiments performed in this work is shown in Figure 4 (Hoener *et al.*, 2020). The gas sample is expanded through an initial needle valve stage into the expansion chamber to drop the pressure from the experimental pressure of 6 bar. This expansion brings the pressure down to a manageable (i.e., < 1 bar) value for sampling through the following fused silica nozzle. The pre-expansion through the needle valve stage allows for simplified control of the gas pressure inside the reactor and for a larger sampling probe orifice size in the molecular beam arrangement.

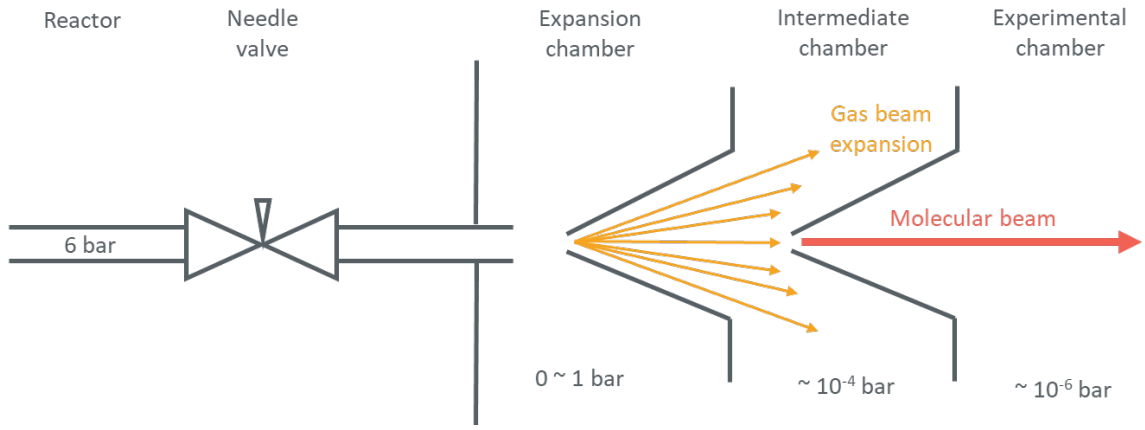

Figure 4: The arrangement of pressure stages across the path of sample generation and injection is shown for the plug-flow reactor experiment coupled to the CRF-PEPICO endstation (Sztáray *et al.*, 2017; Hoener *et al.*, 2020) the reactor pressure is dropped across a manual needle valve and the sample is expanded through a molecular beam interface to form a molecular beam that is injected into the spectrometer.

The gap after the first stage sampling probe leads to the intermediate expansion chamber. The gas expands further through the collimating skimmer forming the molecular beam shown

in red in Figure 4. In the beam interaction region, the light beam intersects orthogonally with the molecular beam to ionize species that have an ionization energy lower than the set monochromatic photon energy.

Molecular-beam set-ups have some advantages for species-conserving sampling of chemically reacting flows:

- Sampling of very hot gases directly from the reaction (for flame sampling)
- Interrupting chemical reactions to freeze the sample in the state it was in at the moment it was removed from the chemically reacting flow
- Dropping the pressure of the sample from the reaction (for flame sampling) or pre-expansion (for reactor sampling) pressure (several mbar to several hundreds of mbar) to the low pressure (high vacuum) required for ionization and manipulation of ions
- Preventing scattering of the sampled gas beam prior to ionization
- Precise transfer of a non-isotropic high-quality gas sample to the beam interaction region where the VUV light beam intersects orthogonally with the molecular beam

This is achieved by the described nozzle-skimmer arrangement, which is widely and successfully used in many combustion experiments, e.g., (Cool *et al.*, 2005; Hansen *et al.*, 2009; Qi, 2013). In the arrangement used in this work, no reactive species can be sampled due to their destruction in the initial needle valve stage and some of the molecular beam sampling advantages cannot be capitalized on (Hoener *et al.*, 2020, 2021). The sampling technique, however, provides a well-established approach for the differential reduction in pressure required for the spectrometer to work. Furthermore, it allows a denser gas sample to be injected into the beam interaction region in a directed and controllable manner. This method provides an expansion cooled gas sample with non-isotropic (i.e., higher velocity in the axial direction) gas beam for sample analysis (Mayer and Baer, 1996).

3.5 Double imaging photoelectron photoion spectroscopy (i^{2}PEPICO)

Samples in this work were analyzed with the CRF-PEPICO endstation (Sztáray *et al.*, 2017) at the Swiss Light Source synchrotron facility of the Paul-Scherrer Institute in Villigen, Switzerland. The endstation provides double imaging capability (Bodi *et al.*, 2012) provided by two delay line detectors. In such an arrangement, the registered position of the particle (i.e., electron and ion) at the detector surface is proportional to the kinetic energy that the neutral species carried in the moment it is ionized by VUV radiation. The single-photon in, single-electron out event is first registered on the electron detector, due to the low mass and extremely brief time-of-flight of the electron to the electron imaging detector. This short time-of-flight allows for an almost instantaneous registration of the ionization event. When an electron event is registered, the time-of-flight measurement for the photoion is started. This technique enables a distinct registration of the ion detection event for every ionization event in coincidence with the ejected photoelectron up to a count rate of 100 kHz (Oßwald *et al.*, 2014; Hoener *et al.*, 2020). Above this count rate several ionization events can take place in such a narrow time window that false coincidences may be registered and hence the maximum count rate is determined by the 100 kHz value.

3.5.1 Velocity-map imaging

To understand the velocity-map imaging (VMI) method, one has to understand that the positions on the VMI detector correspond to the kinetic energy of the imaged particle, i.e., electrons and ions alike. In other words, depending on the kinetic energy of the particle they will hit different positions on the detector (Baer and Tuckett, 2017). The ionized molecules contained in the molecular beam region in the ionized gas sample is visible as the narrow and sharp streak across the top of Figure 5. The visible streak emerging from the ionization region in the center of the photoion detector is not a spatial projection of the molecular beam. It rather shows a transverse and longitudinal kinetic energy distribution within the molecular beam. The transverse part is shown as the broadening of the streak along the short axis and the longitudinal distribution is represented as the length of the streak. In Figure 5 the background gas kinetic energy distribution is visible as the broad spot in the center of the velocity map image (Krüger *et al.*, 2019).

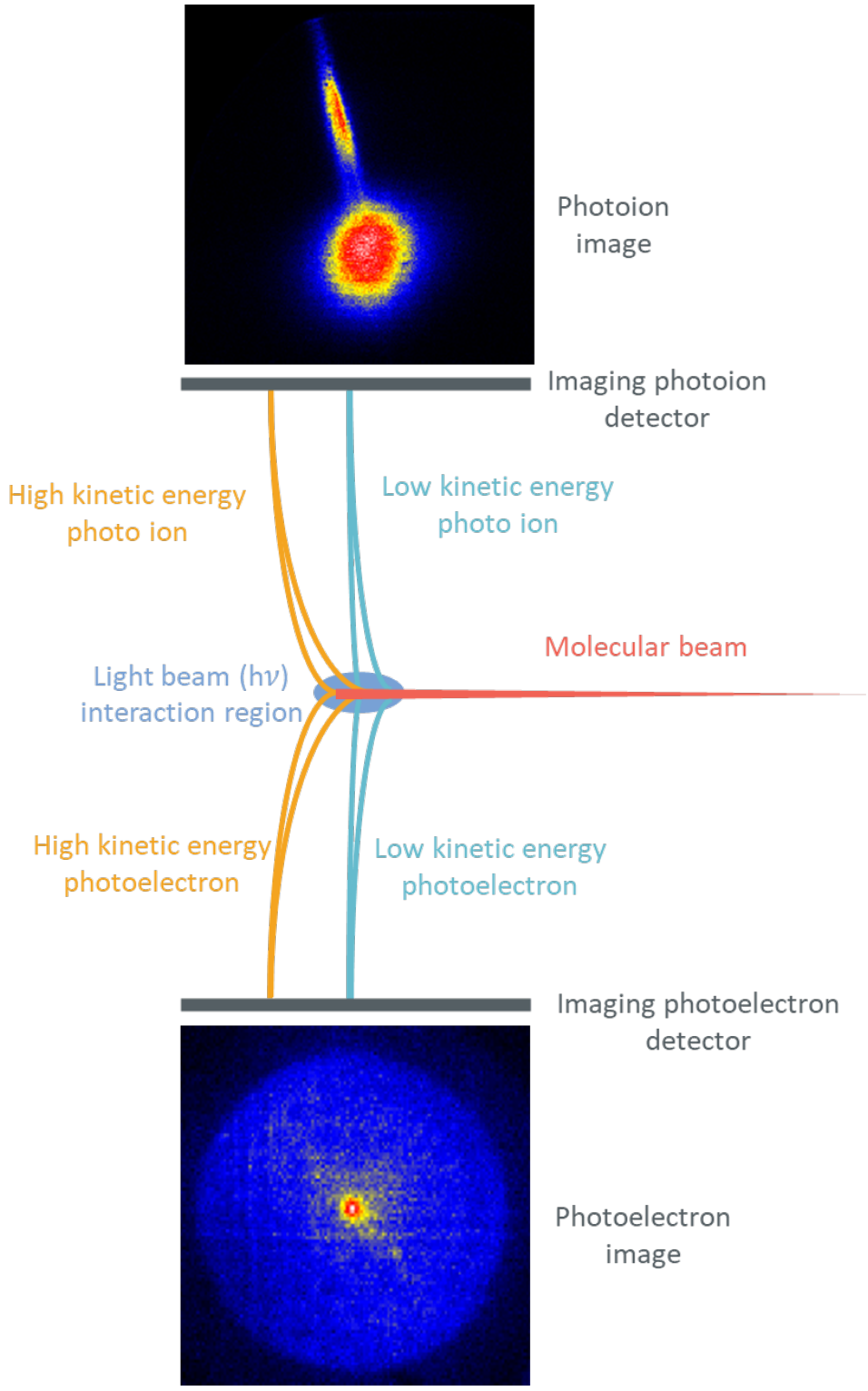

Figure 5: Principle of velocity-map imaging in photoelectron spectroscopy as provided by the CRF-PEP-ICO endstation (Sztáray *et al.*, 2017); the top shows an ion image with the visible background gas (spot in the center) and the streak like molecular-beam image; on the bottom a photoelectron image with the cold electron spot in the center of the detector and a visible ring of kinetic electrons around that center; the molecular beam (red) emerges from the sampling interface to the right, while the light spot in the beam interaction region is perpendicular to the plane of the figure (blue); hot (kinetic electrons) with the same energy are focused on one region of the detector (orange path), while cold electrons are focused in the center (teal path).

The background gas is ionized by the VUV beam passing through the experimental chamber of the spectrometer and shows a rather broad kinetic (thermalized) distribution. It is clearly visible that the transverse distribution of the molecular beam kinetic energies is much narrower than the background kinetic energy distribution, while the longitudinal distribution is quite broad. This may be related to the uncooled momentum distribution inside the very fast molecular beam. A perfectly cooled (i.e., thermalized) molecular beam in which all molecules have the same kinetic energy would appear as a dot on the imaging detector. If the molecular beam appeared in a small imaging region, its internal kinetic energy distribution would be extremely narrow and all ionized molecules would be sharply focused on the same detector region due to the single kinetic energy shared by all molecules in the molecular beam. If no molecular beam was formed behind the molecular beam skimmer, the sample gas diffusively emerging from the skimmer orifice would show up in the background gas spot in the velocity map image and hence, the signals could not be separated.

Though this procedure has not been used in the experiments reported here, the imaging detector enables a separation of the background signal from the signal generated by molecules that are ionized in the molecular beam, when a clear separation of the beam region and the background region on the detector is achieved (Krüger *et al.*, 2019). In the case shown in Figure 5, the velocity distribution of the beam streak on the detector is sufficiently dissimilar from the background kinetic energy distribution to select a region of interest that mostly contains signal generated by gases with the beam velocity distribution (i.e., molecules in the molecular beam). The i^2PEPICO software enables this procedure by allowing the selection of a region resembling either a circular or elliptical spot. Only the signal contained within this region is considered, while the signal outside of the region is discarded. Krüger et al. used this feature in an analysis of the fate of the OH radical after it is injected into the experimental chamber (Krüger *et al.*, 2019). The OH radical data was measured with the CRF-PEPICO molecular beam setup used for flames (Oßwald *et al.*, 2014), which is the predecessor to the setup used in the experiments reported here (Hoener *et al.*, 2020).

3.5.2 Threshold photoelectron spectroscopy

Figure 6 shows the quantum mechanical principle by which vibronic fine structures are obtained in measured photoelectron spectra (Ellis, Feher and Wright, 2005, p. 59; Hansen *et al.*, 2009; Hemberger *et al.*, 2020). The left side of Figure 6 shows the idealized potential well of a species to be ionized with the ground state zeroth energy level. The upper potential well depicts the lowest three energy levels of the first excited state of the (arbitrary) molecule, corresponding to three different vibrational structures or eigenfrequencies of the molecule in this state. The adiabatic transition is the lowest onset of ionization, corresponding to the lowest amount of energy that must be added to the system by the photon (i.e., with the photon energy quantum hv). When a vertical transition takes place, the photon has the right quantum of energy that exactly corresponds to the difference between the zeroth energy level in the ground state v=0, and some energy level in the first excited state. In those cases, the likelihood of an ionization event taking place due to the photon interacting with a valence electron is substantially increased (Hemberger *et al.*, 2020).

This interaction of a photon with the electron leading to a single-photon in single-electron out ionization event is recorded by detecting the extraction of the produced free photoelectron (*vide supra*). A plot of the photoelectron signal intensity against the set photon energy is called a photoelectron spectrum. If the amount (i.e., intensity) of photoelectrons is plotted against the set (i.e., monochromated) photon energy, the larger occurrence of ionization events in the case of an ionization leading to a vertical transition will yield a higher peak in the photoelectron spectrum (top right of Figure 6). The intensity (i.e., peak height or photoelectron signal yield) and the energetic spacing between the vertical transitions (i.e., the train of peaks) in the plot photoelectron spectrum is unique to every molecule. Hence, the photoelectron spectrum yields a kind of fingerprint of the molecules allowing for an assured identification of a species (Krüger *et al.*, 2014; Felsmann *et al.*, 2016).

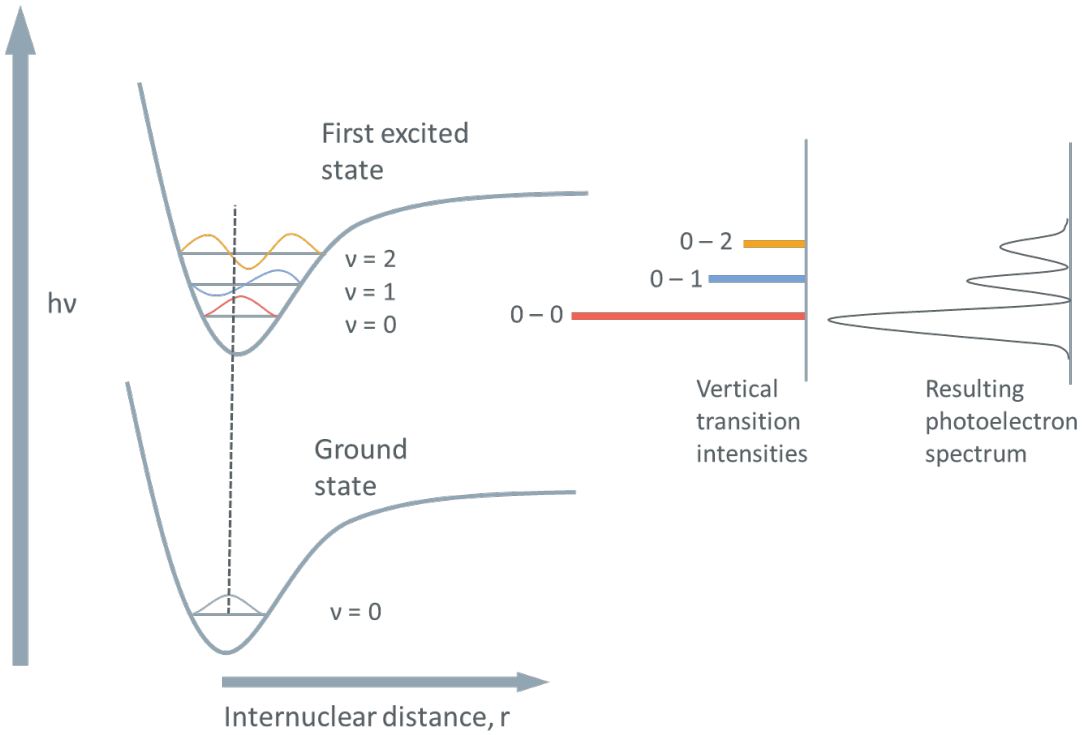

Figure 6: Transitions between a molecular ground state potential well (arbitrary) and an excited state as encountered in photoionization; vertical transition intensities from the overlapping wave functions are shown as colored bars and the resulting measured photoelectron spectrum is shown to the right (according to (Ellis, Feher and Wright, 2005, p. 59; Hansen *et al.*, 2009; Hemberger *et al.*, 2020)).

The velocity map imaging technique employed by the CRF-PEPICO furthermore allows the selection of only the threshold photoelectrons (TPE). TPE are produced when a photon with an energy close to that required to make a vertical transition interacts with an electron and the electron is ejected with close to zero kinetic energy (Bodi *et al.*, 2012; Baer and Tuckett, 2017). When the photon energy is larger than the required energy for ionization, the surplus energy provided by the photon will eject the photoelectron with a kinetic energy component according to energy conservation. The velocity map imaging electron optics will map zero kinetic energy electrons to the center of the detector, while electrons with non-zero kinetic energy will be mapped some distance away from the center (Bodi and Hemberger, 2014). This effect is visible in the photoelectron image at the bottom of Figure 5, as the white and red hotspot in the center of the detector. Since the photoelectrons are measured in coincidence with the photoions, the mass spectrum can be used during data reduction to collect electrons belonging to only one mass channel (i.e., mass range) in the ion spectrum. This way a photoelectron spectrum can be calculated for a single species even when a complex mixture of species is encountered in the sample injected into the spectrometer. When all electrons ejected by the

species in the mixture would be used to plot the photoelectron spectrum, a convoluted spectrum would be obtained. With the selection of photoelectrons by their corresponding parent ion mass channel, ideally, a non-convoluted photoelectron spectrum may be obtained. If more than one isobaric species is ionized, the photoelectron spectrum may still contain all vibronic transitions of those species in the same mass channel. The photoelectron spectrum using mass selection by the time-of-flight mass spectrum and only the near zero kinetic energy photoelectron signal is thus called a mass selected threshold photo electron spectrum (ms-TPES) (Bodi *et al.*, 2013). This spectrum follows very closely the theoretical Franck-Condon factors, since photoelectrons that correspond to lower energy transitions are discarded in the evaluation procedure.

3.6 Data Evaluation and reduction procedure

3.6.1 CRF-PEPICO specifics to the data-reduction procedure

Data evaluation of i^{2}PEPICO sampling poses some special challenges due to the nature of the measurement technique. The low electric field strength of the extraction field required for electron imaging causes a severely diminished mass resolving power of the instrument's ion imaging time-of-flight spectrometer. Since the i^{2}PEPICO suffers from the described extremely low mass resolution (i.e., oftentimes resolutions substantially below R=100=t/2Δt are encountered), relatively clean (i.e., with a low number of species) spectra are highly favorable for data evaluation. The reaction conditions investigated in this work were designed to achieve exactly this. By using the simplest alkane CH_4 as a fuel, product spectra with few species were acquired (Hoener *et al.*, 2021; Hoener and Kasper, 2022).

To exhaustively investigate a reaction condition, different types of measurements are performed. To obtain temperature dependent mole fraction profiles of species, the temperature is ramped in equally spaced steps (i.e., 50 K in the present work) (Hoener *et al.*, 2020, 2021; Hoener and Kasper, 2022). These measurements are called temperature scans or temperature ramping measurements (Hoener *et al.*, 2020). For every temperature, spectra at several different photon energies are taken to obtain non-convoluted spectra of preferably all species. If the spectra were obtained only at high photon energies, species with low ionization energies may be destroyed through dissociative ionization processes negating the VUV soft-ionization

advantages. In this case, fragments would cause mass convolutions and distinguishing species in the gas sample from fragments caused by dissociative ionization would be rendered impossible.

The second kind of measurements that are obtained at fixed temperatures and varying photon energies (i.e., ionization energies, if viewed from the angle of the species to be ionized). The temperature is selected to obtain photoionization curves of the species under closer investigation (Hoener *et al.*, 2020). The onset of ionization in these curves can then be compared to known or calculated ionization energy values. In the reactor experiments the most favorable temperature usually is in the vicinity of the reaction onset temperature for the mixture under investigation. At this temperature the most species are generated in the reacting stream, without being destroyed by further reactions as a non-equilibrium in the reactant stream is achieved. The photon energies are set to discrete values spaced across a narrow grid of energies (Hoener *et al.*, 2020). At every set photon energy a spectrum is acquired with sufficient averaging time to allow for a signal intensity yielding a substantial signal to noise ratio.

In i^2PEPICO measurements an additional criterion is to obtain a sufficient threshold photoelectron signal, since the electrons spread out on the imaging detector. The signal integration procedure must yield sufficient photoelectron counts to acquire photoelectron spectra of acceptable resolution. To resolve the vibronic fine structure of the electron spectrum, also a sufficiently small photon energy spacing must be selected to acquire peaks that contain high frequency components (i.e., peaks with very steep flanks and narrow width).

3.6.2 Photoion spectra

The double imaging photoelectron photoion spectroscopy evaluation procedure is substantially more involved than for the regular non-imaging mass spectrometric measurements as acquired with regular time-of-flight endstations (Hansen *et al.*, 2009; Kasper *et al.*, 2009; Qi, 2013). In addition to the necessity to integrate the photoion spectra to obtain total count values for each mass channel, a secondary procedure is required to evaluate photoelectron spectra. To obtain the photoion spectra the total signal over the whole ion imaging detector is taken and peaks are integrated using a Gaussian fit of the peaks of interest.

The evaluation of photoion spectra poses some additional challenges due to the low mass resolution of the instrument. Even the energy-selective nature of the analytical technique using tunable VUV light is of little help in some instances, where mass convolutions by species yielding large signal intensities are observed. For example, above the ionization energy of the fuel used in the reaction condition, the broadening of the high-intensity fuel peak can cause the peak to grow into neighboring mass channels at its lower bound. These broad peaks sometimes completely obscure some low-yield species. Also, background subtraction can become a problem and a source of substantial error, since the tilted baseline in the flanks of broad peaks cannot in every case be subtracted without causing residuals in the acquired signal.

3.6.3 Photoelectron spectra

To evaluate the photoelectron spectra, two regions of interest (ROI) on the imaging photoelectron detector are defined (Bodi and Hemberger, 2014). The inner region, from here on called spot, selects the near-adiabatic or cold electrons (i.e., low kinetic energy photoelectrons) that hit the detector close to the center of the focusing area for signal integration. The hot (i.e., high kinetic energy photoelectrons) are selected with the ring-like ROI, from here on called ring. This differentiation of hot and cold photoelectrons allows the calculation of the threshold photoelectron spectrum (TPES) that closely follows the theoretically obtainable spectrum (i.e., obtained by calculation) generated of Franck-Condon factors (Hemberger *et al.*, 2020).

The size of the ROIs is determined by the hot-electron contribution to the cold-electron signal (Bodi and Hemberger, 2014). The ROI spot and ring areas are usually kept at a ratio of ca. 3:1. Figure 7 shows some arbitrary ROIs in the photoelectron spectrum concentric to the ring structures of the electron VMI. Hot-electron signal subtraction is then performed according to the ROI area ratios.

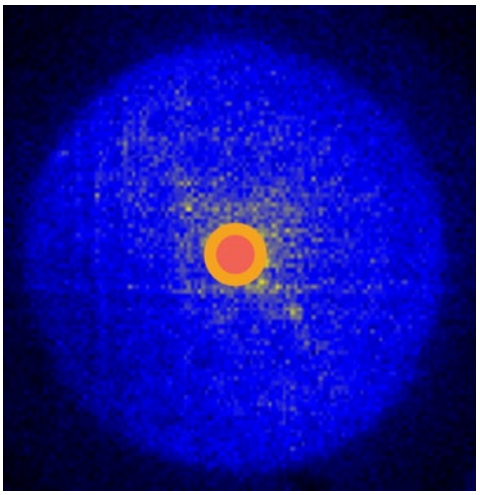

Figure 7: A photoelectron image with the spot (red) and ring (yellow) regions of interest used for the subtraction of hot-electron influence on the cold-electron signal marked in the center of the image.

The signal acquired in the area of the center spot ROI and surrounding ring ROI are then provided as spectra to be externally integrated using a Gaussian best fit or they can be numerically integrated by the i^{2}PEPICO software to yield the signal intensities with respect to the ROIs. A scaling factor according to the selected ratio is used to scale the signal acquired in the ring area with respect to the spot area, so that the ring contains ca. the same amount of hot electrons as the spot. In the next evaluation step the TPES is calculated by subtracting the scaled photoelectron signal selected by the ring ROI from the photoelectron signal selected by the spot ROI, yielding the photoelectron spectrum closely following the theoretical Franck-Condon factors.

3.6.4 Quantitative evaluation procedure for i^{2}PEPICO plug-flow reactor experiments

An adapted procedure for the quantitative evaluation of species mole-fraction profiles was developed in the present work (Hoener *et al.*, 2020), and is presented in a slightly modified way. It follows the general procedure for photoionization flame sampling experiments as published by Kasper et al. (Kasper *et al.*, 2009), that was then adapted to the CRF-PEPICO flame sampling setup by Osswald et al. (Oßwald *et al.*, 2014). The sampling law given in Eq. 19 expresses the relationship between the measured signal intensity for a species in the mass spectrum (i.e., photoion spectrum in the case of i^{2}PEPICO) and the mole fraction of this species,

subject to several influencing factors in the CRF-PEPICO pressurized flow reactor experiment (Hoener *et al.*, 2020).

$$S_i = x_i(T) \cdot D_i(M_i) \cdot t \cdot FKT\left(T_{inj,}\, \bar{M}\right) \cdot c(E) \cdot \sigma_i(E) \cdot \alpha_i(E - E_{EI}) \qquad \text{(Eq. 19)}$$

S_i denotes the measured signal intensity on the left side of the equation. On the right side x_i is the sought mole fraction of the species. The mole fraction is directly related to the measured photoion signal intensity and the dependence is expressed in the remaining factors. $D_i(M_i)$ denotes the mass discrimination dependent on mass M_i of the observed species i. Mass discrimination is an unwanted property in mass spectrometry where the signal intensity varies as some function of species mass. The CRF-PEPICO endstation behaves almost ideal in this respect and empirically shows very little to no mass discrimination. Therefore the data evaluation this factor can be set to unity (Hoener *et al.*, 2020). The factor t denotes the averaging time for the individual spectrum. It is, if no other factor changes the signal intensity, linearly dependent on the averaging time used to acquire the signal (i.e., an averaging time twice as long will yield twice the signal). In practice this factor is accounted for by normalizing the integrated signal intensity for all mass channels of interest to the averaging time, of the measurement. This procedure yields a signal intensity per second of data acquisition for all performed acquisitions. FKT is a sampling function dependent on sample composition and sampling temperature. Due to the very high argon dilution in the experiments performed for this work, the compositional changes are considered negligible. The temperature does not change at the point of sampling, since the mixture is already cooled to the fore line temperature which is heated just enough so that no condensation occurs, Hence, sample injection into the spectrometer is not performed at the process temperature (i.e., $T_{inj} \neq T$; where T_{inj} is the injection temperature) (Hoener *et al.*, 2020). In this work, the sampling was performed isothermally and with negligible changes in composition, yielding a flat FKT. c is a disturbance correction factor that is specific to the machine and setup. The photoionization cross-section is taken into account by the σ_i factor. Known photoionization cross-sections of a neat species at the set photon energy are used to correct for the energy dependence of the ionization cross section of the species i under investigation. Such cross-sections can be found in the literature. For photon energies significantly above the ionization threshold of the species under investigation a correction factor α_i is required. Due to the limited area (or diameter) of the photoelectron detector, the acceptance of photoelectrons is energetically limited. Hence, photoelectrons with high kinetic energy components may not be detected leading to missing coincidences in

the photoion signal. Therefore, a loss of signal intensity of the ion in the time-of-flight mass spectrum must be accounted for. In practice it is advisable to select photon energies for quantification that are close to the adiabatic ionization threshold of the species of interest. Therefore, this factor can be set to unity (Hoener *et al.*, 2020).

With respect to the evaluation procedure for flame sampling experiments, minor changes where required, which are the temperature dependence of the species mole fraction x_i instead of a spatial dependence on the sampling height above the burner face and the index change to the injection temperature of the sample (i.e., FKT(T_{inj})). The reactor experiment, thus, allows for some helpful simplifications to the application of Eq. 19 in practice due to the constant injection temperature and high dilution of the reactant mixture.

3.6.4.1 Main species

Equation 19 is used for the quantitative evaluation of intermediate species yielding results that are accurate to a factor of 2 to 4 (Kasper *et al.*, 2009). For the main species, it is advisable to perform an element balance procedure to find a more accurate closed solution (Bierkandt, 2018). The main species encompass the high-concentration species found in the reactant mixture supplied to the reactor and in the exhaust stream when the mixture is mostly reacted or in partial equilibrium in case of the reactor experiment. These are the hydrocarbons, NO_x and oxidizers in the fresh reactant mixture and the NO_x, H_2, CO, and CO_2 as well as water in the exhaust stream. Every other minor species that may be present in the exhaust is neglected leading to some acceptable error. This simplifies the procedure by keeping the system of equations used to solve for the species concentration in the element balance compact and manageable.

For the nitrogen species-containing reaction condition used in the experiments in this work, a more involved element balancing procedure is required. The NO doping must be taken into account, since the NO is a significant portion of the fresh gas mixture, especially in the conditions containing 1 % of NO with respect to the total flow (Hoener and Kasper, 2022). NO rapidly reacts with oxygen in the fresh mixture, leading to challenges specific to the conditions investigated in this work (Hoener and Kasper, 2022). The reaction between NO and O_2 to form NO_2 must therefore be taken into account for the lowest temperature points in the measurement. The generally adapted element balancing procedure for nitrogen containing reaction conditions is laid out by Lucassen (Lucassen, 2011, pp. 12-15). A system of equations is

formulated that relates the concentrations of two species to their signal intensities via a calibration factor. The equations become solvable through the known element balances of H, C, N, and O. Furthermore, the CO/CO_2 signal relation can be calibrated using a calibration gas mix of CO and CO_2 with known concentrations or the photoionization cross section relation of these two species can be used. The calibration facto k can then be calculated for every species pair as in Eq. 20 (Lucassen, 2011, pp. 13-14).

$$k_{CO/CO_2} = \frac{S_{CO} \cdot x_{CO_2}}{S_{CO_2} \cdot x_{CO}} \qquad \text{(Eq. 20)}$$

Where S is the signal intensity and x is the mole fraction. For the cross-section relation, the formular becomes Eq. 21.

$$k_{CO/CO_2} = \frac{\sigma_{CO}}{\sigma_{CO_2}} \qquad \text{(Eq. 21)}$$

With the known amounts of substance injected into the reactor a linear system of equations can be formulated to calculate the amounts of substance after completion of the reaction in the reactor. For this the amounts are related to the atomic balance of H, O, C, and in the case of reaction conditions containing nitrogen species also N as shown in Eq. 22-25.

$$n_N = n_{NO} + n_{NO_2} \qquad \text{(Eq. 22)}$$

$$n_C = n_{CH_4} + n_{CO_2} + n_{CO} \qquad \text{(Eq. 23)}$$

$$n_O = n_{NO} + 2 \cdot n_{NO_2} + 2 \cdot n_{O_2} + n_{H_2O} + 2 \cdot n_{CO_2} + n_{CO} \qquad \text{(Eq. 24)}$$

$$n_H = 4 \cdot n_{CH_4} + 2 \cdot n_{H_2O} + 2 \cdot n_{H_2} \qquad \text{(Eq. 25)}$$

With signal relations similar to the calibration relation shown in Eq. 21, the system of equations becomes solvable if a sufficient number of signal relations and calibration factors is formulated. These formulas can have the form shown in Eq. 26, Eq. 27, and Eq. 28.

$$k_{CO/CO_2} = \frac{S_{CO} \cdot n_{CO_2}}{S_{CO_2} \cdot n_{CO}} \qquad \text{(Eq. 26)}$$

$$k_{NO/NO_2} = \frac{S_{NO} \cdot x_{NO_2}}{S_{NO_2} \cdot x_{NO}} \qquad \text{(Eq. 27)}$$

$$k_{CH_4/CO_2} = \frac{S_{CH_4} \cdot x_{CO_2}}{S_{CO_2} \cdot x_{CH_4}} \qquad \text{(Eq. 28)}$$

Significantly, the more species are involved in the element balance, the more calibration factors of the form shown in Eq. 26-28 are needed. In these formulas any species and signals occurring in the balance can be set into relationship to create a solvable system of equations. In a more general form, the calibration law can be written as in Eq. 11.

$$k_{j/k} = \frac{S_j \cdot n_k}{S_k \cdot n_j} \qquad \text{(Eq. 29)}$$

Where the indices j and k are species included in the calibration factor k.

For the general calibration procedure, an argon concentration profile can be calculated (Bierkandt, 2018, p. 68). In case of the published procedure for the reactor experiments coupled with the CRF-PEPICO end station, it was decided to skip this step due to the high argon dilution of 90 % leading to only small changes of the mole fraction of argon in the post-reaction mixture (Hoener *et al.*, 2020). Due to the constant argon mole fraction assumption, it can be advantageous to use a temperature averaged argon signal for reference to reduce noise (Hoener and Kasper, 2022).

3.6.4.2 Intermediate species

The intermediate species are calibrated using the argon signal as a reference and are set into relationship to, ideally, the measured photoionization cross-section of the species at the energy the calibration of the species is evaluated. When no photoionization cross-section is available, a value must be estimated (Kasper *et al.*, 2009). The evaluation procedure requires a reference species that has to be present at all times during the reaction. The high dilution of argon gas is a favorable reference in this case. Evaluation is based on the basic formula shown in Eq. 19, used to set the signal of the species under investigation in relation to the (argon or other) reference species as shown in Eq. 30.

$$\frac{S_i}{S_{ref}} = \frac{x_i}{x_{ref}} \cdot \frac{D_i}{D_{ref}} \cdot \frac{t_i}{t_{ref}} \cdot \frac{c(E_i)}{c(E_{ref})} \cdot \frac{\sigma_i(E_i)}{\sigma_i(E_{ref})} \cdot \frac{\alpha_i(E_i - E_{EI})}{\alpha_{ref}(E_{ref} - E_{EI})} \qquad \text{(Eq. 30)}$$

As described above for the reference signal, the reference species must be present and ideally unchanged in quantity for all reaction temperatures. This means in this case the index ref = Ar is favorable. In practice, this relationship can be simplified in the same manner described above. By using energies close to the ionization energy of the species under investigation and by normalizing to the signal acquisition (i.e., averaging) time, the two terms describing these influences can be set to unity (*vide supra*). For the CRF-PEPICO, the mass discrimination factor can also be set to unity, and the function becomes Eq. 31.

$$\frac{S_i}{S_{ref}} = \frac{x_i}{x_{ref}} \cdot \frac{c(E_i)}{c(E_{ref})} \cdot \frac{\sigma_i(E_i)}{\sigma_{ref}(E_{ref})} \qquad (\text{Eq. } 31)$$

To solve for disturbances between the different signals acquired at different photon energies, the so-called scan factors are calculated by solving Eq. 31 for the disturbance factor c, yielding expression shown in Eq. 32.

$$c(E_2) = \frac{S_{ref}}{S_{ref}} \cdot \frac{x_{ref}}{x_{ref}} \cdot \frac{\sigma_{ref}(E_i)}{\sigma_{ref}(E_{ref})} \cdot c(E_1) \qquad (\text{Eq. } 32)$$

For the disturbance, it matters that the reference species used is present at the photon energies that the scan factors are evaluated at (i.e., all set photon energies of the temperature ramping measurement). Therefore, in this case, high-ionization-energy species such as argon are not suitable, but low-ionization energy species should be used for the ref-indexed species in the formula.

3.7 Computational Chemistry

In this work, electronic structure methods were employed to gain a deeper understanding of the photoionization energetics of HONO and its photodissociation properties (Hoener *et al.*, 2021). To perform electronic structure computations and for the determination of molecule energies and calculation of Franck-Condon factors, the Gaussian 16 package was used (Frisch *et al.*, 2016). A partial potential energy surface of the positively charged doublet nitrous acid was calculated (Hoener *et al.*, 2021) based on the work of Sengupta et al. (Sengupta, Sumathi and Peyerimhoff, 1999), and vibronic structures were determined by Franck-Condon simulations.

The solution of energy states and vibrational modes of molecules requires solving the Schrödinger equation (Young, 2001, p. 10). To simplify the solution of the equation software packages such as Gaussian 16 use the Born-Oppenheimer approximation that states that movements of electrons and nuclei can be viewed independently so that the terms for the electron and nuclear energies can be separated and solved independently (Lewars, 2016, pp. 22-23). This approximation is allowed since the mass of nuclei is much higher than that of the electrons, allowing the electrons to always follow the slow nuclear movements, e.g., due to molecular vibrations.

The idea of a molecular geometry is made possible by the Born-Oppenheimer approximation, since it allows to solve for the electronic structure to find the energy state of the molecule independent of nuclear vibrations and hence a fixed structure can be related to an energy state (Lewars, 2016, p. 9).

3.7.1 Calculation of molecular energies

Every geometry (i.e., arrangement of atoms) in a molecule corresponds with the energy state of that molecule. Stable states of molecules correspond to minima on a potential energy surface (PES) in which the molecule rests at an equilibrium state (Lewars, 2016, pp. 9-13). If that equilibrium is disturbed, the molecule wants to return to that energy minimum. This means that molecules stabilize energetically at the minima of the potential energy surface. To illustrate the effect of the potential energy on the stability of a molecule on the PES, Figure 8 shows two types of equilibria. To the left, a stable equilibrium is shown similar to the one experienced by the molecule when it has a minimum energy state. In the unstable equilibrium (right), a small disturbance will cause the potential energy state to drop along the slope of the curved surface. When a molecule is on the slope of the PES, it will seek to find the nearest stable equilibrium. On the potential energy surface, the unstable equilibrium may be comparable to the transition state of a molecule between two slopes on the PES leading to stable minima.

Figure 8: Depiction of a stable (left) and unstable (right) equilibrium to illustrate the idea of stationary points on the PES

This depiction simplifies the idea of equilibria on the PES to a two-dimensional surface. In reality the dimensionality of the surface depends on the number of degrees of freedom, which depends on the amount of atoms N in the molecule, yielding 3N-5 degrees of freedom for linear molecules and 3N-6 degrees of freedom for non-linear molecules (normal vibrational modes) (Hinchliffe, 2008, p. 51). Hence the potential energy U depends on 3N-6 independent degrees of freedom. Normally a two-dimensional projection or simplification is used for the representation of the PES in a graphical manner. In general, as Lewars states, the simplification of the PES makes many complex concepts in computational chemistry much more intuitive (Lewars, 2016, p. 9). In Figure 9, such a two-dimensional non-quantitative partial representation of the PES is shown taken from the PES for $HONO^+$ (Hoener *et al.*, 2021). The curve represents a two-dimensional partial section through the PES along a molecular (or reaction) coordinate. Along the potential energy surface three states of the HONO molecule are shown and the path represents the isomerization of *trans*-HONO to form the *cis*-HONO isomer via a transition state.

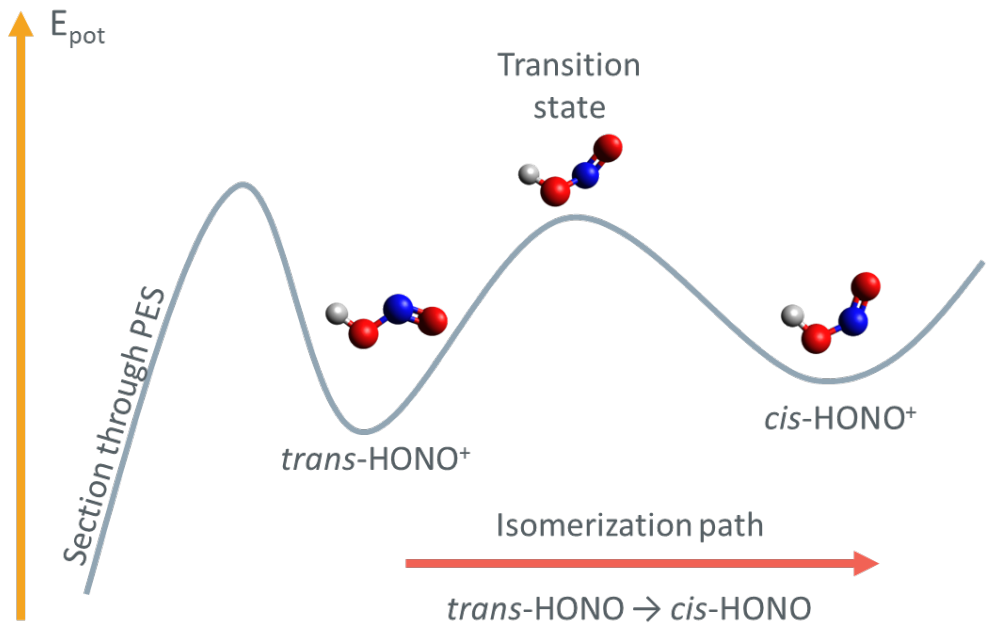

Figure 9: A two dimensional section (arbitrary) through a PES is shown along the isomerization path of a molecule (isomerization of *trans*-$HONO^+$ to *cis*-$HONO^+$); the isomerization moves through a transition state and the PES section shows a change in the potential energy of the molecule; the actual doublet nitrous acid PES can be reviewed in (Hoener *et al.*, 2021) and was calculated as part of this thesis.

Each energy state of the molecule corresponds to a shape or geometry, i.e., a set of bond lengths and angles. The concept of geometry is made possible by the Born-Oppenheimer approximation as stated earlier (Lewars, 2016, p. 9). Each of these states exists in a location on the PES, which describes the potential energy of the molecule (Young, 2001, pp. 173-175; Lewars, 2016, pp. 14-22). To solve for these states the Gaussian software package solves an optimization problem to find a minimum energy state of the molecule (i.e., a stable state or stationary point on the PES) (Young, 2001, p. 173), by optimizing bond lengths and angles, i.e., the geometry of the molecule. This optimization can start from a guessed structure.

To find the transition state, molecular bond lengths and angles can be varied in small steps while calculating the potential energy of the molecule for every configuration. A transition state may show as a maximum on the potential energy plot, when the change in energy for the nuclear coordinate is plotted as shown in Figure 10.

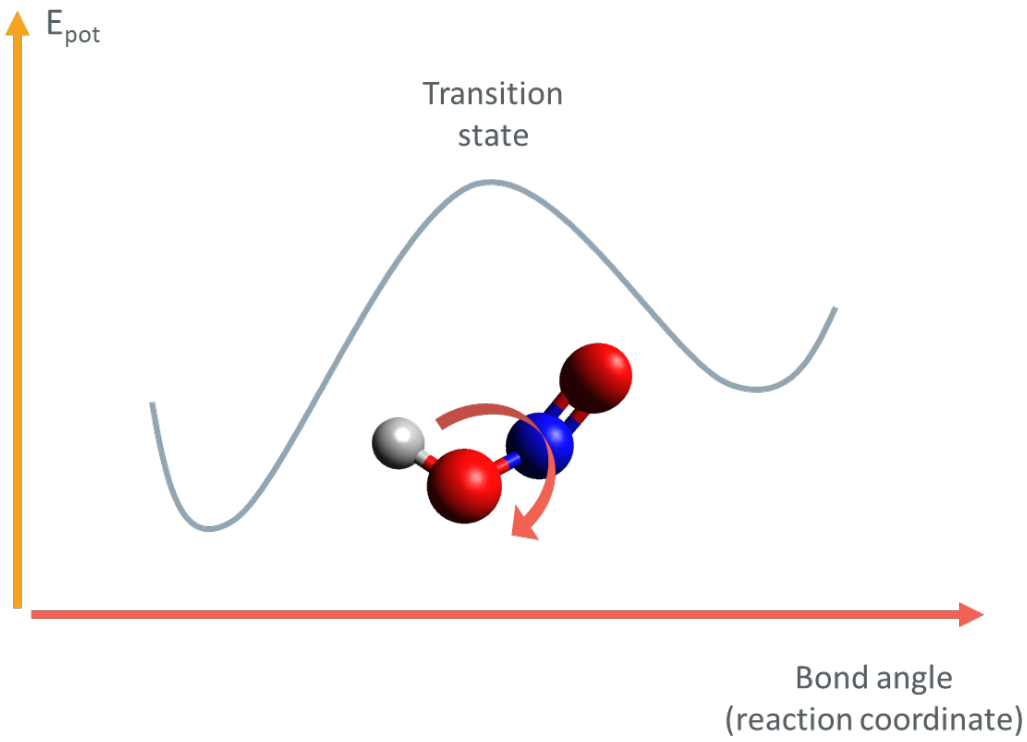

Figure 10: Calculation of the potential energy curve (arbitrary) by step-wise rotation of a molecule, shown here is a rotation of the N-O bond in the HONO molecule as an example; the change of the bond angle causes a change in the molecular energy and the approximate location of the transition state shows as an energy maximum (adapted from (Young, 2001, p. 174; Lewars, 2016, p. 16)).

To find the exact transition state location on the PES, an optimization of the transition state geometry is required. If a transition state is found, the molecular vibrational modes will exhibit one imaginary frequency (i.e., a negative frequency), showing a saddle point on the PES (Lewars, 2016, p. 19). In the present work, the calculation of a PES helped to understand the energetics of the nitrous acid and its photoionization properties (Hoener *et al.*, 2021).

In photoionization mass spectrometry, oftentimes an unknown ionization energy of a molecule is sought for comparison to the ionization energy obtained through the measurement of photoionization curves (*vide supra*). This energy can be obtained by calculating the potential energy of the neutral state molecule and the energy of the ionized species and then taking the difference in energies of these two molecular states. In practice, it is advisable to use different methods for the calculation of energies and compare them to see if they are in approximate agreement. In this work density functional theory (DFT; B3LYP/6-311++G(p,d)), complete basis set theory (CBS-QB3), W1 method with Brueckner Doubles (W1BD) and the G4 method were used (Hoener *et al.*, 2021). The higher-level methods like G4 use energy corrections that allow

for more accurate results (Curtiss, Redfern and Raghavachari, 2007). These methods contain the basis sets that describe the distribution of electrons around the molecule (Lewars, 2016, p. 253).

3.7.2 Calculation of Franck-Condon factors and comparison to photoelectron spectra

To generate photoelectron spectra, Gaussian allows for the calculation of Franck-Codon factors. The factors calculated give transition probabilities between the neutral and ionized species. Since every ionization event (i.e., transition between the two aforementioned states) yields a photoelectron, the measured photoelectron intensity can be compared to the calculated spectrum generated with the Franck-Condon simulation (Hemberger *et al.*, 2020). The Franck-Condon principle states that an electron transits so rapidly that the nuclear positions before and after the transition are almost the same (Ellis, Feher and Wright, 2005, p. 58). This notion is consistent with the Born-Oppenheimer approximation (*vide supra*) (Ellis, Feher and Wright, 2005, p. 8). Therefore, vertical transitions can be calculated from the stationary structures on the neutral and excited PES. Gaussian allows Franck-Condon calculations only using results at the DFT level of theory.

In practice, the structures and hence vibrational modes of the neutral and charged (i.e., ionized) molecule are calculated first and from the overlap of the wave function (Ellis, Feher and Wright, 2005, p. 58) the Franck-Condon factors are calculated by Gaussian 16. The intensities can then be convoluted with a normal distribution to account for broadening in the real measured spectrum and a resulting spectrum that can be compared to the normalized TPES can be calculated as shown in Figure 11.

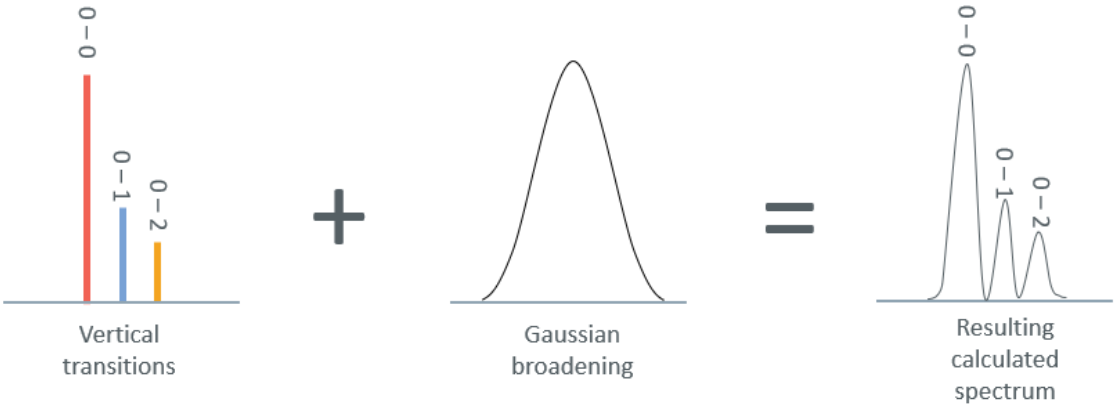

Figure 11: A set of (arbitrary) calculated transition probabilities for the 0-0, 0-1 and 0-2 wave function overlaps are shown to the right, a normal distribution is convoluted with the calculated intensities yielding a broadened spectrum that is directly comparable to the measured photoelectron spectrum.

The TPES is comparable to the spectrum generated from the transition probabilities described by the Franck-Condon calculation, since all contribution of electrons from lower transitions (i.e., kinetic photoelectrons) are subtracted in the evaluation procedure (*vide supra*). It is also important to note that a calculation of Franck-Condon factors is only possible if the geometrical change between the neutral and ionized molecule is not too severe, because a severe change in geometry causes the wave functions to not overlap.

4 Introduction to the research objective of this thesis, concluding remarks and outlook

4.1 Summary of the research objective of this thesis and discussion of the results

The research objective of this work was the investigation of exhaust gas recirculation processes involving the doping of hydrocarbon reactant streams with NO. The research was aimed at understanding the influence of NO and other nitrogenous species formed during combustion. The experiment involved a plug-flow type reactor that allows reactions to take place at elevated pressures up to 6 bar to approximate pressures encountered in practical combustion systems such as gas turbine combustors and internal combustion engines. In particular, the conditions before initiation in homogenous charge compression ignition engines and in pre-flame zones of gas turbine combustors with exhaust gas recirculation are met. Preliminary results were obtained with an existing plug-flow reactor set up coupled to a molecular-beam time-of-flight mass spectrometry using electron ionization (EI-ToF-MBMS). The spectra showed that species at a mass-to-charge ratio (m/z) of 61, 46 and 47 were present. The interesting species were believed to be HONO at m/z=47, NO_2 at m/z=46 and nitromethane (CH_3NO_2) at m/z=61. The isobaric convolution of formaldehyde (CH_2O) and NO at m/z=30 rendered an analysis using element balances futile as the mass resolution of ca. 1500 of the EI-ToF-MBMS set-up used in these experiments was insufficient to resolve this peak. This resolving power limitation and the chance to isolate the HONO intermediate motivated the investigation of the reaction condition with synchrotron vacuum ultraviolet techniques to achieve species resolution and identification. Despite the lack of measured data in the literature at that time (Marrodán *et al.*, 2019), simulation studies and theoretical investigations suggested that HONO plays an important role for the interaction of oxides of nitrogen and hydrocarbons in combustion. The signals at m/z=61 corroborated the notion that nitrogen interactions were at play, since nitromethane was reported before in experiments involving methane and NO (Rasmussen, Rasmussen and Glarborg, 2008). Furthermore, the reactive NO formed NO_2 (m/z=46) at low temperatures already as is expected from the energetics of the reaction of oxygen with NO and its lack of an energy barrier to formation (Glarborg *et al.*, 2018).

To overcome the challenge posed by isobaric convolution and to reliably assign species to the detected masses in the spectrum, it was decided to devise a means to couple the pressurized reactor to the CRF-PEPICO endstation (Sztáray *et al.*, 2017) at the Swiss Light Source synchrotron facility of Paul-Scherrer Institute (Hoener *et al.*, 2020). The CRF-PEPICO was previously used successfully to analyze the complex samples taken from burner-stabilized flat premixed flames (Oßwald *et al.*, 2014). The flame set-up involves spatially resolved molecular-beam sampling and the existing tried-and-true combustion chamber was a logical choice to act as a baseline for the reactor set-up. Also, at the same time an improved combustion chamber was in the design phase and to be used in subsequent flame sampling experiments, freeing up the previous reactor chamber for further development of reactor experiments. Subsequently, the original flame chamber was repurposed for the reactor experiments.

The experiment was designed and commissioned at the CRF-PEPICO endstation in an initial measurement campaign (Hoener *et al.*, 2020). After the initial campaign, the reactor experiment was validated against gas chromatography measurements using an argon diluted, heptane doped CH_4 combustion condition at an equivalence ratio of 8 that was measured with gas chromatography before and has previously been published (Kaczmarek, Atakan and Kasper, 2019; Hoener *et al.*, 2020). The new experiment set-up enables a measurement of complex mixtures in elevated-pressure low-temperature oxidation and has since been used in several campaigns at the Swiss Light Source. Crucial data for the activation effect of ozone and DME on the partial oxidation of natural gas surrogates was generated with the CRF-PEPICO coupled pressurized reactor (Kaczmarek *et al.*, 2023).

For the NO doped CH_4 mixtures, the objective to analyze the aforementioned species was achieved with the novel set-up. Insight was gained into the low-temperature interactions of NO_x and fuel at elevated pressures. It was confirmed that the species at m/z=47 was indeed HONO, for which little data exists. Subsequent analysis of three reaction conditions at equivalence ratios in the lean-to-rich regime at 0.7 and 1.2 doped with 1000 ppm of NO and at 2.1 doped with 1 % of NO yielded a comprehensive dataset for further analysis.

Historically, HONO has proven difficult to detect and no isomer-selective measurement of its three isomers, *trans*-HONO, *cis*-HONO and HNO_2 was achieved until recently in hydrocarbon-containing reaction mixtures (Gossler *et al.*, 2021; Hoener *et al.*, 2021; Zhang *et al.*, 2021). The i^2PEPICO instrument provided insights into the isomer kinetics and energetics of nitrous acid

intermediates in an H/N/C/O system at elevated pressure. By using electronic structure methods and threshold photoelectron spectroscopy, it was found that the preferentially produced *cis*-HONO (Chai and Goldsmith, 2017) isomer is not detectable by photoionization methods. This circumstance arises due to the fact that *cis*-HONO dissociates upon ionization (Hoener *et al.*, 2021). Moreover and significantly, no HNO_2 was detected, despite recent reaction rates suggesting otherwise (Chen, Fuller and Goldsmith, 2019), which led to the conclusion that some pathways for HONO destruction may have been overlooked in theoretical work (Hoener *et al.*, 2021).

In subsequent work, the aforementioned reaction conditions were quantified, and systematic insight was gained into the chemistry of NO doped high-pressure oxidation of CH_4 in lean to rich combustion regimes (Hoener and Kasper, 2022). In light of the finding that *cis*-HONO is undetectable, a special emphasis was put on the challenges encountered when a quantification of the HONO intermediate using photoionization methods is attempted. As a future course of action, it was recommended that isomer-specific modeling of HONO can be highly beneficial to enable a direct comparison of the detected HONO concentration to the simulation (Hoener and Kasper, 2022). Such a species-specific modeling of the two HONO isomers was previously deemed unnecessary (Fuller and Goldsmith, 2019). Recent combustion mechanisms use a lumped assumption for the treatment of the kinetics of both HONO isomers, as this assumption was deemed acceptable for the accuracy of kinetics in modeling (Fuller and Goldsmith, 2019). Since isomer branching ratios cannot be determined by photoionization measurements and only the *trans*-HONO isomer is detectable, simulations would become comparable to the experiment only if the lumped assumption would be dropped. The data also showed interestingly high concentrations of NH_3 in the fuel-rich reaction condition doped with 1 % of NO, which proved the sensitivity of the CRF-PEPICO instrument. This observation gave rise to the conclusion that HNO_2 should have been detectable at the model-predicted concentrations, further supporting the findings of the previous work (Hoener *et al.*, 2021; Hoener and Kasper, 2022)

During the course of this work leading up to the concise present thesis, flame measurements at the ALS synchrotron facility were performed, which led to the publication of insight into the combustion of monoterpenes (Bierkandt, Hoener, *et al.*, 2021). Pinenes, are biofuel candidates and models that may be favorable candidates to replace certain aviation fuels (Bierkandt, Hoener, *et al.*, 2021). While many of the insights presented in this thesis are

obtained on the interface of chemistry and engineering, substantial engineering work was invested in the conception, design, and construction of new hardware for the experiments. The insight gained during this and many other flame measurement campaigns at the Swiss Light Source synchrotron facility enabled the development of an improved flame chamber for the coupling to the CRF-PEPICO endstation. The new flame chamber is optimized in several aspects. It has an attached vacuum linear stage, that enables shorter set-up times and ensures higher spatial data quality. The turnaround time for the set-up of the experiment is greatly reduced, which is an important factor since the measuring time in the synchrotron facility is limited. Also, several improvements to the ease of use were made, such as larger windows for the observation of flame ignition and combustion stability. The new flame chamber was used to gather indispensable flame data in subsequent campaigns to understand the low-temperature chemistry in flames leading to the formation of peroxides and hydroperoxides (Bierkandt, Oßwald, *et al.*, 2021). This data gave novel insight into the low-temperature speciation in flames (Bierkandt, Oßwald, *et al.*, 2021).

The measurement of flames of hydrogen doped with tetramethylethylene led to a deeper understanding of the flame structure and decomposition kinetics of this allylic bound hexene isomer (Bierkandt *et al.*, 2023).

4.2 Conclusions and outlook

Foundational knowledge for this work was gained in a project to develop a tandem mass spectrometer to analyze condensed matter in reacting chemical systems. The involvement in this project enabled a deep understanding of mass spectrometry, which was indispensable in the complex and involved analysis of the nitrous oxide combustion data. This subsequently led to the deep understanding of synchrotron VUV ionized photoelectron photoion spectroscopy, enabling the analysis of the reaction processes. Towards an understanding of the energetics and decomposition kinetics of the nitrous acid intermediates, a key enabler in this work was the use of computational chemistry and electronic structure methods. These methods were used to analyze the energetics of the doublet HONO and HNO_2, for Franck-Condon computations and for the determination of ionization energetics of nitrous acid. The calculations showed that the published kinetics for HONO and HNO_2 decomposition do not enable combustion models to reproduce the measurement. Furthermore, computational chemistry

modeling in combination with spectroscopic measurements led to an understanding of the photodissociation energetics of *cis*-HONO. This insight shows the futility of attempting to measure isomer branching ratios with popular and sensitive photoionization techniques (Hoener and Kasper, 2022).

The knowledge gained progressed via the initial EI-ToF-MBMS experiments over a new photoionization i^{2}PEPICO interfaced reactor experiment (Hoener *et al.*, 2020) towards understanding of the photoionization properties of the HONO combustion intermediates and the kinetics of nitrous acid isomer production and destruction (Hoener *et al.*, 2021). Finally, understanding of the repercussions of HONO's photoionization properties for combustion diagnostics involving photoionization methods and for chemical kinetics modeling was attained (Hoener and Kasper, 2022).

Future steps in the analysis of reaction kinetics should include the measurement of reactive species, sampled in non-equilibrium, and flame sampling of reaction conditions in which nitrogenized species interact with fuel. For the measurement of reactive species at low temperature and atmospheric pressure, an optimized reactor set up was developed (Liaw, Höner and Kasper, 2019). Flame sampling can enable the understanding of higher temperature interactions and deliver spatially resolved species profiles. Furthermore, it enables the understanding of transport phenomena not found in the ideal reactor. To achieve this, several reaction conditions of N_2O oxidized flames of methane, ethylene and butadiene were investigated using i^{2}PEPICO in the course of this work and are currently being prepared for publication.

Concluding, it can be stated that in the course of this work several experimental set-ups have been developed that helped in the acquisition of crucial and indispensable combustion and basic chemistry data. The pressurized reactor experiment coupled to CRF-PEPICO has produced novel low temperature combustion data. Several conditions encompassing the interaction of different hydrocarbons, ozone and oxides of nitrogen under elevated pressure have been investigated and the work has been published. Moreover, understanding of flame chemistry was gained with the improved flame set-up coupled to the CRF-PEPICO. The combination of powerful spectroscopic techniques with electronic structure computations enabled the development of a deep understanding of the kinetics and energetics of the important nitrous acid intermediate in combustion.

A pressurized flow reactor combustion experiment interfaced with synchrotron double imaging photoelectron photoion coincidence spectroscopy

Hoener, M., Kaczmarek, D., Bierkandt, T., Bodi, A., Hemberger, P., Kasper, T.
Review of Scientific Instruments, 2020, 91(4), 045115
DOI: 10.1063/1.5141168

My contribution to this work was the development of the reactor interface to the CRF-PEPICO endstation, manufacturing supervision of the design, the commissioning of the experiment, measurement and analysis of validation data for comparison to known results, writing the manuscript.

Review of Scientific Instruments ARTICLE scitation.org/journal/rsi

A pressurized flow reactor combustion experiment interfaced with synchrotron double imaging photoelectron photoion coincidence spectroscopy

Cite as: Rev. Sci. Instrum. 91, 045115 (2020); doi: 10.1063/1.5141168
Submitted: 4 December 2019 • Accepted: 29 March 2020 •
Published Online: 21 April 2020

M. Hoener,[1,a)] D. Kaczmarek,[1] T. Bierkandt,[2] A. Bodi,[3] P. Hemberger,[3] and T. Kasper[1]

AFFILIATIONS

[1]Mass Spectrometry in Reactive Flows – Institute for Combustion and Gas Dynamics (IVG), University Duisburg-Essen, Duisburg 47057, Germany
[2]German Aerospace Center (DLR) – Institute of Combustion Technology, Stuttgart 70569, Germany
[3]Laboratory for Synchrotron Radiation and Femtochemistry – Paul Scherrer Institute, Villigen 5232, Switzerland

[a)]**Author to whom correspondence should be addressed:** martin.hoener@uni-due.de

ABSTRACT

A new pressurized low-temperature combustion experiment has been commissioned at the Swiss Light Source, Paul Scherrer Institute. The experiment uses photoionization with tunable synchrotron radiation and double imaging photoelectron photoion coincidence (i^2PEPICO) detection at the vacuum ultraviolet beamline. The experimental setup is described, including the high-pressure reactor experiment, sampling interface, and reactant delivery system. The CRF-PEPICO (Combustion Reactions Followed by Photoelectron Photoion Coincidence) endstation and VUV beamline are briefly elaborated. The novel aspects of the apparatus and the new components are elucidated in detail, such as the fluid supply system to the reactor and the reactor integration into the endstation. We also present a system overview of the experimental setup. The technical details are followed by a description of the experimental procedure used to operate the pressurized flow reactor setup. Finally, first experimental results demonstrating the capability of the setup are provided and analyzed. A major advantage of this new experiment is that the excellent isomer resolution capabilities of the i^2PEPICO technique can be transferred to the investigation of reactions at elevated pressures of several bars. This enables the investigation of pressure effects on the reactivity of fuel mixtures and covers more realistic conditions found in technical combustors. The capability to obtain quantitative oxidation data is confirmed, and the main and certain intermediate species are quantified for a selected condition. The results show excellent agreement with a chemical kinetics model and previously published reference measurements performed with a gas chromatography setup.

I. INTRODUCTION

Combustion science investigates interactions of fuels and oxidizers, the kinetics involved in fuel decomposition and oxidation, and the production of pollutants such as soot and NOx. To understand the intricate chemical interactions that take place in combustion processes, universal, highly sensitive, and selective detection methods are required. One established technique is photoionization molecular-beam mass spectrometry (PI-MBMS) coupled to a synchrotron vacuum ultraviolet (VUV) photon source (Cool *et al.*, 2005; Hansen *et al.*, 2009; Qi, 2013; Krüger *et al.*, 2014; Oßwald *et al.*, 2014). The high photon flux and energy resolution of synchrotron VUV sources make the isomer specific identification of reaction intermediates possible using fragmentation-free soft ionization with high sensitivity and excellent signal to noise ratio (Cool *et al.*, 2005; Hansen *et al.*, 2009). The assignment and, ideally, the accurate concentration measurement of the reaction intermediates in complex gas mixtures at high temperatures and pressures, e.g., in simplified model experiments of combustion systems or chemical synthesis processes, are the first steps in the development of reaction mechanisms that describe these complex environments accurately.

The aim of most combustion experiments is to identify and quantify relevant combustion constituents as well as to provide input data and validation for chemical kinetics mechanisms. The advantage of molecular-beam mass spectrometry (MBMS) flame-sampling experiments is that they can shed light on detailed concentration histories of combustion constituents in the flame with high spatial resolution (Hansen *et al.*, 2009; Qi, 2013). Molecular-beam sampling allows for simultaneous identification of all combustion constituents, including that of reactive species, such as radicals, by quenching their destruction reactions by gas beam expansion in a cone-shaped fused silica sampling probe (Hansen *et al.*, 2009; Qi, 2013) before passing them into the analytical stage.

A distinct advantage of gas sampling and species identification using PI-MBMS is the ability to deconvolute isobaric and even isomeric species. This can be achieved by using the energy selective nature of the photoionization process by varying the photon energy of the tunable light source (Cool *et al.*, 2005; Hansen *et al.*, 2009; Oßwald *et al.*, 2014; Pieper *et al.*, 2018). Of particular importance for the development of chemical kinetics mechanisms is the understanding of concentrations and participation of isomeric species in combustion reactions (Krüger *et al.*, 2014; Pieper *et al.*, 2018; Osswald *et al.*, 2007; Cool *et al.*, 2005; Hansen *et al.*, 2009), since they can have significantly different contributions to the reaction network (Cool *et al.*, 2005). The identification of species relies solely on ion yield curves as a function of photon energy (photoionization spectra) in conventional PI-MBMS (Cool *et al.*, 2005; Oßwald *et al.*, 2014; Lucassen *et al.*, 2009). In contrast, the acquired photoelectron spectra using PEPICO allow fingerprinting of species by means of photoion mass selected threshold photoelectron spectra (ms-TPES) (Oßwald *et al.*, 2014; Pieper *et al.*, 2018; Krüger *et al.*, 2014; Bodi *et al.*, 2013; Hemberger *et al.*, 2013). These spectra show unique, compound-specific vibronic transitions according to the Franck–Condon (FC) principle (Bodi *et al.*, 2013; Hemberger *et al.*, 2013; Oßwald *et al.*, 2014; Pieper *et al.*, 2018), which can be compared to both literature references and FC simulation results. Herein lies a particular advantage of photoelectron photoion coincidence (PEPICO) spectroscopy used for combustion diagnostics (Oßwald *et al.*, 2014; Krüger *et al.*, 2014; Pieper *et al.*, 2018). Identification of species using photoionization (PI) spectra is a powerful tool (Oßwald *et al.*, 2014; Krüger *et al.*, 2014) and is particularly useful for quantification as well as identification of combustion intermediates in the sub-ppm range. Quantitative data can be obtained through calibration using stable species, literature ionization cross sections, and by performing element balance computations across the major species (Oßwald *et al.*, 2014; Kasper *et al.*, 2009; Schenk *et al.*, 2013; Osswald *et al.*, 2007). The distinctive advantage of the PEPICO method is to unveil isomeric species using their photoelectron spectrum as an identification criterion in addition to the PI spectrum (Oßwald *et al.*, 2014; Krüger *et al.*, 2014; Pieper *et al.*, 2018; Bodi *et al.*, 2013). Unambiguous identification is an important aspect for quantification, since identification is an imperative prerequisite for accurate subtraction procedures for mass-convoluted species. Advantages of PEPICO for quantitative combustion diagnostics have been thoroughly demonstrated by Felsmann *et al.* (2016) and Oßwald *et al.* (2014). Quantification of isomers based on species selection using the photoelectron signal has also been demonstrated by Oßwald *et al.* and can be used to a limited extent (Oßwald *et al.*, 2014).

A PEPICO flame experiment has been operated at the VUV beamline of the Swiss Light Source (SLS) for several years (Krüger *et al.*, 2018; Bierkandt *et al.*, 2017; Felsmann *et al.*, 2015; Oßwald *et al.*, 2014). The experiment is coupled to an imaging/double imaging photoelectron photoion coincidence (iPEPICO/i^{2}PEPICO) spectrometer (Bodi *et al.*, 2009, 2012; Oßwald *et al.*, 2014; Sztáray *et al.*, 2017). Flame experiments have been performed at the Advanced Light Source (ALS), Berkeley, USA (Cool *et al.*, 2005; Hansen *et al.*, 2009), and the National Synchrotron Laboratory (NSRL), Hefei, China (Qi, 2013), using PI-MBMS, while another double imaging PEPICO combustion experiment is available at the SOLEIL synchrotron, Saint-Aubin, France (Garcia *et al.*, 2013; Krüger *et al.*, 2014; Krüger *et al.*, 2019).

Another class of combustion experiments uses atmospheric and low-pressure flow reactors (Qi, 2013; Moshammer *et al.*, 2015, 2016) coupled to PI-MBMS. These experiments allow the investigation of low-temperature combustion chemistry in oxidizing and non-oxidizing environments while capitalizing on the distinct advantages of PI-MBMS. The well-stirred reactor first described by Matras and Villermaux (1973) has been extensively used in these experiments. It uses gas jets to mix the reactants continuously inside a heated glass sphere, where reactions take place. Currently, such experiments are performed at the ALS (Moshammer *et al.*, 2015, 2016) and at the NSRL (Herbinet *et al.*, 2011).

Although combustion experiments coupled to PI-MBMS have been used to investigate a wide range of combustion conditions and species, they have been limited to pressures up to 1 atm until now (Moshammer *et al.*, 2016, 2015; Hansen *et al.*, 2009; Cool *et al.*, 2005; Qi, 2013; Krüger *et al.*, 2014; Sztáray *et al.*, 2017; Oßwald *et al.*, 2014). To get comprehensive speciation data for low-temperature combustion experiments across a wider pressure range, a high-pressure plug-flow reactor experiment has been commissioned at the VUV beamline of SLS using the CRF-PEPICO (Combustion Reactions Followed by Photoelectron Photoion Coincidence) spectrometer (Sztáray *et al.*, 2017). Similar pressurized plug-flow reactors have been used to generate quantitative speciation data for reaction mechanism development at elevated pressures using different analytics such as gas chromatography and molecular-beam sampling (e.g., Rasmussen *et al.*, 2008; Kaczmarek *et al.*, 2019a; and 2019b).

This work describes the new experimental setup, the interface to the endstation, and first results. The aim of the experiment is to use the ability of the i^{2}PEPICO method to distinguish convoluted species, especially isomers, using photoionization spectra and ms-TPES. In addition, quantification of combustion species is demonstrated, which provides an indispensable capability for reaction mechanism development and validation. In a first campaign, measurements of different diluted

TABLE I. Compound mole fractions and flows for the φ = 8 condition of CH_4 doped with n-heptane.

Reactant	Flow (sccm)	Mole fraction x
Ar	231.9	0.828
O_2	11.2	0.04
CH_4	35.1	0.125
C_7H_{16}	1.76	0.006

reactant mixtures were performed with the new pressurized reactor setup. Some data on the oxidation of n-heptane doped methane (cf. Table I) will be used to demonstrate the capabilities of the new experiment.

II. EXPERIMENTAL SETUP

A. Pressurized flow reactor

A pressurized plug-flow reactor interfaced with the CRF-PEPICO spectrometer is used to investigate the conversion reactions of fuel and oxidizer at a pressure of 6 bar. Plug-flow operation of the reactor is ensured by using an appropriate flow regime (280 sccm total flow in this case). This ensures the applicability of one-dimensional combustion simulations. The flow reactor is integrated into an expansion chamber, leading to the molecular-beam interface. The first expansion stage consists of a manual needle valve (cf. Fig. 2) (GB1H-6M, Hy-Lok, Songjeong-Dong, South Korea). A cutaway view of the expansion chamber setup and the reactor integration is shown in Fig. 1. The reactor is connected to the expansion stage via heated stainless steel pipes of 12 mm outer diameter (OD) and 6 mm OD for the needle valve stage. Both pipes have a wall thickness of 1 mm, providing flow volumes of inner diameter (ID) of 10 mm and 4 mm, respectively. Temperatures of the connecting pipes are kept at 373–423 K to prevent condensation of water and other products while keeping the temperature low enough to prevent further reactions of species in the stream discharged from the reactor. Heating is provided by electrical heating tapes (Type HSQ, HORST GmbH, Lorsch, Germany) controlled by using a digital proportional integral derivative (PID) heating controller.

Gases expand through the transfer line into the expansion chamber, which contains the fused silica sampling probe. A long transfer line is generally undesirable because wall interactions and secondary catalytic reactions may affect the sample composition. However, the molecular-beam skimmer is located ~500 mm from the outer flange of the expansion chamber (cf. Bodi *et al.*, 2012; Oßwald *et al.*, 2014), which required the use of a longer than ideal heated transfer line. It guides the gases directly to the orifice of the fused silica probe. Heating as close as possible to the sampling point is provided by a flange extension of the connector flange (cf. Fig. 1) reaching into the expansion chamber. Heating tape is wrapped around the 12 mm OD stainless steel transfer pipe on the atmospheric side of the flange and around the needle valve all the way to the copper mantle. The transfer pipe and heating tape are insulated using multiple layers of fiberglass insulation wrapping. Insulation and transfer line heating are omitted in Fig. 1 for clarity.

A detailed cutaway view of the reactor internals and the throttling stage is shown in Fig. 2. The reactor consists of an outer pressure shell made of a 12 mm OD AISI 316 stainless steel pipe with a wall thickness of 1 mm and a length of 650 mm that serves as pressure containment. To prevent wall interactions, the heated flow volume contains an inner liner made of a fused silica pipe with an OD of 8 mm and a wall thickness of 1 mm. The liner provides chemically inert, hydraulically smooth walls that cover the outer shell length of 650 mm completely. The fused silica liner is loosely sealed against the stainless steel outer pressure containment on both ends of the reactor using polytetrafluoroethylene (PTFE) tape. This prevents the gases from bypassing the fused silica liner and reacting in the gap between liner and outer shell while allowing a sufficient leakage rate to equalize gap pressure.

The outer stainless steel shell is enclosed by a copper jacket of OD of 35 mm and a length of 450 mm, which distributes the electrical heating power evenly. The copper mantle is split along a horizontal line for assembly around the stainless steel outer reactor shell. The measured temperature profiles of the reactor design for set temperatures of 473–973 K show a nearly perfect isothermal zone (Kaczmarek *et al.*, 2019a, 2019b). The isothermal zone stretches the full 450 mm length of the copper mantle, while temperature ramps are present in the lead-in and lead-out zones both stretching the remaining 100 mm on each end of the reactor. The reactor is operated in the constant flow regime, which leads to lower residence times with increasing temperature.

The round groove in the copper mantle, in which the stainless steel pipe is embedded, is manufactured with a tight fit to the 12 mm pipe. The surface contact between heating mantle and the outer stainless steel reactor shell provides satisfactory thermal conductivity between the components. The copper mantle is wrapped with two electrical heating tapes (Type HSQ, HORST GmbH, Lorsch, Germany) of 6000 mm length each, side-by-side. Each tape is connected to a digital PID temperature controller (HT MC11, HORST GmbH, Lorsch, Germany), and the temperature is measured using two mineral insulated type K thermocouples (TC Mess- und Regeltechnik GmbH, Mönchengladbach, Germany) inserted into 3 mm drilled

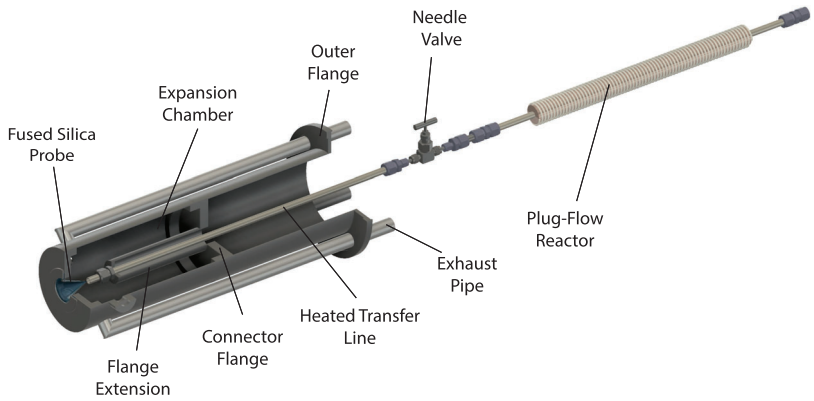

FIG. 1. Cutaway view of the expansion chamber integration of the reactor experiment and first stage of the sampling interface. Transfer line heating and insulation of the transfer line and the reactor are omitted for clarity.

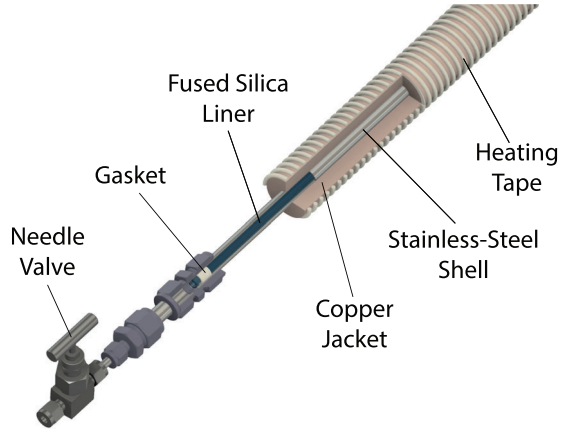

FIG. 2. Cutaway details of the reactor stage internals and expansion stage showing the PTFE seal between liner and outer shell, the arrangement of the electrically heated copper jacket around the isothermal region of the reactor, and the needle valve expansion stage. Insulation of the reactor is omitted for clarity (details in text).

holes in the heat distribution jacket at 25% and 75% length position. The reactor is wrapped in several layers of fiberglass tape insulation and a layer of refractory ceramic fiber insulation. To contain the fibrous insulation material, to facilitate handling of the reactor, and to provide a final convective barrier, the outer insulation layer consists of laboratory aluminum foil. All insulation layers are omitted in Figs. 1 and 2 for clarity. Fluid connections are made using compression fittings.

B. Fluid supply systems and operation

A detailed view of the fluid supply of the setup is shown in Fig. 3. Only the fluid systems are shown, and electrical wiring for the controllers and instrumentation is mostly omitted for the sake of clarity. We describe the system from the left of Fig. 3, progressing to downstream components of the setup to the right. The feed system is set up for experiments using gaseous and liquid fuels with argon (or other) diluent and an oxidizer. Starting from the left of Fig. 3, the supplies of gaseous fuel (F), oxidizer (O), a gaseous dopant (D), and inert diluent (AR) are shown. The liquid feed system for liquid fuels and dopants is shown on the bottom left of Fig. 3 with liquid feedstock coming from a reservoir (L).

The gaseous reactants are fed from gas cylinders. Pressure is reduced by using commercial pressure regulators to a foreline pressure of approximately 7 bar total. Thermal mass flow controllers (MFCs) (MKS Instruments, Inc., Andover, MA, USA) meter gases. All gaseous components are fed through manual isolation valves that allow for the isolation of the individual feed streams from the downstream components and the reactor. Gaseous components are transferred to a mixing point where they intermix by diffusion. The liquid feed system uses the same MFC to supply the argon diluent as in experiments with solely gaseous fuels. When operating the liquid evaporation system, the alternate argon supply line is isolated from the setup and the entire argon dilution gas stream is delivered to the evaporator.

A high-pressure liquid chromatography pump (HPLC) (Bischoff Analysentechnik u. -geräte GmbH, Leonberg, Germany) feeds and meters liquid fuels and dopants to the evaporator consisting of a multiple-bend stainless steel U-pipe. Condensation of the liquid fuel in downstream lines is suppressed by keeping the partial pressure of evaporated liquid below its vapor pressure. With this method, the gas stream is not saturated for the given temperature, and the introduced fuel is directly metered by the HPLC pump instead. If a higher concentration is desired, the unheated line can be replaced by a heated foreline to the reactor, which increases the fuel vapor carrying capacity of the dilution gas stream. The evaporator is kept at constant temperature, above the evaporation temperature of the liquid fuel in an electrically heated and

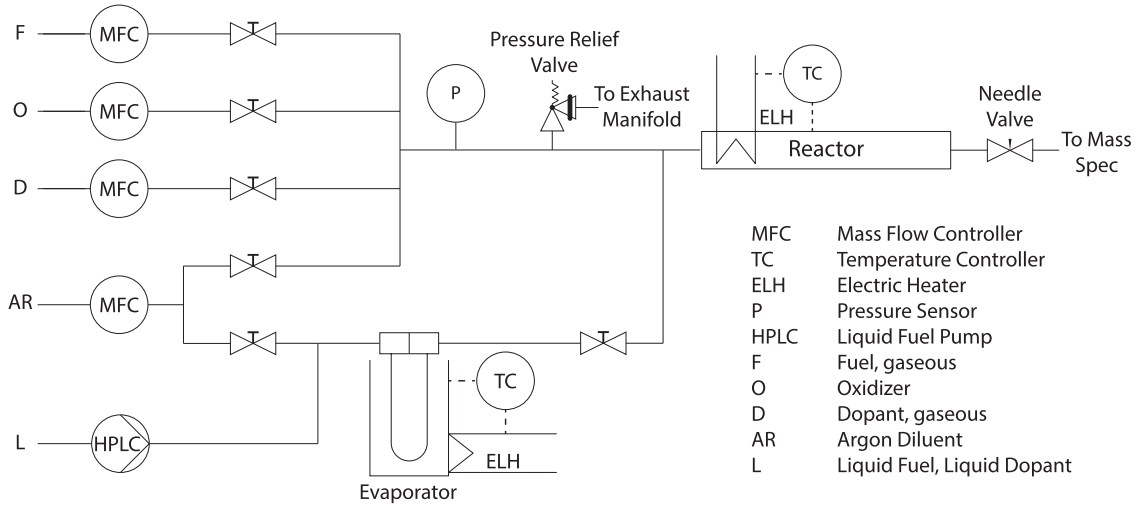

FIG. 3. Diagram of fluid supply and metering system employed to condition the reactant flow to the plug-flow reactor stage. Major components are displayed with symbols partially based on ISO 10628-2.

temperature-controlled bath of silicone oil (thermostat; Julabo GmbH, Seelbach, Germany). The HPLC is used to deliver the liquid reactant with sufficient pressure for introduction into the pressurized diluent stream, and both streams are fed to the evaporator column. The mixed gas stream is then delivered to the mixing point in front of the reactor and intermixed with the remaining gaseous component stream. There are isolation valves in front of and behind the evaporator column. For experiments using gaseous fuels only, the evaporator is isolated from the reactor feed line and argon supply. The feed line connecting the flow controller rig with the reactor is equipped with an adjustable relief valve (Hy-Lok, Songjeong-Dong, South Korea) that opens in case of overpressure in the feed line due to incorrect pressure settings or ignition events in the reaction zone. In normal operation, the safety valve is set to a pressure slightly above the desired pressure for the experiment. The normally closed valve releases any overpressure into the exhaust manifold in case of a blow-off event. The reactor setup with its electrical heating and heating control is also shown as part of the fluid system up to the spectrometer. Behind the reactor, a manual needle valve acts as a throttling stage, followed by the low-pressure stages leading to the i^2PEPICO spectrometer. This constitutes a limitation of the setup because transient species can be destroyed during expansion in the valve stage.

C. CRF-PEPICO endstation, VUV beamline, and experiment integration

The analytical stage used for the experiment is the double imaging CRF-PEPICO endstation, as described by Sztáray *et al.* (2017). A brief description of the system, its capabilities, and the accompanying beamline that delivers the VUV light for ionization is given here. For additional information, the reader is referred to the references describing these systems in more detail (Bodi *et al.*, 2009, 2012; Johnson *et al.*, 2009; Sztáray *et al.*, 2017).

The major systems comprising the analytical capability provided at the SLS are the beamline (Bodi *et al.*, 2009, 2012; Johnson *et al.*, 2009) and the CRF-PEPICO endstation (Bodi *et al.*, 2012; Sztáray *et al.*, 2017) into which the pressurized flow reactor combustion experiment is integrated. The grazing incidence monochromator is a turntable design featuring three positions to accommodate different laminar and blazed gratings. The dispersion of the laminar gratings corresponds to an energy dependent energy resolution of $E/\Delta E \approx 10^4$ (Bodi *et al.*, 2009), while the high-flux blazed grating delivers $E/\Delta E \approx 10^3$ (Bodi *et al.*, 2012) at a photon energy of 10 eV. The light transfer line of the beamline is evacuated to ultrahigh vacuum to prevent loss of photon flux to absorption in the background gas. The differentially pumped gas filter houses the exit slit and is situated directly in front of the ionization chamber at a distance of 500 mm from the ionization region (Bodi *et al.*, 2012). It eliminates higher VUV harmonics passed by the monochromator by absorption in a rare gas mixture (Bodi *et al.*, 2009). In the measurements reported here, for energies $h\nu > 15$ eV, the gas filter is filled with neon, while at energies of 10.6–15.0 eV, the filter utilizes a 75% neon, 25% argon mix (Bodi *et al.*, 2009). For $h\nu < 10.6$ eV, higher harmonics are filtered by a MgF_2 window, which can be manually inserted into the beam line using a screw operated shutter stage. The beamline delivers an energy dependent photon flux to the ionization region with a maximum spot size of 4×2 mm^2 (Bodi *et al.*, 2009; 2012).

The CRF-PEPICO endstation affords simultaneous analysis of photoelectrons and time-of-flight (ToF) analysis of positive ions at a high count rate of up to 10^5 s^{-1} (Bodi *et al.*, 2009). The instrument uses two stage linear ion extraction, which allows electron imaging and first order space focusing ion detection, adhering to Wiley–McLaren conditions (Bodi *et al.*, 2012; Wiley and McLaren, 1955) and double imaging velocity map imaging operation (Sztáray *et al.*, 2017; Bodi *et al.*, 2012). Ions and electrons are continuously extracted from the interaction region toward two RoentDek DLD 40 imaging detectors (RoentDek Handels GmbH, Kelkheim, Germany) utilizing delay lines that allow fast position sensitive detection of photoelectrons and photoions (Bodi *et al.*, 2012). Every coinciding electron and ion event is individually matched. The detected electron events are utilized to start the ToF measurement of positive ions. Data acquisition takes place using PSI in-house developed software.

In the system overview in Fig. 4, the mass spectrometer (MS) is shown schematically to the left, with the reactor integration into the source and expansion chambers shown to the right. The interaction of expansion stages with pressures ranging from 6 bar upstream of the needle valve down to experimental chamber pressures in the beam interaction region is also visible in Fig. 4. The molecular beam (red) is formed by the fused silica probe and collimated by a nickel molecular-beam skimmer with an orifice diameter of 2 mm (Beam Dynamics, Inc., Jacksonville, FL, USA). The skimmer orifice transfers the sample into the experimental chamber where the orthogonal VUV light beam ionizes the sample. Velocity map imaging photoelectron and photoion detection is shown schematically in Fig. 4, and representative false color images of intensity distributions on the imaging detectors are shown.

During the reactor campaign, the experimental chamber was pumped by a cryogenic Leybold COOLVAC 1500 CL. The source chamber was held at the desired pressure in the region of 3×10^{-5} mbar by a COOLVAC 5000 CL cryogenic pump and two turbo pumps (Pfeiffer TPH 1201 UP and HiPace 1200).

After the reactant stream, at a pressure of 6 bar, passes the needle valve that comprises the first expansion stage, it enters the expansion chamber (cf. Figs. 1 and 2). This chamber is also used for the original flame experiment (Oßwald *et al.*, 2014) and is pumped by using a Pfeiffer Adixen ACP 120 G Roots pump. The expansion chamber is kept at a constant operating pressure of 50 mbar by an electrically driven butterfly throttle valve controlled by using a digital/analog pressure controller (MKS Instruments, Andover, MA, USA). The controller reads the chamber pressure by means of a Baratron rough vacuum gauge (MKS Instruments, Andover, MA, USA). The fused silica molecular-beam sampling probe has an orifice diameter of 320 μm. The pressure in the expansion chamber is chosen to provide an acceptable source chamber pressure of $\sim 3 \times 10^{-5}$ mbar. The molecular beam enters the ionization chamber, and its scattering contributes to the background pressure of $\sim 3 \times 10^{-6}$ mbar during experiments.

III. EXPERIMENTAL

A. Overview and motivation of experiments

The reactor setup can accommodate experiments at pressures ranging from 0 bar to 6 bar total at temperatures between room temperature and 973 K. Such conditions allow the investigation of

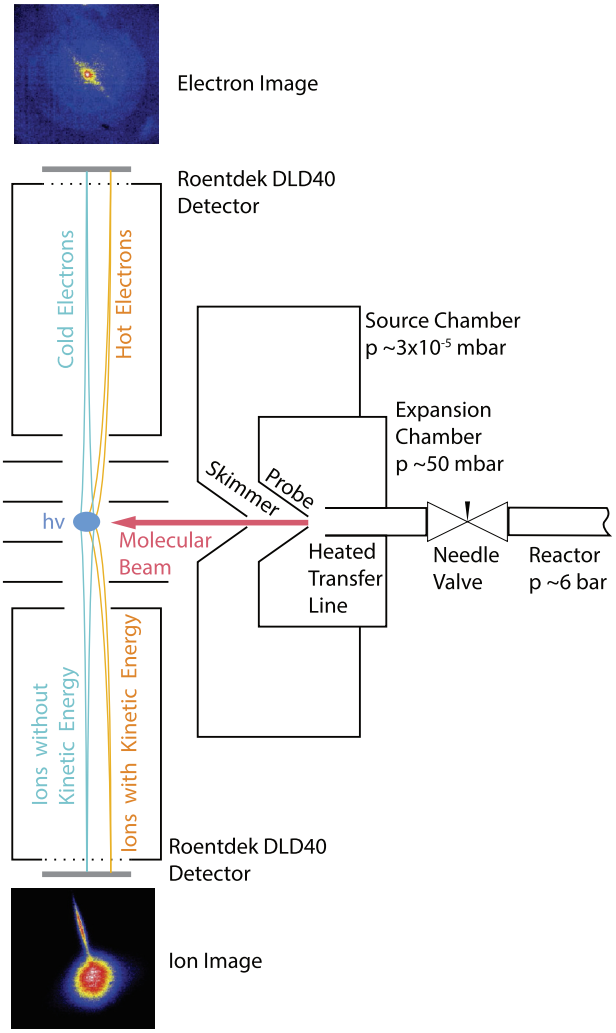

FIG. 4. Schematic view of the CRF-PEPICO spectrometer (Bodi *et al.*, 2012; Sztáray *et al.*, 2017) in double imaging operation, experiment integration, and differential pumping stages used to bring the pressure from reactor pressure (6 bar) down to ionization chamber pressure ($\approx 3 \times 10^{-6}$ mbar) in three expansion stages. The light beam enters the ionization region normal to the plane of illustration, denoted *hν*, in blue. Representative false color intensity maps showing photoelectron and photoion velocity map images are provided at the top and bottom of the schematic.

partial oxidation and fuel conversion in the low-temperature range at pressures relevant for technical combustion processes. Fuel supply systems accommodate the investigation of multi-fuel reactant mixes containing liquid and gaseous fuels as well as dopants. In the first campaign reported here, we have investigated several combustion process conditions using the novel pressurized reactor setup interfaced with the CRF-PEPICO endstation. First results from a conversion experiment using methane (CH_4) doped with n-heptane (C_7H_{16}) as fuels at an equivalence ratio of 8 and diluted with 82.8% argon are presented here because they are best suited to demonstrate the isomer resolution capabilities of the experiment. Mole fractions and reactant flows for the condition are given in Table I. The argon dilution is relatively low due to a minimum flow limitation of the liquid fuel delivery pump. The small amount of dopant would not have been possible at higher dilutions. The addition of highly reactive n-heptane reduces the temperatures required for the onset of reactions converting the stable hydrocarbon CH_4. Similar conditions have been investigated with the goal of providing validation data for reaction mechanism development for hydrocarbon conversion (Kaczmarek *et al.*, 2019a).

The key capability of VUV photoionization to detect species selectively in complex reactive environments is demonstrated by means of ms-TPES and photoionization spectra. Isomer-selective species identification is shown for two isomers at m/z 72. The main species, namely, the reactants O_2, CH_4, and n-heptane as well as the major products CO, CO_2, and water are quantified at the conditions in Table I. Quantification of the low-temperature intermediates methanol (CH_3OH) and acetaldehyde (CH_3CHO) is performed. Mole fraction profiles are compared to a recent combustion mechanism (Zhang *et al.*, 2016) and gas chromatography (GC) reference data (Kaczmarek *et al.*, 2019a). The comparison serves to demonstrate the quality of the quantitative data for reaction mechanism development.

B. Measurement procedure and reactor operation

The pressure in the isothermal reaction zone is kept constant by pre-setting it using the manual needle valve. Temperatures are scanned starting from the lowest desired temperature (in the case of the discussed condition 473 K). The temperature is increased subsequently in steps of 50 K up to a maximum temperature of 973 K. For each step, mass spectra are obtained at different energies in the range of compound ionization energies (IEs) of the species of interest. After the initial temperature ramp (temperature scans), spectra (photon energy scans) are obtained at constant temperature. Selected temperatures for the energy scans are those that show the maximum yield of species of interest during the temperature ramp measurements. These temperatures usually are in the vicinity of the reaction onset temperature of the investigated condition.

C. Separation of isomeric species using threshold photoelectron and photoionization spectra

The main multiplexing advantage of PI-MBMS in general and more specifically synchrotron photoionization is the ability to distinguish species by their mass and their IE (Cool *et al.*, 2005). The IE affords an indispensable secondary selection criterion for the discrimination of compounds. In particular, for the analysis of complex species compositions, which are commonly encountered in combustion experiments, photoionization is a powerful tool (Cool *et al.*, 2005; Hansen *et al.*, 2009; Qi, 2013). In conventional PI-MBMS with time-of-flight (ToF) mass spectrometry, species identification is performed by photoionization spectra. Consecutive spectra are taken at a single height above burner in the flame or a single temperature for reactor experiments, while the photon energy is scanned in small intervals. For a single species, no signal will be acquired, while the set energy of the ionizing VUV light is below the IE of the molecule. When the ionization threshold is reached, a signal is acquired whose intensity increases with increasing photon energy. The signal

intensity increases until the dissociative photoionization of the molecule surpasses the increase in ionization cross section as a function of the photon energy. Species identification is performed by comparing the IE at the onset of the steepest slope of the PI spectrum to the literature or calculated IE values. For convoluted species such as isomers, the additional signal contribution of the isomer with the higher IE creates a further increase in the slope of the ion yield curve. Isomers can be selectively detected by their differing ionization energies. The differing contributions to the PI spectrum can be used to deduce information about ratios of contributing species. These principles were first demonstrated for combustion experiments by Cool *et al.* (2005).

Using double imaging PEPICO mass spectrometry, isomer and species identification can, in general, be performed in the same manner. Moreover, the distinct resonance pattern given by the simultaneously acquired photoelectron spectra results in a unique fingerprint of the species (Oßwald *et al.*, 2014; Bodi *et al.*, 2013). By comparing the measured threshold photoelectron spectrum with literature reference photoelectron spectra and Franck–Condon simulations, a confident identification of species at the same integer mass or identical mass, such as isomers, can be performed (Oßwald *et al.*, 2014; Krüger *et al.*, 2014; Pieper *et al.*, 2018; Bodi *et al.*, 2013). The same principle applies for mass-convoluted non-isomeric species, which can occur frequently due to the low mass resolution of the instrument. The use of imaging PEPICO for acquisition of flame data was first demonstrated by Oßwald *et al.* (2014) at the iPEPICO endstation at SLS and later by Krüger *et al.* (2019) and Pieper *et al.* (2018) at the DELICIOUS III double imaging PEPICO setup at Soleil Garcia *et al.* (2013). Distinct advantages of using double imaging for flame diagnostics and analysis methods specific to double imaging PEPICO have been demonstrated (Krüger *et al.*, 2019; Felsmann *et al.*, 2016). Krüger *et al.* (2019) demonstrated that the ion image can be used to distinguish species in the thermalized background and in the molecular beam, specifically for the case of the transient OH radical in combustion experiments. A summary of double imaging valence photoionization coincidence techniques and accompanying analysis methods was also given by Baer and Tuckett (2017).

For species identification and fingerprinting using PI spectrum and ms-TPES, the peak at m/z 72 is selected. The signal is likely to arise from a convolution of species directly from the major fuel destruction pathways of n-heptane (Ranzi *et al.*, 1995; Curran *et al.*, 1998; Pelucchi *et al.*, 2014; Luck *et al.*, 1973). The energy scan was performed between photon energies of 9.0 eV and 10.3 eV with intervals $\Delta E = 0.025$ eV (cf. Fig. 5). Potential species at lower ionization energies are tetrahydrofuran with an IE close to 9.40 eV (Behan *et al.*, 1976; Doucet *et al.*, 1972; Hernandez, 1963) and the likely species 2-butanone [IE = 9.52 eV (Traeger, 1984)], iso-butanal [IE = 9.71 eV (Hernandez *et al.*, 1977)], and n-butanal [IE = 9.83 eV (Traeger and McAdoo, 1986)]. At higher photon energies, dimethyloxirane isomers may be detected, although they are unlikely to be contributing to the ms-TPES, since their IE is close to the maximum energy of the energy scan (10.3 eV) near 10.0 eV (Eskola *et al.*, 2017). Moreover, dimethyloxiranes are unstable and hence are likely destroyed in the expansion stage. *n*-Pentane and 2-methylbutane can both be excluded as contributors to the photoionization spectrum due to their IEs being close to or above the maximum photon energy of the scan (Watanabe *et al.*, 1962).

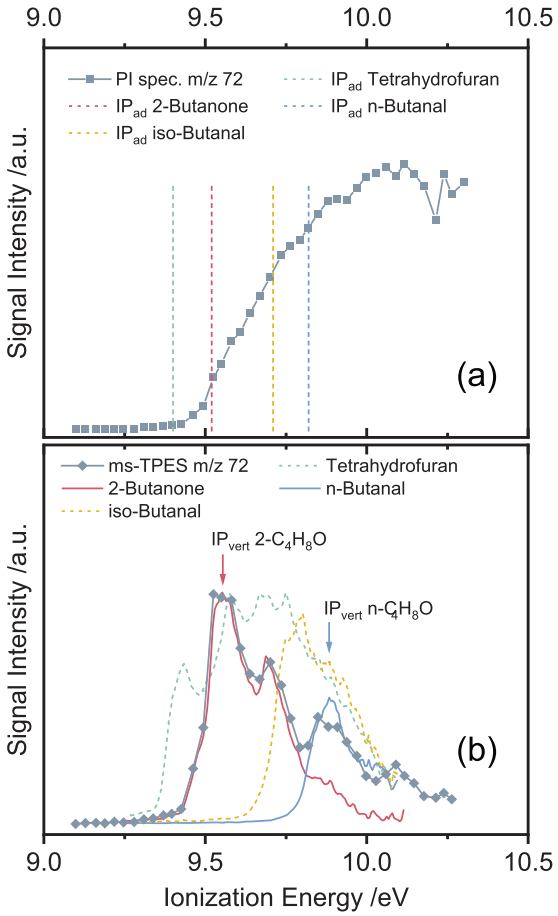

FIG. 5. Photoionization spectrum (PI spec.) (a) and ms-TPES (b) of the m/z 72 peak and comparison to reference literature photoelectron spectra from the work of Pieper *et al.* (2018). Literature values for adiabatic ionization energies for some m/z 72 species candidates are displayed by dashed lines in (a). Identical species color coding is used for the TPE in (b). In (b), the experimental values are displayed as solid lines with symbols and compared to species present in the sample (solid lines) and undetected species (dashed lines).

Ketones and aldehydes are likely species encountered in the sample arising from n-heptane destruction, since they are produced by major low-temperature fuel oxidation and destruction pathways, as described in modeling studies by multiple authors (Pelucchi *et al.*, 2014; Curran *et al.*, 1998; Ranzi *et al.*, 1995). Lumped schemes for the initiation of n-heptane destruction at low temperatures lead through the formation of peroxides and, subsequently, ketohydroperoxides (Ranzi *et al.*, 1995; Pelucchi *et al.*, 2014; Curran *et al.*, 1998), which then branch into lower hydrocarbon ketones and aldehydes (Ranzi *et al.*, 1995; Curran *et al.*, 1998; Luck *et al.*, 1973).

Figure 5(a) shows the PI spectrum and marked literature reference ionization energies (Hernandez, 1963; Doucet *et al.*, 1972; Behan *et al.*, 1976; Traeger, 1984; Hernandez *et al.*, 1977; Traeger and McAdoo, 1986). The late onset of the PI spectrum shows no evidence for the presence of tetrahydrofuran. However, the increase in signal and, thus, ion yield matches the IE of 2-butanone. The reason

for the signal increase preceding the marked adiabatic IE can be seen in the photoelectron spectrum [Fig. 5(b)], where the photoelectron yield increases prior to the adiabatic IE value. Moreover, another contributing factor is that the adiabatic value is particularly close to the vertical IE for this species (Lindstrom *et al.*, 1997). A distinctive feature is visible for n-butanal, while iso-butanal shows no feature in the PI spectrum in Fig. 5(a). Hence, 2-butanone and n-butanal are likely constituents of the sample injected into the spectrometer.

Further and much clearer confirmation of this assignment is given by the data presented in Fig. 5(b). It shows the measured ms-TPES and reference spectra for *m*/*z* 72 species from the work of Pieper *et al.* (2018). Here, the data show no distinctive features of either tetrahydrofuran or iso-butanal, while features consistent with 2-butanone and n-butanal are visible when compared with the reference spectra. The reference spectrum for 2-butanone (Pieper *et al.*, 2018) required a slight shift of ~20 meV to accommodate for a peak position discrepancy. It shows a red shift with respect to the experiment, which may be caused by calibration, the Stark shift, or other contributing factors. The shape of the reference spectrum in comparison to the experiment allows identification with great certainty due to the excellent agreement in the vibrational progression. Identification of species was feasible using ms-TPES despite the high number of possibly convoluted species and the special challenge that arises since many of these species do not show very distinct spectra (Pieper *et al.*, 2018). *iso*-Butanal may only be produced below the detection limit, as no feature hinting at this intermediate is visible in Fig. 5. This observation is also confirmed by GC data (cf. Kaczmarek *et al.*, 2019a).

For the sake of completeness, it has to be mentioned that more isomers exist at *m*/*z* 72, such as the stereoisomers of crotyl alcohol and other butenols. They show no significant contribution to the signal as the vertical IE in available reference spectra of 3-buten-1-ol and 3-buten-2-ol (Pieper *et al.*, 2018) is in the vicinity of that of iso-butenol (cf. Fig. 5).

Under similar process conditions, isomeric contributions can also be resolved by GC measurements. In contrast to the experiments presented here, the presence of the respective isomers must at least be suspected to allow GC measurements because the GC method and column must be matched to the separation problem. The identification of isomers using the PEPICO technique is universal and does not require prior knowledge of the sample composition when the photon energies can be scanned over a wide energy range. This aspect of the measurements makes the new experiment a valuable addition to the available analytical portfolio.

D. Quantification of species and comparison to model simulations and reference data

To enable comparison between experiment and chemical kinetics simulations, quantification of species is an essential capability of any analytical technique for combustion science. This encompasses requirements for the reproducibility of the experimental conditions and also serves as a quality benchmark for the experiment.

The general procedure for quantification of photoionization mass spectrometry combustion data was described in detail in previous publications (Osswald *et al.*, 2007; Kasper *et al.*, 2009; Schenk *et al.*, 2013; Qi, 2013; Oßwald *et al.*, 2014). Peculiarities of the i^{2}PEPICO spectrometer require slight modifications to the procedures, which were described by Oßwald *et al.* (2014) for the flame setup originally used at SLS. Calibration is performed according to the same principles as for photoionization flame experiments (Moshammer *et al.*, 2016). The employment of some calibration or quantification procedure is always necessary for quantitative mass spectrometry. Different systematic (e.g., photon flux, chamber pressure, sample composition, temperature, machine parameters, properties, and geometry) and compound-based contributions (i.e., ionization cross sections) impact signal intensity, and hence, no direct signal-intensity based assertion of species concentration in the sample is possible.

To acquire mole fractions of major species in flames, element balances are established at the burner surface and at a point in the exhaust gas far from the reaction zone, which contains combustion intermediates (Schenk *et al.*, 2013). Hence, the assumption holds that only reactants and minor amounts of CO and CO_2 products are signal contributors at the burner surface and only CO, CO_2, water, and hydrogen are contributors in the exhaust (Schenk *et al.*, 2013). Additionally, oxygen, which can be present in the exhaust gas stream for lean flames and unburned fuel for rich flames, has to be considered. For the element balances, it is further assumed that the argon mass fraction does not change across the flame and an argon profile is later calculated using an internal calibration procedure (Schenk *et al.*, 2013).

Only deviations from the aforementioned procedures will be outlined in this work, as flame data approaches can generally be transferred to reactor measurements (Moshammer *et al.*, 2016). In contrast to flame data, the element balances for the reactor sample are established at the minimum and maximum temperatures of the measured temperature series. Here, the assumption holds that for temperatures below reaction start temperature of the investigated condition, no reactions take place. Hence, the signal contributors are solely the reactants injected into the reactor, which simplifies the element balance compared to flame data evaluation. At high temperatures (maximum temperature of 973 K), the assumption is made that mostly CO, CO_2, hydrogen, water, and fuel for rich conditions and oxygen for lean conditions are present in the sample. This simplification introduces only minor errors in the analysis of major species mole fractions due to the low relative yield of other species at high temperatures. A further simplification of the general procedure arises, since the measured reactor conditions are highly diluted with inert gas. Under these conditions, it can be assumed that the change in argon mole fraction is negligible, and the calculation of an argon mole fraction profile can be omitted. The argon mole fraction is fixed at inlet conditions for calculation of species mole fractions. In some cases, however, determining an argon profile from internal calibration may be useful (Oßwald and Köhler, 2015).

To demonstrate the ability of the experiment to generate quantitative speciation data of elevated pressure combustion, the major species CO, CO_2, water, oxygen, and the two fuels are quantified. The data measured with the CRF-PEPICO are compared to a previously published reference measurement using gas chromatography (GC) (Kaczmarek *et al.*, 2019a) and to a recent combustion mechanism by Zhang *et al.* (2016). The GC measurements do not include H_2O due to the unavailability of a suitable column for this species at the time. The used mechanism contains 5336 reactions, 1268 species, and chemistry required for the simulation of n-heptane conversion (Zhang *et al.*, 2016). Simulations were performed using the plug flow

module of Chemkin 19.2 (Ansys Inc., 2008) and measured temperature profiles (Kaczmarek *et al.*, 2019a) at a pressure of 6 bar. The simulated temperatures correspond to the temperatures at which the measurements were performed.

Figure 6 shows the results of the element balancing procedure. CO, CO_2, H_2O, and CH_4 profiles are quantified from the $h\nu$ = 15.0 eV measurement with an acquisition time of 60 s. The C_7H_{16} signal was analyzed using a temperature scan at $h\nu$ = 10.3 eV and an acquisition time of 300 s. The argon signal was taken from a scan at $h\nu$ = 15.8 eV, only slightly above the ionization threshold of argon, since the signal yield was comparatively large because of the large mole fraction of the argon diluent. Although CO_2 was only present in relatively minor amounts, it was used for quantification since a direct calibration of the CO and CO_2 signals was performed yielding more accurate results in the elemental balance computation. Hydrogen was omitted since it can directly be solved for from the other balanced species and consequently has no influence on the balance used for the profiles shown in Fig. 6.

It is clearly visible in Fig. 6 that the CRF-PEPICO measurements are in very good agreement with both the GC data and the simulation. For the balanced major species in Fig. 6, a 25% estimated error is indicated. Both fuels [(a) and (c)] match perfectly the simulation and GC results. Minor discrepancies can be observed only for O_2 (b) and CO (d) at higher temperatures, while CO_2 (e) shows good agreement with the GC reference measurement. The CO signal was corrected for ethylene (C_2H_4) contribution, a species still present in non-negligible concentration at the highest temperature of 973 K and the same mass-to-charge ratio as CO (m/z 28). The correction was performed by using the m/z 28 signal at $h\nu$ = 11.2 eV and subtracting the C_2H_4 photoionization cross section (Mackie *et al.*, 2003) corrected signal from the m/z 28 signal at 15.0 eV. The imaging photoelectron detector active area in conjunction with the ion optics and applied extraction field gradients employed in the instrument lead to a maximum acceptance for photoelectrons with a kinetic energy of 1.6 eV (Oßwald *et al.*, 2014; Bodi *et al.*, 2012). Thus, a significant loss of electrons for kinetic energies larger than 1.2 eV is expected (Oßwald *et al.*, 2014). For photoelectron kinetic energies getting closer to this value, an increasing number of electrons are not detected. Since ion time-of-flight detection is triggered by photoelectron detection as the start signal, the ion coincidence signal is lost if the electron is lost. To account for this loss of ion signal, the α factor [cf. Eq. (1)], as introduced by Oßwald *et al.* (2014), was directly calibrated using C_2H_4. This calibration was performed in the range of energies used for acquisition of the C_2H_4 correction signal at $h\nu$ = 11.2 eV and the corrected CO signal acquired at $h\nu$ = 15.0 eV. The described corrections might in fact still not eliminate all error associated with the signal convolution in the quantification. This effect may explain the discrepancy at higher

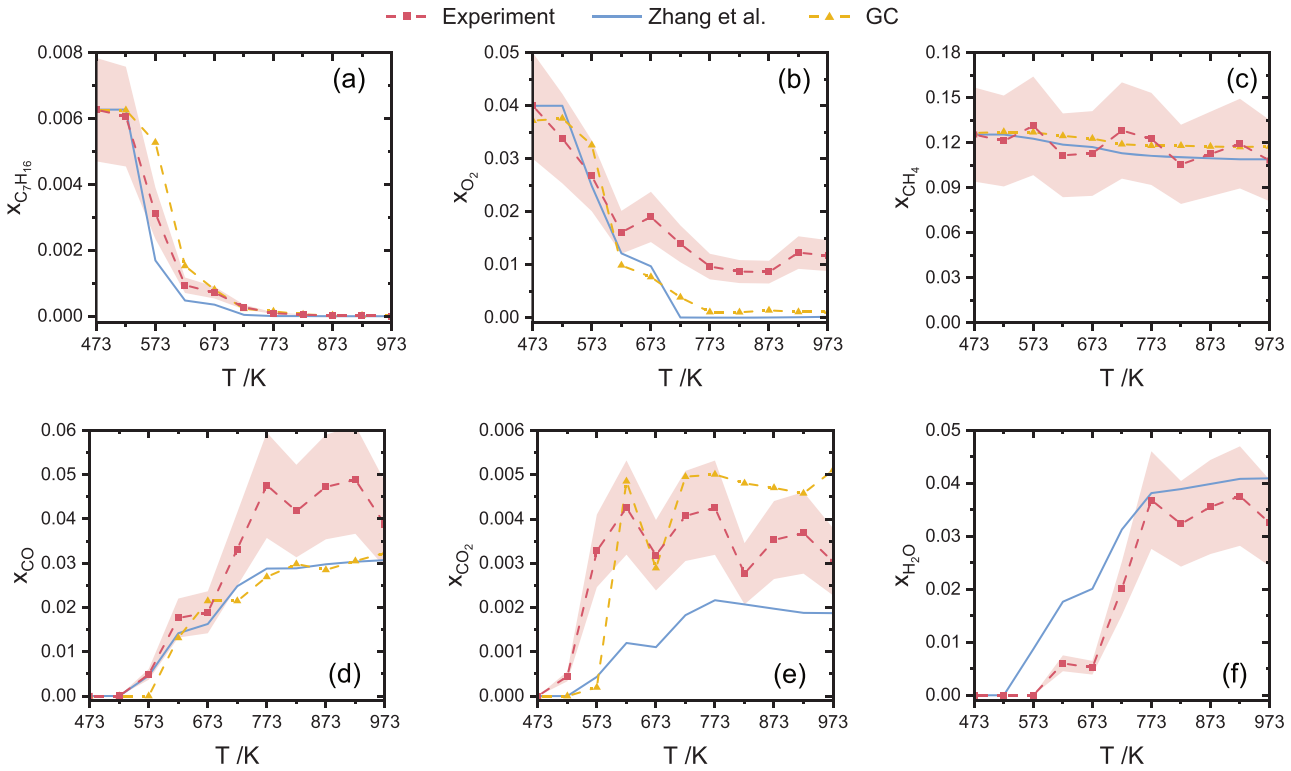

FIG. 6. Mole fraction profiles of C_7H_{16} (a), O_2 (b), CH_4 (c), CO (d), CO_2 (e), and H_2O (f) from the element balance calculation of major species from the reactor experiment (red dashed line with symbols: indicated error of 25%) and comparison to the mechanism by Zhang *et al.* (2016) (blue solid line) and GC reference measurements [cf. Kaczmarek *et al.* (2019a)] (yellow dashed line with symbols).

temperatures in the CO profile at which the C_2H_4 contribution increases, as the measurement matches the model and GC reference perfectly at lower temperatures [cf. Fig. 6(d)]. The oxygen signal shows some contribution of methanol (CH_3OH) for higher temperatures, which cannot be corrected for because of the lack of a suitable photoionization cross section of CH_3OH at 15.0 eV (Cool *et al.*, 2005; Zhou *et al.*, 2009; Person and Nicole, 1971). Mole fractions for lower temperatures match perfectly the chemical kinetics simulation result and GC measurement. An offset from the model and GC reference is visible in Fig. 6 only for temperatures with a significant methanol contribution to the oxygen signal (cf. Fig. 7). The introduced error has no influence on the element balance because it was assumed that no unbound oxygen is present at the final temperature of 973 K due to the full consumption of oxygen at the extremely fuel rich condition of $\varphi = 8$. The water profile (f) in Fig. 6 shows good agreement with the model reference in both progression and concentration. GC measurements of water are typically difficult, and no mole fraction values for water were reported in the GC work (Kaczmarek *et al.*, 2019a). The i^{2}PEPCIO technique can measure water satisfactorily, as can be seen from the good agreement between experimental and simulated profiles. The agreement emphasizes that despite the long transfer stage between reactor outlet and expansion chamber no water has condensed and that the gas composition at the reactor outlet is retained up to the sampling point. Moreover, the good agreement with the reference measurements for all major species shows that the transfer line effect on evaluated molar fraction is negligible.

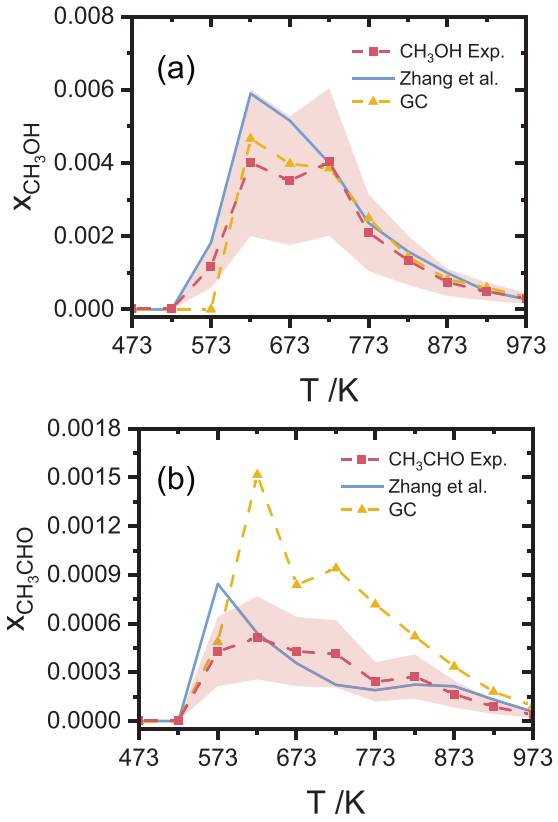

FIG. 7. Quantification of low-temperature intermediate species methanol [CH_3OH, (a)] and acetaldehyde [CH_3CHO, (b)] (red dashed line with symbols: indicated error 50%), comparison to mechanism by Zhang *et al.* (2016) (blue solid line), and GC reference measurements [cf. Kaczmarek *et al.* (2019a)] (yellow dashed line with symbols).

E. Quantification of intermediate species at low temperature

Intermediate species are quantified according to the principles outlined by Oßwald *et al.* (2014) for imaging PEPICO flame data using a modification of the approach for flame experiments (Schenk *et al.*, 2013; Kasper *et al.*, 2009) for the evaluation of PI-MBMS data. The modification was required because of the continuous extraction of ions from the beam interaction region in contrast to pulsed or gated extraction for regular ToF-MS (Oßwald *et al.*, 2014) and the particularities of imaging coincidence detection. The ion signal dependency S_i on experimental and machine parameters for data reduction of the iPEPICO instrument is elaborated by Oßwald *et al.* (2014) and has to be slightly modified for the reactor experiment to account for the difference to flame experiments:

$$S_i = x_i(T) \cdot D_i(M_i) \cdot t \cdot FKT\left(T_{inj}, \bar{M}\right) \cdot c(E) \cdot \sigma_i(E) \cdot \alpha_i(E - IP), \quad (1)$$

where x_i denotes the mole fraction of a species i at a set reactor temperature T; D is a mass discrimination factor dependent on mass M (empirically close to unity for the CRF-PEPICO); t is the signal accumulation time for a spectrum; FKT is the composition and temperature dependent sampling function, T_{inj} is the temperature at which the sample is injected into the spectrometer, i.e., not the process temperature as $T_{\mathrm{inj}} \neq T$; c is a machine and experiment specific factor taking into account several machine and experiment dependent disturbances; σ_i is the partial ionization cross section at the given mass-to-charge ratio; and α corrects for loss of ion coincidence signal due to the limited electron detector kinetic energy acceptance and is required for photon energies 1.2 eV larger than the IE of a compound (Oßwald *et al.*, 2014). This aspect requires quantification of a species within this 1.2 eV boundary to obtain the most accurate result. Modifications to (1) required for the reactor experiment are the dependency of the mole fraction x_i on the set reactor temperature T instead of the height above burner for flame experiments and the changed indexing of the temperature T_{inj} at which the molecular beam is formed and the sample is injected into the spectrometer.

Representative quantification results of two important intermediate species for the condition given in Table I are presented in Fig. 7. Spectra are taken at several photon energies ranging from 8.8 eV to 15.8 eV for all temperatures, considering the requirement of $\Delta E < 1.2$ eV between the IE of any species of interest and the set photon energy for the quantified signal. Intermediate species are evaluated within these bounds; hence, the α factor becomes unity.

Evaluation is performed for the methanol signal at a mass-to-charge ratio of m/z 32 [Fig. 7(a)] and the acetaldehyde signal at m/z 44 [Fig. 7(b)]. The methanol signal is taken from a temperature scan performed at a photon energy of 11.2 eV, while the acetaldehyde signal was acquired at 10.6 eV. The averaging time for acquisition was 180 s for both species. Photoionization cross sections are taken from the work of Cool *et al.*, 2005; Cool *et al.*, 2003. For argon, the lowest

energy absolute cross section available at 15.83 eV is used (Marr and West, 1976). The obtained mole fraction profiles are compared to the mechanism by Zhang *et al.* (2016) and the GC reference data (Kaczmarek *et al.*, 2019a). The profiles show excellent agreement with both the measured and modeled data, as the error margin for the CH_3CHO GC data is reported as factor 2–4 due to the lack of calibration (Kaczmarek *et al.*, 2019a). Experimental values are well within the expected 50% error margin for the PI-MBMS, as indicated in Fig. 7 (Oßwald *et al.*, 2014). This demonstrates the ability to generate quantitative speciation data for combustion experiments with the new reactor setup.

IV. CONCLUSION

This paper describes the first utilization of a pressurized flow reactor for combustion experiments coupled to double imaging PEPICO using tunable synchrotron VUV photoionization. A detailed overview of all systems comprising the experiment, including the supply and support systems, is given. The experimental and evaluation procedures for the new experiment are described.

Application of the setup to combustion research is demonstrated comprehensively, and data are presented. The i^2PEPICO method affords excellent identification of isomers, as shown by deconvoluting the m/z 72 to 2-butanone and n-butanal contributions and ruling out the presence of numerous other isomers. With the technique, isomer branching ratios can be obtained and fed back into reaction mechanism development. Identification using both the ionization potential based photoionization spectra and threshold photoelectron spectra fingerprinting is demonstrated for the two compounds. The experiment is limited to the detection of comparably stable species that survive the expansion stages, while transient radicals are lost in the sampling process. It is shown that this limitation to non-reactive species is not a decisively negative factor in the current experiment because highly reactive radicals are typically produced close to the inlet of the reactor and have been consumed in reactions close to the outlet of the reactor. In fact, the lack of radicals in the sample can be advantageous for complex samples such as the one generated by the higher hydrocarbon n-heptane presented in this work.

Quantitative major and intermediate species profiles obtained from the pressurized reactor experiment coupled to i^2PEPICO are presented. They confirm the capability of the experiment to sensitively, selectively, and accurately detect key combustion species under technically relevant pressure conditions. Availability of reliable experimental quantitative data for fuel oxidation at elevated pressure is limited. Such data is required for developing reaction mechanisms and an understanding of the reactive processes involved. Combined with the capability to identify compounds present in the sample using threshold photoelectron spectra and ion yield curves, the new experiment presents a valuable addition to the analytical techniques employed in combustion research.

ACKNOWLEDGMENTS

The authors would like to thank the Deutsche Forschungsgemeinschaft for financial support under Contracts Nos. KA3871/3-2, KA3871/1-3 and KO4786/2-2. P.H. would like to thank the Swiss Federal Office of Energy for financial support under contract No. SI/501269-01. Experiments were performed at the VUV beamline of the SLS at the Paul Scherrer Institute. The authors would like to thank P. Oßwald for his support in the experiments. The authors would also like to acknowledge Bálint Sztáray and David Osborn for the design of the CRF-PEPICO endstation.

REFERENCES

Ansys Inc., *Ansys Chemkin 19.2* (ANSYS, 2008).

Baer, T. and Tuckett, R. P., "Advances in threshold photoelectron spectroscopy (TPES) and threshold photoelectron photoion coincidence (TPEPICO)," Phys. Chem. Chem. Phys. **19**, 9698–9723 (2017).

Behan, J. M., Dean, F. M., and Johnstone, R. A. W., "Photoelectron spectra of cyclic aromatic ethers. The question of the Mills–Nixon effect," Tetrahedron **32**, 167–171 (1976).

Bierkandt, T., Hemberger, P., Oßwald, P., Köhler, M., and Kasper, T., "Insights in *m*-xylene decomposition under fuel-rich conditions by imaging photoelectron photoion coincidence spectroscopy," Proc. Combust. Inst. **36**, 1223–1232 (2017).

Bodi, A., Hemberger, P., Gerber, T., and Sztáray, B., "A new double imaging velocity focusing coincidence experiment: i^2PEPICO," Rev. Sci. Instrum. **83**, 083105 (2012).

Bodi, A., Hemberger, P., Osborn, D. L., and Sztáray, B., "Mass-resolved isomer-selective chemical analysis with imaging photoelectron photoion coincidence spectroscopy," J. Phys. Chem. Lett. **4**, 2948–2952 (2013).

Bodi, A., Johnson, M., Gerber, T., Gengeliczki, Z., Sztáray, B., and Baer, T., "Imaging photoelectron photoion coincidence spectroscopy with velocity focusing electron optics," Rev. Sci. Instrum. **80**, 034101 (2009).

Cool, T. A., McIlroy, A., Qi, F., Westmoreland, P. R., Poisson, L., Peterka, D. S., and Ahmed, M., "Photoionization mass spectrometer for studies of flame chemistry with a synchrotron light source," Rev. Sci. Instrum. **76**, 094102 (2005).

Cool, T. A., Nakajima, K., Mostefaoui, T. A., Qi, F., Mcllroy, A., Westmoreland, P. R., Law, M. E., Poisson, L., Peterka, D. S., and Ahmed, M., "Selective detection of isomers with photoionization mass spectrometry for studies of hydrocarbon flame chemistry," J. Chem. Phys. **119**, 8356–8365 (2003).

Cool, T. A., Wang, J., Nakajima, K., Taatjes, C. A., and Mcllroy, A., "Photoionization cross sections for reaction intermediates in hydrocarbon combustion," Int. J. Mass Spectrom. **247**, 18–27 (2005).

Curran, H. J., Gaffuri, P., Pitz, W. J., and Westbrook, C. K., "A comprehensive modeling study of *n*-heptane oxidation," Combust. Flame **114**, 149–177 (1998).

Doucet, J., Sauvageau, P., and Sandorfy, C., "The vacuum ultraviolet spectrum of tetrahydrofuran," Chem. Phys. Lett. **17**, 316–319 (1972).

Eskola, A. J., Antonov, I. O., Sheps, L., Savee, J. D., Osborn, D. L., and Taatjes, C. A., "Time-resolved measurements of product formation in the low-temperature (550–675 K) oxidation of neopentane: A probe to investigate chain-branching mechanism," Phys. Chem. Chem. Phys. **19**, 13731–13745 (2017).

Felsmann, D., Lucassen, A., Krüger, J., Hemken, C., Tran, L. S., Pieper, J., Garcia, G. A., Brockhinke, A., Nahon, L., and Kohse-Höinghaus, K., "Progress in fixed-photon-energy time-efficient double imaging photoelectron/photoion coincidence measurements in quantitative flame analysis," Z. Phys. Chem. **230**, 1067–1097 (2016).

Felsmann, D., Moshammer, K., Krüger, J., Lackner, A., Brockhinke, A., Kasper, T., Bierkandt, T., Akyildiz, E., Hansen, N., Lucassen, A., Oßwald, P., Köhler, M., Garcia, G. A., Nahon, L., Hemberger, P., Bodi, A., Gerber, T., and Kohse-Höinghaus, K., "Electron ionization, photoionization and photoelectron/photoion coincidence spectroscopy in mass-spectrometric investigations of a low-pressure ethylene/oxygen flame," Proc. Combust. Inst. **35**, 779–786 (2015).

Garcia, G. A., Cunha De Miranda, B. K., Tia, M., Daly, S., and Nahon, L., "DELICIOUS III A multipurpose double imaging particle coincidence spectrometer

for gas phase vacuum ultraviolet photodynamics studies," Rev. Sci. Instrum. **84**, 053112 (2013).

Hansen, N., Cool, T. A., Westmoreland, P. R., and Kohse-Höinghaus, K., "Recent contributions of flame-sampling molecular-beam mass spectrometry to a fundamental understanding of combustion chemistry," Prog. Energy Combust. Sci. **35**, 168–191 (2009).

Hemberger, P., Trevitt, A. J., Ross, E., and Da Silva, G., "Direct observation of *para*-xylylene as the decomposition product of the *meta*-xylyl radical using VUV synchrotron radiation," J. Phys. Chem. Lett. **4**, 2546–2550 (2013).

Herbinet, O., Battin-Leclerc, F., Bax, S., Gall, H. L., Glaude, P. A., Fournet, R., Zhou, Z., Deng, L., Guo, H., Xie, M., and Qi, F., "Detailed product analysis during the low temperature oxidation of n-butane," Phys. Chem. Chem. Phys. **13**, 296–308 (2011).

Hernandez, G. J., "Vacuum-ultraviolet absorption spectra of the cyclic ethers: Trimethylene oxide, tetrahydrofuran, and tetrahydropyran," J. Chem. Phys. **38**, 2233–2242 (1963).

Hernandez, R., Masclet, P., and Mouvier, G., "Spectroscopie de photoelectron d'aldehydes et de cetones aliphatiques," J. Electron Spectrosc. Relat. Phenom. **10**, 333–347 (1977).

Johnson, M., Bodi, A., Schulz, L., and Gerber, T., "Vacuum ultraviolet beamline at the Swiss Light Source for chemical dynamics studies," Nucl. Instrum. Methods Phys. Res., Sect. A **610**, 597–603 (2009).

Kaczmarek, D., Atakan, B., and Kasper, T., "Investigation of the partial oxidation of methane/n-heptane-mixtures and the interaction of methane and n-heptane under ultra-rich conditions," Combust. Flame **205**, 345–357 (2019).

Kaczmarek, D., Atakan, B., and Kasper, T., "Plug-flow reactor study of the partial oxidation of methane and natural gas at ultra-rich conditions," Combust. Sci. Technol. **191**, 1571–1584 (2019).

Kasper, T., Oßwald, P., Struckmeier, U., Kohse-Höinghaus, K., Taatjes, C. A., Wang, J., Cool, T. A., Law, M. E., Morel, A., and Westmoreland, P. R., "Combustion chemistry of the propanol isomers—Investigated by electron ionization and VUV-photoionization molecular-beam mass spectrometry," Combust. Flame **156**, 1181–1201 (2009).

Krüger, D., Oßwald, P., Köhler, M., Hemberger, P., Bierkandt, T., Karakaya, Y., and Kasper, T., "Hydrogen abstraction ratios: A systematic iPEPICO spectroscopic investigation in laminar flames," Combust. Flame **191**, 343–352 (2018).

Krüger, D., Oßwald, P., Köhler, M., Hemberger, P., Bierkandt, T., and Kasper, T., "The fate of the OH radical in molecular beam sampling experiments," Proc. Combust. Inst. **37**, 1563–1570 (2019).

Krüger, J., Garcia, G. A., Felsmann, D., Moshammer, K., Lackner, A., Brockhinke, A., Nahon, L., and Kohse-Höinghaus, K., "Photoelectron-photoion coincidence spectroscopy for multiplexed detection of intermediate species in a flame," Phys. Chem. Chem. Phys. **16**, 22791–22804 (2014).

Lindstrom, P. J., Mallard, W. G., and National Institute of Standards and Technology (U.S.), *NIST Chemistry Webbook* (NIST, 1997).

Lucassen, A., Oßwald, P., Struckmeier, U., Kohse-Höinghaus, K., Kasper, T., Hansen, N., Cool, T. A., and Westmoreland, P. R., "Species identification in a laminar premixed low-pressure flame of morpholine as a model substance for oxygenated nitrogen-containing fuels," Proc. Combust. Inst. **32**, 1269–1276 (2009).

Luck, C. J., Burgess, A. R., Desty, D. H., Whitehead, D. M., and Pratley, G., "A study of the combustion of *n*-heptane in an engine using a novel high-speed sampling technique," Symp. (Int.) Combust., [Proc.] **14**, 501–512 (1973).

Mackie, R. A., Scully, S. W. J., Sands, A. M., Browning, R., Dunn, K. F., and Latimer, C. J., "A photoionization mass spectrometric study of acetylene and ethylene in the VUV spectral region," Int. J. Mass Spectrom. **223-224**, 67–79 (2003).

Marr, G. V. and West, J. B., "Absolute photoionization cross-section tables for helium, neon, argon, and krypton in the VUV spectral regions," At. Data Nucl. Data Tables **18**, 497–508 (1976).

Matras, D. and Villermaux, J., "Un reakteur continu parfaitement agité par jets gazeux pour l'étude cinétique de réactions chimiques rapides," Chem. Eng. Sci. **28**, 129–137 (1973).

Moshammer, K., Jasper, A. W., Popolan-Vaida, D. M., Lucassen, A., Diévart, P., Selim, H., Eskola, A. J., Taatjes, C. A., Leone, S. R., Sarathy, S. M., Ju, Y., Dagaut, P., Kohse-Höinghaus, K., and Hansen, N., "Detection and identification of the keto-hydroperoxide ($HOOCH_2OCHO$) and other intermediates during low-temperature oxidation of dimethyl ether," J. Phys. Chem. A **119**, 7361–7374 (2015).

Moshammer, K., Jasper, A. W., Popolan-Vaida, D. M., Wang, Z., Bhavani Shankar, V. S., Ruwe, L., Taatjes, C. A., Dagaut, P., and Hansen, N., "Quantification of the keto-hydroperoxide ($HOOCH_2OCHO$) and other elusive intermediates during low-temperature oxidation of dimethyl ether," J. Phys. Chem. A **120**, 7890–7901 (2016).

Oßwald, P., Hemberger, P., Bierkandt, T., Akyildiz, E., Köhler, M., Bodi, A., Gerber, T., and Kasper, T., "*In situ* flame chemistry tracing by imaging photoelectron photoion coincidence spectroscopy," Rev. Sci. Instrum. **85**, 025101 (2014).

Oßwald, P. and Köhler, M., "An atmospheric pressure high-temperature laminar flow reactor for investigation of combustion and related gas phase reaction systems," Rev. Sci. Instrum. **86**, 105109 (2015).

Osswald, P., Struckmeier, U., Kasper, T., Kohse-Höinghaus, K., Wang, J., Cool, T. A., Hansen, N., and Westmoreland, P. R., "Isomer-specific fuel destruction pathways in rich flames of methyl acetate and ethyl formate and consequences for the combustion chemistry of esters," J. Phys. Chem. A **111**, 4093–4101 (2007).

Pelucchi, M., Bissoli, M., Cavallotti, C., Cuoci, A., Faravelli, T., Frassoldati, A., Ranzi, E., and Stagni, A., "Improved kinetic model of the low-temperature oxidation of *n*-heptane," Energy Fuels **28**, 7178–7193 (2014).

Person, J. C. and Nicole, P. P., "Isotope effects in the photoionization yields and in the absorption cross sections for methanol, ethanol, methyl bromide, and ethyl bromide," J. Chem. Phys. **55**, 3390–3397 (1971).

Pieper, J., Schmitt, S., Hemken, C., Davies, E., Wullenkord, J., Brockhinke, A., Krüger, J., Garcia, G. A., Nahon, L., Lucassen, A., Eisfeld, W., and Kohse-Höinghaus, K., "Isomer identification in flames with double-imaging photoelectron/photoion coincidence spectroscopy (i^2PEPICO) using measured and calculated reference photoelectron spectra," Z. Phys. Chem. **232**, 153–187 (2018).

Qi, F., "Combustion chemistry probed by synchrotron VUV photoionization mass spectrometry," Proc. Combust. Inst. **34**, 33–63 (2013).

Ranzi, E., Gaffuri, P., Faravelli, T., and Dagaut, P., "A wide-range modeling study of n-heptane oxidation," Combust. Flame **103**, 91–106 (1995).

Rasmussen, C. L., Hansen, J., Paul, M., and Glarborg, P., "Experimental measurements and kinetic modeling of $CO/H_2/O_2/NO_x$ conversion at high pressure," Int. J. Chem. Kinet. **40**, 454–480 (2008).

Schenk, M., Leon, L., Moshammer, K., Oßwald, P., Zeuch, T., Seidel, L., Mauss, F., and Kohse-Höinghaus, K., "Detailed mass spectrometric and modeling study of isomeric butene flames," Combust. Flame **160**, 487–503 (2013).

Sztáray, B., Voronova, K., Torma, K. G., Covert, K. J., Bodi, A., Hemberger, P., Gerber, T., and Osborn, D. L., "CRF-PEPICO: Double velocity map imaging photoelectron photoion coincidence spectroscopy for reaction kinetics studies," J. Chem. Phys. **147**, 013944 (2017).

Traeger, J. C., "Heat of formation for the SH radical by photoionization mass spectrometry," Org. Mass Spectrom. **19**, 514–516 (1984).

Traeger, J. C. and McAdoo, D. J., "Decomposition thresholds and associated translational energy releases for eight $C_4H_8O^{+\cdot}$ isomers," Int. J. Mass Spectrom. Ion Processes **68**, 35–48 (1986).

Watanabe, K., Nakayama, T., and Mottl, J., "Ionization potentials of some molecules," J. Quant. Spectrosc. Radiat. Transfer **2**, 369–382 (1962).

Wiley, W. C. and McLaren, I. H., "Time-of-flight mass spectrometer with improved resolution," Rev. Sci. Instrum. **26**, 1150–1157 (1955).

Zhang, K., Banyon, C., Bugler, J., Curran, H. J., Rodriguez, A., Herbinet, O., Battin-Leclerc, F., B'Chir, C., and Heufer, K. A., "An updated experimental and kinetic modeling study of *n*-heptane oxidation," Combust. Flame **172**, 116–135 (2016).

Zhou, Z., Xie, M., Wang, Z., and Qi, F., "Determination of absolute photoionization cross-sections of aromatics and aromatic derivatives," Rapid Commun. Mass Spectrom. **23**, 3994–4002 (2009).

Threshold photoionization shows no sign of nitryl hydride in methane oxidation with nitric oxide

Hoener, M., Bodi, A., Hemberger, P., Endres, T., Kasper, T.
Physical Chemistry Chemical Physics, 2021, 23(2), pp. 1265–1272
DOI: 10.1039/d0cp04924g

My contribution to this work was the development of the reactor interface to the CRF-PEPICO endstation, manufacturing supervision of the design, the commissioning of the experiment, design of the experiment, measurement and analysis of the reactor data analysis of the literature and data towards an understanding of the energetics and dissociation kinetics of HONO and the kinetics of production and residence of HNO_2, performance of electronic structure computations and Franck-Condon simulations, writing of the manuscript.

PCCP

ROYAL SOCIETY OF CHEMISTRY

PAPER

View Article Online
View Journal | View Issue

Cite this: *Phys. Chem. Chem. Phys.*, 2021, **23**, 1265

Threshold photoionization shows no sign of nitryl hydride in methane oxidation with nitric oxide†

Martin Hoener, *[a] Andras Bodi, [b] Patrick Hemberger, [b] Torsten Endres[c] and Tina Kasper[a]

Received 17th September 2020,
Accepted 6th December 2020

DOI: 10.1039/d0cp04924g

rsc.li/pccp

Methane was doped with nitric oxide and oxidized in a high-pressure flow reactor. The nitrogen chemistry during partial oxidation was studied using photoelectron photoion coincidence spectroscopy with vacuum ultraviolet synchrotron radiation. The adiabatic ionization energy of nitrous acid, HONO, has been determined as 10.95 ± 0.03 eV. The HONO breakdown diagram was plotted based solely on the measured parent signal and the computed Franck–Condon envelope of *trans*-HONO, confirming the *trans*-HONO dissociative photoionization threshold to NO^+ + •OH at 11.34 eV. The spectra show strong indication for the presence of *cis*-HONO. We expected the *m*/*z* 47 photoion mass selected threshold photoelectron signal to rebound near 12 eV, *i.e.*, at the ionization energy of nitryl hydride, the third HNO_2 isomer. Recent computational studies suggest nitryl hydride is formed at a rate similar to *trans*-HONO, is more thermally stable than nitrous acid, its cation is bound, and its photoelectron spectrum is predicted to exhibit a strong origin band near 12 eV. The absence of its mass selected threshold photoelectron signal shows that nitryl hydride is either not formed in measurable amounts or is consumed faster than nitrous acid, for instance by isomerization to *trans*-HONO.

I. Introduction

Although nitrous acid is well known in the solvent phase and its salts are ubiquitous, it is an elusive species in the gas phase. However, it plays an important role in the kinetics of energetic materials[1,2] as well as in combustion[3,4] and atmospheric chemistry,[5] where it acts as an •OH radical source by HO–NO bond dissociation.[6,7] All three HNO_2 isomers depicted in Fig. 1, *trans*-HONO, *cis*-HONO and O_2N–H, *i.e.*, the nitrous acid stereoisomers and nitryl hydride, are proposed to be produced in combustion.[8] Their photoisomerization was studied by McDonald and Shirk by matrix isolation spectroscopy.[9] The barrier to *cis*/*trans* isomerization was computed to be on the order of 40 kJ mol^{-1}, implying that they readily interconvert at elevated temperatures.[7,10] The Active Thermochemical Tables (ATcT) predict the third isomer, nitryl hydride, O_2N–H, to be 36 kJ mol^{-1} less stable,[11] but it is proposed to be trapped in a 200 kJ mol^{-1} deep potential energy well,[7] which establishes it as a distinct species even in a combustion environment. It is therefore not surprising that the formation and the subsequent destruction mechanisms of HNO_2 are computed to be isomer-specific.[3,7,8]

NO and NO_2 are major contributors to HNO_2 formation in combustion.[8,12] The resonance stabilized NO_2 is the most active

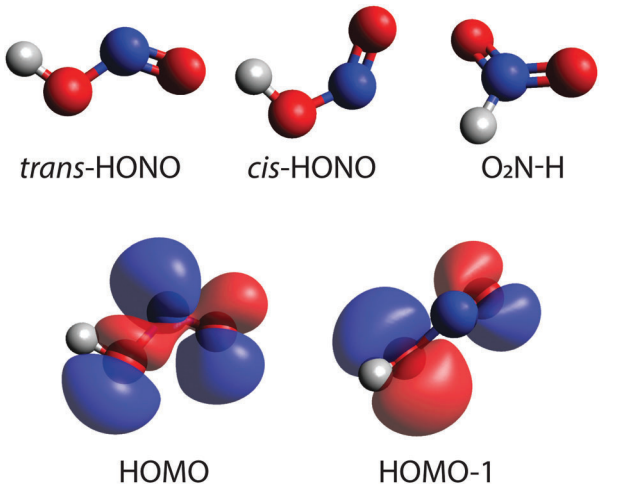

Fig. 1 Structures of the three HNO_2 isomers: *trans*-HONO, *cis*-HONO, and O_2N–H (top). HOMO, HOMO–1 of *trans*-HONO computed at the B3LYP/6-311++G(d,p) level of theory (bottom).

[a] *Mass Spectrometry in Reactive Flows – Institute for Combustion and Gas Dynamics (IVG), University Duisburg-Essen, Duisburg 47057, Germany. E-mail: martin.hoener@uni-due.de*
[b] *Laboratory for Synchrotron Radiation and Femtochemistry, Paul Scherrer Institute, Villigen, 5232, Switzerland*
[c] *Reactive Fluids – Institute for Combustion and Gas Dynamics (IVG), University Duisburg-Essen, Duisburg 47057, Germany*

† Electronic supplementary information (ESI) available: Details of the experimental setup, tabulated volume flow rates and mole fractions, specifics of the reference and reactive measurements, and tabulated computational energy results. See DOI: 10.1039/d0cp04924g

precursor, because each atom has a radical character and can perform H abstraction.[3,7] Depending on the active site and the direction of addition, O_2N–H, *cis*-, or *trans*-HONO is formed,[3,7] whereby calculated rate constants are about an order of magnitude higher for *cis*-HONO production than for O_2N–H and *trans*-HONO formation at 720 K.[3,7] *trans*- (or *anti*-)HONO is more stable than the *cis* or *syn* isomer (*cis*-HONO), but only by 1.6 kJ mol^{-1}.[11] O_2N–H was previously believed to mostly undergo isomerization yielding *trans*-HONO.[10] In contrast, Chen *et al.* suggested in a recent theoretical study that unimolecular decomposition yielding •OH and NO is its dominant reaction pathway.[7] Once formed, HONO may undergo *cis*/*trans* isomerization,[7,10,13] decomposition to NO, NO_2 and water in a bimolecular reaction,[14] or the classical disproportionation reaction to HNO_3, NO and water. The unimolecular decomposition into •OH and NO renders nitrous acid an important source of •OH radicals.[6,7] This underlines its role in the formation of secondary oxidation products in atmospheric chemistry, *e.g.*, ozone production in polluted regions,[5] and in low-temperature and ignition chemistry, *e.g.*, when exhaust gas is recirculated or when NO_x releasing fuel additives, such as cetane enhancers, are used.[4,15–17] Understanding HNO_2 formation and destruction kinetics is crucial to develop rational strategies to mitigate emissions and control ignition. Although *trans*- and *cis*-HONO as well as O_2N–H are postulated to be important combustion intermediates,[8] nitrous acid has mostly evaded spectroscopic detection in reactive mixtures. Marrodán *et al.* reported the infrared spectrum of HONO in a hydrocarbon system doped with NO by cavity ring-down spectroscopy[4] based on an absolute HONO absorption cross section in the near infrared.[18] Weng *et al.* detected the HONO signal at *m*/*z* 47 in nitromethane oxidation by photoionization mass spectrometry.[19] To determine the ionization energy (IE) of HONO and to confirm the proton affinity of NO_2, Taatjes *et al.* recorded the *m*/*z* 47 photoionization (PI) spectrum in a premixed hydrogen flame doped with NO_2 by synchrotron photoionization molecular beam mass spectrometry, which they assigned to *trans*-HONO.[20] The PI spectrum exhibited a steep and short rise over *ca.* 0.5 eV, followed by a plateau. This shape was at odds with the Franck–Condon simulation, which predicted a much broader first band in the photoelectron spectrum and a differently shaped PI spectrum. The cation potential energy surface was suggested to be anharmonic thanks to the facile formation of the stable $HO\cdots NO^+$ ion–dipole complex, which was proposed to reduce Franck–Condon factors at higher energies compared with the harmonic model.[20] The photoelectron spectrum has since been measured by Wang *et al.*, and it seems to support the validity of the harmonic Franck–Condon simulation and is at odds with the PI spectrum.[21] All in all, experimental data appear to be contradictory or at best incomplete. Despite the assumed isomer-dependence of HNO_2 kinetics, isomer specific and quantifiable spectroscopic data are lacking to understand HNO_2 chemistry and validate reaction mechanisms and rate constants. As a result, current models frequently lump the reactions of HNO_2 isomers in the reaction mechanism.[8]

We present a direct analytical probe by photoionization (PI) and photoion mass-selected threshold photoelectron spectroscopy (ms-TPES) using double imaging photoelectron photoion coincidence spectroscopy (i^2PEPICO). We compare the ms-TPES with the calculated Franck–Condon envelope and discuss the cationic HNO_2 potential energy surface. The ion signal is mostly determined by photoionization of *trans*-HONO, with some *cis*-HONO contribution, and, most notably, the absence of nitryl hydride, O_2N–H.

II. Methods

A. Photoion–photoelectron coincidence spectroscopy

Photoionization in general[22,23] and (double) imaging photoelectron photoion coincidence, $i^{(2)}$PEPICO, in particular[24–26] have been shown to be universal, sensitive, isomer-selective and multiplexed analytical techniques to detect reactive intermediates in complex environments.[27–29] Central reactive intermediates, such as the Criegee intermediate, were postulated decades ago, but could only recently be detected conclusively thanks to photoionization experiments.[30] Here, we prepare HNO_2 in a plug-flow reactor and detect it by PEPICO spectroscopy.

We used a pressurized plug-flow reactor[31] coupled to the double imaging CRF-PEPICO endstation[28] at the VUV beamline[32] of the Swiss Light Source and ionized the sample in the gas phase using monochromatic vacuum ultraviolet (VUV) radiation. The supporting information provides further details of the experiment. Electrons and ions are velocity map imaged and detected in delayed coincidence[33] in space focusing conditions for the ions. Electrons are imaged up to *ca.* 2 eV kinetic energy onto the detector. Accepting them all as start signal allows us to plot the photoionization spectrum of arbitrary mass channels. By discriminating for close to zero kinetic energy electrons,[34] the threshold ionization mass spectrum is recorded. The data can be used to plot the photoion mass-selected threshold photoelectron spectrum (ms-TPES) of an *m*/*z* ion channel, or the breakdown diagram by evaluating the fractional parent and fragment ion abundances as a function of photon energy.[25] Bands in the ms-TPES correspond to cation electronic states and vibrational progressions are often observed. They provide an isomer-specific fingerprint and can almost always be modeled reliably by calculating Franck–Condon factors based on density functional theory (DFT) harmonic frequency calculations. The breakdown diagram, on the other hand, characterizes the fragmentation of the parent ion as a function of its internal energy, and can be used to derive energetics and thermochemical data. In a fast, first fragmentation step, the threshold can easily be established as the disappearance energy of the parent ion from the breakdown diagram, *i.e.*, the energy at which even zero energy neutrals gain enough energy to fragment upon photoionization.[35]

B. Computational

Electronic structure computations were carried out using Gaussian 16.[36] Geometry optimization and frequency computations to obtain adiabatic ionization energies were first performed using DFT at the B3LYP/6-311++G(p,d) level of theory[37,38] for the neutral singlet and cation doublet *trans*-, *cis*-HONO and O_2N–H structures. Confirmation of the results was sought by

calculating the total energy of the three combustion relevant neutral and cationic isomers (*i.e.*, *trans*-HONO, *cis*-HONO and HNO_2) using the CBS-QB3,[39] G4,[40] and W1BD[41] composite methods. Frequency analysis confirmed the optimized structures to be minima.

To interpret the spectra and understand the isomerization and dissociation processes on the HNO_2^+ cation surface, we recalculated the previously reported[6] potential energy surface (PES) at the G4 level of theory. Gaussian-4 theory was used since it generally suffers from errors smaller than 3.5 kJ mol^{-1} (36 meV) across a wide range of molecules.[40] Furthermore, equation-of-motion ionization potential coupled cluster singles and doubled (EOM-IP-CCSD) calculations were carried out to predict the location of excited-state bands in the photoelectron spectrum using Q-Chem 4.3.[42]

Franck–Condon factors were calculated for the vibrational transitions between the singlet neutral and doublet cation state of the *trans*- and *cis*-HONO as well as O_2N–H isomers in Gaussian 16 based on the B3LYP/6-311++G(d,p) Hessian. Energies of all optimized structures can be found in Table S3 (ESI†).

C. Reaction conditions

The reactant stream consisted of 1% nitric oxide, 4.6% methane, and 4.4% oxygen (corresponding to an equivalence ratio of 2.1), diluted with 90% of argon at a total flow of 280 sccm (Table S1, ESI†) and a total pressure of 6 bar in the reactor. A sample was expanded and entered the ionization chamber through two stages of differential pumping.[31] We used methane to promote the isolation of nitrogen chemistry and specifically the HNO_2 intermediates. The reactor temperature was ramped up from 473 K to 973 K and spectra were recorded at 50 K intervals (bottom panel of Fig. 2). The top panel of Fig. 2 show a mass spectrum of the reactor at 723 K and a photon energy of 12.2 eV. The peak at *m*/*z* 61 shows the presence of nitromethane (CH_3NO_2), an expected by-product of the reaction.[43] Methane at *m*/*z* 16 only shows a minor peak due to scattered light at this photon energy (the adiabatic ionization energy of methane is 12.61 eV)[44] and is omitted from the spectrum to show the relevant mass range.

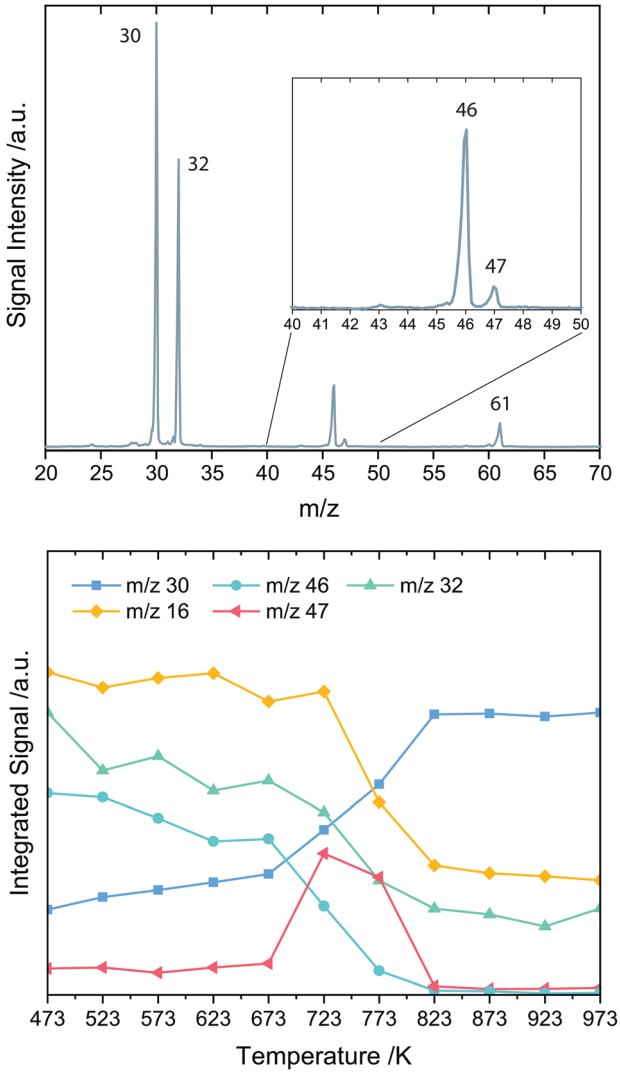

Fig. 2 Top panel: Mass spectrum of the sample at 723 K and 12.2 eV photon energy. Bottom panel: Signal intensity as a function of reactor temperature. The *m*/*z* 47 and 30 channels are scaled for better visibility of the temperature dependence. Profiles measured at a photon energy of 15 eV for *m*/*z* 16 and *m*/*z* 32, 10.6 eV for *m*/*z* 30 and *m*/*z* 46 and 12 eV for *m*/*z* 47.

III. Results and discussion

Nitrogen dioxide (*m*/*z* 46) is formed *in situ* from NO and O_2. Substantial quantities of NO_2 were present at low temperatures already, and the rise of the HNO_2 signal at *m*/*z* 47 mirrors the decay of NO_2. The HNO_2 signal then decreases after a peak at 723–773 K, while the NO abundance at *m*/*z* 30 increases. Reactive $^\bullet$OH radicals at *m*/*z* 17 are not expected to survive the expansion stages used for sampling[31] from the reactor and have not been seen. These temperature dependent profiles confirm that NO_2 is the precursor in HNO_2 production by several reactions such as H abstraction from the fuel[3] and secondary reactions with hydrogen and hydrogen containing radicals.[10] The photon energy was scanned and the ms-TPES recorded between 10.4 and 12.2 eV with a scan resolution of 30 meV at a reactor temperature of 723 K. At this temperature, *cis*-HONO is predicted to be formed at a rate *ca.* 10 times higher than the *trans* and O_2N–H isomers.[3] However, *cis*/*trans* isomerization of HONO is prompt due to well merging.[7] Because of their comparable stability, both HONO isomers should exist in the sample stream discharged from the reactor in thermal equilibrium and their configuration will be maintained upon vertical photoionization. Thus, both should contribute distinctly to the photoionization and photoelectron spectra. In a recent theoretical study by Chen *et al.*, the lifetime for unimolecular decomposition of O_2N–H and HONO to NO + $^\bullet$OH has been calculated to be *ca.* 1 s and 800 ms, respectively, at approximately our reactor conditions, implying a longer lifetime for O_2N–H than for *trans*-HONO.[7] The same study argues that isomerization of O_2N–H to HONO has a *ca.* 10 times lower reaction rate than decomposition,[7] implying that the constitutional isomeric identity of HNO_2 is

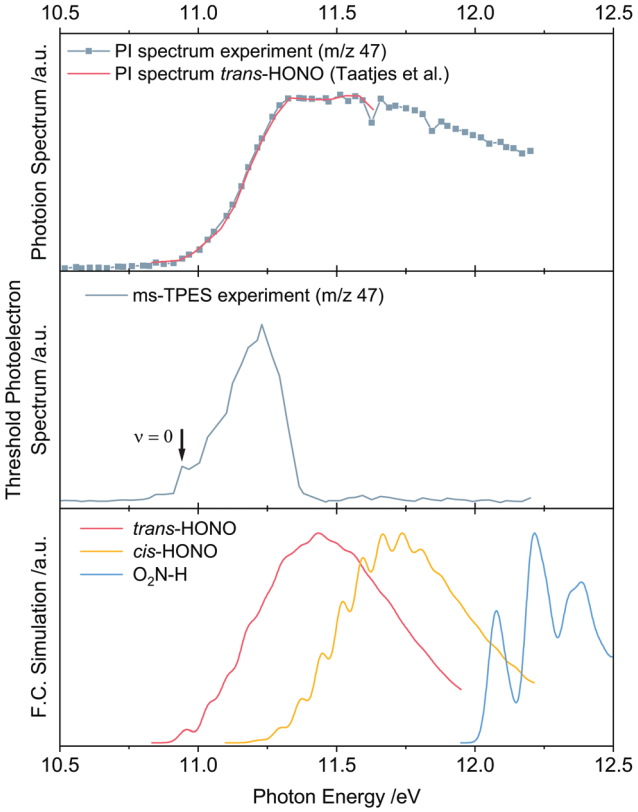

Fig. 3 Photoion (top) and photoion mass-selected threshold photoelectron spectrum (center) of *m*/*z* 47 combustion intermediate shown together with calculated Franck–Condon envelopes (bottom) for the three HNO_2 isomers.

conserved during its lifetime. As a result, the nitryl hydride isomer should also be observable experimentally. In contrast to this and according to the earlier results of Rasmussen *et al.*,[10] the isomerization rate of O_2N–H to HONO is on the order of 10^4 s^{-1} at our conditions, close to the high-pressure limit. This could lead to rapid formation of *trans*-HONO, which may decompose subsequently, leading to a depletion of both species. Fig. 3 shows the measured *m*/*z* 47 photoionization spectrum together with that recorded by Taatjes *et al.*,[20] as well as the experimental ms-TPES and the calculated Franck–Condon envelopes for the three HNO_2 isomers. The two PI spectra agree perfectly, which suggests that the carrier of the *m*/*z* 47 signal was the same in the NO_2-doped hydrogen flame as in our NO-doped methane-rich reaction mixture, *i.e.*, *trans*-HONO. Note that the precipitous drop in the ms-TPES at *ca.* 11.3 eV coincides with the plateauing PI spectrum.

The adiabatic ionization energies of the HNO_2 isomers were previously calculated by Sengupta *et al.*[6] The *trans*-HONO isomer was reported to have the lowest IE at 10.86 and 10.98 eV using DFT and the G2 composite method, respectively. Taatjes *et al.* analyzed two independently recorded *m*/*z* 47 photoionization spectra and arrived at ionization energies of 10.965 and 10.977 ± 0.030 eV, confirming the G2-computed result.[20] We applied the more recent CBS-QB3, G4, and W1BD composite methods to recalculate the adiabatic IEs (Table 1). The results agree that the ionization energy of *cis*-HONO is

Table 1 Adiabatic ionization energies in eV for the three HNO_2 isomers

Isomer	CBS-QB3	G4	W1BD	Experimental[a]
trans-HONO	10.95	10.96	10.95	10.95 ± 0.03
cis-HONO	11.28	11.22	11.25	
HNO_2	12.04	12.05	12.11	

[a] Assignment of origin transition based on Franck–Condon modeling of the ms-TPES and taking the Stark shift of 0.01 eV into account.

about 0.3 eV and that of O_2N–H *ca.* 1 eV higher than that of *trans*-HONO. Franck–Condon factors at the B3LYP/6-311++G(d,p) level of theory were used to simulate the photoelectron spectrum within the double harmonic approximation. The Franck–Condon envelopes were shifted to the respective G4 ionization energies.[40] The molecular beam sampling is not expected to be accompanied by significant cooling due to the low injection temperature of the sample of 373 K and the low pre-expansion pressure.[31] Thus, hot and sequence band transitions are minor and the FC spectra in Fig. 3 are plotted at an assumed temperature of 350 K. The envelopes were obtained by performing a convolution with a 30 meV half width at half maximum (242 cm^{-1}) Gaussian function, accounting for the rotational envelope.

The highest occupied molecular orbital (HOMO) of *trans*-HONO is of a′ symmetry as depicted in Fig. 1. The geometry change is moderate upon removal of a HOMO electron, which leads to a shortening of the HO–NO bond by 0.13 Å. The removal of an a″ electron from HOMO−1 (Fig. 1) yields an excited state, which relaxes into the $HO\cdots NO^+$ ion–dipole complex. EOM-IP-CCSD/cc-pVTZ calculations suggest that the vertical ionization energy is on the order of 12.8 eV, *i.e.*, beyond the energy range covered here, and the A″ band in the TPES is expected to be broad and weak because of the large geometry change.

The origin transition is observable in the center panel of Fig. 3, and the rising edge of the TPES is in good agreement with the Franck–Condon simulation. This allows us to determine the *trans*-HONO adiabatic ionization energy experimentally as 10.95 ± 0.03 eV, which is compared to the computed values in Table 1. The Franck–Condon simulation predicts *cis*-HONO to exhibit a more resolved vibrational fine structure than *trans*-HONO, and O_2N–H is expected to have a strong and well-resolved origin peak at the adiabatic ionization energy. However, the ms-TPES rapidly declines at energies above 11.2 eV and vanishes at 11.4 eV. Based on these observations, we can rule out *cis*-HONO or HNO_2 as significant contributors to the *m*/*z* 47 ms-TPES, and, consequently also as carriers of the *m*/*z* 47 PI spectrum.

Taatjes *et al.* proposed that the poor fit of the calculated PI spectrum was due to declining vibrational transition intensities, as photoionization of *trans*-HONO may yield the stable $HO\cdots NO^+$ ion–dipole complex[6] close above the ionization energy.[20] However, the steep fall in the *m*/*z* 47 ms-TPES is unlikely to be caused by smoothly changing FC factors on an anharmonic potential energy surface. In fact, although the photoelectron spectrum reported by Wang *et al.* is not well-resolved and rather noisy, it clearly shows that the *trans*-HONO ground state

band continues, as is predicted by the Franck–Condon simulation.[21] Thus, the plateauing of the PI and the sudden drop of the ms-TPE spectrum is related to the ion selection: $HONO^+$ will fragment and form NO^+ close to the ionization onset. The HONO TPES corresponds to the sum of the signals in these two mass channels. However, as will be discussed later, nitric oxide and formaldehyde also contribute to the *m*/*z* 30 signal, and signal apportioning to the individual carriers is nontrivial.

The G4-computed potential energy surface in Fig. 4 confirms that dissociative photoionization (DPI) is at play. The G4-calculated HO–NO^+ bond dissociation energy, 0.35 eV, is much lower than the previously reported DFT value of 0.84 eV,[6] and it agrees with the 0.39 eV bond energy calculated with the help of 0 K enthalpies of formation of *trans*-$HONO^+$, $^\bullet OH$ and NO^+ as tabulated in the ATcT.[11] As *cis*-$HONO^+$ is 0.31 eV higher in energy than *trans*-$HONO^+$, this also means that the *cis* cation is only bound by 0.04 eV. Based on these calculations, *cis*-$HONO^+$ may only show up as a minor perturbation in the *m*/*z* 47 ms-TPES close to the *cis*-HONO ionization energy and will mostly contribute to the *m*/*z* 30 ms-TPES. The *m*/*z* 47 ms-TPES vanishes at *ca.* 11.4 eV photon energy, which can be compared with the G4-calculated dissociative photoionization threshold for *trans*-HONO → NO^+ + $^\bullet OH$ + e^- of 11.31 eV, or the 11.34 eV reaction energy based on the ATcT.[11] Thus, dissociative ionization is responsible for the observed drop in the *m*/*z* 47 ms-TPE signal, and the sum of the parent *m*/*z* 47 and the daughter *m*/*z* 30 ms-TPES yields the ms-TPES of the *trans*/*cis*-HONO mixture below 11.7 eV, where O_2N–H is not yet expected to contribute.

This observation is corroborated by the *m*/*z* 30 ms-TPES. In the reaction mixture (*cf.* Table S1, ESI†), formaldehyde (H_2CO, *m*/*z* 30) shows a clear origin transition at its IE = 10.88 eV,[44] sitting on top of the NO signal (IE = 9.26 eV,[44] also at *m*/*z* 30 in the top panel of Fig. 5). Based on the H_2CO reference spectrum by Kimura *et al.*,[45] formaldehyde barely contributes to the ms-TPES beyond 11.3 eV. The drop in the *m*/*z* 47 ms-TPES takes place in-between NO and H_2CO resonances (Fig. 3), and

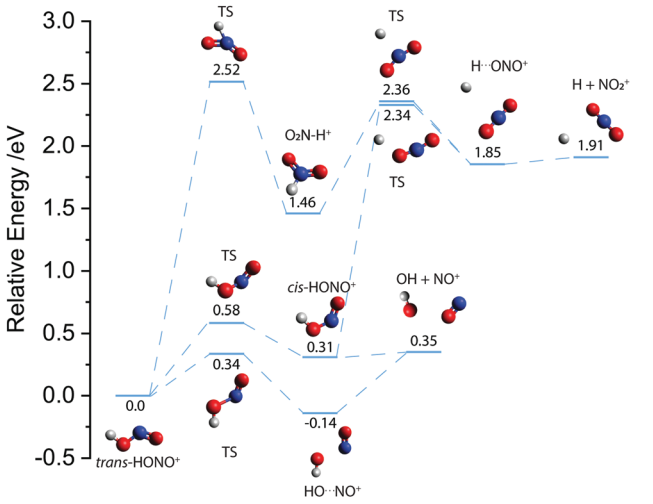

Fig. 4 Partial potential energy surface of doublet HNO_2^+ calculated at the G4 level of theory. Energies are given relative to *trans*-$HONO^+$.

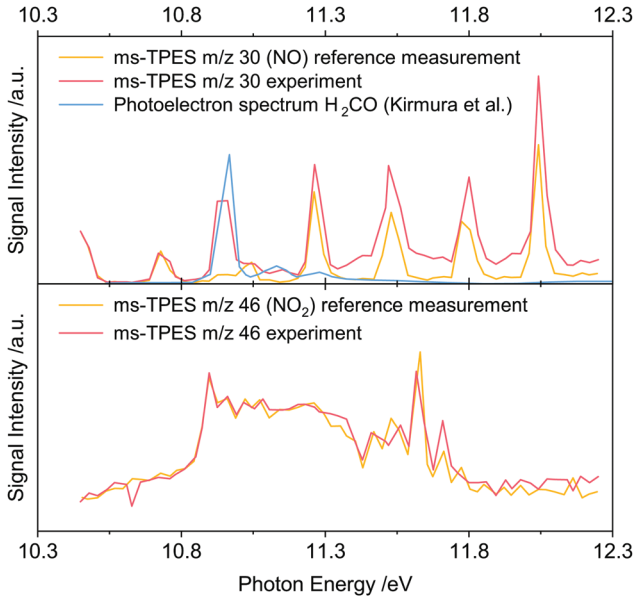

Fig. 5 Top panel: *m*/*z* 30 ms-TPES of the hydrocarbon reaction condition in comparison with an H_2CO reference photoelectron spectrum,[45] and an NO spectrum from a reference measurement of an NO/O_2 mixture in Ar. Bottom panel: Comparison of *m*/*z* 46 ms-TPES from the reaction and reference condition.

the coincident rise of the *m*/*z* 30 signal can be qualitatively assigned to HONO dissociative photoionization. This is supported by the observation that the *m*/*z* 30 baseline in the reference measurement (top panel of Fig. 5 and Table S2, ESI†) remains flat in this range.

The *m*/*z* 30 ms-TPES is, however, not suitable to plot the experimental breakdown diagram of HONO, because of the large abundance of NO^+ ions from NO and some formaldehyde contributions also at *m*/*z* 30. This signal convolution poses an experimental limit to the accurate detection of the sum of the signals of interest. In a perfectly cooled molecular beam, velocity map imaging of the ions could be used to separate these contributions from the dissociative photoionization NO^+ signal of HONO based on kinetic energy release. Here, the imperfect molecular beam cooling precludes signal separation based on kinetic energy release. Furthermore, the modest mass resolution, a consequence of the mild fields needed to maintain electron kinetic energy resolution, does not allow for the separation of the isobaric NO and H_2CO peaks, either.

Therefore, and for the first time, we rely solely on the renormalized Franck–Condon simulation as a function of photon energy, FC($h\nu$), and the experimental $HONO^+$ ion signal $S_{m/z\,47}(h\nu)$ to evaluate the fractional abundance of the parent and daughter ions, $BD_{HONO^+}(h\nu)$ and $BD_{NO^+}(h\nu)$, and construct the breakdown diagram:

$$BD_{HONO^+}(h\nu) = S_{m/z\,47}(h\nu)/FC(h\nu) \quad (1)$$

$$BD_{NO^+}(h\nu) = 1 - BD_{HONO^+}(h\nu) \quad (2)$$

The result (Fig. 6), agrees with the ATcT-calculated appearance energy of E_0 = 11.34 eV and a model temperature of 350 K.[11,35]

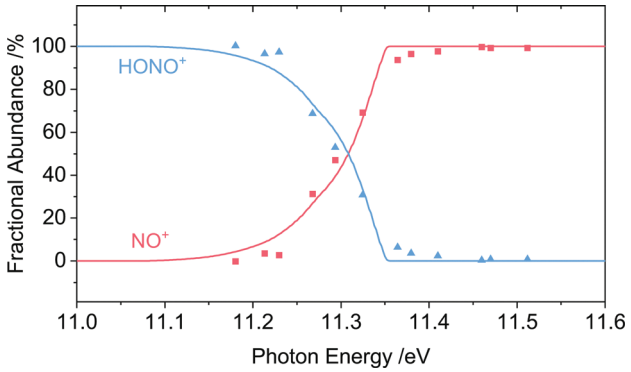

Fig. 6 Reconstructed breakdown diagram of •OH loss from $HONO^+$ based on the FC simulation and the *m*/*z* 47 ms-TPES signal (triangles and squares) together with a model calculation (continuous lines) assuming 350 K sample temperature and the literature E_0 of 11.34 eV. See text for details.

This proof-of-concept dissociative photoionization analysis shows that the ms-TPES of only the parent ion can be used together with a computed Franck–Condon envelope to (i) understand the photoionization mechanism and (ii) derive estimated appearance energies that are virtually identical to the exact value, hence, quantitative energetics. We would like to point out that valence autoionizing states leading to a different parent ion internal energy distribution would be visible as distinct resonances in the breakdown diagram[46] whereas a broadened or narrowed band shape with respect to the FC-simulated ground state band would distort the breakdown diagram and result in an unphysical model temperature. Neither effect would affect the appearance energy, and the fact that they would be observable, yet are not, validates our approach.

The baseline of the *m*/*z* 30 ms-TPES appears to level off at a higher intensity above 11.5 eV in Fig. 5 compared with the NO reference ms-TPES. As the Franck–Condon envelope to the ground electronic state of *trans*-$HONO^+$ closes and its first electronic excited state is only expected to show up as a broad band with a vertical ionization energy at *ca.* 12.8 eV (*vide supra*), the elevated baseline of the *m*/*z* 30 ms-TPES beyond 11.2 eV can be tentatively assigned to *cis*-HONO. Despite the multiple contributors to the *m*/*z* 30 signal, this is a strong indication that *cis*-HONO is present in the sample. The *m*/*z* 47 ms-TPE signal in Fig. 3 drops to the baseline up to 12.2 eV photon energy. At first glance, this only seems logical because of its dissociative photoionization threshold to NO^+ at 11.34 eV. However, as also seen in the potential energy surface in Fig. 4, the nitryl hydride cation, $O_2N–H^+$, is bound at the ionization energy by almost 1 eV and Franck–Condon simulations predict a strong origin transition in its photoelectron spectrum (Fig. 3). Moreover, the ms-TPES at *m*/*z* 46 (bottom panel of Fig. 5), is identical in both measurements. This indicates that no NO_2 fragment is produced by dissociative photoionization above the adiabatic ionization energy of $O_2N–H$, ruling out decomposition of $O_2N–H^+$ to H and NO_2^+. As mentioned earlier, based on the reaction rates proposed by Chen *et al.*, neutral nitryl hydride is expected to decompose with a similar rate as *trans*-HONO and should not isomerize significantly to *trans*-HONO.[7] Since *trans*-HONO was detected here, $O_2N–H$ should also be detectable as distinct isomer. The fact that the *m*/*z* 47 signal does not rebound near 12 eV is strong evidence that nitryl hydride is not present in the sample. We offer three explanations as to why this could be the case, which cannot be differentiated by our experiment. First, higher unimolecular reaction rates for the $O_2N–H \rightleftharpoons$ *trans*-HONO isomerization, as proposed by Rasmussen *et al.*,[10] with a substantial forward rate to the energetically favorable[13] *trans*-HONO isomer can explain the depletion of $O_2N–H$. Second, nitryl hydride could be formed, but it may be more reactive than nitrous acid and, thus, more rapidly consumed in the reactor. Assuming it is formed with appreciable steady-state concentrations,[7] plausible destruction pathways involve it being an H-donor to, *e.g.*, methane-derived radical intermediates. The third explanation is that nitryl hydride is not formed, and NO_2 preferentially reacts to nitrous acid, which, however, is not reflected by reaction rates suggested for isomer specific kinetics of $O_2N–H$ formation.[3,8,10]

IV. Conclusions

We studied the nitrogen chemistry in the oxidation of methane doped with nitric oxide by threshold photoionization. Below 12.2 eV, HNO_2 contributes to the *m*/*z* 47 and *m*/*z* 30 ion channels, the latter by dissociative photoionization by •OH loss. The parent ion channel was analyzed to determine the *trans*-HONO ionization energy and, in a proof-of-concept analysis, to confirm the 0 K appearance energy of NO^+ based solely on the parent ion signal and the computed Franck–Condon envelope of *trans*-HONO. Although the *m*/*z* 30 signal is perturbed by nitric oxide and formaldehyde, its raised baseline past the *trans*-HONO FC band indicates the presence of *cis*-HONO. Our calculations agree with literature results that the nitryl hydride cation, $O_2N–H^+$, is bound. The photoelectron spectrum is expected to exhibit a strong origin transition at *ca.* 12 eV. Yet, the missing *m*/*z* 47 signal in this energy range shows that nitryl hydride is absent in the sample: it is either not formed or is rapidly consumed in unimolecular or bimolecular reactions and the proposed literature reaction rates for known consumption reactions are in disagreement. These insights demonstrate the prowess of threshold ionization mass spectrometry by i^2PEPICO to identify isomeric mixtures of elusive species in difficult experimental conditions and may pave the way for the validation of kinetic models on the specific reactivity of HNO_2 isomers.

Conflicts of interest

There are no conflicts to declare.

Acknowledgements

Experiments were carried out at the VUV beamline of the Swiss Light Source of the Paul Scherrer Institute. The financial support of the Swiss Federal Office for Energy (BFE Contract

No. SI/501269-01) is gratefully acknowledged. All authors thank the Deutsche Forschungsgemeinschaft for financial support under contract KA3871/3-2.

Notes and references

1 R. W. Molt, T. Watson, A. P. Bazanté, R. J. Bartlett and N. G. J. Richards, *Phys. Chem. Chem. Phys.*, 2016, **18**, 26069–26077.
2 F. A. Akin and G. Kıyak, *Struct. Chem.*, 2019, **30**, 201–211.
3 J. Chai and C. F. Goldsmith, *Proc. Combust. Inst.*, 2017, **36**, 617–626.
4 L. Marrodán, Y. Song, O. Herbinet, M. U. Alzueta, C. Fittschen, Y. Ju and F. Battin-Leclerc, *Chem. Phys. Lett.*, 2019, **719**, 22–26.
5 J. Kleffmann, *ChemPhysChem*, 2007, **8**, 1137–1144.
6 D. Sengupta, R. Sumathi and S. D. Peyerimhoff, *Chem. Phys.*, 1999, **248**, 147–159.
7 X. Chen, M. E. Fuller and F. C. Goldsmith, *React. Chem. Eng.*, 2019, **4**, 323–333.
8 M. E. Fuller and C. F. Goldsmith, *Proc. Combust. Inst.*, 2019, **37**, 695–702.
9 P. A. McDonald and J. S. Shirk, *J. Chem. Phys.*, 1982, **77**, 2355–2364.
10 C. L. Rasmussen, J. Hansen, M. Paul and P. Glarborg, *Int. J. Chem. Kinet.*, 2008, **40**, 454–480.
11 B. Ruscic, R. E. Pinzon, M. L. Morton, G. Von Laszevski, S. J. Bittner, S. G. Nijsure, K. A. Amin, M. Minkoff and A. F. Wagner, *J. Phys. Chem. A*, 2004, **108**, 9979–9997.
12 Y. Zhang, O. Mathieu, E. L. Petersen, G. Bourque and H. J. Curran, *Combust. Flame*, 2017, **182**, 122–141.
13 R. Asatryan, J. W. Bozelli and J. M. Simmie, *Int. J. Chem. Kinet.*, 2007, **39**, 378–398.
14 A. M. Mebel, M. C. Lin and C. F. Melius, *J. Phys. Chem. A*, 1998, **102**, 1803–1807.
15 A. M. Ickes, S. V. Bohac and D. N. Assanis, *Energy Fuels*, 2009, **23**, 4943–4948.
16 D. A. Knyazkov, A. G. Shmakov, I. V. Dyakov, O. P. Korobeinichev, J. De Ruyck and A. A. Konnov, *Proc. Combust. Inst.*, 2009, **32**, 327–334.
17 A. B. Dempsey, N. R. Walker and R. Reitz, *SAE Int. J. Fuels Lubr.*, 2013, **6**, 170–187.
18 C. Jain, P. Morajkar, C. Schoemaecker, B. Viskolcz and C. Fittschen, *J. Phys. Chem. A*, 2011, **115**, 10720–10728.
19 J. J. Weng, Z. Y. Tian, K. W. Zhang, L. L. Ye, Y. X. Liu, L. N. Wu, D. Yu, J. Z. Yang, C. C. Cao and J. B. Zou, *Combust. Flame*, 2019, **203**, 247–254.
20 C. A. Taatjes, D. L. Osborn, T. A. Cool and K. Nakajima, *Chem. Phys. Lett.*, 2004, **394**, 19–24.
21 W. Wang, M. Ge, L. Yao, X. Zeng and Z. Wang, *Chin. Sci. Bull.*, 2007, **52**, 3056–3060.
22 C. A. Taatjes, N. Hansen, D. L. Osborn, K. Kohse-Höinghaus, T. A. Cool and P. R. Westmoreland, *Phys. Chem. Chem. Phys.*, 2008, **10**, 20–34.
23 N. Hansen, T. A. Cool, P. R. Westmoreland and K. Kohse-Höinghaus, *Prog. Energy Combust. Sci.*, 2009, **35**, 168–191.
24 A. Bodi, P. Hemberger, D. L. Osborn and B. Sztáray, *J. Phys. Chem. Lett.*, 2013, **4**, 2948–2952.
25 T. Baer and R. P. Tuckett, *Phys. Chem. Chem. Phys.*, 2017, **19**, 9698–9723.
26 P. Hemberger, J. A. Van Bokhoven, J. Pérez-Ramírez and A. Bodi, *Catal. Sci. Technol.*, 2020, **10**, 1975–1990.
27 D. Krüger, P. Oßwald, M. Köhler, P. Hemberger, T. Bierkandt, Y. Karakaya and T. Kasper, *Combust. Flame*, 2018, **191**, 343–352.
28 B. Sztáray, K. Voronova, K. G. Torma, K. J. Covert, A. Bodi, P. Hemberger, T. Gerber and D. L. Osborn, *J. Chem. Phys.*, 2017, **147**, 013944.
29 D. Felsmann, A. Lucassen, J. Krüger, C. Hemken, L. S. Tran, J. Pieper, G. A. Garcia, A. Brockhinke, L. Nahon and K. Kohse-Höinghaus, *Z. Phys. Chem.*, 2016, **230**, 1067–1097.
30 O. Welz, J. D. Savee, D. L. Osborn, S. S. Vasu, C. J. Percival, D. E. Shallcross and C. A. Taatjes, *Science*, 2012, **335**, 204–207.
31 M. Hoener, D. Kaczmarek, T. Bierkandt, A. Bodi, P. Hemberger and T. Kasper, *Rev. Sci. Instrum.*, 2020, **91**, 045115.
32 M. Johnson, A. Bodi, L. Schulz and T. Gerber, *Nucl. Instrum. Methods Phys. Res., Sect. A*, 2009, **610**, 597–603.
33 A. Bodi, B. Sztáray, T. Baer, M. Johnson and T. Gerber, *Rev. Sci. Instrum.*, 2007, **78**, 1–8.
34 B. Sztáray and T. Baer, *Rev. Sci. Instrum.*, 2003, **74**, 3763–3768.
35 B. Sztáray, A. Bodi and T. Baer, *J. Mass Spectrom.*, 2010, **45**, 1233–1245.
36 M. J. Frisch, G. W Trucks, H. B. Schlegel, G. E Scuseria, M. A. Robb, J. R. Cheeseman, G. Scalmani, V. Barone, G. A. Petersson, H. Nakatsuji, X. Li, M. Caricato, A. V. Marenich, J. Bloino, B. G. Janesko, R. Gomperts, B. Mennucci, H. P. Hratchian, J. V. Ortiz, A. F. Izmaylov, J. L. Sonnenberg, D. Williams-Young, F. Ding, F. Lipparini, F. Egidi, J. Goings, B. Peng, A. Petrone, T. Henderson, D. Ranasinghe, V. G. Zakrzewski, J. Gao, N. Rega, G. Zheng, W. Liang, M. Hada, M. Ehara, K. Toyota, R. Fukuda, K. J. Hasegawa, M. Ishida, T. Nakajima, Y. Honda, O. Kitao, H. Nakai, T. Vreven, K. Throssell, J. A. Montgomery Jr., J. E. Peralta, F. Ogliaro, M. J. Bearpark, J. J. Heyd, E. N. Brothers, K. N. Kudin, V. N. Staroverov, T. A. Keith, R. Kobayashi, J. Normand, K. Raghavachari, A. P. Rendell, J. C. Burant, S. S. Iyengar, J. Tomasi, M. Cossi, J. M. Millam, M. Klene, C. Adamo, R. Cammi, J. W. Ochterski, R. L. Martin, K. Morokuma, O. Farkas, J. B. Foresman and D. J. Fox. *Gaussian 16, Revision C.01*, Gaussian, Inc., Wallingford CT, 2016.
37 A. D. McLean and G. S. Chandler, *J. Chem. Phys.*, 1980, **72**, 5639–5648.
38 R. Krishnan, J. S. Binkley, R. Seeger and J. A. Pople, *J. Chem. Phys.*, 1980, **72**, 650–654.
39 J. A. Montgomery, M. J. Frisch, J. W. Ochterski and G. A. Petersson, *J. Chem. Phys.*, 1999, **110**, 2822–2827.

40 L. A. Curtiss, P. C. Redfern and K. Raghavachari, *J. Chem. Phys.*, 2007, **126**, 084108.
41 E. C. Barnes, G. A. Petersson, J. A. Montgomery, M. J. Frisch and J. M. L. Martin, *J. Chem. Theory Comput.*, 2009, **5**, 2687–2693.
42 Y. Shao, *et al.*, *Phys. Chem. Chem. Phys.*, 2006, **8**, 3172–3191.
43 C. L. Rasmussen, A. E. Rasmussen and P. Glarborg, *Combust. Flame*, 2008, **154**, 529–545.
44 P. J. Lindstrom, W. G. Mallard and National Institute of Standards and Technology (US), *Gaussian-4 theory*, 1997.
45 K. Kimura, S. Katsumata, Y. Achiba, T. Yamazaki and S. Iwata, *Handbook of Hel photoelectron spectra of fundamental organic molecules*, 1981.
46 A. Bodi, N. S. Shuman and T. Baer, *Phys. Chem. Chem. Phys.*, 2009, **11**, 11013–11021.

Nitrous acid in high-pressure oxidation of CH_4 doped with nitric oxide: Challenges in the isomer-selective detection and quantification of an elusive intermediate

Hoener, M., Kasper, T.
Combustion and Flame, 2022, 243, 112096
DOI: 10.1016/j.combustflame.2022.112096

My contribution to this work was the development of the reactor interface to the CRF-PEPICO endstation, manufacturing supervision of the design, the commissioning of the experiment, design of the experiment, measurement and quantitative analysis of the reactor data, composition of the combustion mechanism, performance of chemical kinetics simulation, writing of the manuscript.

Combustion and Flame 243 (2022) 112096

Contents lists available at ScienceDirect

Combustion and Flame

journal homepage: www.elsevier.com/locate/combustflame

Nitrous acid in high-pressure oxidation of CH_4 doped with nitric oxide: Challenges in the isomer-selective detection and quantification of an elusive intermediate

Martin Hoener*, Tina Kasper

Mass Spectrometry in Reactive Flows – Institute for Combustion and Gas Dynamics (IVG), University Duisburg-Essen, Duisburg 47057, Germany

ARTICLE INFO

Article history:
Received 28 September 2021
Revised 28 February 2022
Accepted 28 February 2022
Available online 23 March 2022

Keywords:
HONO
HNO_2
Photoionization
Partial oxidation
PEPICO
isomers

ABSTRACT

The nitrous acid combustion intermediate has recently been detected in several reaction conditions using hydrocarbon fuels with different analytical techniques. Three of the several isomers of nitrous acid are expected to be produced during combustion: *trans*-HONO, *cis*-HONO and HNO_2. It has recently been shown that *cis*-HONO dissociates upon ionization, rendering isomer selective quantification with methods requiring photoionization prior to detection impossible. This fact is of importance, since *cis*-HONO is produced at a ten times higher rate than *trans*-HONO according to recently published isomer branching ratios, possibly leading to sensitivity issues when a detection of the isomer mix is attempted with photoionization methods. We provide a quantitative glimpse at the *trans*-HONO isomer in a systematic set of measurements of NO doped methane oxidized in a plug-flow reactor covering three reaction conditions in the lean and rich regimes. Reactions take place at equivalence ratios of 0.7 and 1.2 with 1000 ppm NO and at an equivalence ratio of 2.1 doped with 1% NO. Double imaging photoelectron photo ion coincidence spectroscopy, i^2PEPICO, was used to selectively and assuredly detect and assign *trans*-HONO. We touch on the difficulties encountered when attempting to detect cis-HONO. HNO_2 remained undetectable despite recently published reaction rates for HNO_2 decomposition suggesting modelled concentrations of this species two orders of magnitude larger than previously believed, yet 10 times lower than the reported isomer branching ratio. The recent reaction rates add a new path for HNO_2 decomposition leading to formation of OH and NO which in turn influences the remaining decomposition kinetics of HNO_2. A literature model is modified to include the recently published reaction rates for HONO and HNO_2 decomposition and isomerization and compared to the measurements. Despite the higher predicted concentration of HNO_2, that should be sufficient for detection, no HNO_2 is detected in the experiment. Other nitrogen containing species, such as nitromethane and NO_2, the precursor of both HONO and nitromethane, have also been detected. Interestingly, ammonia was also present in significant concentration, albeit exclusively in the fuel-rich conditions, despite the relatively low maximum temperature of 923 K at which the experiments have been performed. We conclude that, facing the unfavorable photoionization properties of *cis*-HONO as well as the decomposition and formation kinetics of HNO_2, a measurement of isomer branching fractions by means of selective and sensitive photoionization methods may remain unattainable.

1. Introduction

Emissions of oxides of nitrogen (NO_x) from combustion devices are harmful and heavily regulated pollutants. A general understanding of nitrogen fuel interactions is required to understand the formation of oxides of nitrogen in combustion processes, and to mitigate their emissions [1]. Nitrogen interactions in combustion play an important role wherever fuels are oxidized by air but also in cases where the fuel or oxidizer themselves contain the nitrogen. When oxides of nitrogen are injected directly into the combustible gas mix, for example in NO_x re-burning and exhaust gas recirculation (EGR) processes [1], reactions involving nitrogen interact with low-temperature fuel chemistry [2]. The same applies for the addition of NO_x releasing additives like cetane enhancers to fuels [3]. Nitrous acid and its isomers are crucial intermediates in the reaction networks that lead to the formation of pollutants and influence the combustion properties of the system [4]. An intermediate like HONO may play a decisive role, since it can be contained

* Corresponding author.
E-mail address: martin.hoener@uni-due.de (M. Hoener).

https://doi.org/10.1016/j.combustflame.2022.112096

in the recirculated gasses or be formed at low temperatures to subsequently decompose yielding OH and thus, influence ignition [2].

Both NO and NO_2 are involved in nitrous acid formation in combustion [5–7]. Three of the several existing isomers of nitrous acid [8] can be produced in combustion processes [9]. These are *trans*-HONO, *cis*-HONO and HNO_2 [10]. NO_2 is the most active species in HONO formation, as all atoms in this resonance stabilized molecule have radical character [7,9], perform H abstraction [7,10], and interact in several disproportionation reactions involving intermediate species [9]. Depending on which atom of NO_2 performs H abstraction either HNO_2 or one of the HONO rotamers can be formed [7]. In case of H addition to the nitrogen, HNO_2 is produced. Moreover, competing decomposition reactions such as the bimolecular HONO decomposition to NO, NO_2 and water [11] and ground state *cis*/trans isomerization exist [7,8,12].

Conditions highly enriched with NO, such as the ones investigated here, are relevant for high enthalpy flows and combustion under such conditions as, e.g., encountered in the engines of air breathing hypersonic vehicles [13]. Formation of oxides of nitrogen, primarily NO, due to the conditions (i.e., high temperature, high enthalpy) under which the air ingestion and combustion takes place can be substantial. Hence, inlet conditions in hypersonic combustion can deviate substantially from the anticipated scope of air constituents under lower enthalpy conditions. In hypersonic combustion, high concentrations of NO can be expected in the range of several thousand ppm, similar to the conditions investigated in this work [13]. Under testing conditions, additional air dissociation and NOx formation can be caused by the testing apparatus, such as, e.g., in arc heating devices used to increase the enthalpy of the flow in high enthalpy wind tunnel facilities [14]. From a more fundamental kinetic point of view, large NO_x concentrations in the inlet can be helpful to enhance the reaction pathways involving these molecules and facilitate their investigation.

While several studies encompassing reaction conditions that investigate fuel-nitrogen interactions have been performed, only few have been able to unambiguously detect the HONO intermediate directly. Taatjes et al. reported the *trans*-HONO intermediate measured by synchrotron photoionization molecular beam mass spectrometry (PI-MBMS) in a premixed hydrogen flame doped with NO_2 [15], while they were unable to detect the *cis* isomer. Weng et al. detected HONO in the pyrolysis of nitromethane by PI-MBMS [16]. In a recent study by Zhang et al., a peak at mass-to-charge ratio (*m/z*) 47 was detected in the NO doped oxidation of dimethyl ether and dimethoxymethane analyzed with electron ionization (EI)-MBMS and assigned to HONO by the authors [17]. In premixed flames of morpholine, a signal at *m/z* 47 was detected by Lucassen et al. using EI-MBMS, while no such signal was found in the same flame analyzed with PI-MBMS [18]. Marrodán et al. reported the first measurement of HONO in a reacting hydrocarbon system doped with NO using continuous wave cavity-ring-down spectroscopy [2]. The reference spectra used for the identification were measured in an isomer mix [19] and hence no isomer selectivity was achieved. The first conclusive mass spectrometric data using photoionization methods from the investigation of an oxidized hydrocarbon/NO_x system was recently published by Yuan et al. [20], who assigned the *m/z* 47 peak detected in the partial oxidation of propylene to *trans*-HONO, and Gossler et al. detected HONO in NO doped butane using PI-MBMS [21]. In summary, few quantitative isomer selective combustion speciation data exist for nitrous acid isomers and open questions remain concerning the formation and destruction pathways of the nitrous acid isomers and their rates. One reason are the experimental difficulties involved in the accurate quantitative detection of these intermediates.

In a recent publication by Hoener et al. examining the threshold photoelectron spectrum of HONO, the limits to detectability of the *cis* isomer of HONO by photoionization mass spectrometry were treated thoroughly [22]. A low barrier of 40 meV for dissociative ionization of *cis*-HONO was found with accurate electronic structure methods at the G4 level of theory [23]. Their analysis confirmed that dissociative photoionization is at play, which causes the lack of a distinct *cis*-HONO signal in the threshold photoelectron spectrum, selected for *m/z* 47. The results suggest that no stable ion of *cis*-HONO can be formed upon ionization and the compound is therefore not detectable with methods that require photoionization prior to detection. Moreover, and in contrast to expectations, no sign of the HNO_2 isomer was detected in the same experiment. In a recent theoretical quantum computational chemistry study, Chen et al. found that HNO_2 is formed at a rate similar to *trans*-HONO and destruction of *trans*-HONO is energetically favored, making HNO_2 more thermally stable than *trans*-HONO [7]. Hoener et al. concluded, that since *trans*-HONO is present in the exhaust stream, then HNO_2 should also be detectable.

The available experimental data for the HONO intermediate are limited and especially lacking isomer selective measurements. This paper presents quantitative and comparative data across lean and rich conditions doped with NO measured with double imaging photoelectron photo ion coincidence spectroscopy (i^2PEPICO). We supply some explanation for the difficulties in HONO and HNO_2 detection. The experiment allows the simultaneous measurement of the isomeric composition of the nitrous acid isomers and the other components of the reacting mixture. The cumulative quantitative data of all species are valuable validation data for reaction mechanism development. To test how the rate coefficients for the formation of the nitrous acid isomers suggested by Chen et al. [7] influence the predicted mole fractions of the theses species, we implement them in the reaction mechanism of Glarborg et al. [4]. The simulation results are compared to the experimental data.

2. Methods

2.1. Experimental

The experiment used a pressurized reactor set up. Chemical composition analysis of the sample, as a function of reactor temperature, was performed with the CRF-PEPICO endstation [24] of the X04DB VUV beamline [25] at the Swiss Light Source synchrotron facility. A thorough description of the experimental setup is reported in [26]. The electrically heated reactor consists of a stainless-steel outer pressure containment, which is enclosed by a copper heat-distribution jacket. The reactor maintains an isothermal zone of 450 mm at a reactor length of 650 mm. Temperature ramps from inlet or outlet temperature to the temperature of the reactor of length 100 mm exist at the upstream and downstream ends of the reactor. An inner fused silica liner prevents wall interactions of the reacting mixture with the outer stainless-steel shell. The internal flow volume has a diameter of 6 mm. Deviating from the set-up described in [26], here, the NO dopant was injected directly in front of the reactor to prevent interactions in the reactant feed system and make sure that the NO only reacts in the temperature controlled zone of the reactor. The pressure is reduced behind the heated reactor by an initial needle valve stage and two subsequent differential pumping stages. In this initial expansion stage, transient radicals are lost, and only stable species are sampled [26]. The sample is transferred to the molecular beam interface by a heated transfer line. It is then injected into the mass spectrometer after expansion in the interface and ionized in the beam interaction region. The grazing incidence monochromator of the beam line used in the experiments, delivers ionizing vacuum ultra-violet (VUV) light with an energy dependent energy resolution of approximately 10^3 $E/\Delta E$ at 10 eV [27]. Contamination of higher harmonics is removed by a gas filter filled with neon above photon energies

Table 1
Mole fractions of reactants for the reaction conditions at a total flow of 280 sccm.

Condition	CH_4	O_2	NO	Ar	φ
RC1	0.026	0.073	0.001	0.9	0.7
RC2	0.037	0.062	0.001	0.9	1.2
RC3	0.046	0.044	0.01	0.9	2.1

of 15 eV, and a neon/argon mix below this energy and energies above 10.3 eV. Below 10.3 eV a MgF_2 window, that can be inserted into the light path, is used. Synchrotron VUV photoionization affords an additional criterion for distinction of species in the sample by their respective ionization energy in addition to the mass-to-charge ratio of the photo ion [26]. The multiplexed measuring method of the double imaging photo ion photoelectron coincidence spectrometer (i^2PEPICO) allows mass selective detection of photo ions and mass selection of the photoelectron signal [27]. The coincidence of every ion with the ejected photoelectron of every ionization event is recorded at high maximum count rates of up to 100 kHz. The recorded vibronic progressions of the mass selective photoelectron spectra (ms-TPES) allow detection and fingerprinting identification of isobaric species. The method is advantageous especially for distinction of isomers in complex combustion conditions [28]. Identification is performed by comparing the ms-TPES with literature references and simulated Frack-Condon envelopes in addition to the use of photo ion (PI) spectra. The molecular beam is ionized at fixed photon energies for different reactor temperatures. For species identification, the photon energy is scanned and PI spectra and ms-TPES are recorded [26]. Temperatures for the photon energy scans are selected by analyzing the recorded temperature dependent measurements and selecting temperatures where maximum reactivity occurs.

2.1.1. Reaction conditions

The three reaction conditions investigated in this work are presented in Table 1. For the experiments, a total flow of 280 sccm was maintained to allow for plug-flow conditions, leading to temperature dependent residence times. All conditions are diluted by addition of 90% argon so that the reactive components constitute the remaining 10%. The diluent acts as a collider and heat sink for exothermic reactions. It has been shown for a similar experiment that the influence of exothermic reactions is insignificant [29].

The investigated reaction conditions were designed with an emphasis on isolation of nitrogen chemistry and more specifically the nitrous acid intermediate in a C/H/N/O system. For this reason, the smallest alkane CH_4 was selected as fuel. This approach reduces the number of species and effectively prevents isobaric convolution in the mass spectrum. An excessive amount of 1% NO was doped into the system to enable a high occurrence of interactions of the fuel and dopant in the condition at an equivalence ratio (Φ) of 2.1 (RC3 in Table 1). The influence of lean and rich regimes on the process was probed with two conditions at equivalence ratios of 0.7 and 1.2 (RC1 and RC2, respectively Table 1). An NO dopant concentration of 1000 ppm was selected for these conditions to approximate more closely the lower concentrations expected in technical combustion systems. All experiments were performed at a total pressure of 6 bar, which increases the collision rate substantially. Temperatures were set at intervals of 50 K between 473 and 973 K for the temperature ramping measurements in both the $\Phi = 0.7$ (RC1) and the $\Phi = 2.1$ (RC3) condition. Since no significant reactions were observable for temperatures below 673 K, the measurement at $\Phi = 1.2$ (RC2) was started at a temperature of 573 K, to economize on measurement time. The elevated pressure of 6 bar for all equivalence ratios allows for the investigation of conditions close to those encountered in technical combustion systems, such as gas turbines and internal combustion engines before ignition initiates combustion.

2.1.2. Data evaluation

The data evaluation was performed according to an adapted procedure for the reactor experiment as elaborated in [26]. Main species were evaluated by an element balance considering the NO dopant and reactions taking place between NO and O_2 forming NO_2 at low temperatures. The element balancing procedures leads to concentrations with an estimated error of 25%. Due to the high argon dilution of 90%, the argon mole fraction is assumed to be constant, and the temperature averaged signal of argon was used for evaluation. Mole fractions of minor species are calculated with absolute cross sections from literature, where possible, yielding an estimated error of 50%. The cross section of the *trans*-HONO intermediate is not known. For this species a typical estimated cross section of 1×10^{-21} m^2 was used, introducing an error of factor 2 to 4 [30]. Since NO is highly reactive and present in high concentration in the reactant stream, it consumes significant amounts of oxygen at low temperatures to form NO_2. Consequently, a nitrogen balance has to be taken into account. This additional balancing caused the procedure to be more intricate and may also introduce a larger error in the resulting mole fractions. All evaluated data are provided in the supplementary information without the scaling and background removal used for some of the plots. All estimated errors are indicated in the plots.

2.2. Simulation

Chemical kinetics simulations were performed with the plug-flow module of Chemkin-Pro 19.2 [31]. We used measured temperature profiles of the reactor for the simulation inputs [29]. The temperatures at which the simulations were performed are identical to the temperatures at which the spectra were recorded. Profiles of all conditions are compared to a simulation with the NOx mechanism by Glarborg et al. [4], that has been modified by recent nitrous acid reactions reported by Chen et al. [7]. Some comparison is sought to the unmodified version of the same mechanism for RC3 regarding HNO_2 decomposition pathways and predicted concentration of this species. The differences in the modified mechanism are limited to the isomerization and the dissociation of HONO and HNO_2. The modifications to the mechanism by Glarborg et al. [4] with the rate expressions reported by Chen et al. [7] are detailed in the SI. The thermodynamic data remain unmodified.

Of significance for the present work is the treatment of nitrous acid isomer chemistry in the models. The mechanism treats the *cis* and trans rotamers of HONO in a lumped fashion (i.e. isomer chemistry remains untreated in the mechanism), while the HNO_2 isomer is treated separately [4,9]. Lumping of HONO rotamers is thought to be acceptable due to insensitivity of the mechanism to individual isomer chemistry [9]. The reaction rates published by Chen et al. suggest that isomerization of HNO_2 to HONO plays no significant role compared to unimolecular decomposition of HNO_2 yielding OH and NO. In contrast to their findings, isomerization to HONO was thought to be the most significant reaction leading to consumption of HNO_2 [32], as implemented in the original mechanism by Glarborg et al. [4].

Moreover, recently, a spontaneous thermal interconversion of *trans*- and *cis*-HONO was mentioned as a preliminary result published by Chen et al. [7]. Their results indicate, that at the pressures and temperatures used in our reaction conditions *trans*- and *cis*-HONO lose their distinct identities due to instantaneous isomerization between the two rotamers caused by HO–NO bond rotation [7]. According to theoretical assessments of reaction rates for HONO production, *cis*-HONO dominates in the gas phase [7,11,33]. Chen et al. suggest that the rate for *trans*/*cis* isomerization of

ground state HONO is high and both species should be present in equilibrium. With 10.6 kcal/mole they suggest a slightly smaller energetic barrier for the isomerization than older work, but state that a high rate of $2 \times 10^9\ s^{-1}$ for this process exists, leading to rapid equilibration [7]. Previously and in contrast to this assessment, it was believed that a barrier of 11.7 kcal/mol exists for this process and both rotamers would maintain their identity [6].

Results obtained with both mechanisms for all reaction conditions can be found in the SI, while the mole fraction profiles in the following sections are solely compared to the modified mechanism, since they show little difference, except for HONO and HNO_2.

3. Results and discussion

3.1. Main species

3.1.1. Excessively NO enriched condition at an equivalence ratio of 2.1 with 1% NO addition (RC3)

The ms-TPES measured in this condition was published by Hoener et al. [22] in their study of the photoionization properties of HONO and used to assess the lack of HNO_2 in the sample stream. Here, we provide a quantification of the dataset to investigate the kinetics and photoionization properties of the nitrous acid isomers and the absence of HNO_2.

The quantitative data for the reaction condition at an equivalence ratio of 2.1 (RC3) show good agreement with the modified mechanism [4,7] for the fuel and product species. Some disagreement is found in the mole fraction profiles as function of temperature of oxygen and nitrogen main species (i.e. NO and NO_2). The profiles are compared in Fig. 1. The CO and H_2O profiles show that fuel conversion starts at a temperature of 723 K, while the mechanism predicts reactions to commence at about 50 K above this value. The difference in the onset of reactions is significant, albeit below the temperature resolution of the experiment, showing an underestimation of reactivity of the mixture by the model. The onset of conversion is less discernible in the fuel profile, since only a minor amount of CH_4 is consumed at this temperature. A reaction path analysis of the model was performed at 723 K, as most intermediates reach detectable quantities at this temperature. The reaction path analysis shows that fuel conversion is mostly initiated by hydrogen abstraction involving OH, while abstraction by NO_2 to form the nitrous acid isomers plays a less pronounced, but still significant role:

$$CH_4 + OH = CH_3 + H_2O \quad (R1)$$

$$CH_4 + NO_2 = CH_3 + HONO \quad (R2)$$

$$CH_4 + NO_2 = CH_3 + HNO_2 \quad (R3)$$

Since HONO and HNO_2 decompose to form OH [7] they take part in the initiation of fuel decomposition reactions. OH drives chain branching and, thus, the presence of NO_x may play a significant role in ignition, e.g., in EGR processes [2,34]. At lower temperatures, prior to major fuel conversion, (R2) and (R3) dominate, also hinting at their role in ignition and initiation of combustion. For high temperatures, (R1) becomes even more dominant, also a significant fraction of fuel is converted by reacting with atomic H to form hydrogen and methyl. Furthermore, (R2) and (R3) show the role of NO_2 as the most important precursor to nitrous acid formation [9].

The progression of the O_2 profile is not well reproduced by the mechanism for low temperatures, while still yielding a reasonably good result. The discrepancy can be attributed to the low mass resolution of the instrument, the very high NO concentration in the mixture, and the resulting very broad NO peak, at *m/z* 30, in the mass spectrum. The wide NO peak influences mass channels up to and beyond *m/z* 32 and hence influences the background subtraction, which may contribute to the error of the profile. Since little fuel conversion takes place below 773 K the oxygen is consumed by reacting with NO to form NO_2 at low temperatures Fig. 1 shows that the NO_2 concentration is highest at the lowest temperature and declines for rising temperatures. At higher temperatures the reaction of NO with HO_2 dominates, releasing OH:

$$NO + HO_2 = NO_2 + OH \quad (R4)$$

The decline of NO_2 tracks the increase in the NO concentration for increasing temperature and at higher temperatures NO_2 is mostly converted to NO by reacting with H, CH_3 and HNO:

$$NO_2 + H = NO + OH \quad (R5)$$

$$NO_2 + CH_3 = NO + CH_3O \quad (R6)$$

$$NO_2 + HNO = NO + HONO \quad (R7)$$

Similar observations for R5 were made by Zhang et al. in the low-temperature conversion of NO doped dimethyl ether and dimethoxymethane [17]. The discrepancies in both NO to NO_2 conversion influence the concentration of products formed mainly from NO_2 (i.e. HONO and CH_3NO_2), which may cause discrepancies between the model and the experiment regarding formation of those products and cause the shift in the reaction start temperature. The NO concentration in the investigated conditions is substantially higher than under most investigated combustion conditions and available validation data [2,5,17,20,21,32], which may explain the different behavior of the experiment with respect to the modelled prediction.

The onset of product formation in the experimental data is more gradual than in the prediction, where a steep increase in concentration of products is visible. The model under-predicts the maximum CO concentration while over-predicting the CO_2 concentration with a large overshoot at 823 K. The modelled water concentration is mostly within the error bounds of the quantification, progressions match perfectly, and product species are generally in good agreement with the experiment. The concentration of H_2 is severely under-predicted, which may also be an artifact of the element balancing procedure. The decline of the oxygen concentration takes place much more gradually than predicted by the mechanism.

3.1.2. Comparison of the NO doped lean and rich low-temperature regimes (RC1 and RC2)

In the comparison of lean and rich combustion regimes (Fig. 2) doped with 1000 ppm NO a similar picture, as described above, emerges regarding the reaction start temperature. Fuel decomposition is similar in lean and rich regimes and follows the kinetics elaborated for reaction condition RC3 (vide supra). Comparable to RC3, the reaction commences at 723 K, about 50 K lower than the model predicted reaction start temperature for both conditions, observable in the first increase in the product concentrations of CO and CO_2, as well as water. The higher modelled reaction start temperature indicates an underestimation of the reactivity of the investigated, highly NO enriched, conditions. The measured fuel profiles are in excellent agreement with the simulation, and the O_2 profiles are in good agreement. Sensitization of reactions due to NO addition has been observed for CH_4 [5,6] and is unsurprising in this regard. The known sensitizing effect of NO on the reactions may not be well captured for most species by the model for the comparatively high NO concentrations in the investigated conditions, which may lead to an exaggeration of the sensitization.

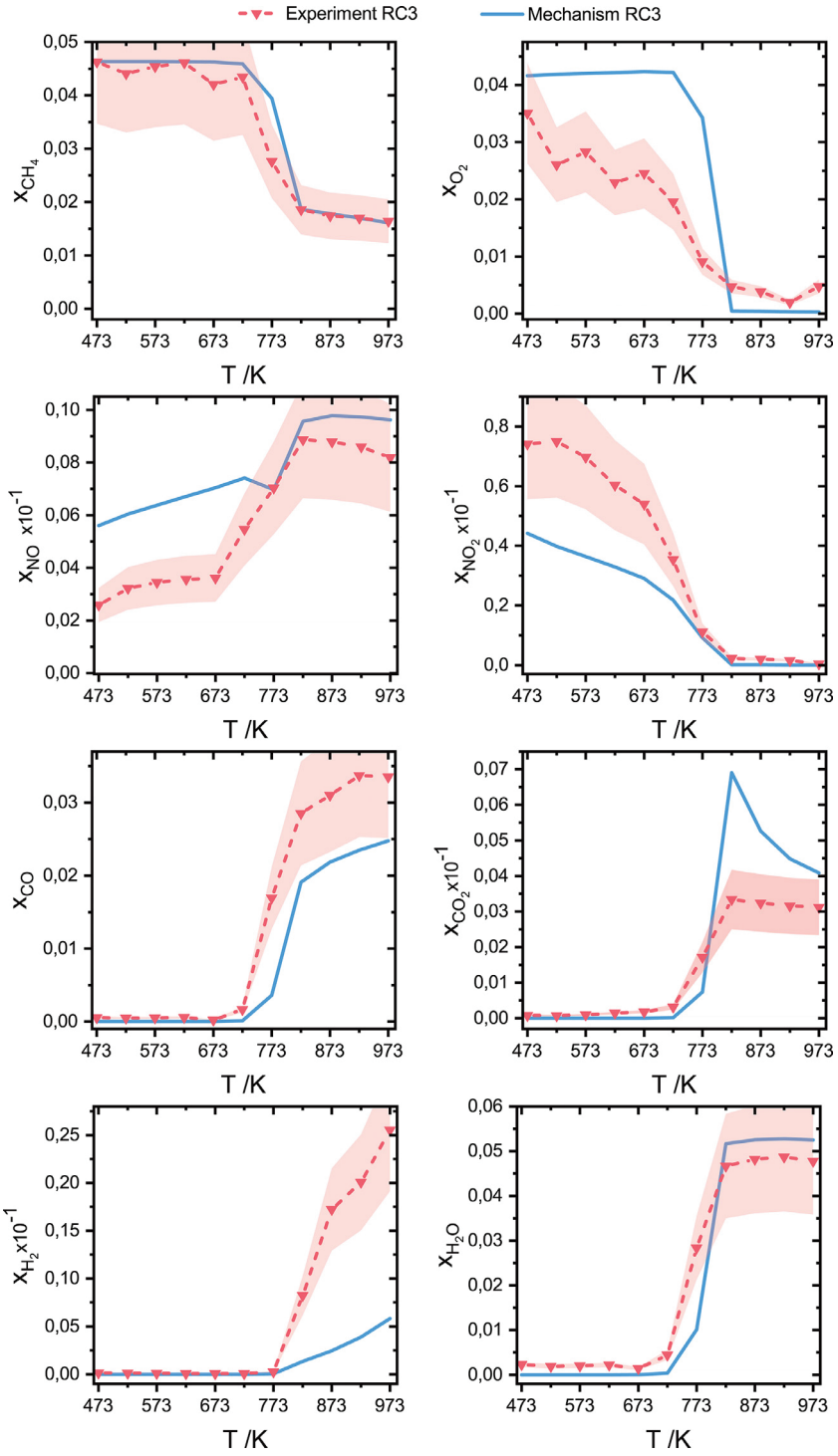

Fig. 1. Main species mole fraction profiles at an equivalence ratio of $\varphi = 2.1$, with addition of 1% NO with respect to total flow of 280 sccm at an argon dilution of 90% (RC3) and comparison to the modified mechanism [4,7], an estimated error of 25% is indicated in the plots.

Some observations are possible regarding the comparison of the lean and rich regimes, especially with respect to the nitrogen chemistry initiated by the NO dopant. The conversion of NO to NO_2 by reacting with O_2 shows differing concentrations in the presence of a higher O_2 partial pressure in the lean condition, indicating an equilibrium. In both instances, the calculated NO and NO_2 profiles show some deviation from the experiment, however, they predict the similarity of conversion for those species well. In the case of NO_2 the mechanism also reproduces the fact, that NO_2 is fully consumed at higher temperatures in the fuel-rich condition, while still being present in the lean condition in the presence of oxygen at those temperatures. Consumption of NO_2 in the rich condition is caused by the reaction with H according to (R5), while the lack of atomic H in the lean condition leads to the higher concentration of NO_2. Conversion of NO to NO_2 at low temperatures is underestimated, consistent with the observation of the $\Phi = 2.1$ condition (RC3) (vide supra). Some of the deviation in the NO_2 profiles arises from convoluted dimethyl ether that is being produced around 723 K, which was not separable from the NO_2 signal. Unsurprisingly, in the highly oxidizing environment of the lean

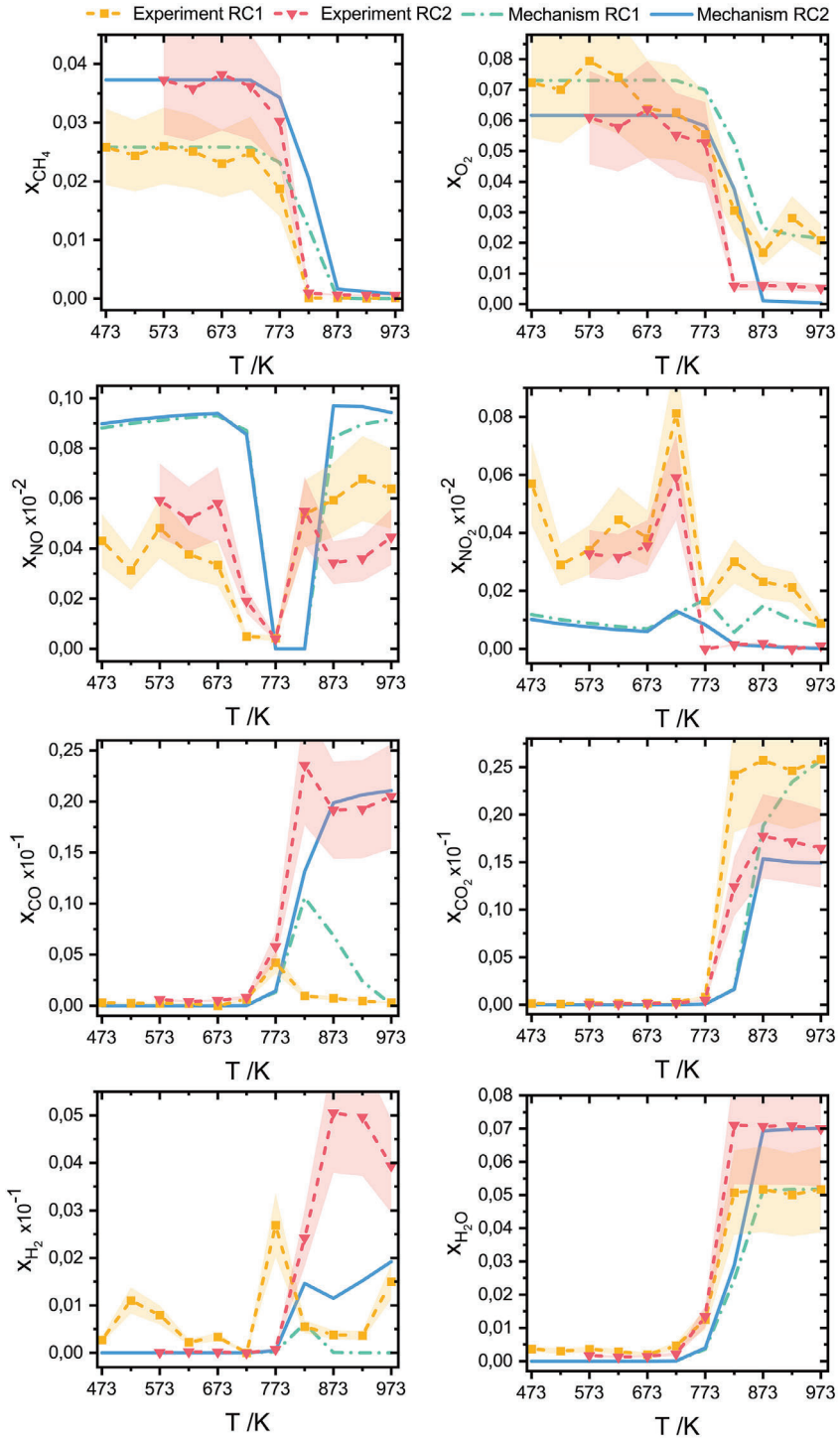

Fig. 2. Main species mole fraction profiles at an equivalence ratio of $\varphi = 0.7$ (RC1) and $\varphi = 1.2$ (RC2), with addition of 1000 ppm NO with respect to total flow of 280 sccm at an argon dilution of 90% and comparison to the modified mechanism [4,7], an estimated error of 25% is indicated in the plots.

condition, H_2 and CO are only present in minor amounts, at intermediate temperatures and are fully converted to water and CO_2 respectively, at higher temperatures.

3.2. Intermediates

3.2.1. Identification and quantification of nitrogenous species

The main advantage of PEPICO detection is the ability to distinguish species by their mass selective photoelectron spectra (ms-TPES) in addition to the energy selective identification based on photo ion (PI) spectra. The procedure used here to acquire the photon energy scans is given in [26]. Photon energy scans were performed at a temperature of 723 K for the conditions at equivalence ratios of 0.7 (RC1) and 2.1 (RC3). No energy scan was performed at the 1.2 equivalence ratio (RC2), since it is unlikely that this intermediate condition would yield different species in the respective mass channels. Photon energy scans were performed between energies of 10.6 eV and 12.2 eV in RC3 and 10.6 to 11.8 eV in RC1. The energy scan at an equivalence ratio of 2.1 (RC3) had a scan resolution of 30 meV and a long averaging time of 900 s. These long

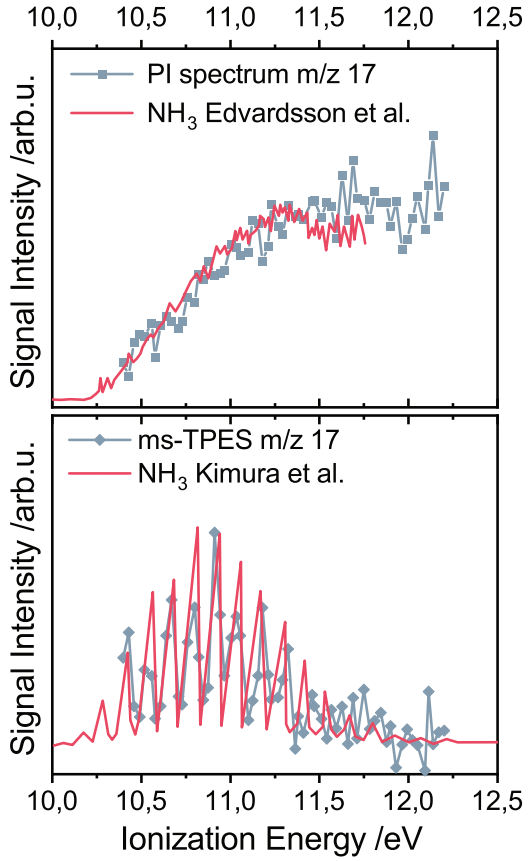

Fig. 3. PI spectrum of *m/z* 17 measured in RC3 at a temperature of 723 K compared to a literature spectrum of NH_3 published by Edvardsson et al. [35] (top panel) and ms-TPES of *m/z* 17 in comparison to a literature photoelectron spectrum of NH_3 [36] (bottom panel).

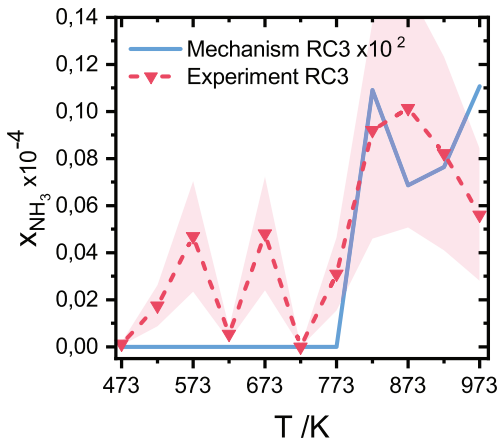

Fig. 4. Mole fraction profile of NH_3 (scaled by a factor of 100) measured at an equivalence ratio of 2.1 and 1% NO addition (RC3) and comparison to the model prediction by the modified mechanism [4,7], showing a discrepancy of two orders of magnitude, error areas indicate an estimated error of 50%.

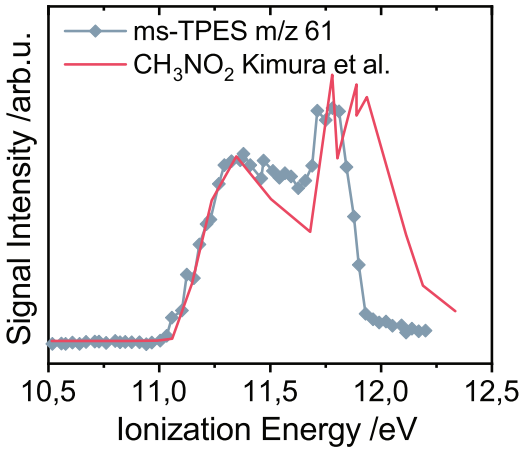

Fig. 5. ms-TPES of *m/z* 61 measured in RC3 at a temperature of 723 K in comparison to a literature photoelectron spectrum of nitromethane (CH_3NO_2) [36].

averaging times for every photon energy allowed for identification and assignment of trace intermediates. The scan at $\Phi = 0.7$ (RC1) was performed at the same resolution, but with a shorter averaging time of 600 s.

The photon energy range of the scans is suitable for the identification of nitromethane (CH_3NO_2), and *trans*-HONO. Surprisingly, a substantial amount of ammonia (NH_3) is present for temperatures above 823 K. A weaker signal is also present at 723 K, which is sufficient for species identification thanks to the long averaging time of the photon energy scan. That signal makes an identification by comparison of the PI spectrum to a literature spectrum [35] and the ms-TPES to a literature photoelectron spectrum [36] possible, albeit at a relatively low signal-to-noise ratio. It has to be noted that, the signal in the *m/z* 17 channel cannot stem from OH radicals, since transient species are destroyed in the first expansion stage of the reactor sampling interface [26] and no OH^+ water fragment due to dissociative photoionization is produced at the energies used in the photon energy scan Fig. 3 shows the ms-TPES and the PI spectrum of the signal acquired at *m/z* 17. The ms-TPES shows the distinctive vibronic transition pattern of ammonia and a clear vertical transition at 10.85 eV [36]. While the slope and progression of the PI spectrum is in good agreement with the literature spectrum [35], the scan was not performed all the way down to the adiabatic ionization energy of the compound. Despite this limitation the data is clear proof of detectable amounts of ammonia being present in the sample stream.

In comparison to the modeled prediction, the measured mole fraction of NH_3 is significantly higher by two orders of magnitude, as shown in Fig. 4. NH_3 was quantified by a measured photoionization cross section, so an estimated error of about 50% can be expected, suggesting a substantial under-prediction of ammonia production in those conditions. The relatively low signal to noise ratio at lower temperatures can be attributed to a high signal background and the required background subtraction procedure during signal integration. No signal at *m/z* 17 was present in RC1, but a signal was acquired for RC2, yielding a less pronounced profile, which can be found in the SI. The concentration of NH_3 can be considered to have significant influence on interactions involving NO, and NH_x/NO interactions are known to lead to inhibition of NO formation [37]. Reaction flow analysis shows that, furthermore, NH_3 is involved in the production of HONO by reacting with NO_2 [38], is formed by H abstraction from the fuel by amino radicals and thus involved in fuel decomposition to form CH_3. It also acts as an OH scavenger to form water and cycle NH_2.

The predominant nitrogen-containing hydrocarbon species detected in the investigated reaction condition is nitromethane (CH_3NO_2). Formation of CH_3NO_2 is expected in the high-pressure oxidation of CH_4 in the presence of NO [6] Fig. 5 shows the measured ms-TPES in comparison to a literature photoelectron spectrum [36].

Despite the envelope not matching well for transitions occurring at higher photon energy, the slopes after the initial onset of ionization and the vertical transition at 11.28 eV [36] are in excellent agreement, allowing for a clear identification and

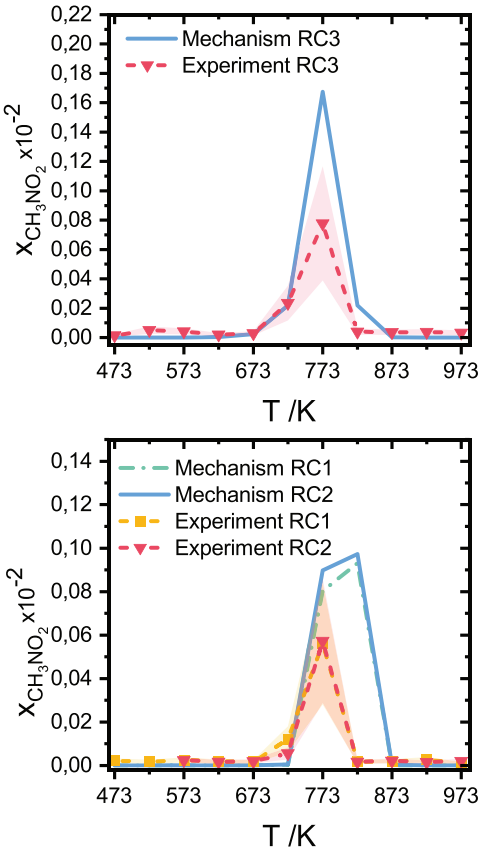

Fig. 6. Mole fraction profiles of CH_3NO_2 measured in RC3 (top panel) and in RC1 and RC2 (bottom panel) and comparison to the model prediction by the modified mechanism [4,7], error areas indicate an estimated error of 50%.

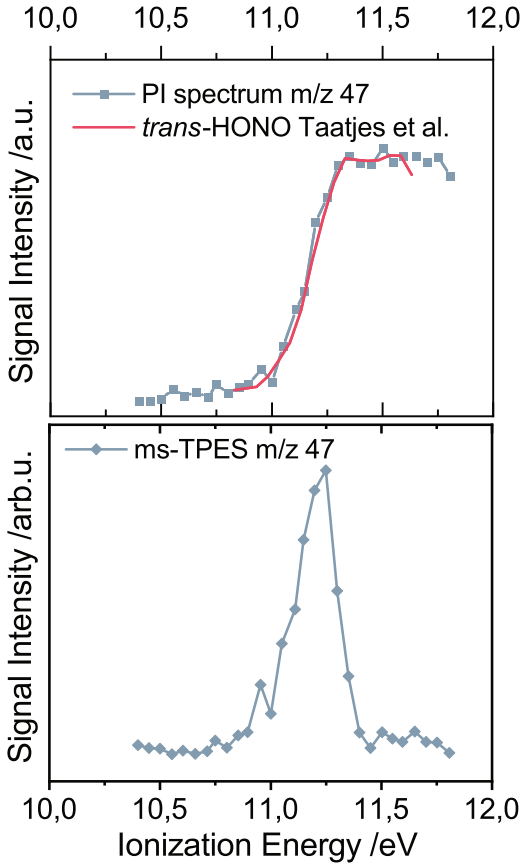

Fig. 7. PI spectrum of *m/z* 47 measured in RC1 at a temperature of 723 K compared to a literature spectrum of distinctly *trans*-HONO published by Taatjes et al. [15] (top panel) and the ms-TPES of *m/z* 17 showing a steep decline above the threshold for dissociative photoionization of this compound.

assignment of nitromethane for the compound at *m/z* 61 Fig. 6 shows the nitromethane mole fraction profiles for all reaction conditions. No substantial difference can be seen in the profile progressions in all conditions and the concentration peaks at 773 K. For RC3 the temperature at peak CH_3NO_2 concentration is in good agreement with the mechanism. The higher maximum CH_3NO_2 concentration in the $\Phi = 2.1$ condition (RC3) (top panel), can be attributed to the higher NO concentration and the resulting higher concentration of NO_2 in the presence of higher CH_4 concentration, the predominant precursors of nitromethane. In RC1 and RC2, however, the mechanism predicts a broader temperature range for the formation of peak CH_3NO_2 concentrations. The most dominant reaction to produce CH_3NO_2 is:

$$CH_3 + NO_2 + (M) = CH_3NO_2 + (M) \quad (R8)$$

Reaction (R8) has a substantial forward rate [38,39] and interaction of nitromethane with nitrous acid chemistry takes place by direct production of HONO through hydrogen abstraction by NO_2 from nitromethane:

$$CH_3NO_2 + NO_2 = CH_2NO_2 + HONO \quad (R9)$$

Nitrous acid is also involved in nitromethane kinetics by hydrogen abstraction from the fuel to form HONO and HNO_2 and the simultaneous release of CH_3 radicals according to (R2) and (R3), which are scavenged by NO_2 to produce nitromethane by reaction (R8). The analysis shows the intricate interaction of the nitrogen-containing compounds and NO_x species with each other and with fuel decomposition and ignition chemistry under NO enriched conditions.

4. Isomer-selective detection and quantification of the nitrous acid intermediate and arising challenges for photoionization methods

The selective identification by photoionization methods of the HONO isomers, expected to be produced during combustion, poses significant challenges. Of the three isomers *trans*-HONO, *cis*-HONO and HNO_2 only *trans*-HONO and HNO_2 produce a stable ion upon ionization, while *cis*-HONO dissociates with a threshold of only 40 meV above its adiabatic ionization energy of 11.22 eV to form NO^+ and OH [22]. The top panel of Fig. 7 shows *trans*-HONO identified using a literature PI spectrum reported by Taatjes et al. [15] measured in a NO_2 doped hydrogen flame. The spectrum from the lean combustion condition at $\Phi = 0.7$ (RC1) is in agreement with the spectra taken in the $\Phi = 2.1$ condition (RC3) reported in [22]. Assignment by means of the ms-TPES shown in the bottom panel of Fig. 7 is possible but problematic (i.e. a direct comparison to the calculated Franck-Condon envelope is futile) [22]. Comparability is impaired by the diminishing transition intensity for higher photon energies, caused by dissociative photoionization, 350 meV above the adiabatic ionization threshold of *trans*-HONO. This phenomenon limits the applicability of harmonically approximated Franck-Condon factors for comparison. The behavior is visible in the steep decline in the photoelectron spectrum starting at 11.25 eV. The ionization properties leading to the ionization efficiency of this compound are elaborated in great detail in [22]. No sign of *cis*-HONO appears in the photoelectron spectrum, but strong evidence of *cis*-HONO can be found in the NO^+ fragment ms-TPES signal as reported in [22].

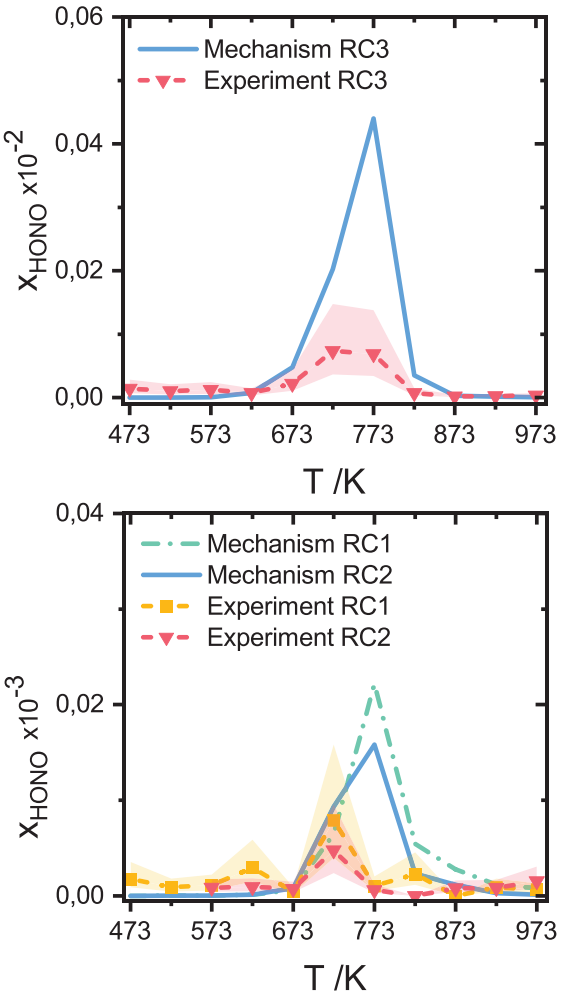

Fig. 8. Mole fraction profiles of unambiguously *trans*-HONO measured in RC3 (top panel) and in RC1 and RC2 (bottom panel) and comparison to the lumped model prediction by the modified mechanism [4,7] considering both *trans*-HONO and *cis*-HONO, and an indicated error of factor 2.

Hence, Fig. 8 unambiguously shows the mole fraction profiles of solely *trans*-HONO in the investigated reaction conditions, while dissociative photoionization prevents the detection of the *cis*-HONO isomer in the temperature ramping measurement. Most HONO at the concentration peak is produced by hydrogen abstraction from formaldehyde (CH_2O) and HNO by NO_2, while HNO_2 is produced mostly by abstraction from CH_2O only:

$$NO_2 + CH_2O = HNO_2 + CHO \qquad (R10)$$

CH_2O was present in substantial concentration. Separation from the NO signal at *m/z* 30 was possible thanks to the advantages of photoionization mass spectrometry and the mole fraction profiles can be found in the SI.

The very low threshold to dissociative photoionization of *cis*-HONO illustrates the problem encountered in the detection of HONO by photoionization molecular beam methods. Isomer branching fractions predict that *trans*-HONO is produced at a rate one order of magnitude lower than *cis*-HONO [10], which may impede the detection of HONO, since, consequently, only about 10% of the total HONO concentration can be detected. The discrepancy between the measured HONO concentration and the modeled one, shown in Fig. 8 supports this notion further. Since HONO is modelled in a lumped fashion the simulated profile represents the sum of both HONO isomers. Another observation pointing in this direction was made by Lucassen et al., who detected a signal at *m/z* 47, which they assigned to HONO in EI-MBMS measurements of morpholine flames, while no such signal was detected using PI-MBMS in the same flame conditions [18].

The question if *cis*- and *trans*-HONO can be considered as the same species (and be lumped) or if they should be modelled as distinct species remains open. In a multi-well unimolecular decomposition, intermediates with different energies have to be considered. If these intermediates must be treated as distinct species depends on the transition state energy (i.e. the energy barrier between the reaction wells), and the thermal energy of the reactants. Chen et al., based on their preliminary results from quantum chemistry computations, state that the HONO isomers exist in a unified energetic state between temperatures of 650 K and 800 K at pressures between 0.01 bar and 100 bar, which renders them indistinguishable [7]. Below these temperatures, the two rotamers are distinct, but the reaction rate for their interconversion is large, causing them to equilibrate rapidly [7]. The reaction conditions investigated here are in the range of these temperatures and pressures and could have been suitable to explore the temperature limits stated by Chen et al. if the determination of an isomer ratio of *cis*-HONO to *trans*-HONO was possible. Given the inability of photoionization in general and, hence, the reported measurements to detect *cis*-HONO, the data remain inconclusive to this point. It is still instructive to compare the experimental measurement of *trans*-HONO to the simulation of the lumped species in Fig. 8. For RC3, the predicted mole fractions are approximately a factor of ten higher than the measured values. For RC1 and RC2, the differences are closer to a factor of 2. The uncertainty of the measured values is approximately a factor of 2–4, indicated in Fig. 8. With the assumed error bounds of quantification [30], no conclusion that the mechanism substantially over or under predicts the concentration of HONO is admissible. Chen et al. give a rate for trans-*cis* interconversion of $2 \times 10^9\ s^{-1}$ leading to a short lifetime of 0.5×10^{-10} s for *cis*-HONO [7]. The residence time in the reactor is on the order of seconds (ca. 1.5 s) and, thus, should be sufficient for a rapid isomerization of *cis*-HONO to the more stable *trans*-HONO isomer. This process may yield a thermal equilibrium between the HONO isomers, while the overall reaction is sampled from the reactor in non-equilibrium.

If thermal equilibration plays a role, it will tilt the balance from the more rapidly produced *cis*-HONO towards the more stable *trans*-HONO [40], which also happens to be the only detectable isomer [22]. Therefore, the measured mole fraction should move closer to the modeled one. If any of the *cis*-HONO produced in the process remains upon sampling (which was demonstrated by Hoener et al. [22]), then that fraction of *cis*-HONO cannot be directly detected with photoionization mass spectrometry, due to dissociative photoionization. Thus, comparability of experiment and model is impaired, and the lack of isomer resolution has to be taken into account in the comparative analysis of photoionization measurement and model.

Fuller et al. conclude, that lumped modeling of HONO is acceptable in terms of model accuracy and with respect to the influence of HONO isomers on the subsequent reaction network [9]. We, in contrast, conclude that, for the sake of comparability to measurements, isomer specific modeling of HONO would be immensely beneficial. Such a model would have to include reactions for the formation, interconversion and, subsequently, destruction of both HONO isomers individually. A detailed model of the isomer chemistry would allow a glimpse at the isomeric concentrations in the process and could be directly compared to the distinct *trans*-HONO concentration obtained with photoionization mass spectrometry.

The CRF-PEPICO measurements and their comparison to the model demonstrate, that the interplay of *cis*- and *trans*-HONO formation, destruction, and isomerization is complex, and requires

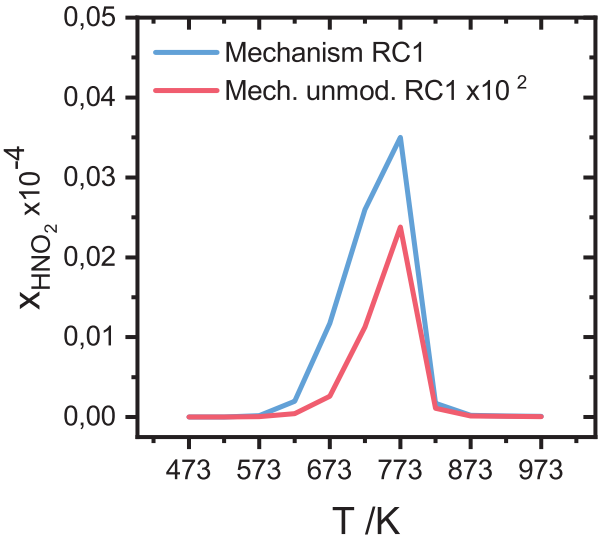

Fig. 9. Simulated mole fraction profiles from the modified [4,7] and the unmodified [4] mechanism showing a difference of about two orders of magnitude in concentration of HNO_2.

more experimental and theoretical work to be fully understood. This conclusion is further enforced by the observation that the temperature dependence of the *trans*-HONO mole fraction profile is captured better for RC3 than for RC1 and RC2, where most HONO is produced at a single temperature (i.e. 723 K). The measured profiles in RC1 and RC2 contrast the wider temperature range for HONO production predicted by the model.

The third isomer of nitrous acid also poses challenges regarding detection and model comparability. As shown in Fig. 9, the multi-step mechanism by Glarborg et al. [4] modified with the reaction rates for HONO and HNO_2 decomposition and isomerization reported by Chen et al. [7] predicts a pronounced shift of the reaction to lower temperatures for HNO_2. The HNO_2 concentration is about two orders of magnitude higher in the modified than in the unmodified mechanism, albeit still an order of magnitude lower than the theoretically predicted isomer branching ratio for nitrous acid production suggested by Chai & Goldsmith [10].

This can in part be attributed to how the rate of progress of the reaction of HNO_2 with OH to form NO_2 and water is influenced by the different decomposition kinetics of HNO_2 suggested by Chen et al.:

$$HNO_2 + OH = NO_2 + H_2O \quad (R11)$$

The rate of progress of this reaction increases by an order of magnitude with the reaction rates for HONO decomposition proposed by Chen et al. [7] Fig. 10 compares the relative flow of reactions for (lumped) HONO and HNO_2 decomposition for the unmodified (left) and modified (right) mechanism. Substantial differences are visible in both the reaction paths and the relative reaction flows. The unmodified mechanism lacks the pathway for direct decomposition of HNO_2 to form NO and OH (blue arrow in Fig. 10) suggested by Chen et al. [7]:

$$HNO_2 = NO + OH \quad (R12)$$

Decomposition in the unmodified mechanism progresses via isomerization of HNO_2 to HONO which subsequently decomposes forming NO and OH:

$$HNO_2 + (M) = HONO + (M) \quad (R13)$$

$$HONO + (M) = NO + OH + (M) \quad (R14)$$

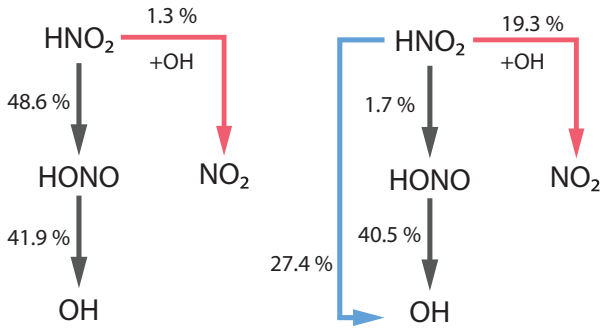

Fig. 10. Relative rates of production with respect to nitrogen flux for the nitrous acid isomer pathways of decomposition and destruction, considering the most significant reactions (R11), (R12), (R13) and (R14) for the unmodified model (left) and the modified model (right); the modification of the mechanism adds a new pathway for decomposition of HNO_2 to form OH and NO (blue) and the pathway involving the reaction of HNO_2 with OH (red) is greatly enhanced by the added kinetics.

The modified kinetics include the new pathway for unimolecular decomposition of HNO_2 (R12), while the reaction rate for isomerization, according to (R13), is greatly reduced [7,32]. The direct decomposition pathway shown as the blue arrow in Fig. 10 bypasses the isomerization reaction. The red arrow in Fig. 10 shows the pathway with the pronounced difference in the rate of production of (R11), which has become substantial. This may be caused by the higher OH concentration due to HNO_2 unimolecular decomposition according to (R12) [7] and also causes a more pronounced cycling of NO_2, that acts as a precursor for HONO and HNO_2 formation.

The detection threshold of the CRF-PEPICO can be qualitatively and quantitatively illustrated by the detection of NH_3 in the photon energy scan at extremely low concentrations (cf Fig. 3 and Fig. 4). The concentration of NH_3 at 723 K (i.e. the temperature at which the photon energy scan was performed) are on the order of those predicted for HNO_2 by the modified mechanism (i.e.$<< 10^{-6}$ mole fraction). Despite the high observed sensitivity and low detection threshold of the instrument, the sufficiently large expected production of HNO_2, and its favorable decomposition kinetics and thermal stability compared to *trans*-HONO, no HNO_2 was detected in our measurements [22].

While reactions of NO_2 with fuel and hydrogen in the mechanism originate from recent theoretical work [10], reaction (R10) has not been revised recently [41]. An overestimation of HNO_2 production according to (R10) may explain the higher than observed HNO_2 concentration in the model prediction, and further investigation should be aimed at this reaction.

5. Conclusions

In this work we present quantitative and isomer selective data for NO_x hydrocarbon interaction across lean and rich regimes in the partial oxidation of CH_4. The data can contribute to the understanding of fuel and equivalence ratio specific interaction of NO_x and hydrocarbons and serve as validation data for combustion mechanisms. Data regarding the HONO intermediate is still limited and only few successful studies have been reported so far. The high concentration of HONO at the sampling interface shows the relatively high stability of this intermediate. It is conceivable that HONO may be emitted by combustion processes to interact in atmospheric chemistry, and release OH to influence ignition when exhaust gasses are recirculated.

Measurements were compared to a modified mechanism implementing recently published decomposition kinetics for HNO_2 and HONO, that predicts substantial differences in HNO_2 concentrations in the investigated reaction conditions compared to the

unmodified model. The major nitrogen containing intermediate CH_3NO_2 was identified and quantified from the measurement. Surprisingly, relatively high concentrations of NH_3 were found contrasting the model and demonstrating the high sensitivity and selectivity of PEPICO spectroscopy.

While the *trans*-HONO combustion intermediate was detected in substantial quantity, *cis*-HONO remains undetectable, due to dissociative photoionization close to the adiabatic ionization energy of this compound. This observation leads to the conclusion that the comparability of experiment and model could be greatly enhanced if isomer specific kinetics of HONO would be included in future models. HNO_2 remains undetectable, despite the demonstrated ability of the CRF-PEPICO to detect concentrations of constituents at or below the model predicted concentration of HNO_2. This conjunction of circumstances gives rise to the conclusion that isomer selective quantification and detection of all nitrous acid isomers and, thus, the experimental determination of isomer branching fractions will remain infeasible by means of photoionization methods and motivate the development of alternative detection methods.

Supporting information

si_mole_fraction_profiles.xls si_mechanism_modification.docx

Declaration of Competing Interest

The authors declare that they have no known competing financial interests or personal relationships that could have appeared to influence the work reported in this paper.

Acknowledgments

The CRF-PEPICO experiments were carried out at the VUV beamline of the Swiss Light Source at the Paul Scherrer Institute with the support of P. Hemberger and A. Bödi. The authors thank the Deutsche Forschungsgemeinschaft (DFG) for financial support under contract KA3871/3-2. We thank J.-M. Wenning for his support in preparing the plots used in this work.

Supplementary materials

Supplementary material associated with this article can be found, in the online version, at doi:10.1016/j.combustflame.2022.112096.

References

[1] D.A. Knyazkov, A.G. Shmakov, I.V. Dyakov, O.P. Korobeinichev, J. De Ruyck, A.A. Konnov, 2009 Proc. Combust. Inst., 32 327–334.
[2] L. Marrodán, Y. Song, O. Herbinet, M.U. Alzueta, C. Fittschen, Y. Ju, F. Battin-Leclerc, 2019 Chem. Phys. Lett., 719 22–26.
[3] A.M. Ickes, S.V. Bohac, D.N. Assanis, 2009 Energy and Fuels, 23 4943–4948.
[4] P. Glarborg, J.A. Miller, B. Ruscic, S.J. Klippenstein, 2018 Prog. Energy Combust. Sci., 67 31–68.
[5] Y. Song, L. Marrodán, N. Vin, O. Herbinet, E. Assaf, C. Fittschen, A. Stagni, T. Faravelli, M.U. Alzueta, F. Battin-Leclerc, 2019 Proc. Combust. Inst., 37 667–675.
[6] C.L. Rasmussen, A.E. Rasmussen, P. Glarborg, 2008 Combust. Flame, 154 529–545.
[7] X. Chen, M.E. Fuller, F.C. Goldsmith, 2019 React. Chem. Eng., 4 323–333.
[8] R. Asatryan, J.W. Bozelli, J.M. Simmie, 2007 Int. J. Chem. Kinet., 39 378–398.
[9] M.E. Fuller, C.F. Goldsmith, 2019 Proc. Combust. Inst., 37 695–702.
[10] J. Chai, C.F. Goldsmith, 2017 Proc. Combust. Inst., 36 617–626.
[11] A.M. Mebel, M.C. Lin, C.F. Melius, 1998 J. Phys. Chem. A, 102 1803–1807.
[12] F. Richter, M. Hochlaf, P. Rosmus, F. Gatti, H.D. Meyer, 2004 J. Chem. Phys., 120 1306–1317.
[13] A. Ingenito, 2016 Aerosp. Sci. Technol., 59 189–198.
[14] R. Matsuzaki, 1987 Jpn. J. Appl. Phys., 26 1844–1849.
[15] C.A. Taatjes, D.L. Osborn, T.A. Cool, K. Nakajima, 2004 Chem. Phys. Lett., 394 19–24.
[16] J.J. Weng, Z.Y. Tian, K.W. Zhang, L.L. Ye, Y.X. Liu, L.N. Wu, D. Yu, J.Z. Yang, C.C. Cao, J.B. Zou, 2019 Combust. Flame, 203 247–254.
[17] H. Zhang, S. Schmitt, L. Ruwe, K. Kohse-Höinghaus, 2021 Combust. Flame, 224 94–107.
[18] A. Lucassen, P. Oßwald, U. Struckmeier, K. Kohse-Höinghaus, T. Kasper, N. Hansen, T.A. Cool, P.R. Westmoreland, 2009 Proc. Combust. Inst., 32 I 1269–1276.
[19] C. Jain, P. Morajkar, C. Schoemaecker, B. Viskolcz, C. Fittschen, 2011 J. Phys. Chem. A, 115 10720–10728.
[20] W. Yuan, L. Ruwe, S. Schwarz, C. Cao, J. Yang, O. Deutschmann, K. Kohse-Höinghaus, F. Qi, 2021 Proc. Combust. Inst., 38 795–803.
[21] S. Gossler, L. Ruwe, W. Yuan, J. Yang, X. Chen, S. Schmitt, L. Maier, K. Kohse-Höinghaus, F. Qi, O. Deutschmann, 2021.
[22] M. Hoener, A. Bodi, P. Hemberger, T. Endres, T. Kasper, 2021 Phys. Chem. Chem. Phys., 23 1265–1272.
[23] L.A. Curtiss, P.C. Redfern, K. Raghavachari, 2007.
[24] B. Sztáray, K. Voronova, K.G. Torma, K.J. Covert, A. Bodi, P. Hemberger, T. Gerber, D.L. Osborn, 2017.
[25] M. Johnson, A. Bodi, L. Schulz, T. Gerber, 2009 Nucl. Instrum. Methods Phys. Res. Sect. A, 610 597–603.
[26] M. Hoener, D. Kaczmarek, T. Bierkandt, A. Bodi, P. Hemberger, T. Kasper, 2020.
[27] A. Bodi, P. Hemberger, T. Gerber, B. Sztáray, 2012.
[28] P. Oßwald, P. Hemberger, T. Bierkandt, E. Akyildiz, M. Köhler, A. Bodi, T. Gerber, T. Kasper, 2014.
[29] D. Kaczmarek, B. Atakan, T. Kasper, 2019 Combust. Flame, 205 345–357.
[30] T. Kasper, P. Oßwald, U. Struckmeier, K. Kohse-Höinghaus, C.A. Taatjes, J. Wang, T.A. Cool, M.E. Law, A. Morel, P.R. Westmoreland, 2009 Combust. Flame, 156 1181–1201.
[31] Ansys Inc., (2019).
[32] C.L. Rasmussen, J. Hansen, M. Paul, P. Glarborg, 2008 Int. J. Chem. Kinet., 40 454–480.
[33] Y. Zhang, O. Mathieu, E.L. Petersen, G. Bourque, H.J. Curran, 2017 Combust. Flame, 182 122–141.
[34] D.A. Knyazkov, A.G. Shmakov, I.V. Dyakov, O.P. Korobeinichev, J. De Ruyck, A.A. Konnov, 2009 Proc. Combust. Inst., 32 I 327–334.
[35] D. Edvardsson, P. Baltzer, L. Karlsson, B. Wannberg, D.M.P. Holland, D.A. Shaw, E.E. Rennie, 1999 J. Phys. B At. Mol. Opt. Phys., 32 2583–2609.
[36] K. Kimura, S. Katsumata, Y. Achiba, T. Yamazaki, S. Iwata, Handbook of HeI Photoelectron Spectra of Fundamental Organic Compounds, 1981.
[37] O.A. Powell, P. Papas, C.B. Dreyer, 2011 Proc. Combust. Inst., 33 1053–1062.
[38] R. Sivaramakrishnan, K. Brezinsky, G. Dayma, P. Dagaut, 2007 Phys. Chem. Chem. Phys., 9 4230–4244.
[39] P. Glarborg, A.B. Bendtsen, J.A. Miller, 1999 Int. J. Chem. Kinet., 31 591–602.
[40] Y. Guo, D.L. Thompson, 2003 J. Chem. Phys., 118 1673–1678.
[41] Z.F. Xu, M.C. Lin, 2003 Int. J. Chem. Kinet., 35 184–190.

Experimental flat flame study of monoterpenes: Insights into the combustion kinetics of α-pinene, β-pinene, and myrcene

Bierkandt, T., Hoener, M., Gaiser, N., Hansen, N., Köhler, M., Kasper, T.
Proceedings of the Combustion Institute, 2021, 38(2), pp. 2431–2440
DOI: 10.1016/j.proci.2020.06.204

My contribution to this work was support in the measurement of data, co-authoring of the manuscript.

Available online at www.sciencedirect.com

ScienceDirect

Proceedings of the Combustion Institute 38 (2021) 2431–2440

Proceedings of the Combustion Institute

www.elsevier.com/locate/proci

Experimental flat flame study of monoterpenes: Insights into the combustion kinetics of α-pinene, β-pinene, and myrcene

Thomas Bierkandt [a,*], Martin Hoener [b], Nina Gaiser [a], Nils Hansen [c], Markus Köhler [a], Tina Kasper [b]

[a] *Institute of Combustion Technology, German Aerospace Center (DLR), Pfaffenwaldring 38-40, 70569 Stuttgart, Germany*
[b] *Mass Spectrometry in Reactive Flows, IVG, University of Duisburg-Essen, 47057 Duisburg, Germany*
[c] *Combustion Research Facility, Sandia National Laboratories, Livermore, CA 94550, USA*

Received 7 November 2019; accepted 7 June 2020
Available online 23 August 2020

Abstract

Pinenes and pinene dimers have similar energy densities to petroleum-based fuels and are regarded as alternative fuels. The pyrolysis of the pinenes is well studied, but information on their combustion kinetics is limited. Three stoichiometric, flat premixed flames of the $C_{10}H_{16}$ monoterpenes α-pinene, β-pinene, and myrcene were investigated by synchrotron-based photoionization molecular-beam mass spectrometry (PI-MBMS) at the Advanced Light Source (ALS). This technique allows isomer-resolved identification and quantification of the flame species formed during the combustion process. Flame-sampling molecular-beam mass spectrometry even enables the detection of very reactive radical species. Myrcene was chosen because of its known formation during β-pinene pyrolysis. The quantitative speciation data and the discussed decomposition steps of the fuels provide important information for the development of future chemical kinetic reaction mechanisms concerning pinene combustion. The main decomposition of myrcene starts with the unimolecular cleavage of the carbon-carbon single bond between the two allylic carbon atoms. Further decompositions by β-scission to stable combustion intermediates such as isoprene (C_5H_8), 1,2,3-butatriene (C_4H_4) or allene (aC_3H_4) are consistent with the observed species pool. Concentrations of all detected hydrocarbons in the β-pinene flame are closer to the myrcene flame than to the α-pinene flame. These similarities and the direct identification of myrcene by its photoionization efficiency spectrum during β-pinene combustion indicate that β-pinene undergoes isomerization to myrcene under the studied flame conditions. Aromatic species such as phenylacetylene (C_8H_6), styrene (C_8H_8), xylenes (C_8H_{10}), and indene (C_9H_8) could be clearly identified and have higher concentrations in the α-pinene flame. Consequently, a higher sooting tendency can generally be expected for this monoterpene. The presented quantitative speciation data of flat premixed flames of the three monoterpenes α-pinene, β-pinene, and myrcene give insights into their combustion kinetics.

Keywords: Monoterpene; Pinene; Biofuel; Photoionization; Molecular-beam mass spectrometry

* Corresponding author.
E-mail address: thomas.bierkandt@dlr.de (T. Bierkandt).

https://doi.org/10.1016/j.proci.2020.06.204

1. Introduction

Over the past 25 years, the global production of biofuels as an alternative to fossil fuels for the transport sector has continuously increased [1] as they enable a reduction of CO_2 emissions and other harmful pollutants. The stringent requirements for aviation fuels, e.g., a high energy density and a low freezing point [2], typically restrict the direct use of conventional biofuels as an alternative to petroleum-based aviation fuels. Currently commercially available biojet fuels, e.g., hydroprocessed esters and fatty acids (HEFA) or farnesane, are suitable as drop-in components for Jet A-1 used in civil aviation, while alternatives to petroleum-based fuels with even higher energy densities for power-intensive aircraft, rockets, and missiles are limited. For such applications, the pinene dimers, which have a similar energy density to the tactical fuel JP-10, could be a promising alternative [3,4]. Hydrogenated pinene dimers ($C_{20}H_{34}$) were synthesized in high yield by dimerization of β-pinene and subsequent hydrogenation over PtO_2 during chemical catalysis [3]. Highest yields of more than 90% were reached with Nafion as catalyst and a reaction time of six hours at 100 °C and atmospheric pressure [3]. Meylemans et al. have also synthesized hydrogenated terpene dimers as potential high energy density fuels from α-pinene, two other terpenes, and turpentine by selective dimerization and subsequent hydrogenation [4]. The high viscosity of such terpene dimers prevents their use as single fuel component, but 50:50 blends with conventional fuels, e.g., JP-8 and JP-10, have acceptable viscosity even at lower temperatures [5]. A promising method for obtaining pinenes as precursors for pinene dimers from readily accessible raw materials is the synthesis of pinenes from conversion of glucose by engineered *Escherichia coli* bacteria [6]. Currently, the yield is low, e.g., Sarria et al. have achieved 1.2% of the technically possible yield, and it must increase to at least 26% to be an economical alternative to JP-10 [6].

Pinenes ($C_{10}H_{16}$) are unsaturated, bicyclic compounds and belong to the class of terpenes. They have a similar energy density to conventional diesel [6]. Pinenes, also known as monoterpenes, are the simplest terpenes and consist of two isoprene building blocks. Two constitutional isomers, i.e., α- and β-pinene, exist, but α-pinene is the more abundant isomer. Both have two stereocenters and overall four enantiomers of the pinenes occur in nature (see Fig. S1 for their structure). A natural source of pinenes is turpentine, which is mainly obtained by tapping pines or as a by-product of papermaking [7].

Previous investigations on the combustion of pinene isomers are limited and focus mainly on the combustion properties of α-pinene. The minimum ignition energies [8] and the laminar burning speeds as well as the Markstein lengths [9] were determined for different α-pinene/benzene/air mixtures. Measurements of minimum ignition energies [10] and laminar burning speeds [11] are also available for α-pinene/air mixtures. It has been reported by Raman et al. that pure α-pinene is suitable for gasoline engines, but observed soot concentrations are higher than those of FACE A and EURO V fuel standards [12].

Early pyrolysis studies of pinenes showed that both α-pinene and β-pinene isomerize to different $C_{10}H_{16}$ species including the acyclic monoterpenes alloocimene from α-pinene and myrcene from β-pinene [13,14]. Burwell published a mechanism explaining the formation of the observed isomerization products during the pyrolysis of pinenes via diradical transition states [14]. Recent studies on the pyrolysis of pinenes show that α-pinene produces mainly alloocimene and limonene and β-pinene mainly limonene, myrcene, and Ψ-limonene via diradical transition states [15,16]. Figure 1 shows the structural formulas of $C_{10}H_{16}$ isomers formed during pyrolysis of pinenes by opening the four-membered ring in the pinene molecule. The monocyclic terpenes are formed by hydrogen shift reaction from the biradicals, while formation of the acyclic terpenes needs C–C bond scission and intramolecular radical recombination [15]. For alloocimene, fast isomerization from the acyclic β-ocimene is assumed [16].

In this work, the first quantitative speciation dataset of combustion intermediates from flat premixed low-pressure flames with α- and β-pinene as fuel are shown. Moreover, the combustion of myrcene, which is considered as the main pyrolysis product of β-pinene, was investigated. Chemical structures of the three investigated $C_{10}H_{16}$ monoterpenes are shown in Fig. 1.

2. Experiment

Three stoichiometric (Φ=1.0), flat premixed flames of the three $C_{10}H_{16}$ isomers (-)-α-pinene (Sigma-Aldrich, ≥97%), (-)-β-pinene (Sigma-Aldrich, ≥97%), and myrcene (Sigma-Aldrich, ≥95%) were investigated at the Advanced Light Source. The total gas flow was 4 slm (2 slm Ar, 1.867 slm O_2, and 0.133 slm $C_{10}H_{16}$) with a cold gas velocity of 87.5 cm/s at 300 K for all three flames. Flames were stabilized at 30 mbar on a McKenna burner with a sintered stainless steel matrix 6 cm in diameter. Table S1 summarizes the flame conditions. The photoionization molecular-beam mass spectrometry experiment is described in detail in [17] and in the supplementary material. The data evaluation process to obtain species mole fraction profiles is also described in the supplementary material. Energy resolution was 50 meV for all measured photoionization efficiency (PIE) spectra. Uncertainty of calculated species mole fractions is estimated to be 15–20% for main species, 30–50%

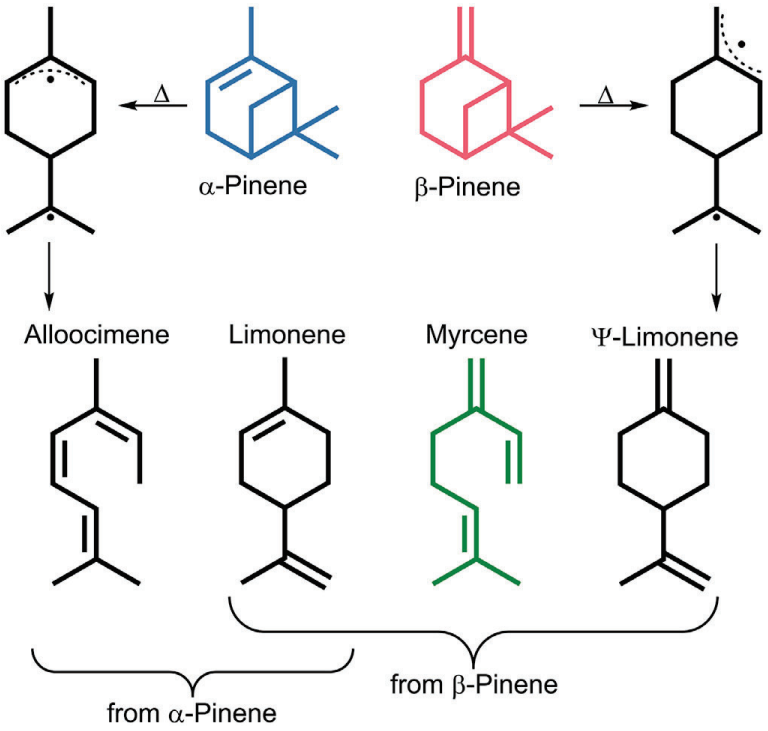

Fig. 1. Isomeric main products in pyrolysis of α- and β-pinene formed by diradical transition states.

for intermediate species with measured photoionization cross sections (PICS), and a factor of 2–4 for species with unknown PICS. Species with unknown PICS were quantified from scans not more than 0.5 eV above their ionization energy so that their estimated PICS from chemically similar species are typically between 5 and 10 Mb. Uncertainties in flame-sampling MBMS were further discussed in [18]. Exhaust gas temperatures were measured in the flames with a type R thermocouple coated with SiO_2 to minimize catalytic effects. Temperature profiles were determined from the temperature dependence of the sampling rate through the sampling nozzle [19]. Uncertainty of the temperature profiles is expected to be 5–10%.

3. Results

Understanding of the combustion chemistry of monoterpenes becomes of scientific importance due to the increasing interest in biomass-derived, alternative fuels. To gain fundamental knowledge about the decomposition of the three monoterpenes, i.e., α-pinene, β-pinene, and myrcene, and the formation of combustion intermediates, flames are compared with each other. The isomer-resolved speciation data can also be used as a starting point for future mechanism development and validation.

3.1. Major species

The three investigated fuels have the same elemental composition, i.e., $C_{10}H_{16}$, and the input composition of the gas phase mixtures is identical for all three flames. With similar heating values, the exhaust gas temperatures and the exhaust gas concentrations of the major species should be nearly equal. The heats of combustion of several terpenes including the three investigated monoterpenes of this study were determined by Hawkins and Eriksen [20]. The values at standard conditions are 1483.0 kcal/mol for α-pinene, 1485.1 kcal/mol for β-pinene, and 1490.4 kcal/mol for myrcene [20] and are therefore close to each other. For comparison, volumetric heat of combustion of JP-10, practically a single-component fuel (*exo*-tetrahydrodicyclopentadiene) and an isomer of the three investigated terpenes, is about 7% higher than for the pinenes [3].

Profiles of the major species (Ar, H_2, H_2O, CO, CO_2, O_2, and fuel) were determined experimentally for the stoichiometric α-pinene, β-pinene, and myrcene flames (for data, see supplementary material). As expected, the mole fraction profiles are very similar for all three isomers and measured exhaust gas temperatures only differ by 20 K. Differences in the exhaust gas concentrations at 30 mm are below 10% except for hydrogen, whose mole fraction is very small compared to the mole fraction of H_2O (ratio of about 1:10). Deviations in the mole fraction of H_2O, which are within the error margin of the equivalence ratio set by thermal mass flow controllers, lead to significant deviations of the hydrogen mole fraction, when calculated from the element balance. A small difference is observed for the mole fraction profiles of the fuels. α-Pinene degrades at slower rate

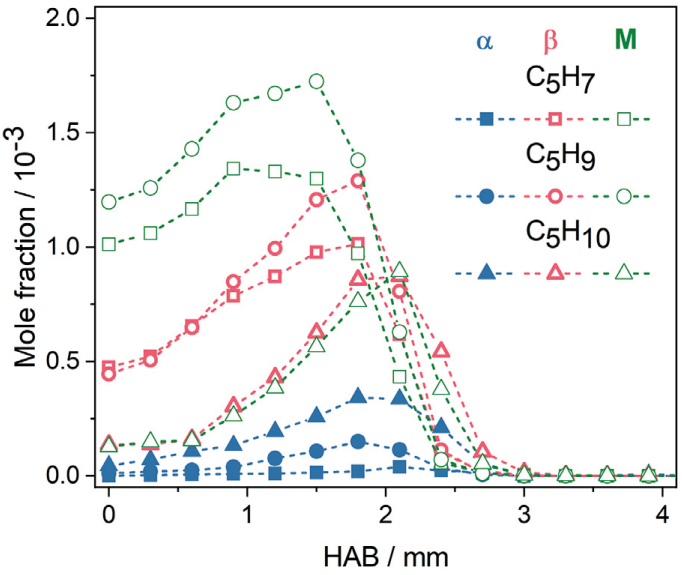

Fig. 2. Mole fraction profiles of C_5H_x species measured in stoichiometric terpene flames. Blue symbols: α-Pinene (α); Red symbols: β-Pinene (β); Green symbols: Myrcene (M).

than β-pinene and myrcene, but all three fuels are completely consumed at a height above the burner (HAB) of 2.7 mm. In addition, O_2 degradation is slightly faster for both pinene isomers compared to myrcene. These differences are within the uncertainty of the experiment, so that the major species mole fraction profiles do not differ significantly. Any differences in the reaction kinetics of the fuels are linked to the different fuel destruction pathways and must be deduced from comparison of mole fraction profiles of combustion intermediates.

3.2. Unimolecular dissociation of myrcene and comparison of species pool

More than 50 combustion intermediates could be quantified in each of the flames and complete speciation datasets are provided as supplementary material. Most of the identified species were detected in all three flames, but in different concentrations. Differences between the two bicyclic pinene isomers are greater than those between β-pinene and the acyclic monoterpene myrcene. For example, distinct differences are observed for some C_5H_x species as shown in Fig. 2. Compared to the α-pinene flame, the concentrations of C_5H_7 and C_5H_9 radicals in the β-pinene flame are about one order of magnitude higher. Concentrations of both radicals are even higher in the myrcene flame. It is obvious that the observed differences in the formation of C_5H_7 and C_5H_9 radicals may be directly related to the first fuel decomposition steps.

Myrcene is an acyclic terpene with three types of C–H bonds and H-abstraction is principally possible at the vinylic, allylic or primary carbon atoms. Figure 3 shows the three types of carbon atoms in myrcene. Hydrogen abstraction at the allylic carbon atoms is most likely because the allylic C–H bond is the weakest C–H bond in myrcene. According to Blanskby and Ellison, the bond dissociation energy of an allylic C–H bond is only 88.8 kcal/mol, which is much smaller than for a vinylic (110.7 kcal/mol) or primary (104.9 kcal/mol) C–H bond [21]. A systematic study of H-abstraction ratios for simple hydrocarbons shows that this order of bond strengths is also relevant in flat premixed flames [22]. H-abstraction reactions followed by β-scissions cannot explain the formation of the C_5H_7 or the C_5H_9 radical in myrcene combustion.

In the combustion of higher alkenes, unimolecular cleavage of C–C single bonds in allylic position plays a role and is a common decomposition pathway of the fuel. Hansen et al. showed that the unimolecular C–C bond breaking in 1-hexene to directly form allyl and *n*-propyl radicals is the most important decomposition pathway in flames [23]. In the high-temperature oxidation of alkenes, a C–C bond cleavage typically results in the formation of a resonance-stabilized radical and an alkyl radical [24]. For myrcene, only the cleavage of one C–C single bond leads directly to C_5H_7 and C_5H_9 radicals (see Fig. 3) and can explain the high concentrations of these radicals in the myrcene flame. Cleavage of this C–C bond is very likely because both of the radicals are resonance-stabilized. Stolle and Ondruschka also proposed a unimolecular bond breaking in the pyrolysis of myrcene [25]. The radicals shown in Fig. 3 are 2-methylene-3-butenyl (C_5H_7) and 3-methyl-1-buten-3-yl (C_5H_9). Measured photoionization efficiency (PIE) spectra of C_5H_7 and C_5H_9 from the three terpene flames are shown in Fig. S3. Shape of the PIE

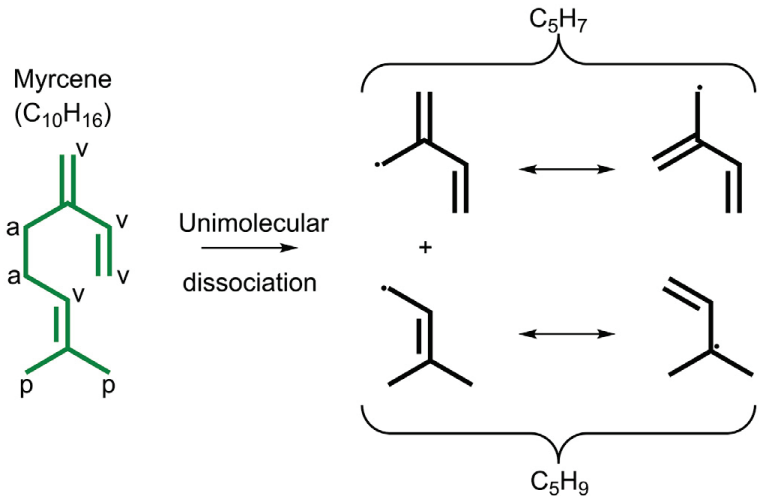

Fig. 3. Labeling of vinylic (v), allylic (a), and primary (p) carbon atoms in myrcene and scheme for the formation of resonance-stabilized C_5H_7 and C_5H_9 radicals by unimolecular dissociation of myrcene.

spectra of C_5H_7 is nearly identical for all flames in the range of 7.9–10 eV, but signal intensity for α-pinene is more than a factor of 10 smaller compared to the other two fuels. The onset in signal intensity at 7.9 eV fits to the estimated ionization energy (IE) of 7.9 eV for the resonance-stabilized 2-methylene-3-butenyl radical [26]. Ionization energies of other C_5H_7 isomers are less than 7.6 eV [26], so that their presence can be excluded. PIE spectra of C_5H_9 from 7.9–10 eV are shown in Fig. S3. The onset is below 7.9 eV preventing an exact determination of the IE. The 3-methyl-1-buten-3-yl radical has an IE of 7.13 eV [26] and formation is likely as discussed. Shapes of the PIE spectra are again nearly the same in all three flames. It can be assumed that the same radical pool is formed, but that concentrations between the two pinenes may be considerably different.

It seems plausible that mole fractions of the C_5H_x radicals are significantly smaller in the α-pinene flame compared to myrcene since the direct formation of C_5H_7 or C_5H_9 radicals from the fuel is not expected due to the bicyclic structure. One would expect the same for β-pinene, which also has a bicyclic structure. For both fuels, significantly higher concentrations were observed in comparison to α-pinene, so that it can be concluded that the fuel decomposition of β-pinene differs significantly from α-pinene and there are more similarities to myrcene. There are several other C_3–C_6 species whose concentrations differ between the two pinene flames, while more similarities are observed between β-pinene and myrcene. Figure 4 compares the maximum mole fractions of eight combustion intermediates from the three flames including the previously discussed C_5H_7 and C_5H_9 radicals. Because photoionization cross sections for these radicals as well as for C_4H_5 are not known, estimated values are used for quantification. Since profile shapes of the PIE spectra for these radicals are very similar in all flames and quantification was done from scans with the same photon energy, comparability of the mole fractions is still given. Stable intermediates from Fig. 4 are, e.g., allene (aC_3H_4), 1,2,3-butatriene (C_4H_4), and isoprene (C_5H_8). Their formation is discussed below, but comparison of the maximum mole fractions further confirms that the species pool formed in the β-pinene flame is more equal to myrcene than to α-pinene. This observation might indicate that β-pinene isomerizes to myrcene during combustion in a flame as seen in pyrolysis where myrcene is a major product besides *p*-mentha-1,8-diene (limonene) and *p*-mentha-1(7),8-diene (ψ-limonene) [15].

3.3. Isomerization of the pinenes

Figure 5 compares PIE curves of $C_{10}H_{16}$ obtained at HAB of 2.1 mm (α- and β-pinene) and 1.8 mm (myrcene) in the reaction zone of the terpene flames with the fragmentation scans of the pure substances. Pure substances were vaporized at 180 °C, i.e., just above the boiling point, and diluted with argon. Isomerization can be excluded at these conditions. In pyrolysis, the isomerization of α- and β-pinene starts at 300 °C [16] and 350 °C [15], respectively. Measured ionization energies of 8.15 eV for α-pinene and 8.45 eV for β-pinene agree well with the known values of 8.07 eV [27] and 8.45 eV [28] from the literature. The observed adiabatic IE of myrcene at 8.35 eV is lower than for β-pinene. Similar differences are known for the vertical ionization energies of these two terpenes. Sabljic and Güsten measured vertical ionization energies of 8.61 eV for myrcene and 8.68 eV for β-pinene, respectively [29].

It is obvious that the onset of the PIE spectrum of $C_{10}H_{16}$ measured in the α-pinene flame is below 7.9 eV, which is significantly smaller than the IE of pure α-pinene. There is also no clear in-

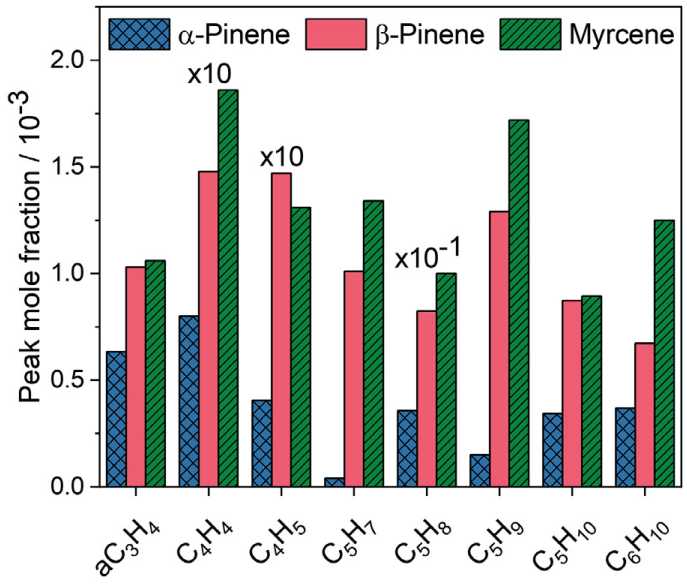

Fig. 4. Peak mole fractions of C_3–C_6 combustion intermediates measured in α-pinene, β-pinene, and myrcene flames.

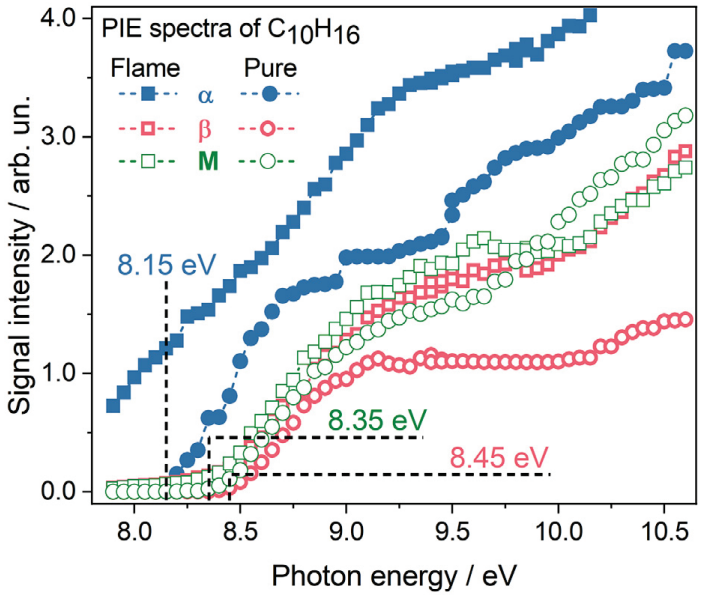

Fig. 5. Comparison of photoionization efficiency (PIE) spectra of $C_{10}H_{16}$ obtained from the three terpene flames with the pure substances. Blue symbols: α-Pinene (α); Red symbols: β-Pinene (β); Green symbols: Myrcene (M).

crease in the PIE spectrum at the ionization energy of α-pinene. Complete isomerization of α-pinene seems to be relevant at least at this position in the flame. In the pyrolysis of α-pinene, the main products of isomerization above 300 °C are the acyclic alloocimene and the monocyclic limonene (see Fig. 1). Méjean et al. measured ionization energies of several monoterpenes by atmospheric pressure photoionization (APPI) at the SOLEIL synchrotron in France and determined an IE of 8.54 eV for limonene [30]. This value is significantly higher than the IE of α-pinene and there is also no increase in the measured PIE spectrum at this photon energy, which would indicate the formation of limonene in the flame. Adiabatic ionization energies of several diastereomeric structures of alloocimene are located between 7.32 and 7.66 eV at the G4 level of theory (see Table S2) and were calculated with Gaussian 16 [31]. The calculations show that alloocimene has a lower IE than α-pinene and this terpene would be a plausible isomerization product of α-pinene as known from pyrolysis experiments [16]. A few species with mass-to-charge ratio larger than α-pinene, e.g., C_{11} species, are observed in the flame. Since their ionization energies are higher than 7.9 eV, they cannot contribute to the signal of $C_{10}H_{16}$ below 7.9 eV in Fig. 5.

A further species, which may be formed by isomerization of α-pinene, is α-phellandrene. Kolicheski et al. observed the formation of β-phellandrene during the pyrolysis of β-pinene [32] and a possible explanation for the formation

of this species was given by Stolle and Ondruschka, who proposed a sigmatropic [1,3]-H-shift from the diradical structure after ring opening of β-pinene [25]. In analogy to β-pinene, α-phellandrene could be formed from α-pinene. A vertical ionization energy of 7.79 eV was calculated by Nauduri and Greenberg [33]. Thus, α-phellandrene would be a second terpene that has a lower IE than α-pinene and may be formed under our flame conditions. The observations suggest that unimolecular isomerization of α-pinene is an important fuel consumption pathway in flames. Fuel consumption by unimolecular isomerization under ring opening was also identified as important decomposition step in methylcyclohexane flames [34].

PIE spectra of $C_{10}H_{16}$ from β-pinene and myrcene flames are very similar as shown in Fig. 5 and the PIE spectrum of pure myrcene fits to these spectra in the measured range, while the PIE spectrum of the pure β-pinene significantly changes near 8.9 eV. Based on these observations, an isomerization of β-pinene to the acyclic myrcene during its combustion can be assumed. The unimolecular decomposition of myrcene discussed before also explains the high concentrations of C_5H_7 and C_5H_9 radicals in the β-pinene flame. A small onset below the ionization energy of myrcene is observed in the myrcene flame and a possible explanation might be the formation of small amounts of $C_{10}H_{16}$ isomers by H-addition and subsequent C–H-β-scission from myrcene to yield β-ocimene or α-myrcene.

3.4. Decomposition of C_5H_7 and C_5H_9 radicals

A scheme for further decomposition of C_5H_7 and C_5H_9 radicals, which will be relevant for myrcene and β-pinene flames, is shown in Fig. 6. β-Scission of the C–C single bond between the two vinylic carbon atoms in the 2-methylene-3-butenyl radical (C_5H_7) leads to allene (aC_3H_4) and vinyl radicals (C_2H_3). Mole fraction of allene measured in both the β-pinene and myrcene flame is about 1.6 times higher than for the α-pinene flame. For 3-methyl-1-buten-3-yl radicals (C_5H_9), C–C-β-scission is not possible and C–H-β-scission will lead to the formation of the C_5H_8 isomers 3-methyl-1,2-butadiene and isoprene. Ionization energies of 3-methyl-1,2-butadiene and isoprene are 8.95 and 8.85 eV, respectively [35]. The measured onset in the PIE spectrum of C_5H_8 from the β-pinene flame is about 8.8 eV. A comparison of this measured PIE spectrum with PIE spectra of 3-methyl-1,2-butadiene [36] and isoprene [37] from the literature shows that mainly isoprene is formed since the PIE spectrum from the flame is best reproduced by the PIE spectrum of isoprene (see Fig. S4). Although the spectrum of 3-methyl-1,2-butadiene fits up to a photon energy of 9.2 eV, it clearly differs from the measured spectrum at higher energies. Since the shapes of all measured PIE spectra of C_5H_8 are identical in all three flames, isoprene is also the major component of all C_5H_8 isomers in the myrcene and α-pinene flame. A possible explanation for the absence of 3-methyl-1,2-butadiene might be a very rapid isomerization to isoprene as reported by Ruwe et al. in the combustion of 2-methyl-2-butene, where 3-methyl-1,2-butadiene could be detected, but the concentration of isoprene was 9 times higher [38]. Isomerization to isoprene would be analogous to isomerization of 1,2-butadiene to 1,3-butadiene via [1,2]-H-shift [39]. Isoprene is formed in high concentrations in the β-pinene and myrcene flame with peak mole fractions of $8{\cdot}10^{-3}$ and $1{\cdot}10^{-2}$, respectively, as shown in Fig. 4. For comparison, the concentration of isoprene in the α-pinene flame is only about 45% of the value in the β-pinene flame.

Starting from 3-methyl-1,2-butadiene and isoprene, another H-abstraction followed by C–C-β-scission leads to 1,2,3-butatriene (C_4H_4) or allene (aC_3H_4) as shown in the scheme in Fig. 6. The C_4H_4 isomer vinylacetylene is the more abundant isomer in all three investigated flames with maximum mole fraction of a factor of 6–8 higher than 1,2,3-butatriene. Since the formation of 3-methyl-1,2-butadiene could not be confirmed, 1,2,3-butatriene is mainly formed via C_4H_5 radicals such as vinylacetylene [40]. Concentrations of both, 1,2,3-butatriene and the C_4H_5 radical, are significantly larger in the β-pinene and myrcene flame. The stable combustion intermediate allene opens additional channels to obtain propyne (pC_3H_4) by isomerization and propargyl radicals (C_3H_3) by H-abstraction [41].

A competing decomposition pathway of myrcene by H-abstraction reactions is discussed in the supplementary material and shows the formation of $C_{10}H_{14}$, C_8H_{12}, C_4H_5, and C_6H_{10}. Similarities between myrcene and β-pinene for these species are consistent with the isomerization of β-pinene.

3.5. Aromatic species and larger hydrocarbons

Figure 7 shows peak mole fractions of C_3H_7 radicals and larger C_8–C_{10} hydrocarbons from the three terpene flames. Again, results for β-pinene and myrcene are more similar, but maximum mole fractions of shown species are now significantly higher for the α-pinene flame. Aromatic species, e.g., phenylacetylene (C_8H_6), styrene (C_8H_8), xylenes (C_8H_{10}), and indene (C_9H_8), were clearly identified by their ionization energies. Larger concentrations of these species indicate that soot formation is potentially higher in the combustion of α-pinene. The mole fraction of benzene is also higher in the α-pinene flame (about a factor of 1.5 compared to β-pinene). During combustion of α-pinene in a gasoline engine, it was also observed that α-pinene even produces more soot

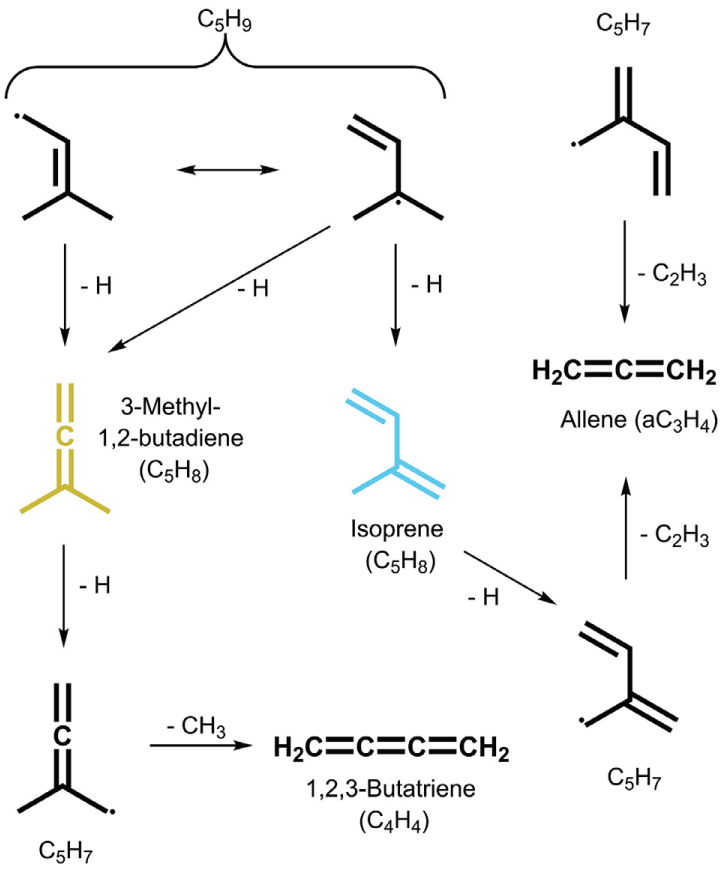

Fig. 6. Scheme for further decomposition of the C_5H_7 and C_5H_9 radicals.

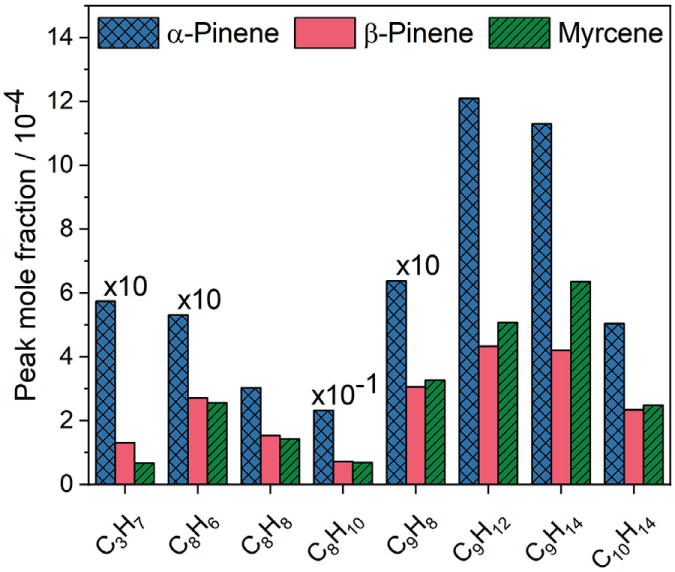

Fig. 7. Peak mole fractions of some combustion intermediates measured in higher concentrations in the α-pinene flame.

than conventional gasoline [12]. The observations made here suggest that β-pinene would be better suited as fuel than α-pinene with respect to avoidance of soot emissions. Other C_9–C_{10} hydrocarbons were detected in higher concentrations in the α-pinene flame. However, the ionization energy of the first ionized species of C_9H_{12}, C_9H_{14}, and $C_{10}H_{14}$ is smaller than the starting point of the energy scan, i.e., smaller than 7.90 eV. If α-phellandrene is an isomerization product during α-pinene combustion as discussed above, its decomposition would lead to *p*-cymene ($C_{10}H_{14}$) after H-abstraction or to the smaller combustion intermediates toluene (C_7H_8) and C_3H_7.

Dehydrogenation of the pinenes without ring-breaking, i.e., H-abstraction and subsequent β-scission of a C–H bond, would lead to the formation of the bicyclic verbenene or under cleavage of the C_4-ring to substituted cyclohexadienes as shown in Fig. S5 for α-pinene. The formation of substituted cyclohexadienes might be a further explanation for the higher concentrations of aromatic hydrocarbons in the α-pinene flame. For example, Law et al. have demonstrated for a stoichiometric cyclohexane flame that the stepwise dehydrogenation to benzene made a significant contribution to the total benzene concentration [42]. Here, the lack of known ionization energies does not allow further conclusions on the identity of the $C_{10}H_{14}$ species formed in our investigated flames.

4. Conclusions

Growing interest in biomass-derived alternative fuels makes a fundamental understanding of the combustion chemistry of monoterpenes scientifically important, but investigations on the combustion of the pinenes and myrcene are so far limited. In this work, the combustion of the pinene isomers (α- and β-pinene) and myrcene, which is an isomerization product in pyrolysis of β-pinene, were investigated in flat premixed, low-pressure flames at 30 mbar by photoionization molecular-beam mass spectrometry at the Advanced Light Source in Berkeley. More than 50 combustion intermediates formed during combustion of the three studied stoichiometric flames were identified and their mole fractions calculated. The comprehensive speciation data give an insight into the combustion kinetics of the monoterpenes and is made available herein for subsequent model validation. Observed similarities in the species pool between β-pinene and myrcene suggest that β-pinene isomerizes to myrcene during combustion, so that the identified main decomposition steps are the same for both fuels. A detailed decomposition pathway is formulated for myrcene. The speciation data of all three flames provide important information for the development of reaction mechanisms. Given the complexity of the flame chemistry of these fuels and their propensity for isomerization, additional data sets for other possible isomers may be needed to allow meaningful future reaction mechanism development. The most important isomers could be identified and give first experimental evidence for possible reaction pathways that should be included in chemical kinetic modeling. It is also shown that α-pinene isomerizes during combustion, since the formation of a $C_{10}H_{16}$ isomer with significantly lower ionization energy than α-pinene was directly observed. However, the decomposition of α-pinene without previous isomerization needs further investigation, because the clear identification of some larger C_9 and C_{10} hydrocarbons was not possible due to unknown ionization energies of candidate compounds. To fully understand the formation of higher aromatic hydrocarbons, it is necessary to determine the ionization energies of possible C_9 and C_{10} hydrocarbons. The results show that α-pinene has a higher propensity to form aromatic hydrocarbons and soot. For example, benzene, phenylacetylene, xylenes, styrene and naphthalene were detected in all flames, but the concentrations of all aromatic hydrocarbons are significantly higher in α-pinene under the same conditions. For β-pinene and myrcene, higher levels of unsaturated non-cyclic hydrocarbons were detected, in particular, hydrocarbons having four and five carbon atoms, e.g., 1,3-butadiene and isoprene.

Declaration of Competing Interest

The authors declare that they have no known competing financial interests or personal relationships that could have appeared to influence the work reported in this paper.

Acknowledgments

The authors gratefully acknowledge Paul Fugazzi for technical assistance and Patrick Hemberger for calculation of adiabatic ionization energies. TK acknowledges support from the German Research Foundation (DFG) under contract KA3871/3–2. NH acknowledges support from the U.S. DOE, Office of Science, Office of Basic Energy Sciences. Sandia National Laboratories is a multi-mission laboratory managed and operated by National Technology and Engineering Solutions of Sandia, LLC., a wholly owned subsidiary of Honeywell International, Inc., for the U.S. Department of Energy's National Nuclear Security Administration under contract DE-NA0003525. The experiments were conducted at the Advanced Light Source, Berkeley National Laboratory, Berkeley, CA, USA. The Advanced Light Source is supported by the Director, Office of Science, Office of Basic Energy Sciences, of the U.S. DOE under Contract No. DEAC02–05CH11231. This paper describes objective technical results and analysis. Any subjective views or opinions that might be expressed in the paper do not necessarily represent the views of the U.S. DOE or the U.S. Government.

Supplementary material

Supplementary material associated with this article can be found, in the online version, at doi:10.1016/j.proci.2020.06.204.

References

[1] D. Thrän, K. Naumann, E. Billig, M. Millinger, K. Oehmichen, D. Pfeiffer, K. Zech, Data on biofuels production, trade, and demand, in: M.R. Riazi, D. Chiaramonti (Eds.), Biofuels production and processing technology, Taylor & Francis, Boca Raton, 2018, pp. 55–100.

[2] S. Blakey, L. Rye, C.W. Wilson, *Proc. Combust. Inst.* 33 (2011) 2863–2885.

[3] B.G. Harvey, M.E. Wright, R.L. Quintana, *Energy Fuels* 24 (2010) 267–273.

[4] H.A. Meylemans, R.L. Quintana, B.G. Harvey, *Fuel* 97 (2012) 560–568.

[5] H.A. Meylemans, L.C. Baldwin, B.G. Harvey, *Energy Fuels* 27 (2013) 883–888.

[6] S. Sarria, B. Wong, H.G. Martin, J.D. Keasling, P. Peralta-Yahya, *ACS Synth. Biol.* 3 (2014) 466–475.

[7] A. Behr, L. Johnen, *ChemSusChem* 2 (2009) 1072–1095.

[8] B. Coudour, K. Chetehouna, S. Rudz, P. Gillard, J.-P. Garo, *J. Hazard. Mater.* 283 (2015) 507–511.

[9] B. Coudour, K. Chetehouna, F. Halter, C. Mounaïm-Rousselle, J.-P. Garo, *Combust. Sci. Technol.* 188 (2016) 2128–2136.

[10] S. Rudz, K. Chetehouna, C. Strozzi, P. Gillard, *Combust. Sci. Technol.* 186 (2014) 1597–1605.

[11] L. Courty, K. Chetehouna, F. Halter, F. Foucher, J.-P. Garo, C. Mounaïm-Rousselle, *Combust. Flame* 159 (2012) 1385–1392.

[12] V. Raman, V. Sivasankaralingam, R. Dibble, S.M. Sarathy, *SAE Tech. Pap.* (2016) 2016-01-2171.

[13] L.A. Goldblatt, S. Palkin, *J. Am. Chem. Soc.* 63 (1941) 3517–3522.

[14] R.L. Burwell, *J. Am. Chem. Soc.* 73 (1951) 4461–4462.

[15] A. Stolle, C. Brauns, M. Nüchter, B. Ondruschka, W. Bonrath, M. Findeisen, *Eur. J. Org. Chem.* (2006) 3317–3325.

[16] A. Stolle, B. Ondruschka, M. Findeisen, *J. Org. Chem.* 73 (2008) 8228–8235.

[17] T.A. Cool, A. McIlroy, F. Qi, P.R. Westmoreland, L. Poisson, D.S. Peterka, M. Ahmed, *Rev. Sci. Instrum.* 76 (2005) 094102.

[18] T. Bierkandt, P. Hemberger, P. Oßwald, D. Krüger, M. Köhler, T. Kasper, *Proc. Combust. Inst.* 37 (2019) 1579–1587.

[19] U. Struckmeier, P. Oßwald, T. Kasper, L. Böhling, M. Heusing, M. Köhler, A. Brockhinke, K. Kohse-Höinghaus, *Z. Phys. Chem.* 223 (2009) 503–537.

[20] J.E. Hawkins, W.T. Eriksen, *J. Am. Chem. Soc.* 76 (1954) 2669–2671.

[21] S.J. Blanksby, G.B. Ellison, *Acc. Chem. Res.* 36 (2003) 255–263.

[22] D. Krüger, P. Oßwald, M. Köhler, P. Hemberger, T. Bierkandt, Y. Karakaya, T. Kasper, *Combust. Flame* 191 (2018) 343–352.

[23] N. Hansen, W. Li, M.E. Law, T. Kasper, P.R. Westmoreland, B. Yang, T.A. Cool, A. Lucassen, *Phys. Chem. Chem. Phys.* 12 (2010) 12112–12122.

[24] M. Mehl, G. Vanhove, W.J. Pitz, E. Ranzi, *Combust. Flame* 155 (2008) 756–772.

[25] A. Stolle, B. Ondruschka, *J. Anal. Appl. Pyrolysis* 81 (2008) 136–138.

[26] F.P. Lossing, J.C. Traeger, *Int. J. Mass Spectrom. Ion Phys.* 19 (1976) 9–22.

[27] M.I. Al-Joboury, D.W. Turner, *J. Chem. Soc.* (1964) 4434–4441.

[28] M. Cao, J. Chen, W. Fang, Y. Li, S. Ge, X. Shan, F. Liu, Y. Zhao, Z. Wang, L. Sheng, *Eur. J. Mass Spectrom.* 20 (2014) 419–428.

[29] A. Sabljic, H. Güsten, *Atmospheric Environ.* 24 (1990) 73–78.

[30] M. Méjean, A. Giuliani, A. Brunelle, D. Touboul, *Eur. J. Mass Spectrom.* 20 (2014) 403–407.

[31] M.J. Frisch, G.W. Trucks, H.B. Schlegel, G.E. Scuseria, M.A. Robb, J.R. Cheeseman, G. Scalmani, V. Barone, G.A. Petersson, H. Nakatsuji, X. Li, M. Caricato, A.V. Marenich, J. Bloino, B.G. Janesko, R. Gomperts, B. Mennucci, H.P. Hratchian, J.V. Ortiz, A.F. Izmaylov, J.L. Sonnenberg, D. Williams-Young, F. Ding, F. Lipparini, F. Egidi, J. Goings, B. Peng, A. Petrone, T. Henderson, D. Ranasinghe, V.G. Zakrzewski, J. Gao, N. Rega, G. Zheng, W. Liang, M. Hada, M. Ehara, K. Toyota, R. Fukuda, J. Hasegawa, M. Ishida, T. Nakajima, Y. Honda, O. Kitao, H. Nakai, T. Vreven, K. Throssell, J.A. Montgomery, J.E. Peralta, F. Ogliaro, M.J. Bearpark, J.J. Heyd, E.N. Brothers, K.N. Kudin, V.N. Staroverov, T.A. Keith, R. Kobayashi, J. Normand, K. Raghavachari, A.P. Rendell, J.C. Burant, S.S. Iyengar, J. Tomasi, M. Cossi, J.M. Millam, M. Klene, C. Adamo, R. Cammi, J.W. Ochterski, R.L. Martin, K. Morokuma, O. Farkas, J.B. Foresman, D.J. Fox, *Gaussian 16, Revision A.03*, Gaussian, Inc., Wallingford, CT, 2016.

[32] M.B. Kolicheski, L.C. Cocco, D.A. Mitchell, M. Kaminski, *J. Anal. Appl. Pyrolysis* 80 (2007) 92–100.

[33] D. Nauduri, A. Greenberg, *Struct. Chem.* 20 (2009) 417–421.

[34] S.A. Skeen, B. Yang, A.W. Jasper, W.J. Pitz, N. Hansen, *Energy Fuels* 25 (2011) 5611–5625.

[35] G. Bieri, F. Burger, E. Heilbronner, J.P. Maier, *Helv. Chim. Acta* 60 (1977) 2213–2233.

[36] B. Yang, J. Wang, T.A. Cool, N. Hansen, S. Skeen, D.L. Osborn, *Int. J. Mass Spectrom.* 309 (2012) 118–128.

[37] X. Liu, W. Zhang, Z. Wang, M. Huang, X. Yang, L. Tao, Y. Sun, Y. Xu, X. Shan, F. Liu, L. Sheng, *J. Mass Spectrom.* 44 (2009) 404–409.

[38] L. Ruwe, K. Moshammer, N. Hansen, K. Kohse-Höinghaus, *Combust. Flame* 175 (2017) 34–46.

[39] R.D. Kern, H.J. Singh, C.H. Wu, *Int. J. Chem. Kinet.* 20 (1988) 731–747.

[40] J.M. Ribeiro, A.M. Mebel, *Phys. Chem. Chem. Phys.* 19 (2017) 14543–14554.

[41] N. Hansen, J.A. Miller, P.R. Westmoreland, T. Kasper, K. Kohse-Höinghaus, J. Wang, T.A. Cool, *Combust. Flame* 156 (2009) 2153–2164.

[42] M.E. Law, P.R. Westmoreland, T.A. Cool, J. Wang, N. Hansen, C.A. Taatjes, T. Kasper, *Proc. Combust. Inst.* 31 (2007) 565–573.

Observation of low-temperature chemistry products in laminar premixed low-pressure flames by molecular-beam mass spectrometry

Bierkandt, T., Oßwald, P., Gaiser, N., Krüger, D., Köhler, M., Hoener, M., Shaqiri, S., Kaczmarek, D., Karakaya, Y., Hemberger, P., Kasper, T.
International Journal of Chemical Kinetics, 2021, 53(10), pp. 1063–1081
DOI: 10.1002/kin.21503

My contribution to this work was the design and optimization, manufacturing supervision and commissioning of the combustion chamber used for measuring part of the flame data investigated in this work, support in the measurement of data, co-authoring of the manuscript.

Received: 23 June 2020 | Revised: 22 April 2021 | Accepted: 23 April 2021

DOI: 10.1002/kin.21503

INTERNATIONAL JOURNAL OF CHEMICAL KINETICS WILEY

RESEARCH ARTICLE

Observation of low-temperature chemistry products in laminar premixed low-pressure flames by molecular-beam mass spectrometry

Thomas Bierkandt[1] | **Patrick Oßwald**[1] | **Nina Gaiser**[1] | **Dominik Krüger**[1] | **Markus Köhler**[1] | **Martin Hoener**[2] | **Shkelqim Shaqiri**[2] | **Dennis Kaczmarek**[2] | **Yasin Karakaya**[2] | **Patrick Hemberger**[3] | **Tina Kasper**[2]

[1] German Aerospace Center (DLR), Institute of Combustion Technology, Stuttgart, Germany

[2] Mass Spectrometry in Reactive Flows, University of Duisburg-Essen, Duisburg, Germany

[3] Laboratory for Synchrotron Radiation and Femtochemistry, Paul Scherrer Institute, Villigen, Switzerland

Correspondence
Thomas Bierkandt, Institute of Combustion Technology, German Aerospace Center (DLR), Stuttgart 70569, Germany.
Email: thomas.bierkandt@dlr.de

Funding information
European Community's Seventh Framework Program (FP7/2007-2013), Grant/Award Number: 312284; German Research Foundation, Grant/Award Numbers: KA3871/3-2, KO4786/2-2; Swiss Federal Office of Energy, Grant/Award Number: SI/501269-01

Abstract

The formation of typical low-temperature oxidation products is observed in laminar premixed low-pressure flames investigated by photoionization molecular-beam mass spectrometry at the Swiss Light Source. The C_1–C_4 alkyl hydroperoxides can be identified in *n*-butane- and 2-butene-doped hydrogen flames by their photoionization efficiency spectra at *m/z* 48, 62, 76, and 90. C_1–C_3 alkyl hydroperoxides are also observed in a propane-doped hydrogen flame and in a neat propane flame. In addition, threshold photoelectron spectra reveal the presence of the alkyl hydroperoxides. In the 2-butene/H_2 flame, the photoionization spectrum at *m/z* 88 also enables the identification of butenyl hydroperoxides by comparison with calculated ionization energies of the alkenyl hydroperoxides and a literature spectrum. The low-temperature species are formed close to the burner surface with maximum mole fractions at 0.25–0.75 mm above the burner. At 0.5 mm, even the methylperoxy radical (CH_3OO) is measured for the first time in a laminar premixed flame. The rate of production analyses show that consumption of the hydroperoxyalkyl radicals results in the formation of cyclic ethers. In the *n*-butane/H_2 flame, ethylene oxide, oxetane, and methyloxirane are identified. Besides expected small oxygenated species, for example, formaldehyde or acetaldehyde, the larger C_4 oxygenates butanone ($C_2H_5COCH_3$) and 2,3-butanedione ($C_4H_6O_2$) are formed in the two C_4 hydrocarbon-doped hydrogen flames. Quantification of alkyl hydroperoxides with estimated photoionization cross sections based on the corresponding alcohols, which have similar photoelectron structures to the alkyl hydroperoxides, shows that mole fractions are on the order of 10^{-5}–10^{-6} in the *n*-butane/H_2 flame. Measurements are corroborated by simulations, which also predict the presence of some peroxides in detectable concentrations, that is, mole fractions larger than 10^{-7}, under the investigated

conditions. The observation of peroxide species and cyclic ethers in the investigated laminar premixed flames give new insights into the contribution of low-temperature combustion chemistry in a flame.

KEYWORDS
flame-sampling molecular-beam mass spectrometry, hydroperoxides, low-temperature oxidation, photoelectron photoion coincidence spectroscopy, photoionization

1 | INTRODUCTION

Advanced combustion strategies and novel fuels are a key factor in future energy supply and transportation as they promise improved efficiencies and reductions of carbon dioxide and air pollutant emissions. Fuel composition also plays a crucial role in the exhaust emissions from internal combustion in engines[1,2] or gas turbines.[3,4] A particular focus of engine development is the use of combustion processes at low temperatures.[5,6] The low-temperature combustion (LTC) can have a positive impact on the trade-off between nitrogen oxides (NO_x) and soot.[6–8] LTC is implemented in various forms, for example, as homogeneous charge compression ignition (HCCI) or reactivity controlled compression ignition (RCCI).[6,9] In all of these processes, a homogeneous mixture of fuel and air is autoignited by compression. To control these processes, understanding the ignition and oxidation properties of various fuels is essential but challenging.[10] The typical LTC regime is located between 450 and 850 K[11] and a reaction sequence for the low-temperature oxidation of an alkane (RH) is shown in Figure 1. The LTC is especially relevant for cool flames and low-temperature ignition in automotive engines.

Fuel consumption is mostly initiated by OH radicals to produce the corresponding alkyl radicals (R), for example, 1-butyl and 2-butyl radicals (C_4H_9) in the oxidation of *n*-butane (C_4H_{10}). This is also the main initiation step for the fuel consumption in the high-temperature combustion, for example, in a laminar premixed flame. In such a flame environment, a β-scission follows the initiation step of fuel decay, while the alkyl radicals react with molecular oxygen (O_2) in the low-temperature regime to alkylperoxy radicals (ROO) as presented in Figure 1. Further reactions of the ROO radical lead to the formation of alkyl hydroperoxides (ROOH), alkenes, or hydroperoxyalkyl radicals (QOOH). The hydroperoxyalkyl radical is formed by isomerization via internal H-abstraction.[13] Consumption pathways of the QOOH radical into cyclic ethers, aldehydes, or ketones and reaction to alkenyl hydroperoxides by β-scission contribute to the negative temperature coefficient behavior,[11] while a second O_2 addition to the QOOH radical can result into the formation of hydroperoxyalkylperoxy radicals (OOQOOH). Further branching agents of the OOQOOH radical may be ketohydroperoxides, alkenyl hydroperoxides, or diones. The isomerization of the OOQOOH radical also opens the pathway for a third O_2 addition. For example, Wang et al. detected highly oxygenated species formed by a third O_2 addition during the oxidation of 2,5-dimethylhexane[14] and *n*-heptane.[15] The fate of the OOQOOH radical during *n*-pentane oxidation in a jet-stirred reactor towards ketohydroperoxides and their further decomposition to carboxylic acids was recently studied by electron-ion coincidence mass spectrometry.[16]

The alkylperoxy radical can react with the hydroperoxyl radical (HO_2), the smallest peroxide, to form an alkyl hydroperoxide (ROOH) as shown in Figure 1 and mentioned above. DeCorpo et al. quantified the methyl hydroperoxide (CH_3OOH) in 1973 by mass spectrometry in a cool acetaldehyde flame, which was stabilized in a flow reactor operated at atmospheric pressure.[17]

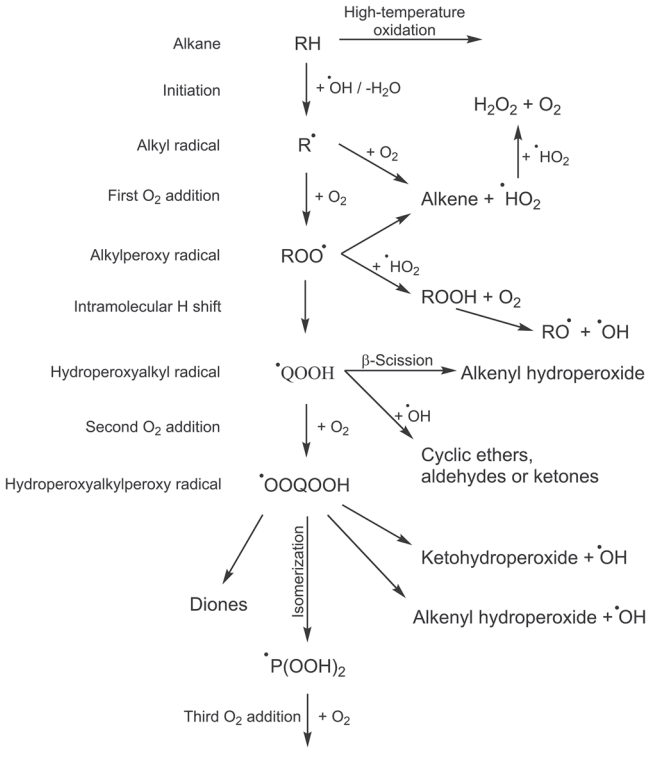

FIGURE 1 Scheme for the low-temperature oxidation of an alkane (after Wang et al.[12])

In another early study, Taylor identified some peroxide species, for example, hydrogen peroxide (H_2O_2) and *tert*-butyl hydroperoxide (C_4H_9OOH), by paper chromatography below and above the cool-flame limit of isobutane.[18] Hydroperoxides were intensely studied in the last 10 years during the low-temperature oxidation of alkanes in jet-stirred reactors. A current overview was given by Wang et al.,[12] while Herbinet et al.[19] summarized the period from 1990 to 2013. The reactors were often coupled to a time-of-flight mass spectrometer with photoionization to allow isomer-resolved in situ detection of the elusive peroxide species, but in some works also gas chromatography, FTIR spectroscopy, or infrared cavity ring-down spectroscopy were used as the analytical method to capture the low-temperature chemistry.[12] Detailed speciation data of hydroperoxides were measured for the first time by Battin-Leclerc et al. for the oxidation of *n*-butane between 560 and 720 K.[20] Methyl, ethyl, and butyl hydroperoxides were identified based on their ionization energies by photoionization efficiency (PIE) spectra in the photon energy range from 8.5 to 11.5 eV.[20,21] Further progress in the detection of low-temperature species and in understanding the LTC of hydrocarbons was reported for the oxidation of propane,[22,23] *n*-butane,[24–26] *n*-pentane,[27] *n*-heptane,[28] or 1-hexene.[29] Recently, Bourgalais et al.[30] coupled a jet-stirred reactor (JSR) for the first time to a double imaging photoelectron photoion coincidence (i^2PEPICO) spectrometer at the synchrotron SOLEIL to obtain threshold photoelectron (TPE) spectra for species generated upon low-temperature oxidation of *n*-pentane. They measured photoelectron spectra of the smallest alkyl hydroperoxides, that is, methyl and ethyl hydroperoxide, and were able to resolve isomers at mass-to-charge ratios of 72, 84, 86, and 88.[30]

In laminar premixed flames, the temperature rises rapidly from the preheat zone to the end of the reaction zone and hence high-temperature combustion is the dominant oxidation mechanism. However, low-temperature species from the scheme in Figure 1 may also be formed in the preheat zone of the flame close to the burner. Under some conditions, the flame temperature in this zone can be smaller than 850 K and thus trigger low-temperature oxidation. After leaving the preheat zone, low-temperature species will decompose quickly with rising temperature at the transition to intermediate (850–1200 K) and high-temperature oxidation (>1200 K). The dominant consumption pathway of alkyl hydroperoxides (ROOH) is the decomposition into alkoxy (RO) and OH radicals by dissociation of the oxygen–oxygen bond.[12] At intermediate temperatures, the small peroxide species H_2O_2 contributes to chain branching by decomposing into two OH radicals.[31] Hydrogen peroxide (H_2O_2) itself is stable up to 1100 K and is formed by H-abstraction reactions of HO_2.[13] The first reliable quantification of H_2O_2 formed during LTC was presented by Bahrini et al. for the oxidation of *n*-butane.[32]

Experimental detection of alkyl hydroperoxides in flame-sampling experiments was recently reported by Zhang et al. for ethylene, ethane, propene, and *n*-butane laminar premixed, low-pressure flames.[33] Kinetic modeling of flames with a reaction mechanism that has included low-temperature chemistry and probe-perturbed temperature profiles have shown that these elusive species may be formed closer to the burner,[33] where the flame temperatures are generally lower. Zhang et al. also showed for an ethylene flame that model results can be significantly improved by using the probe-disturbed temperature profile. They concluded that formation of low-temperature species in the preheat zone of their investigated flames originated from the temperature reduction by the sampling probe perturbation.[33] However, concentrations of only some low-temperature related combustion intermediates, for example, ethanol, were affected, while the formation of typical high-temperature combustion intermediates from the reaction zone was not influenced.[33]

We report about the formation of alkyl hydroperoxides, the methylperoxy radical, and cyclic ethers in alkane- (*n*-butane and propane) and alkene-doped (2-butene) hydrogen flames and in a neat propane flame. Species were identified by their PIE and TPE spectra measured by photoelectron photoion coincidence (PEPICO) spectroscopy. For the *n*-butane/H_2 flame, all detected species were quantified so that a comprehensive dataset including low-temperature species is available.

2 | EXPERIMENT

2.1 | Investigated flames

Fuel-rich, laminar premixed hydrogen flames doped with *n*-butane (*n*-C_4H_{10}), *trans*-2-butene (2-C_4H_8), and propane (C_3H_8) and a neat propane flame at the same equivalence ratio (Φ) of 1.25 were investigated at the vacuum ultraviolet (VUV) beamline of the Swiss Light Source. The flames were stabilized on a flat flame burner at 40 mbar and diluted with argon. Argon dilution was 25% and 50% for the hydrocarbon-doped hydrogen flames and the neat propane flame, respectively. Argon (99.998%), O_2 (99.998%), H_2 (99.995%), and propane (99.5%) were delivered by Carbagas, *n*-butane (99.95%) by Air Liquide, and *trans*-2-butene (99.5%) by Linde. To allow for comparable conditions, the three hydrocarbon-doped hydrogen flames had the same C, H, and O flow as used in a previous work.[34] The exact gas flows are summarized in Table 1.

Flame gases were sampled by molecular-beam technique and analyzed by PEPICO spectroscopy as described

TABLE 1 Flame conditions of the hydrocarbon-doped hydrogen flames and the neat propane flame

Flame	Φ	d_{Burner} (mm)	p (mbar)	$v_{298\,K}$ (cm/s)	$\dot{V}_{Hydrocarbon}$ (sccm)	$\dot{V}_{H_2}$ (sccm)	$\dot{V}_{O_2}$ (sccm)	$\dot{V}_{Ar}$ (sccm)
n-C_4H_{10}/H_2	1.25	60	40	65.20	100	1700	1200	1000
2-C_4H_8/H_2	1.25	60	40	66.83	100	1800	1200	1000
C_3H_8/H_2	1.25	60	40	65.20	133	1667	1200	1000
C_3H_8	1.25	60	40	65.20	400	0	1600	2000

in detail in the Supporting Information. Except for the n-butane/H_2 flame, the i^{2}PEPICO setup[35,36] was used for the investigation of the flames. The i^{2}PEPICO setup is also described by Sztáray et al.[36] and Hoener et al.[37] for photolysis and pyrolysis experiments to study reaction kinetics and a new high-pressure reactor experiment, respectively. A schematic sketch of this setup is shown in Figure S1 in the Supporting Information. The n-butane-doped hydrogen flame was measured with the single-imaging photoelectron photoion coincidence (iPEPICO) setup as described by Oßwald et al.[38] for flame-sampling molecular-beam mass spectrometry. The difference between these two setups is that the photoions are also velocity map imaged with the i^{2}PEPICO spectrometer.

Several burner scans, where the photon energies remain constant and the burner positions are varied between 0.25 and 30.25 mm with respect to the sampling probe, were performed in the n-butane/H_2 flame for photon energies of 7.59, 8.5, 9.15, 9.4, 9.7, 10.02, 10.36, 11.5, 12.3, 13.02, 13.7, 14.35, and 16.2 eV. Photon energies are selected to allow for a comprehensive separation of isomers. This flame is part of a series of alkane- and alkene-doped hydrogen flames designed to systematically study the hydrogen abstraction and fuel radical formation.[34] The mole fraction profiles of the 1-butyl and 2-butyl radicals and the major species that are most relevant for the discussion of fuel radical formation and branching ratios were presented previously by Krüger et al.[34] Here, we provide the experimental mole fraction dataset for more than 30 combustion species of the n-butane/H_2 flame within the Supporting Information and focus on the identification and formation of low-temperature species in the following discussion. The large number of photon energies used for the burner scans helps to determine mole fractions of most intermediates at photon energies close to their ionization energies. Burner scans in the n-butane/H_2 flame were performed from 0.25 to 4.25 mm with a step size of 0.25 mm, from 4.25 to 7.25 mm with 0.5 mm steps, from 7.25 to 12.25 mm with 1 mm steps, and from 12.25 to 30.25 mm with 2 mm steps. Energy scans at a fixed height above the burner (HAB) and different photon energies were performed in the preheat zone at HAB of 0.5 and 0.75 mm in the hydrocarbon-doped hydrogen flames and the neat propane flame, respectively. The photon energies were typically between 9 and 11.5 eV for identification of the alkyl hydroperoxides and other combustion intermediates by their PIE or photoelectron spectra. The scan resolution was 25 meV for all energy scans. The photon energy was calibrated by measuring the autoionization states of argon (11s′–13s′) between 15.75 and 15.83 eV in both the first and second order. The procedure for calculation of the mole fraction profiles is described in detail by Oßwald et al. for the flame-sampling setup at the VUV beamline of the Swiss Light Source.[38] Uncertainty of the experimental mole fractions is estimated to be 15–20% for the main species and 30–50% for the intermediate combustion species with known photoionization cross sections. For species with unknown photoionization cross section, the mole fraction uncertainties of a factor of 2–4 can be expected.[39] Overall uncertainties in flame-sampling molecular-beam mass spectrometry were discussed by Egolfopoulos et al.[40]

2.2 | Modeling of the n-butane-doped hydrogen flame

The AramcoMech 2.0 [Ref. 41] by the Combustion Chemistry Centre at NUI Galway was used without modifications for modeling of combustion species mole fraction profiles in the n-butane/H_2 flame. This mechanism builds upon the AramcoMech 1.3 [Ref. 42] and contains low-temperature and high-temperature chemistry for hydrogen, C_1–C_4 hydrocarbons and some oxygenated fuels. It was well validated against numerous experiments including flames, jet-stirred reactors, and shock tubes and therefore covers a wide range of different combustion parameters reliably. It was shown by Jithin et al.[43] that the AramcoMech 2.0 provides good agreement to capture the effect of hydrogen addition in the laminar burning velocity of n-butane/air flames. For autoignition, Jiang et al.[44] and Lee and Song[45] showed that the AramcoMech 2.0 is also able to predict ignition delay times of hydrogen/n-butane mixtures measured in a shock tube and with a rapid compression machine, respectively. It is expected that this model performs well for the investigation of the low-temperature chemistry in our n-butane-doped hydrogen flame.

We used the Cantera flame reactor module for burner-stabilized flames within the Chemical Workbech[46]

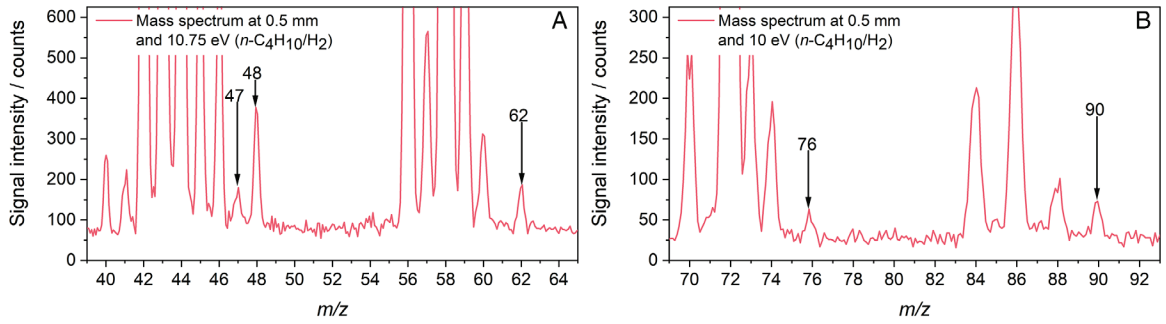

FIGURE 2 (A) Mass spectra at 10.75 and (B) 10 eV obtained for the *n*-butane/H_2 flame at a distance of 0.5 mm from the burner surface

(Kintech Lab) for the chemical kinetics simulation with the AramcoMech 2.0. The multicomponent transport model considering thermodiffusion was used. The experimentally determined temperature profile reported by Krüger et al.[34] for the *n*-butane/H_2 flame was used as input for the simulation. The exhaust gas temperature of the *n*-butane-doped hydrogen flame was measured by a coated thermocouple, and the temperature profile was then determined from the temperature dependence of the gas flow through the sampling nozzle to obtain a probe-perturbed temperature profile.[34] The experimental mole fraction profiles of the major species were well predicted by the ArmacoMech 2.0 using this temperature profile as shown by Krüger et al.[34]

3 | RESULTS AND DISCUSSION

The focus of this study is on the identification of some low-temperature species for a series of hydrocarbon-doped hydrogen flames and in a neat propane flame investigated by molecular-beam mass spectrometry. PIE and TPE spectra are used in the following to identify low-temperature species. At *m/z* 47, 48, 62, 76, and 90, the methylperoxy radical and alkyl hydroperoxides have been identified. Furthermore, the isomer composition of other oxygenates at *m/z* 44, 58, and 72 are explored. For the *n*-butane/H_2 flame, only PIE spectra of the low-temperature species can be presented, because the signal intensity was too low to obtain high-quality TPE spectra. For the other flames, averaging times were increased to successfully record TPE spectra of low-temperature species. These are presented here. For the sake of brevity, not all measured spectra from the four flames are shown. Identification is accompanied by the interpretation of possible reaction pathways obtained from AramcoMech 2.0.[41] This mechanism is suitable for reproducing the mole fractions of many stable C_1-C_4 combustion intermediates measured in the *n*-butane/H_2 flame (see Figure S2 and discussion in the Supporting Information). The further focus is therefore on quantification of alkyl hydroperoxides and other oxygenated combustion intermediates to provide more insights into their combustion kinetics. For example, the formation of 2,3-butanedione is observed, that is, a species that is not included in the kinetic model.

3.1 | Identification of low-temperature species in the four investigated flames

Figure 2 shows the mass spectra obtained at 10.75 and 10 eV for the *n*-butane-doped hydrogen flame at a distance of 0.5 mm from the burner surface. This position corresponds to a flame temperature of about 708 K considering the experimental temperature profile provided by Krüger et al.[34] As mentioned above, the probe-perturbed temperature profile was obtained from the temperature dependence of the gas flow through the sampling probe by using a measured exhaust gas temperature. Peaks at *m/z* 48, 62, 76, and 90 indicate the formation of alkyl hydroperoxides under the investigated conditions in the *n*-butane/H_2 flame, while the signal at *m/z* 47 is assigned to the methylperoxy radical (CH_3OO), as discussed below. The alkyl hydroperoxides follow the trend of decreasing ionization energy with increasing number of carbon atoms. Averaging times were 240 and 600 s for the mass spectra in Figure 2 at 10.75 and 10 eV, respectively, in order to get a good signal-to-noise ratio. PIE spectra of the alkyl hydroperoxides are known from JSR measurements of various fuels, for example, dimethyl ether,[47] *n*-butane[20] or propane,[22] and are used for comparison with our flame-sampled spectra. Furthermore, the PIE spectrum of the methylperoxy radical was experimentally determined by Meloni et al.[48]

3.1.1 | Detection and identification of *m/z* 47: The methylperoxy radical (CH_3OO)

Figure 3A shows the experimental PIE spectra of *m/z* 47 in the *n*-butane/H_2 and 2-butene/H_2 flame in comparison with the measured PIE spectrum of the methylperoxy

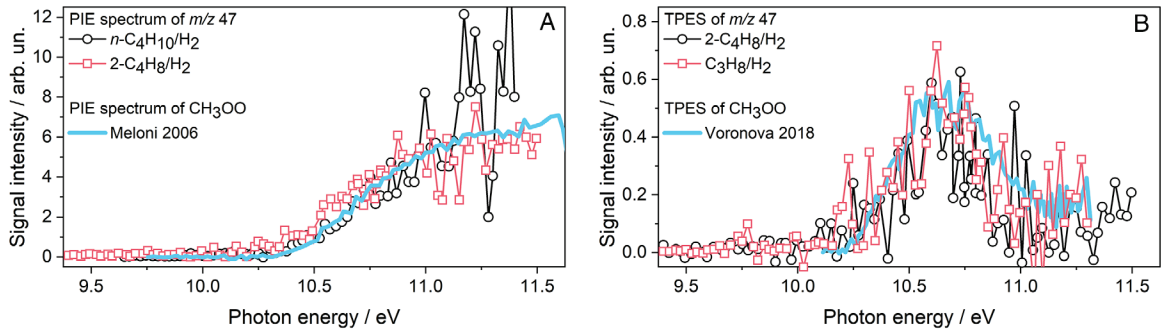

FIGURE 3 (A) Flame-sampled PIE spectra of *m/z* 47 in comparison with the PIE spectrum of the methylperoxy radical (CH_3OO) by Meloni et al.[48] (B) Flame-sampled TPE spectrum of *m/z* 47 in comparison with the TPE spectrum of the methylperoxy radical (CH_3OO) by Voronova et al.[50]

radical (CH_3OO) by Meloni et al.[48] The adiabatic ionization energy of 10.33 eV for the CH_3OO radical from Meloni et al.[48] is in good agreement with the onset of our PIE spectra confirming the formation of CH_3OO in the flame. The signal at *m/z* 47 was corrected for contributions of the ^{13}C isotope of *m/z* 46. Fragmentation of the methyl hydroperoxide to *m/z* 47 starts at higher photon energies of 11.4 eV as shown by Covert et al. who investigated the dissociative photoionization process of methyl hydroperoxide.[49] The comparison of the measured TPE spectra of *m/z* 47 from the 2-butene- and propane-doped hydrogen flame with the TPE spectrum of CH_3OO by Voronova et al.[50] also confirms clearly the formation of the CH_3OO radical in the flame as seen in Figure 3B. In low-temperature oxidation, alkylperoxy radicals are formed by oxidation of the corresponding alkyl radical with molecular oxygen. These radicals can subsequently react to alkyl hydroperoxides or isomerize (for ROO with R > CH_3) by internal hydrogen transfer to hydroperoxyalkyl radicals (QOOH), which are very weakly bound species.[13] The QOOH radical can undergo a second oxygen addition and chain branching. In the flame environment, where the temperature strongly rises, the formation of alkyl hydroperoxides is expected. No species related to the second oxygen addition, for example, keto hydroperoxides, were observed under the investigated conditions. However, the formation of alkyl hydroperoxides can be confirmed as discussed in the following. The lack of higher alkylperoxy radical signal in the measurements is not contrary to the presence of higher alkyl hydroperoxides in the flame, because these radicals have unstable cations as corroborated by Meloni et al.[48] The mass spectrometric detection is therefore not feasible.

3.1.2 | Detection and identification of *m/z* 48: Methyl hydroperoxide (CH_3OOH)

The smallest alkyl hydroperoxide is methyl hydroperoxide (CH_3OOH) with *m/z* 48. The measured PIE spectra at this mass-to-charge ratio from the *n*-butane/H_2 and 2-butene/H_2 flame are presented in Figure 4A. They show an onset slightly below 9.9 eV, which matches well to the adiabatic ionization energies of 9.77 and 9.83 eV for methyl hydroperoxide calculated at two different levels of theory by Moshammer et al.[47] They identified this hydroperoxide during oxidation of dimethyl ether in a jet-stirred reactor by photoionization mass spectrometry.[47] Their measured PIE spectrum with the onset at 9.85 eV is also shown in Figure 4A and confirms the formation of methyl hydroperoxide in the investigated flames. The only possible second isomer is methanediol ($HOCH_2OH$), which has a distinctly larger ionization energy. The calculated ionization energy of methanediol depends on its conformer and lies between 10.33 and 11 eV.[47] Because no significant rise in the PIE spectra of *m/z* 48 is observed in this energy range, the formation of detectable quantities of methanediol under our investigated conditions can be excluded at this position in the flame. Our calculation of the adiabatic ionization energy at the G4 [Ref. 51] level of theory with Gaussian 16 [Ref. 52] gives a value of 10.99 eV for the trans-conformer of methanediol. A Franck–Condon (FC) simulation at 500 K was performed with the program ezSpectrum[53] and is presented together with the TPE spectra of *m/z* 48 measured in the 2-butene/H_2 and propane/H_2 flames in Figure 4B. The TPE spectra show a rise at the adiabatic ionization energy of methyl hydroperoxide and have a broad band as observed in typical photoelectron spectra of alkanes and in the TPE spectrum of the CH_3OO radical. The FC simulation for the trans-conformer of methanediol shows a well-structured spectrum but does not overlap with our measured flame-sampled spectra. Recently, Bourgalais et al. measured a TPE spectrum of *m/z* 48 during the low-temperature oxidation of *n*-pentane in a JSR at a temperature of 585 K and identified methyl hydroperoxide.[30] Their spectrum shows a threshold at about 9.8 eV (see Figure 4B) with a slightly more pronounced maximum at 10.8 eV. The overall spectrum has a similar width as our spectrum. The presence of another conformer of methanediol could be

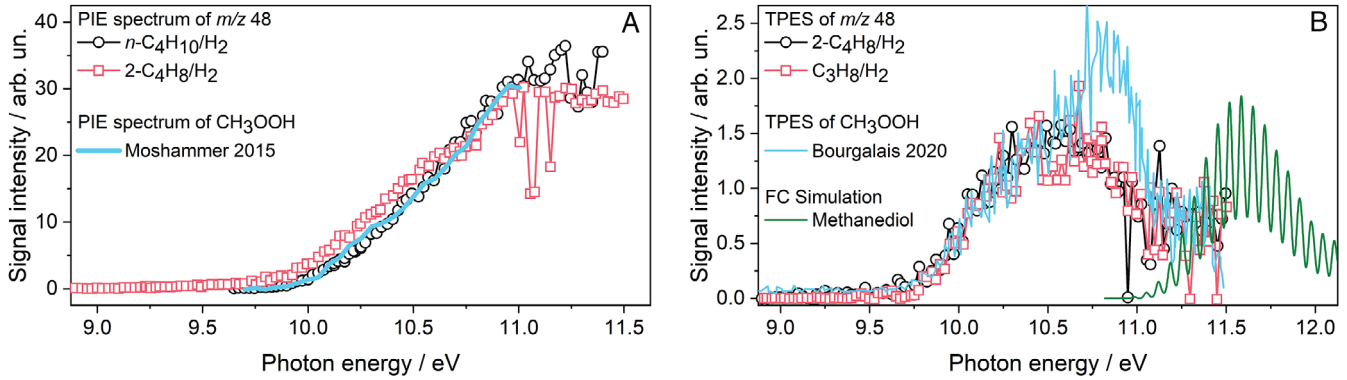

FIGURE 4 (A) Flame-sampled PIE spectra of m/z 48 in comparison with the PIE spectrum of the methyl hydroperoxide (CH_3OOH) by Moshammer et al.[47] (B) Flame-sampled TPE spectra of m/z 48 in comparison with the TPE spectrum of CH_3OOH by Bourgalais et al.[30] and a FC simulation of methanediol

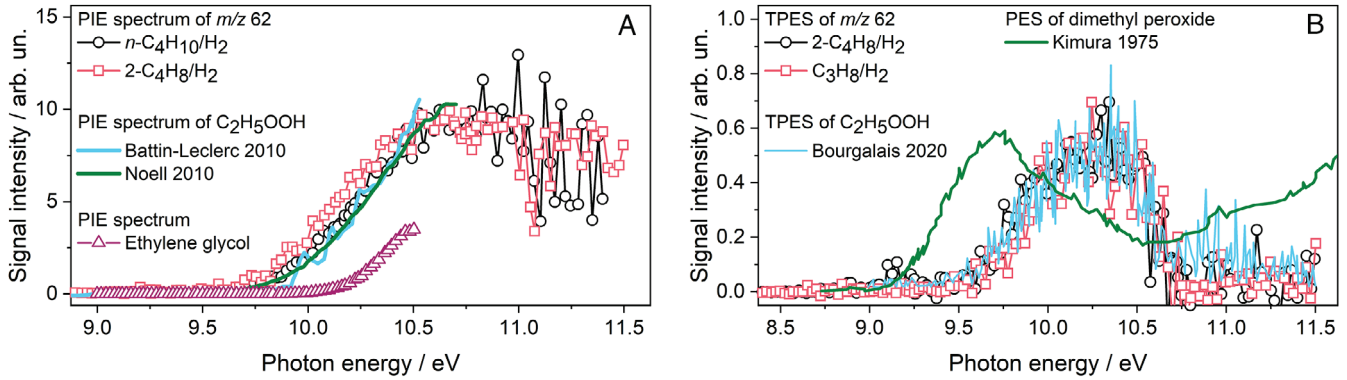

FIGURE 5 (A) Flame-sampled PIE spectra of m/z 62 in comparison with the PIE spectrum of the ethyl hydroperoxide (C_2H_5OH) by Battin-Leclerc et al.[20] and Noell[54] and our measured PIE spectrum of ethylene glycol. (B) Flame-sampled TPE spectra of m/z 62 in comparison with the TPE spectrum of C_2H_5OOH by Bourgalais et al.[30] and the PES of dimethyl peroxide by Kimura and Osafune[55]

conceivable here and may explain the differences in the spectra.

3.1.3 | Detection and identification of m/z 62: Ethyl hydroperoxide (C_2H_5OOH)

Ethyl hydroperoxide (C_2H_5OOH) with m/z 62 is the next member of the homologous series of alkyl hydroperoxides. Figure 5 shows our measured PIE spectra of m/z 62 obtained from the *n*-butane- and 2-butene-doped hydrogen flame and the TPE spectra of the same m/z ratio from the 2-butene/H_2 and propane/H_2 flame. Ethyl hydroperoxide was identified during the low-temperature oxidation of *n*-butane by Battin-Leclerc et al.[20] and their JSR-sampled PIE spectrum matches well with our flame-sampled PIE spectrum showing that ethyl hydroperoxide is also formed in flames. Noell has studied the self-reactions of C_2H_5OO by time-resolved photoionization mass spectrometry and also measured the PIE spectrum of ethyl hydroperoxide.[54] The PIE spectrum reported by Noell has the same onset at about 9.6 eV and a matching shape. The flame-sampled TPE spectra of m/z 62 from Figure 5B also match the experimental TPE spectrum of the ethyl hydroperoxide from the work of Bourgalais et al.[30] and additionally confirms the formation of this smaller alkyl hydroperoxide in the flame-sampling experiment.

Other stable, oxygenated species are theoretically possible at m/z 62, but can be excluded due to the following reasons. Isobaric species with the elemental composition CH_2O_3 have significantly higher calculated ionization energies than the observed onset, that is, 10.87 eV for methaneperoxoic acid and 11.29 eV for carbonic acid.[47] The two isomers of ethyl hydroperoxide with the elemental composition $C_2H_6O_2$ also have higher ionization energies. The PIE spectrum of ethylene glycol ($HOCH_2CH_2OH$) was directly measured by us at the Swiss Light Source and is shown in Figure 5A. The PIE spectrum does not fit to

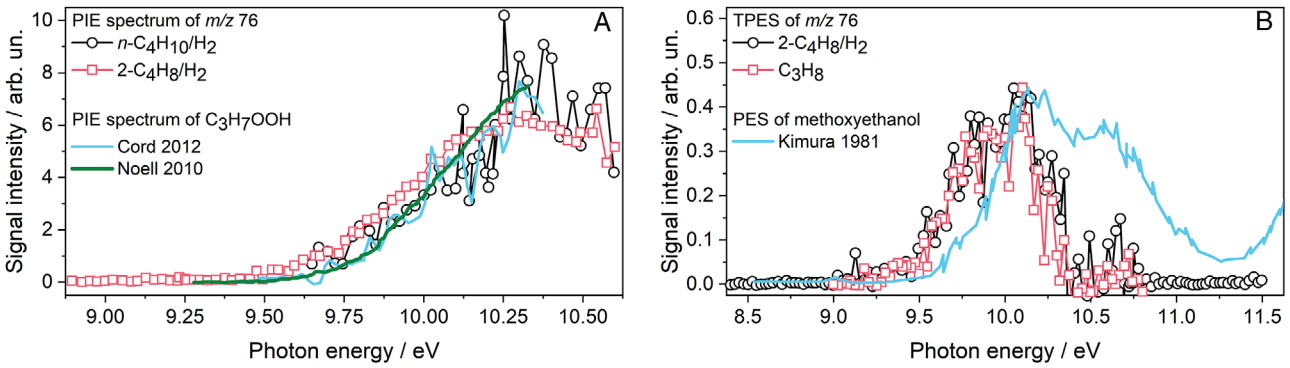

FIGURE 6 (A) Flame-sampled PIE spectra of *m/z* 76 in comparison with the PIE spectrum of propyl hydroperoxide (C_3H_7OOH) by Cord et al.[22] and Noell.[54] (B) Flame-sampled TPE spectra of *m/z* 76 in comparison with the PES of methoxyethanol by Kimura et al.[57]

the flame-sampled spectrum, and no onset at the adiabatic ionization energy is observed so that formation of ethylene glycol can be excluded. No experimental value for the ionization energy of methoxymethanol (CH_3OCH_2OH) is reported in the literature, but ionization energy of 10.05 eV calculated by Moshammer et al.[47] is higher than the observed onset. A third isomer is dimethyl peroxide (CH_3OOCH_3) with an adiabatic and vertical ionization energy of 9.1 and 9.71 eV, respectively.[55] The photoelectron spectrum (PES) of dimethyl peroxide is shown in Figure 5B, and the comparison with our measured TPE spectra clearly shows that this isomer is absent in the investigated flames. The position of the first band in the PES of dimethyl peroxide is at significantly lower photon energy than the observed band in the flame-sampled TPE spectra of *m/z* 62.

3.1.4 | Detection and identification of *m/z* 76: Propyl hydroperoxides (C_3H_7OOH)

For propyl hydroperoxide and larger alkyl hydroperoxides, regioisomers have to be considered. To clarify, the sum of *n*-propyl and isopropyl hydroperoxide is defined as propyl hydroperoxide (C_3H_7OOH). Flame-sampled PIE and TPE spectra of *m/z* 76 are presented in Figure 6. One PIE spectrum of propyl hydroperoxide was taken from the work of Cord et al., who identified intermediates at *m/z* 76 during the low-temperature oxidation of propane as the sum of both isomers and also calculated adiabatic ionization energies of 9.5 and 9.42 eV for *n*-propyl and isopropyl hydroperoxide, respectively.[22] The second PIE spectrum of propyl hydroperoxide presented in Figure 6A with the onset of 9.6 eV was measured by Noell during the dissociative ionization of the propylperoxy radical.[54] The onset in our flame-sampled PIE spectra is about 9.5 eV and in good agreement with the literature PIE spectra. One isomer with known ionization energy in the energy range of the observed onset is dimethoxymethane (methylal), but it does not have a stable parent ion at *m/z* 76 and directly undergoes dissociation losing hydrogen to form the fragment ion at *m/z* 75.[56] A second isomer is methoxyethanol ($CH_3OC_2H_5OH$) with a vertical ionization energy of 10.13 eV.[57] This value would agree with the second peak in the measured TPE spectra in Figure 6B, but the band in the PES of methoxyethanol is broader and does not match to our spectra. It is important to note that the shape of conventional photoelectron spectra can differ from the mass-selected TPE spectra, especially when the molecule undergoes dissociative photoionization. The observed sharp signal drop in the measured TPE spectra may be caused by such a dissociative photoionization process of the propyl hydroperoxides or the methoxyethanol. Therefore, the presence of methoxyethanol cannot be completely excluded. From a chemical point of view, the formation of the propyl peroxides is more likely and its formation is further supported by the matching of the literature PIE spectra and the presence of the smaller alkyl hydroperoxides, which were clearly identified. The same conclusions apply to the butyl and butenyl hydroperoxides discussed below. The two observed peaks at about 9.85 and 10.1 eV in Figure 6B may therefore represent the two propyl hydroperoxide isomers, which are formed from the reaction of the *n*-propyl and isopropyl radical with molecular oxygen. No experimental or theoretical photoelectron spectra are available in the literature for propyl hydroperoxide. Our TPE spectrum of *m/z* 43 clearly shows that both radicals, that is, *n*-propyl and isopropyl hydroperoxide, are formed in the propane-doped hydrogen flame, and the onset in the PIE spectra of *m/z* 43 from the *n*-butane- and 2-butene-doped hydrogen flame at least shows that the isopropyl radical is present (spectra not shown here).

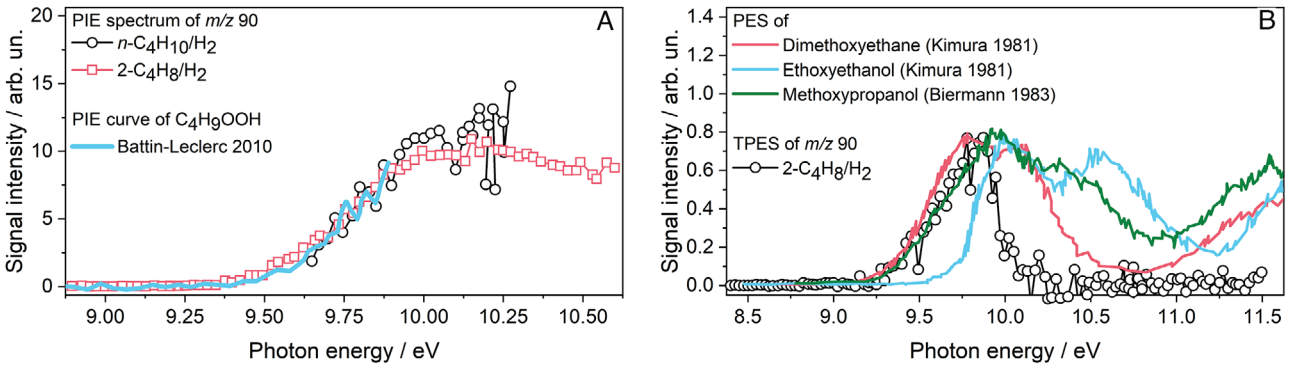

FIGURE 7 (A) Flame-sampled PIE spectra of *m/z* 90 in comparison with the PIE spectrum of butyl hydroperoxide (C_4H_9OOH) by Battin-Leclerc et al.[20] (B) Flame-sampled TPE spectra of *m/z* 90 in comparison with the photoelectron spectra of dimethoxyethane and ethoxyethanol by Kimura et al.[57] and methoxypropanol by Biermann and Morton[58]

3.1.5 | Detection and identification of *m/z* 90: Butyl hydroperoxides (C_4H_9OOH)

Butyl hydroperoxide can only be found in the C_4-doped hydrogen flames where butyl radicals are formed by hydrogen abstraction from *n*-butane or by hydrogen addition to 2-butene. Krüger et al.[34] investigated the hydrogen abstraction for the *n*-butane-doped flame in detail and observed that the secondary 2-butyl radical and the primary 1-butyl radical are formed in equal amounts with maximum mole fractions of 1.7×10^{-5}. Taking into account the number of primary and secondary C–H bonds in *n*-butane, there is a stronger preference towards abstraction of a hydrogen atom from a secondary carbon atom.[34] For the 2-butene flame, the PIE and the TPE spectra of *m/z* 57 indicate that at least the 2-butyl radical is formed (spectra not shown here). In principle, four butyl hydroperoxide isomers exist, but only the formation of 1-butyl and 2-butyl hydroperoxide is expected due to the structure of the investigated C_4 fuels. Figure 7 shows the flame-sampled PIE spectra of *m/z* 90 from the two C_4-doped hydrogen flames and the TPE spectrum of *m/z* 90 from the 2-butene/H_2 flame. Battin-Leclerc et al. investigated the oxidation of *n*-butane in a JSR and concluded that butyl hydroperoxide is formed at *m/z* 90 due to accordance with their observed onset in the PIE spectrum with calculated ionization energies of 1-butyl and 2-butyl hydroperoxide and the sharp peak in the mole fraction profile, which is typical for very reactive molecules that decompose quickly when temperature increases.[20] Their PIE spectrum matches well to our flame-sampled PIE spectra as seen in Figure 7A. Further isomers are possible, and photoelectron spectra of species with known ionization energy (IE) close to the observed onset at 9.4 eV, that is, dimethoxyethane,[57] ethoxyethanol,[57] and methoxypropanol,[58] are shown in Figure 7B in comparison to the TPE spectrum of *m/z* 90 measured in the 2-butene/H_2 flame. The first band in the photoelectron spectra of these species is significantly broader than our measured TPE spectrum, but dissociative photoionization cannot be excluded as discussed for the identification of the propyl hydroperoxides. Ashmore and Burgess recorded the photoelectron spectra of larger alkyl hydroperoxides (C_4–C_7) and measured an adiabatic ionization energy of 9.36 eV and a vertical ionization energy of 9.75 eV for 1-butyl hydroperoxide, but spectra were not reported in their work.[59] However, they mentioned that the photoelectron spectra of the *n*-alkyl hydroperoxides resemble those of the normal alcohols.[59] In addition, the values for the adiabatic and vertical ionization energy match to our measured spectra. The vertical ionization energy of *tert*-butyl hydroperoxide is 10.24 eV,[60] which is significantly higher than our measured maximum. The formation of *tert*-butyl hydroperoxide is therefore not expected, and this result corroborates our assertion that only 1-butyl and 2-butyl radicals are formed.

3.1.6 | Detection and identification of *m/z* 55 and 88: The 1-methylallyl radical and butenyl hydroperoxides

2-Butene is the only alkene whose combustion was studied here. The direct fuel radicals formed by hydrogen abstraction are C_4H_7 and the TPE spectrum in Figure 8A clearly shows that the resonance-stabilized 1-methylallyl radical is solely formed. Our measured TPE spectrum of *m/z* 55 from the 2-butene/H_2 flame perfectly matches to the experimentally determined TPE spectrum of the 1-methylallyl radical by Lang et al.[61] who used 3-penten-1-yl nitrite as precursor to generate the *z*-conformer of 1-methylallyl. They observed both conformers, because the rotational barrier for isomerization is very low.[61] Figure 8A also displays the convolution of the FC simulation for the two conformers, that is, (*E*)-1-methylallyl and (*Z*)-1-methylallyl, and their

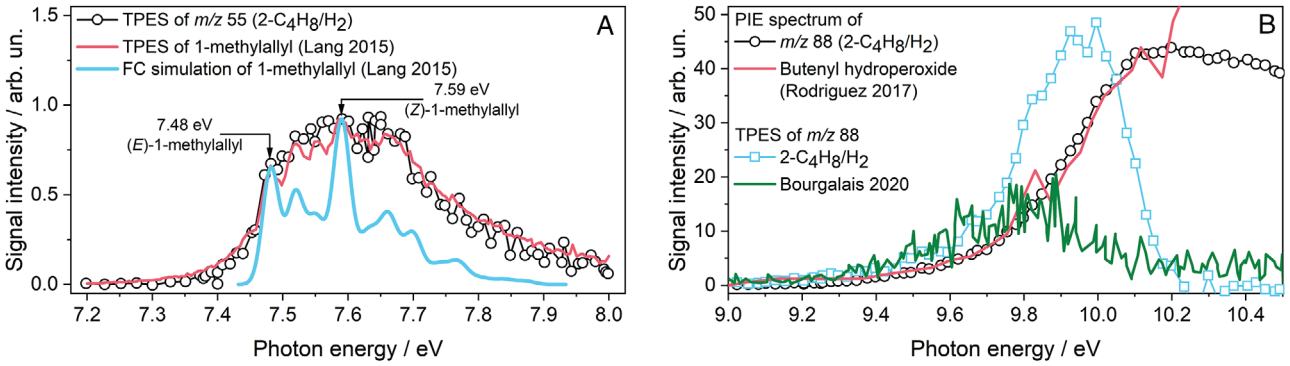

FIGURE 8 (A) Flame-sampled TPE spectrum of *m/z* 55 in comparison with a measured TPE spectrum and a FC simulation of the 1-methylallyl radical by Lang et al.[61] (B) Flame-sampled PIE and TPE spectrum of *m/z* 88 in comparison with the PIE spectrum of butenyl hydroperoxide by Rodriguez et al.[27] and a JSR-sampled TPE spectrum of *m/z* 88 from the oxidation of *n*-pentane by Bourgalais et al.[30]

adiabatic ionization energy from the work of Lang et al.[61] We used *trans*-2-butene for our flame investigations and were able to observe the formation of both conformers of the 1-methylallyl radical.

Principally, alkenyl hydroperoxides can also be formed during the low-temperature oxidation analogous to the formation of alkyl hydroperoxides. For example, Rodriguez et al. identified allyl hydroperoxide (C_3H_5OOH) at *m/z* 74, butenyl hydroperoxides (C_4H_7OOH) at *m/z* 88, and pentenyl hydroperoxides (C_5H_9OOH) at *m/z* 102 during the oxidation of *n*-pentane in a jet-stirred reactor.[27] They also detected C_3–C_7 alkenyl hydroperoxides during the oxidation of *n*-heptane and C_3–C_6 and C_9–C_{10} alkenyl hydroperoxides during the oxidation of *n*-decane.[28] From the observation that only the resonance-stabilized 1-methylallyl radical is formed in the 2-butene/H_2 flame, we would expect the formation of but-1-enyl 3-hydroperoxide and but-2-enyl 1-hydroperoxide. The PIE and TPE spectra of *m/z* 88 from the 2-butene/H_2 flame are shown in Figure 8B. The observed onset in the PIE spectrum and the general shape up to 10.2 eV fit well to the measurement of butenyl hydroperoxides in the *n*-pentane oxidation by Rodriguez et al.[27] The onset of our measured PIE spectrum is at 9.2 eV. This value is in accordance with our calculation of 9.18 eV for the adiabatic ionization energy of but-2-enyl 1-hydroperoxide. The presence of but-1-enyl 3-hydroperoxide is also possible, because the calculated ionization energy of this isomer is somewhat higher than 9.33 eV. Adiabatic ionization energies of these two isomers were calculated in this work at the CBS-QB3 level of theory with Gaussian 16.[52] Bourgalais et al. measured a TPE spectrum of *m/z* 88 during oxidation of *n*-pentane in a JSR at 585 K[30] (see Figure 8B). Since their spectrum overlapped to an FC analysis of the but-1-enyl 3-hydroperoxide, they concluded that this isomer may be formed during *n*-pentane oxidation. The onset in our TPE spectrum of *m/z* 88 matches to the onset in the JSR-sampled TPE spectrum and confirms the presence of but-1-enyl 3-hydroperoxide in the 2-butene/H_2 flame. This accordance and the well-reproduced experimental PIE spectrum by the literature data let us conclude that butenyl hydroperoxides are formed under the investigated conditions. However, the observed maximum at about 10 eV in the TPE spectrum is not reproduced and a further species may be present in the 2-butene/H_2 flame. Isomers with known ionization energies are butanoic acid, *n*-propyl formate, and methyl propionate, but their adiabatic ionization energies at 10.17, 10.54, and 10.15 eV[62] are larger than 10 eV. The mass resolution of the endstation does not allow a determination of the exact elemental composition. Besides the formation of $C_4H_8O_2$ isomers, the formation of $C_5H_{12}O$ isomers, which are mostly ethers and alcohols, is principally possible requiring further investigations. A signal at *m/z* 88 is also observed in the *n*-butane-doped hydrogen flame as seen in the mass spectrum of Figure 2B. No information about the onset in the PIE spectrum of *m/z* 88 from the *n*-butane/H_2 flame is available, because the energy scan was started above the ionization energy of the butenyl hydroperoxides. Due to the observation of the 1-methylallyl radical in the *n*-butane/H_2 flame, the formation of butenyl hydroperoxides can be inferred as likely in this flame.

3.1.7 | Detection and identification of *m/z* 44 and 58: Cyclic ethers and common oxygenates

Besides the formation of alkyl hydroperoxides from alkylperoxy radicals, chain-propagation of QOOH radicals is also likely in the low-temperature oxidation and may lead to cyclic ethers and OH,[13] for example, oxetane and methyloxirane from $CH_2CH_2CH_2OOH$ and

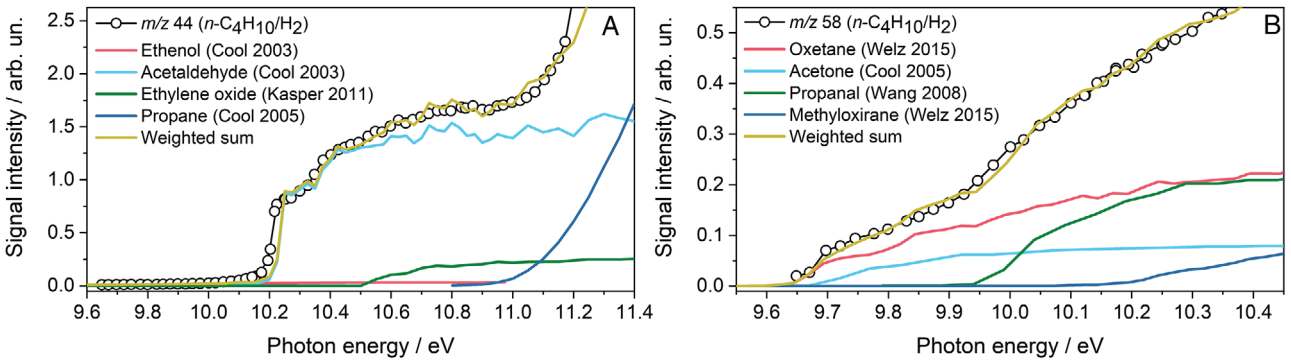

FIGURE 9 (A) PIE spectrum of *m/z* 44 from the *n*-butane/H_2 flame in comparison with PIE spectra of ethenol,[63] acetaldehyde,[63] ethylene oxide,[64] and propane[65] and with a weighted sum. (B) PIE spectrum of *m/z* 58 from the *n*-butane/H_2 flame in comparison with PIE spectra of oxetane,[23] acetone,[66] propanal,[67] and methyloxirane,[23] and with a weighted sum

CH_3CHCH_2OOH, respectively. The QOOH radicals are generally formed by isomerization via internal hydrogen abstraction from the corresponding alkylperoxy radical.[13] Therefore, the observation of cyclic ethers would be further evidence for the low-temperature oxidation in flames. Figure 9 displays the flame-sampled PIE spectra of *m/z* 44 and 58. Oxygenated three- and four-ring species are expected at these mass-to-charge ratios during low-temperature oxidation. For *m/z* 44, the best fit is a weighted sum of the photoionization spectra of ethenol,[63] acetaldehyde,[63] ethylene oxide,[64] and propane.[65] Considering only the three C_2H_4O isomers, the percentages are 1.4% ethenol, 83% acetaldehyde, and 15.6% ethylene oxide. Only one cyclic ether can be formed from the OH loss of C_2H_4OOH, while for C_3H_6OOH two regioisomers are possible and the formation of oxetane and methyloxirane must be considered. The flame-sampled PIE spectrum is the best fit of the PIE spectra of oxetane,[23] acetone,[66] propanal,[67] and methyloxirane[23] in the energy range of 9.65 and 10.35 eV. The percentages for the four isomers at this position (i.e., HAB of 0.5 mm) in the energy scan are 38.4% for oxetane, 10.8% for acetone, 35.4% for propanal, and 15.4% for methyloxirane. Mole fraction profiles of oxetane and methyloxirane could not be separated from acetone and propanal, respectively. However, reliable mole fraction profiles of the two isomer pairs oxetane and acetone and methyloxirane and propanal are determined with the ratios from the energy scan. At 0.5 mm, the mole fractions are 1.4×10^{-4} (oxetane and acetone) and 5.4×10^{-5} (methyloxirane and propanal). These values show the relevance of low-temperature oxidation products under the investigated conditions. PIE spectra of both *m/z* 44 and 58 reveal contributions of cyclic ethers, that is, ethylene oxide, oxetane, and methyloxirane. Rate of production analyses at HAB of 0.5 and 0.75 mm indicate that ethylene oxide is directly formed from the ethylperoxy radical ($C_2H_5O_2 = C_2H_4O1$-2 + OH), while oxetane and methyloxirane originate from the decomposition of C_3H_6OOH radicals. In detail, oxetane (C_3H_6O1-3) is only formed by decomposition of the $CH_2CH_2CH_2OOH$ radical (C_3H_6OOH1-3 = C_3H_6O1-3 + OH) and methyloxirane (C_3H_6O1-2) from decomposition of CH_3CHCH_2OOH (C_3H_6OOH1-2 = C_3H_6O1-2 + OH) and $CH_2CH(CH_3)OOH$ radicals (C_3H_6OOH2-1 = C_3H_6O1-2 + OH). Welz et al. also concluded for the low-temperature oxidation of propane that the oxygenated cyclic species oxetane and methyloxirane can only be formed by QOOH radicals.[23] Thus, the observation of these species is an indication of the low-temperature chemistry in our investigated flame.

3.1.8 | Detection and identification of *m/z* 72 and 86: Ketones

Besides the formation of expected small oxygenated combustion intermediates like formaldehyde and acetaldehyde, larger C_4 oxygenates were identified by their photoelectron spectra in the 2-butene/H_2 flame as shown in Figure 10. The recorded TPE spectrum of *m/z* 72 has an intensive peak at 9.52 eV and a smaller band at 9.67 eV. The TPE spectrum of butanone ($C_2H_5COCH_3$) measured by Kercher et al.[68] fits perfectly to the flame-sampled spectrum indicating that this species is formed in the flame at HAB of 0.5 mm. The formation of butanone may result from the decomposition of the 2-C_4H_8OOH radical and competes with the formation of cyclic ethers (2,3-dimethyloxirane, 2-methyloxetane, or 2-ethyloxirane).[26] The ionization energy of 2-methyloxetane is close to the value of butanone, while 2,3-dimethyloxirane (9.8 eV) and 2-ethyloxirane have higher ionization energies.[26] Our spectrum does not show any contributions from other species at *m/z* 72. Similar observations were made for the

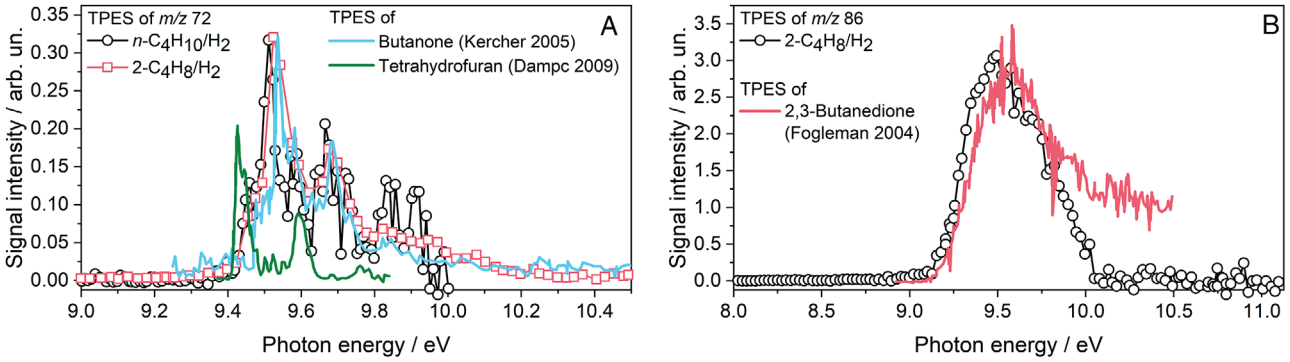

FIGURE 10 TPE spectra of *m/z* 72 and 86 recorded in C_4 hydrocarbon-doped flames in comparison with the TPE spectra of tetrahydrofuran,[69] butanone,[68] and 2,3-butanedione[70]

n-butane/H_2 flame. The TPE spectrum of *m/z* 72 from the *n*-butane-doped hydrogen flame is also plotted in Figure 10. However, peak positions of the two major bands of butanone could not be replicated sufficiently. There is a redshift of about 0.02 eV, but the peak intensities are well represented. This spectrum was recorded at HAB of 0.75 mm. As already discussed, 1-butyl and 2-butyl radicals are formed in the oxidation of *n*-butane. Additional decomposition products of the 1-C_4H_8OOH must therefore be considered, for example, tetrahydrofuran (THF) and *n*-butanal (C_3H_7CHO). Ionization energies of THF and *n*-butanal are 9.4 and 9.82 eV, respectively.[62] The TPE spectrum of THF measured by Dampc et al.[69] mismatches our flame-sampled TPE spectrum (see Figure 10). No information about the PE or TPE spectrum of 2-methyloxetane is given in the literature. Since its ionization energy is close to butanone, minor contributions cannot be excluded. Eskola et al. investigated detailed product formation in the low-temperature oxidation of *n*-butane by using deuterated butane (*n*-butane-d_6 and *n*-butane-d_4) in time-resolved experiments.[26] When considering their individual photoionization spectra of C_4H_8 isomers, our PIE spectrum of *m/z* 72 from the *n*-butane/H_2 flame is best represented by a weighted sum of butanone and 2-methyloxirane up to the ionization energy of *n*-butanal (spectrum not shown here). However, butanone seems to be the major combustion intermediate at *m/z* 72 for both C_4 fuels. Butanone was also the sole combustion product at *m/z* 72 in the low-temperature oxidation of *n*-pentane.[30]

2,3-Butanedione ($C_4H_6O_2$), also known as diacetyl, is a second C_4 oxygenate, which can be identified by its TPE spectrum (see Figure 10). The spectrum was recorded in the 2-butene/H_2 flame and is well represented by the TPE spectrum of the pure substance by Fogleman et al.[70] A small difference can be seen starting from 9.85 eV, where our spectrum drops more sharply. The spectrum differs from butanone and has a very broad band. The ionization energy was determined to be 9.21 eV.[70] The TPE spectrum of *m/z* 86 in the *n*-butane/H_2 flame had a low signal-to-noise ratio, but the shape of the PIE curve and the onset at about 9.2 eV agree with the PIE spectrum from the 2-butene/H_2 flame. It is therefore likely that 2,3-butanedione is also the major combustion intermediate at *m/z* 86 in the *n*-butane/H_2 flame under the investigated conditions.

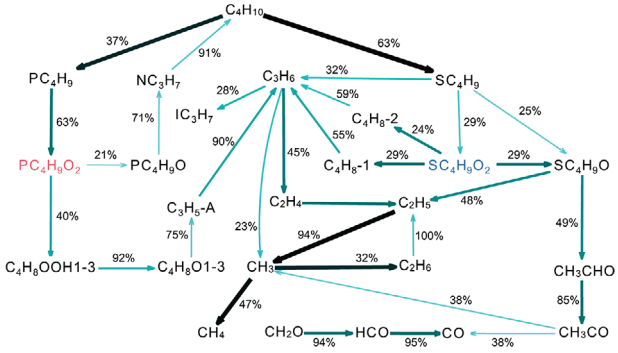

FIGURE 11 Reaction path analysis for the *n*-butane/H_2 flame at HAB of 1 mm (766 K). Thickness of arrows represents the carbon flux from one species to another. Only carbon fluxes above 10% of the total carbon flux are shown. Percentages next to arrows give individual contributions to the consumption of a species

3.2 | Reaction path analysis and quantification of low-temperature species in the *n*-butane-doped hydrogen flame

Figure 11 shows a reaction path analysis for the *n*-butane/H_2 flame to identify the main consumption pathway of the fuel. The analysis was done for a HAB of 1 mm at 766 K, where the temperature is still in the low-temperature regime and half of the *n*-butane is already consumed. The thickness of the arrows represents the carbon flux from one species to another. Only carbon fluxes above 10% of the total flux are presented. Percentages

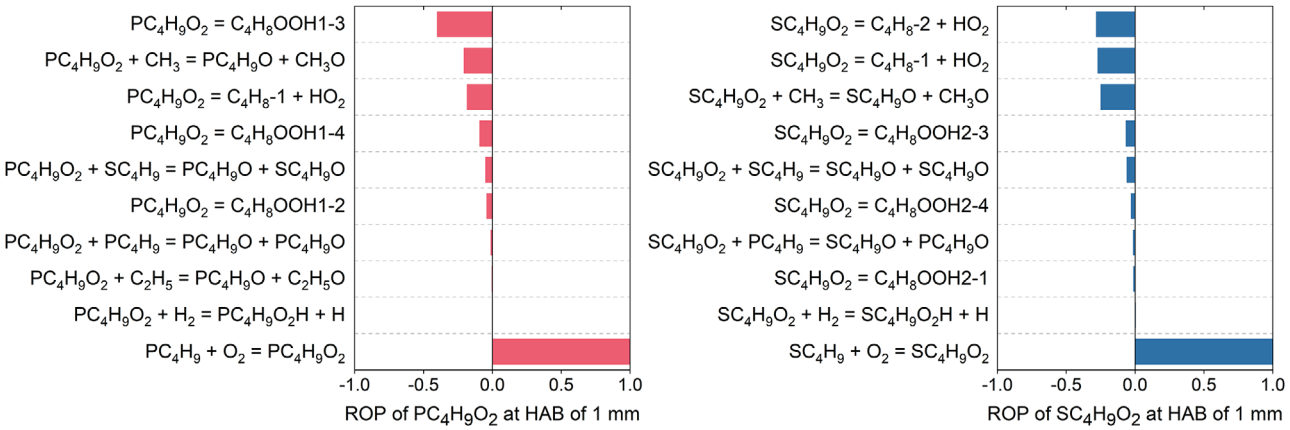

FIGURE 12 Rate of production analyses of the 1-butylperoxy ($PC_4H_9O_2$) and 2-butylperoxy radical ($SC_4H_9O_2$)

next to arrows give individual contributions to the consumption of a species. Fuel decay starts by hydrogen abstraction, preferably forming 2-butyl radicals (SC_4H_9). The ratio between 1-butyl (PC_4H_9) and 2-butyl radicals is about 40:60. For both fuel radicals, the formation of the corresponding butylperoxy radical by reaction with molecular oxygen is the main consumption pathway, that is, the 1-butylperoxy ($PC_4H_9O_2$) and 2-butylperoxy radical ($SC_4H_9O_2$) from the 1-butyl and 2-butyl radical, respectively.

Smaller alkylperoxy radicals and C_1–C_4 alkyl hydroperoxides seem to play a minor role in the mechanism in terms of the total carbon flow. From the general low-temperature oxidation mechanism as shown in Figure 1, it is expected that the butylperoxy radicals react with HO_2 to butyl hydroperoxides and O_2, decompose to butenes and HO_2 or isomerize to hydroperoxybutyl radicals. In the AramcoMech 2.0, only the latter two pathways are relevant as demonstrated by rate of production analyses of the two butylperoxy radicals (see Figure 12). Both C_4H_9OO radicals are exclusively formed by the reaction of molecular oxygen with the 1-butyl and 2-butyl radical, respectively. Isomerization to hydroperoxybutyl radicals (C_4H_8OOH1-3 and C_4H_8OOH1-4), decomposition to 1-butene (C_4H_8-1) and HO_2, and reaction with CH_3 to the 1-butoxy (PC_4H_9O) and methoxy radical (CH_3O) are the major sinks for the 1-butylperoxy radical. The decomposition of the 2-butylperoxy radical also largely leads to the formation of 1-butene and HO_2 as shown by Figure 12. In addition, 2-butene and HO_2 are formed by unimolecular decomposition and the 2-butoxy and methoxy radical by reaction with the methyl radical. A stronger impact of the low-temperature oxidation in the investigated flame than predicted by the model may be an explanation for the deviations of the mole fractions of propene, 1-butene, and 2-butene. When O_2 addition to the 2-butyl radical is more favored than hydrogen abstraction, the concentration of both butene isomers would be higher and that of propene lower as observed. Since the alkyl hydroperoxides were observed (see Section 3.1), they may also be an indicator of the importance of the low-temperature oxidation.

The butyl hydroperoxides are mainly formed by the reaction of the 1-butylperoxyl or 2-butylperoxyl radical with HO_2 as shown in the general low-temperature oxidation scheme. But compared to the other branching agents, they play only a minor role in the mechanism. Mole fractions of the butylperoxy radicals are more than two orders of magnitude higher than for the butyl hydroperoxides. Since the direct measurement of larger alkylperoxy radicals by mass spectrometry is due to their unstable cations not possible, it is beneficial that the alkyl hydroperoxides seem to be formed only by one reaction from the alkylperoxy radicals. The position and magnitude of the alkyl hydroperoxides are directly related to the alkylperoxy radical profiles so that it can be used to indirectly validate the simulated profiles of the alkylperoxy radicals. For the further breakdown of the two butoxy radicals, only two reactions are important. The 1-butoxy radical decomposes to the *n*-propyl radical (NC_3H_7) and formaldehyde (CH_2O), while the ethyl radical (C_2H_5) and acetaldehyde (CH_3CHO) are formed from the 2-butoxy radical. This means that two smaller alkyl radicals are formed, which may subsequently undergo low-temperature oxidation. But in contrast to the stable species in Figure S2, the photoionization cross sections of the alkyl hydroperoxides are unknown and must be estimated. Ashmore and Burgess have shown that the photoelectron spectra of the C_4–C_7 1-hydroperoxides resemble those of the normal alcohols.[59] Based on this observation, we quantified the mole fractions of the alkyl hydroperoxides in the *n*-butane-doped hydrogen flame by using photoionization cross sections of the structurally similar alcohols, that is, photoionization cross sections of methanol,

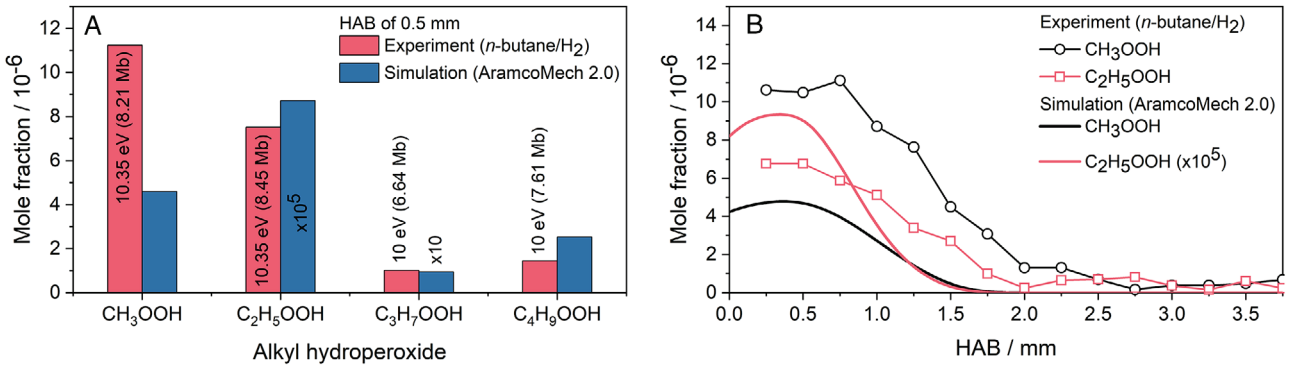

FIGURE 13 (A) Quantification of alkyl hydroperoxides in the *n*-butane-doped hydrogen flame from the energy scan measured at HAB of 0.5 mm and (B) mole fraction profiles of methyl and ethyl hydroperoxide in comparison with the results of the AramcoMech 2.0

ethanol, and 1-propanol by Cool et al.[66] and 1-butanol from the work of Xie et al.[71] Methyl and ethyl hydroperoxide are quantified at 10.35 eV, while a photon energy of 10 eV is used for propyl and butyl hydroperoxide. The photon energies are 0.5–0.7 eV above the ionization energies of the alkyl hydroperoxides, where fragmentation may be negligible. Distinct dissociative photoionization starts at higher photon energies as seen from the measured photoelectron spectra of the alkyl hydroperoxides. The total photoionization cross sections of the corresponding alcohol without considering fragmentation is therefore used for quantification. Figure 13 displays the calculated mole fractions of the C_1–C_4 alkyl hydroperoxides from the energy scan measured at HAB of 0.5 mm in the *n*-butane/H_2 flame and the mole fraction profiles of methyl and ethyl hydroperoxide from this flame. Measured mole fractions of alkyl hydroperoxides are about 10^{-5}–10^{-6} and are compared to the simulation results of the AramcoMech 2.0 in Figure 13. C_3H_7OOH represents the sum of *n*-propyl and isopropyl hydroperoxide and C_4H_9OOH the sum of 1-butyl and 2-butyl hydroperoxide, neglecting *tert*-butyl and isobutyl hydroperoxide, which play no role in the combustion of *n*-butane.

The modeling results also confirm that some hydroperoxides are formed in detectable concentrations close to the burner, where the flame temperature is lower. Mole fractions of methyl and butyl hydroperoxide have the same order of magnitude in experiment and simulation, while the mole fractions of propyl hydroperoxide and ethyl hydroperoxide are clearly underestimated. It is interesting to note that ethyl hydroperoxide is actually not formed at all according to the mechanism under our investigated conditions, whereas in the experiment the mole fraction is almost as high as that of the methyl hydroperoxide. The reaction path analysis in Figure 11 shows that the reaction of $C_2H_5 + H = CH_3 + CH_3$ is the major sink of ethyl radicals. This also applies to positions closer to the burner. Therefore, the consumption pathway of ethyl radicals by O_2 addition to form the ethylperoxy radical is not as relevant as for the butyl radicals. This behavior can explain the observed differences in the mole fraction of ethyl hydroperoxide. Zhang et al. demonstrated that O_2 addition is an important consumption pathway of the ethyl radical in an ethylene flame close to the burner at temperatures of 755 K and that the subsequent reaction of the C_2H_5OO radical is a source of ethyl hydroperoxide.[33] Overall, experimental mole fractions of alkyl hydroperoxides are typically higher than the modeling results except for butyl hydroperoxides. Caution has to be exerted in the interpretation of the mole fraction because photoionization cross sections of the alkyl hydroperoxides are unknown, and the mole fractions have higher uncertainties. Theoretical calculation of the photoionization cross section of methyl hydroperoxide by Moshammer et al.[72] shows that the cross section might be even lower than our assumed value based on methanol. The experimental mole fraction would be even bigger with a smaller photoionization cross section causing a bigger discrepancy between experimental and simulated results.

Besides the ethyl and propyl hydroperoxide, mole fractions of further oxygenated species, whose formation may be affected by the low-temperature oxidation pathways, are underestimated by the model. Their mole fraction profiles are presented in Figure 14. For example, the maximum mole fraction of ethanol is 2.7×10^{-4} at HAB of 0.5 mm in our investigated *n*-butane/H_2 flame compared to 1×10^{-6} in the simulation. The two most important reactions for the formation of ethanol (C_2H_5OH) at 0, 0.5, and 1 mm are $C_2H_5 + OH = C_2H_5OH$ and $CH_3 + CH_2OH = C_2H_5OH$ in the reaction mechanism. Low-temperature oxidation was observed by Zhang et al. in an ethylene flame.[33] They observed that the formation of ethanol was influenced by the low-temperature chemistry and identified the reaction $C_2H_5OO + OH = C_2H_5OH + O_2$ as the main source of ethanol at low temperatures.[33] However, the simulated

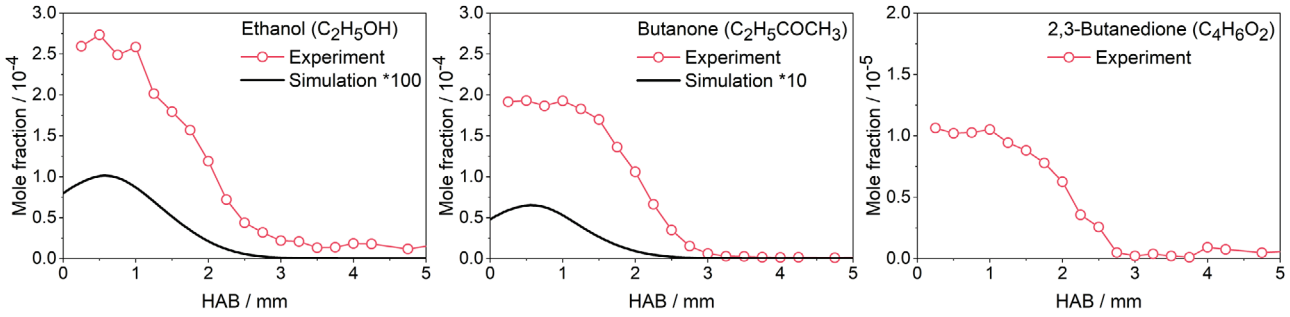

FIGURE 14 Experimental mole fraction profiles of ethanol (C_2H_5OH), butanone ($C_2H_5COCH_3$), and 2,3-butanedione ($C_4H_6O_2$) in the *n*-butane/H_2 flame compared to modeling results

mole fraction of the ethylperoxy radical is orders of magnitude smaller than for the other alkylperoxy radicals under the investigated conditions. The absence of this radical may be a reason for the underestimated mole fraction of ethanol. Since we clearly observed the ethyl hydroperoxide, the presence of the ethylperoxy radical is also likely and can explain the higher experimental mole fraction of ethanol.

The two QOOH radicals C_4H_8OOH1-3 and C_4H_8OOH1-4 decompose in the further reaction progress into 2-methyloxetane (C_4H_8O1-3) and THF, respectively. In our C_4 flames, butanone is the main C_4H_8O isomer. The maximum experimental mole fraction of butanone is 1.9×10^{-4} in the *n*-butane-doped hydrogen flame. In contrast, the simulated maximum mole fraction of butanone is only 6.5×10^{-6}, which is about 30 times lower compared to the experimental value. Since its photoionization cross section is unknown, we used the photoionization cross section of the chemically similar species *n*-butanal by Yang et al.[56] to calculate the mole fraction. The main formation pathway of butanone in the mechanism is the unimolecular decomposition of the 2-butoxy radical (SC_4H_9O), but its total contribution to the carbon flow is small. Further major consumption pathways of butanone are hydrogen abstractions followed by β-C-C-scission to yield $C_2H_4 + CH_3CO$ and $C_2H_4 + CH_2CO$ (ketene). The second C_4 oxygenate is 2,3-butanedione with an experimental mole fraction of 1.15×10^{-5} calculated using the photoionization cross section of *n*-butanal. The maximum mole fraction of 2,3-butanedione is about one order of magnitude lower than for butanone. 2,3-Butanedione and butanone may be formed from oxidation of 2-butanol as shown by Togbé et al.[73] in jet-stirred reactor measurements. 2-Butanol is formed in both investigated C_4 flames. In high-temperature combustion, consumption of 2,3-butanedione leads to ketene as shown by Sun et al. for a laminar premixed, low-pressure flame of 2,3-butanedione investigated by photoionization mass spectrometry.[74] Ketene (CH_2CO) is also formed from acetaldehyde (CH_3CHO) by the reaction sequence $CH_3CHO \rightarrow CH_3CO \rightarrow CH_2CO$. Since the mole fraction of acetaldehyde is significantly higher than that of 2,3-butanedione, the contribution to ketene formation may play a minor role compared to acetaldehyde.

Our measurements suggest that smaller hydroperoxides seem to play a more important role than the larger ones and LTC may have an influence on the formation of some oxygenated species in flames. The formation of C_1–C_4 alkyl hydroperoxides was also observed by Zhang et al.[33] in ethylene, ethane, propene, and *n*-butane flames by photoionization molecular-beam mass spectrometry. Here, we additionally measured the butenyl hydroperoxides and cyclic ethers, which also originate from low-temperature chemistry, in hydrocarbon-doped hydrogen flames. Alkyl hydroperoxides are not only identified by PIE spectra, but also by their TPE spectra. The methylperoxy radical (CH_3OO) is measured for the first time in laminar premixed flames. Measurements at different burner positions indicate that the alkyl hydroperoxides are only formed very close to the burner, where the perturbation of the probe is especially strong, and rapidly decomposes when the temperature increases. In general, the sampling probe lowers the temperature of the flame as experimentally determined in several works[75–78] and recently by Zhang et al.[33] during the investigation of the contribution of the low-temperature chemistry in a premixed, low-pressure ethylene flame. However, there are further aspects that may influence the particular temperature history of the sampled gas. Zhang et al. concluded that future investigations of geometry effects of sampling probe influence on the flame chemistry are warranted.[33] Such effects may be spatial in nature, and investigation should include effects of dimensionality assumptions on flame perturbation. This view is corroborated by two-dimensional (2D) fluid dynamics simulations, which provide deep insights into the sampling procedure,[79,80] and by the findings of Hansen et al.,[81] who investigated the probe perturbations on the temperature field one- and two-dimensionally by means of X-ray fluorescence. Recent 2D simulations of the sampling situation in a molecular-beam setup by Karakaya et al.[82] indicate that the suction effect of the probe is a decisive

disturbance of the flame structure, that is, gases are also sampled up- and downstream of the probe orifice and on the centerline in front of the probe, suction pulls a gas sample towards the probe orifice which leads to deformed temperature isolines. This suction effect overlaps with the general cooling effect of the sampling probe, but is not sufficiently considered in nozzle-perturbed temperature profiles used in one-dimensional simulations and can especially explain deviations close to the burner.[82] The limits of one-dimensional simulations for peroxide species are beyond the scope of this study but must be investigated in future work.

4 | CONCLUSIONS

PEPICO spectroscopy in combination with photoionization molecular-beam mass spectrometry is a powerful analytical tool to achieve high sensitivity to elusive species. Thanks to this technique, alkyl hydroperoxides and the methylperoxy radical are clearly identified by their PIE curves and photoelectron spectra in laminar premixed alkane- and alkene-doped hydrogen flames and even in a neat propane flame. The observation and identification of these low-temperature species in a flame environment are a hint for the low-temperature oxidation under these conditions. To the best of our knowledge, the measurement of TPE spectra of the larger alkyl hydroperoxides, that is, propyl- and butyl-hydroperoxides, has not yet been reported in the literature. Cyclic ethers are decomposition products of hydroperoxyalkyl radicals (QOOH) and are identified in the *n*-butane-doped hydrogen flame. They also serve as markers that the low-temperature oxidation may play a role at flame conditions.

The formation of higher C_4 oxygenates and ethanol might be influenced by the low-temperature oxidation and is observed in significantly larger extent than in the simulation results of the AramcoMech 2.0. Low-temperature oxidation chemistry is often neglected in flame simulations. The present results indicate at least the presence of reaction channels of this type and should be included when modeling laminar premixed low-pressure flames to consider all relevant formation pathways of those oxygenated species. For example, the detected diketone, 2,3-butanedione, is not at all considered in the mechanism and its formation can be explained by low-temperature chemistry via 2-butanol. For the *n*-butane/H_2 flame, a comprehensive dataset of mole fraction profiles for low-temperature and high-temperature oxidation products is provided. This dataset may serve for future model validation. It can help to improve the chemical modeling of the kinetics of transition from low-temperature to high-temperature oxidation in flames in a complex combustion environment that includes up- and downstream diffusion of the reactive species.

It should be noted that the peroxide species are only formed close to the burner, where the flame temperature is low and the flame perturbation by the sampling probe plays a significant role. Nevertheless, it cannot be concluded that the formation of the observed alkyl hydroperoxides is the result of the introduction of the sampling probe only. The detection of these species in a flame is a great opportunity to investigate the impact of the transition of the low-temperature oxidation to intermediate and high-temperature oxidation. It can also be stated that for a reliable model simulation, the probe-disturbance needs to be considered. As initial approach, the disturbed temperature profile is included in the provided dataset. Quantitative information is given for the alkyl hydroperoxides in the *n*-butane-doped hydrogen flame with mole fractions on the order of 10^{-5}-10^{-6}. Simulations with the perturbed temperature profile show that alkyl hydroperoxides are formed very close to the burner and some of them in detectable amounts. In future work, quantification of hydroperoxides in the other flames will give further insights into the low-temperature oxidation chemistry in flame-sampling experiments.

ACKNOWLEDGMENTS

The authors gratefully acknowledge Luka Debenjak for technical assistance and Andras Bodi for experimental research support. All authors thank the German Research Foundation (DFG) for financial support under contract KA3871/3-2 and KO4786/2-2. Patrick Hemberger thanks the Swiss Federal Office of Energy for financial support under contract SI/501269-01. The research leading to these results has received funding from the European Community's Seventh Framework Program (FP7/2007-2013) under grant agreement no. 312284. The experiments were performed at the Swiss Light Source of the Paul Scherrer Institute in Villigen, Switzerland.

DATA AVAILABILITY STATEMENT

The data that supports the findings of this study are available in the Supporting Information of this article.

REFERENCES

1. Bergthorson JM, Thomson MJ. A review of the combustion and emissions properties of advanced transportation biofuels and their impact on existing and future engines. *Renewable Sustainable Energy Rev*. 2015;42:1393-1417.
2. Geng P, Cao E, Tan Q, Wei L. Effects of alternative fuels on the combustion characteristics and emission products from diesel engines: a review. *Renewable Sustainable Energy Rev*. 2017;71:523-534.
3. Taamallah S, Vogiatzaki K, Alzahrani FM, Mokheimer EMA, Habib MA, Ghoniem AF. Fuel flexibility, stability and

emissions in premixed hydrogen-rich gas turbine combustion: technology, fundamentals, and numerical simulations. *Appl Energy*. 2015;154:1020-1047.
4. Nemitallah MA, Rashwan SS, Mansir IB, Abdelhafez AA, Habib MA. Review of novel combustion techniques for clean power production in gas turbines. *Energy Fuels*. 2018;32:979-1004.
5. Jacobs TJ, Assanis DN. The attainment of premixed compression ignition low-temperature combustion in a compression ignition direct injection engine. *Proc Combust Inst*. 2007;31:2913-2920.
6. Agarwal AK, Singh AP, Maurya RK. Evolution, challenges and path forward for low temperature combustion engines. *Prog Energy Combust Sci*. 2017;61:1-56.
7. Pachiannan T, Zhong W, Rajkumar S, He Z, Leng X, Wang Q. A literature review of fuel effects on performance and emission characteristics of low-temperature combustion strategies. *Appl Energy*. 2019;251:113380.
8. Krishnamoorthi M, Malayalamurthi R, He Z, Kandasamy S. A review on low temperature combustion engines: performance, combustion and emission characteristics. *Renewable Sustainable Energy Rev*. 2019;116:109404.
9. Ju Y, Reuter CB, Yehia OR, Farouk TI, Won SH. Dynamics of cool flames. *Prog Energy Combust Sci*. 2019;75:100787.
10. Kohse-Höinghaus K. Combustion chemistry diagnostics for cleaner processes. *Chem – Eur J*. 2016;22:13390-13401.
11. Curran HJ. Developing detailed chemical kinetic mechanisms for fuel combustion. *Proc Combust Inst*. 2019;37:57-81.
12. Wang Z, Herbinet O, Hansen N, Battin-Leclerc F. Exploring hydroperoxides in combustion: history, recent advances and perspectives. *Prog Energy Combust Sci*. 2019;73:132-181.
13. Zádor J, Taatjes CA, Fernandes RX. Kinetics of elementary reactions in low-temperature autoignition chemistry. *Prog Energy Combust Sci*. 2011;37:371-421.
14. Wang Z, Zhang L, Moshammer K, et al. Additional chain-branching pathways in the low-temperature oxidation of branched alkanes. *Combust Flame*. 2016;164:386-396.
15. Wang Z, Chen B, Moshammer K, et al. *n*-Heptane cool flame chemistry: unraveling intermediate species measured in a stirred reactor and motored engine. *Combust Flame*. 2018;187:199-216.
16. Battin-Leclerc F, Bourgalais J, Gouid Z, et al. Chemistry deriving from OOQOOH radicals in alkane low-temperature oxidation: a first combined theoretical and electron-ion coincidence mass spectrometry study. *Proc Combust Inst*. 2021;38:309-319.
17. DeCorpo JJ, McDowell MV, Sheinson RS, Wyatt JR. Quantitative measurement of methyl hydroperoxide in the acetaldehyde cool flame. *J Chem Soc, Chem Commun*. 1974:533-534.
18. Taylor GW. Peroxides in the combustion of isobutane. *Can J Chem*. 1958;36:1213-1216.
19. Herbinet O, Battin-Leclerc F. Progress in understanding low-temperature organic compound oxidation using a jet-stirred reactor. *Int J Chem Kinet*. 2014;46:619-639.
20. Battin-Leclerc F, Herbinet O, Glaude PA, et al. Experimental confirmation of the low-temperature oxidation scheme of alkanes. *Angew Chem, Int Ed*. 2010;49:3169-3172.
21. Herbinet O, Battin-Leclerc F, Bax S, et al. Detailed product analysis during the low temperature oxidation of n-butane. *Phys Chem Chem Phys*. 2011;13:296-308.
22. Cord M, Husson B, Lizardo Huerta JC, et al. Study of the low temperature oxidation of propane. *J Phys Chem A*. 2012;116:12214-12228.
23. Welz O, Burke MP, Antonov IO, et al. New insights into low-temperature oxidation of propane from synchrotron photoionization mass spectrometry and multiscale informatics modeling. *J Phys Chem A*. 2015;119:7116-7129.
24. Cord M, Sirjean B, Fournet R, Tomlin A, Ruiz-Lopez M, Battin-Leclerc F. Improvement of the modeling of the low-temperature oxidation of *n*-butane: study of the primary reactions. *J Phys Chem A*. 2012;116:6142-6158.
25. Bahrini C, Morajkar P, Schoemaecker C, et al. Experimental and modeling study of the oxidation of *n*-butane in a jet stirred reactor using cw-CRDS measurements. *Phys Chem Chem Phys*. 2013;15:19686-19698.
26. Eskola AJ, Welz O, Savee JD, Osborn DL, Taatjes CA. Synchrotron photoionization mass spectrometry measurements of product formation in low-temperature *n*-butane oxidation: toward a fundamental understanding of autoignition chemistry and n-$C_4H_9 + O_2$/s-$C_4H_9 + O_2$ reactions. *J Phys Chem A*. 2013;117:12216-12235.
27. Rodriguez A, Herbinet O, Wang Z, et al. Measuring hydroperoxide chain-branching agents during *n*-pentane low-temperature oxidation. *Proc Combust Inst*. 2017;36:333-342.
28. Rodriguez A, Herbinet O, Meng X, et al. Hydroperoxide measurements during low-temperature gas-phase oxidation of *n*-heptane and *n*-decane. *J Phys Chem A*. 2017;121:1861-1876.
29. Meng X, Rodriguez A, Herbinet O, Wang T, Battin-Leclerc F. Revisiting 1-hexene low-temperature oxidation. *Combust Flame*. 2017;181:283-299.
30. Bourgalais J, Gouid Z, Herbinet O, et al. Isomer-sensitive characterization of low temperature oxidation reaction products by coupling a jet-stirred reactor to an electron/ion coincidence spectrometer: case of *n*-pentane. *Phys Chem Chem Phys*. 2020;22:1222-1241.
31. Westbrook CK. Chemical kinetics of hydrocarbon ignition in practical combustion systems. *Proc Combust Inst*. 2000;28:1563-1577.
32. Bahrini C, Herbinet O, Glaude P-A, Schoemaecker C, Fittschen C, Battin-Leclerc F. Quantification of hydrogen peroxide during the low-temperature oxidation of alkanes. *J Am Chem Soc*. 2012;134:11944-11947.
33. Zhang X, Zhang Y, Li T, et al. Low-temperature chemistry triggered by probe cooling in a low-pressure premixed flame. *Combust Flame*. 2019;204:260-267.
34. Krüger D, Oßwald P, Köhler M, et al. Hydrogen abstraction ratios: a systematic iPEPICO spectroscopic investigation in laminar flames. *Combust Flame*. 2018;191:343-352.
35. Bodi A, Hemberger P, Gerber T, Sztáray B. A new double imaging velocity focusing coincidence experiment: i^{2}PEPICO. *Rev Sci Instrum*. 2012;83:083105.
36. Sztáray B, Voronova K, Torma KG, et al. CRF-PEPICO: double velocity map imaging photoelectron photoion coincidence spectroscopy for reaction kinetics studies. *J Chem Phys*. 2017;147:013944.
37. Hoener M, Kaczmarek D, Bierkandt T, Bodi A, Hemberger P, Kasper T. A pressurized flow reactor combustion experiment interfaced with synchrotron double imaging photoelectron photoion coincidence spectroscopy. *Rev Sci Instrum*. 2020;91:045115.
38. Oßwald P, Hemberger P, Bierkandt T, et al. *In situ* flame chemistry tracing by imaging photoelectron photoion coincidence spectroscopy. *Rev Sci Instrum*. 2014;85:025101.

39. Hansen N, Cool TA, Westmoreland PR, Kohse-Höinghaus K. Recent contributions of flame-sampling molecular-beam mass spectrometry to a fundamental understanding of combustion chemistry. *Prog Energy Combust Sci*. 2009;35:168-191.
40. Egolfopoulos FN, Hansen N, Ju Y, Kohse-Höinghaus K, Law CK, Qi F. Advances and challenges in laminar flame experiments and implications for combustion chemistry. *Prog Energy Combust Sci*. 2014;43:36-67.
41. Li Y, Zhou C-W, Somers KP, Zhang K, Curran HJ. The oxidation of 2-butene: a high pressure ignition delay, kinetic modeling study and reactivity comparison with isobutene and 1-butene. *Proc Combust Inst*. 2017;36:403-411.
42. Metcalfe WK, Burke SM, Ahmed SS, Curran HJ. A hierarchical and comparative kinetic modeling study of C_1−C_2 hydrocarbon and oxygenated Fuels. *Int J Chem Kinet*. 2013;45:638-675.
43. Jithin EV, Dinesh K, Mohammad A, Velamati RK. Laminar burning velocity of *n*-butane/hydrogen/air mixtures at elevated temperatures. *Energy*. 2019;176:410-417.
44. Jiang X, Pan Y, Sun W, Liu Y, Huang Z. Shock-tube study of the autoignition of *n*-butane/hydrogen mixtures. *Energy Fuels*. 2018;32:809-821.
45. Lee S, Song S. A rapid compression machine study of hydrogen effects on the ignition delay times of *n*-butane at low-to-intermediate temperatures. *Fuel*. 2020;266:116895.
46. Chemical Workbench. http://www.kintechlab.com/, Version 4.1.19528, 2017. Accessed June 21, 2020.
47. Moshammer K, Jasper AW, Popolan-Vaida DM, et al. Detection and identification of the keto-hydroperoxide ($HOOCH_2OCHO$) and other intermediates during low-temperature oxidation of dimethyl ether. *J Phys Chem A*. 2015;119:7361-7374.
48. Meloni G, Zou P, Klippenstein SJ, et al. Energy-resolved photoionization of alkylperoxy radicals and the stability of their cations. *J Am Chem Soc*. 2006;128:13559-13567.
49. Covert KJ, Voronova K, Torma KG, Bodi A, Zádor J, Sztáray B. Thermochemistry of the smallest QOOH radical from the roaming fragmentation of energy selected methyl hydroperoxide ions. *Phys Chem Chem Phys*. 2018;20:21085-21094.
50. Voronova K, Ervin KM, Torma KG, et al. Radical thermometers, thermochemistry, and photoelectron spectra: a photoelectron photoion coincidence spectroscopy study of the methyl peroxy radical. *J Phys Chem Lett*. 2018;9:534-539.
51. Curtiss LA, Redfern PC, Raghavachari K. Gaussian-4 theory. *J Chem Phys*. 2007;126:084108.
52. Frisch MJ, Trucks GW, Schlegel HB, et al. *Gaussian 16, Revision A.03*. Wallingford, CT: Gaussian; 2016.
53. Mozhayskiy VA, Krylov AI, *ezSpectrum*. http://iopenshell.usc.edu/downloads. Accessed June 21, 2020.
54. Noell AC, Laboratory studies of the self and cross reactions of atmospheric peroxy radicals. PhD thesis, California Institute of Technology, 2010.
55. Kimura K, Osafune K. Photoelectron spectroscopic study of skew compounds. III. N,N′-Dimethylhydrazine, dimethyl peroxide, and dimethyl disulfide. *Bull Chem Soc Jpn*. 1975;48:2421-2427.
56. Yang B, Wang J, Cool TA, Hansen N, Skeen S, Osborn DL. Absolute photoionization cross-sections of some combustion intermediates. *Int J Mass Spectrom*. 2012;309:118-128.
57. Kimura K, Katsumata S, Achiba Y, Yamazaki T, Iwata S. *Handbook of HeI Photoelectron Spectra of Fundamental Organic Molecules*. Tokyo: Japan Scientific Societies Press; 1981.
58. Biermann HW, Morton TH. Reversible tautomerization of radical cations. Photoionization of 2-methoxyethanol and 3-methoxy-1-propanol. *J Am Chem Soc*. 1983;105:5025-5030.
59. Ashmore FS, Burgess AR. Study of some medium size alcohols and hydroperoxides by photoelectron spectroscopy. *J Chem Soc, Faraday Trans 2*. 1977;73:1247-1261.
60. Batich C, Adam W. The photoelectron spectra of alkylperoxides. *Tetrahedron Lett*. 1974;15:1467-1470.
61. Lang M, Holzmeier F, Hemberger P, Fischer I. Threshold photoelectron spectra of combustion relevant C_4H_5 and C_4H_7 isomers. *J Phys Chem A*. 2015;119:3995-4000.
62. Linstrom PJ, Mallard WG, Eds. *NIST Chemistry WebBook*. NIST Standard Reference Database Number 69. Gaithersburg MD: NIST. https://doi.org/10.18434/T4D303. Accessed June 21, 2020.
63. Cool TA, Nakajima K, Mostefaoui TA, et al. Selective detection of isomers with photoionization mass spectrometry for studies of hydrocarbon flame chemistry. *J Chem Phys*. 2003;119:8356-8365.
64. Kasper T, Lucassen A, Jasper AW, et al. Identification of tetrahydrofuran reaction pathways in premixed flames. *Z Phys Chem*. 2011;225:1237-1270.
65. Cool TA, McIlroy A, Qi F, et al. Photoionization mass spectrometer for studies of flame chemistry with a synchrotron light source. *Rev Sci Instrum*. 2005;76:094102.
66. Cool TA, Wang J, Nakajima K, Taatjes CA, McIlroy A. Photoionization cross sections for reaction intermediates in hydrocarbon combustion. *Int J Mass Spectrom*. 2005;247:18-27.
67. Wang J, Yang B, Cool TA, Hansen N, Kasper T. Near-threshold absolute photoionization cross-sections of some reaction intermediates in combustion. *Int J Mass Spectrom*. 2008;269:210-220.
68. Kercher JP, Fogleman EA, Koizumi H, Sztáray B, Baer T. Heats of formation of the propionyl ion and radical and 2,3-pentanedione by threshold photoelectron photoion coincidence spectroscopy. *J Phys Chem A*. 2005;109:939-946.
69. Dampc M, Mielewska B, Siggel-King MRF, King GC, Zubek M. Threshold photoelectron spectra of tetrahydrofuran over the energy range 9–29 eV. *Chem Phys*. 2009;359:77-81.
70. Fogleman EA, Koizumi H, Kercher JP, Sztáray B, Baer T. Heats of formation of the acetyl radical and ion obtained by threshold photoelectron photoion coincidence. *J Phys Chem A*. 2004;108:5288-5294.
71. Xie M, Zhou Z, Wang Z, Chen D, Qi F. Determination of absolute photoionization cross-sections of oxygenated hydrocarbons. *Int J Mass Spectrom*. 2010;293:28-33.
72. Moshammer K, Jasper AW, Popolan-Vaida DM, et al. Quantification of the keto-hydroperoxide ($HOOCH_2OCHO$) and other elusive intermediates during low-temperature oxidation of dimethyl ether. *J Phys Chem A*. 2016;120:7890-7901.
73. Togbé C, Mzé-Ahmed A, Dagaut P. Kinetics of oxidation of 2-butanol and isobutanol in a jet-stirred reactor: experimental study and modeling investigation. *Energy Fuels*. 2010;24:5244-5256.
74. Sun W, Wang J, Huang C, Hansen N, Yang B. Providing effective constraints for developing ketene combustion mechanisms: a detailed kinetic investigation of diacetyl flames. *Combust Flame*. 2019;205:11-21.

75. Stepowski D, Puechberty D, Cottereau MJ. Use of laser-induced fluorescence of OH to study the perturbation of a flame by a probe. *Symp (Int) Combust*. 1981;18:1567-1573.
76. Biordi JC, Lazzara CP, Papp JF. Molecular beam mass spectrometry applied to determining the kinetics of reactions in flames. I. Empirical characterization of flame perturbation by molecular beam sampling probes. *Combust Flame*. 1974;23:73-82.
77. Desgroux P, Gasnot L, Pauwels JF, Sochet LR. Correction of LIF temperature measurements for laser absorption and fluorescence trapping in a flame. *Appl Phys B*. 1995;61:401-407.
78. Struckmeier U, Oßwald P, Kasper T, et al. Sampling probe influences on temperature and species concentrations in molecular beam mass spectroscopic investigations of flat premixed low-pressure flames. *Z Phys Chem*. 2009;223:503-537.
79. Gururajan V, Egolfopoulos FN, Kohse-Höinghaus K. Direct numerical simulations of probe effects in low-pressure flame sampling. *Proc Combust Inst*. 2015;35:821-829.
80. Deng L, Kempf A, Hasemann O, Korobeinichev OP, Wlokas I. Investigation of the sampling nozzle effect on laminar flat flames. *Combust Flame*. 2015;162:1737-1747.
81. Hansen N, Tranter RS, Moshammer K, et al. 2D-imaging of sampling-probe perturbations in laminar premixed flames using Kr X-ray fluorescence. *Combust Flame*. 2017;181:214-224.
82. Karakaya Y, Sellmann J, Wlokas I, Kasper T. Influence of the sampling probe on flame temperature, species, residence times and on the interpretation of ion signals of methane/oxygen flames in molecular beam mass spectrometry measurements. *Combust Flame*. 2021;229:111388.

SUPPORTING INFORMATION

Additional supporting information may be found online in the Supporting Information section at the end of the article.

How to cite this article: Bierkandt T, Oßwald P, Gaiser N, et al. Observation of low-temperature chemistry products in laminar premixed low-pressure flames by molecular-beam mass spectrometry. *Int J Chem Kinet*. 2021;53:1063–1081. https://doi.org/10.1002/kin.21503

A combustion chemistry study of tetramethylethylene in a laminar premixed low-pressure hydrogen flame

Bierkandt, T., Hemberger, P., Oßwald, P., Gaiser, N., Hoener, M., Krüger, D., Kasper, T., Köhler, M.
Proceedings of the Combustion Institute, 2023, 39(2), pp. 1699–1708
DOI: 10.1016/j.proci.2022.07.205

My contribution to this work was the support in the measurement of data, co-authoring of the manuscript.

Available online at www.sciencedirect.com

ScienceDirect

Proceedings of the Combustion Institute 39 (2023) 1699–1708

Proceedings of the Combustion Institute

www.elsevier.com/locate/proci

A combustion chemistry study of tetramethylethylene in a laminar premixed low-pressure hydrogen flame

Thomas Bierkandt [a,*], Patrick Hemberger [b], Patrick Oßwald [a], Nina Gaiser [a], Martin Hoener [c], Dominik Krüger [d], Tina Kasper [c,e], Markus Köhler [a]

[a] *Institute of Combustion Technology, German Aerospace Center (DLR), Pfaffenwaldring 38-40, 70569 Stuttgart, Germany*
[b] *Laboratory for Synchrotron Radiation and Femtochemistry, Paul Scherrer Institute, 5232 Villigen, Switzerland*
[c] *Mass Spectrometry in Reactive Flows, University of Duisburg-Essen, Lotharstraße 1, 47057 Duisburg, Germany*
[d] *Division 9, State Health Office, Nordbahnhofstraße 135, 70191 Stuttgart, Germany*
[e] *Technical Thermodynamics, Paderborn University, 33098 Paderborn, Germany*

Received 5 January 2022; accepted 24 July 2022
Available online 22 September 2022

Abstract

The combustion chemistry of tetramethylethylene (TME) was studied in a premixed laminar low-pressure hydrogen flame by combined photoionization molecular-beam mass spectrometry (PI-MBMS) and photoelectron photoion coincidence (PEPICO) spectroscopy at the Swiss Light Source (SLS) of the Paul Scherrer Institute in Villigen, Switzerland. This hexene isomer with the chemical formula C_6H_{12} has a special structure with only allylic C–H bonds. Several combustion intermediate species were identified by their photoionization and threshold photoelectron spectra, respectively. The experimental mole fraction profiles were compared to modeling results from a recently published kinetic reaction mechanism that includes a TME sub-mechanism to describe the TME/H_2 flame structure. The first stable intermediate species formed early in the flame front during the combustion of TME are 2-methyl-2-butene (C_5H_{10}) at a mass-to-charge ratio (m/z) of 70, 2,3-dimethylbutane (C_6H_{14}) at m/z 86, and 3-methyl-1,2-butadiene (C_5H_8) at m/z 68. Isobutene (C_4H_8) is also a dominant intermediate in the combustion of TME and results from consumption of 2-methyl-2-butene. In addition to these hydrocarbons, some oxygenated species are formed due to low-temperature combustion chemistry in the consumption pathway of TME under the investigated flame conditions.

Keywords: Tetramethylethylene; 2,3-Dimethyl-2-butene; Synchrotron vacuum ultraviolet (VUV) photoionization; Molecular-beam mass spectrometry (MBMS); Photoelectron photoion coincidence (PEPICO) spectroscopy

* Corresponding author.
E-mail address: thomas.bierkandt@dlr.de (T. Bierkandt).

https://doi.org/10.1016/j.proci.2022.07.205

Introduction

Tetramethylethylene (TME), also known as 2,3-dimethyl-2-butene, has the chemical formula C_6H_{12} and is the simplest tetra-substituted alkene. Its special structure opens the opportunity to study the combustion of a hydrocarbon that has only allylic C–H bonds. In total, tetramethylethylene has 12 allylic C–H bonds, in which the hydrogen atom is bound to a sp^3 carbon atom in vicinity to a C–C double bond. Any hydrogen abstraction results in the same resonance-stabilized C_6H_{11} radical and allylic C–H bonds are significantly weaker than primary (alkylic) or vinylic C–H bonds [1]. Despite its interesting structure, combustion of TME is not well-studied. Hydrogen abstraction of TME to form the 2,3-dimethyl-2-buten-1-yl radical (C_6H_{11}) was investigated by Krüger et al. [2] in previous work and compared to different C_2 (ethane) and C_4 (*n*-butane, isobutane, 1-butene, and isobutene) hydrocarbons under similar conditions utilizing doped hydrogen flames. They found a clear hydrogen abstraction order of tertiary > primary, secondary > primary, and allylic > non-resonance-stabilized for the investigated hydrocarbon fuels. McEnally and Pfefferle [3] studied the decomposition of tetramethylethylene and all other hexene isomers in methane/air laminar non-premixed flames by photoionization mass spectrometry. They showed that isomerization is a minor decomposition step of TME in contrast to all other hexenes and instead formation of 2,3-dimethyl-1,3-butadiene (C_6H_{10}) by scission of allylic C–H bonds is favored. For the hexene isomers, and for alkene fuels in general, it can be concluded that the more allylic C–H bonds present, the less reactive the fuel is [4] and TME is the only hexene isomer which has only allylic and no vinylic C–H bonds. Wu et al. [5] used TME in a five components surrogate gasoline fuel to cover the alkene content of commercial gasoline. Baldwin et al. [6] investigated the addition of HO_2 radicals to ethylene (C_2H_4) and TME (C_6H_{12}) by formation of oxirane and tetramethyloxirane, respectively. They found that tetramethylethylene has a significantly lower activation energy for this addition reaction. Absolute rate constants for the addition of oxygen atoms to tetramethylethylene, which showed a strong negative temperature dependence, were investigated by Biehl et al. [7] in the temperature range of 200 to 370 K. Some authors [8–11] have also studied the ozonolysis of tetramethylethylene.

We report the investigation of the chemical structure of a TME-doped H_2 flame. Several combustion intermediates were identified by their photoionization or photoelectron spectra and quantified to present mole fraction profiles. Decomposition of tetramethylethylene is discussed based on the experimental results and the kinetic modeling results of the recently published high-temperature mechanism NUIGMech1.1_HT from NUI Galway [12–14]. For main intermediates in TME decomposition, additional modeling results from a modified version of NUIGMech1.1_HT and the new NUIGMech1.2 [15] with detailed high- and low-temperature chemistry are also considered.

Experiment

The total gas flow of the TME-doped hydrogen flame was 4067 sccm (1.65 mol-% TME, 44.26 mol-% H_2, 29.50 mol-% O_2, and 24.59 mol-% Ar). This fuel-rich flame with an equivalence ratio of 1.25 was stabilized at 40 mbar on a water-cooled McKenna-type burner with a porous sintered bronze matrix that has a diameter of 60 mm. Combustion gasses were sampled by a quartz nozzle with an orifice diameter of about 300 µm directly from the flame. Due to the large pressure drop between the flame chamber and the first pumping stage, a molecular beam is formed. The central core of this molecular beam is skimmed and sampled molecules were analyzed by photoelectron photoion coincidence spectroscopy (PEPICO), i.e., ions and electrons are measured after the ionization event in coincidence [16]. The molecular-beam technique prevents a change of the gas composition during the sampling process and even allows for the detection of very elusive and reactive species such as radicals. Experiments were realized at the VUV beamline of the Swiss Light Source (SLS), where vacuum ultraviolet (VUV) synchrotron radiation enables the identification of isomers due to the high energy resolution and the tunability of the photon energy. A more detailed description of the flame experiment and the beamline was given by Oßwald et al. [17] and in a recently published review article by Hemberger et al. [18]. Photoionization (PI) and threshold photoelectron (TPE) spectra were obtained by scanning the photon energy at a constant burner position of 1.75 mm in the reaction zone of the flame. Isomer-resolved mole fraction profiles were measured by sampling the gas composition at heights above the burner (HAB) between 0.25 and 30.25 mm for several photon energies.

Results and discussion

A study by Krüger et al. [2] investigated the hydrogen abstraction from TME to produce the fuel radical C_6H_{11} (2,3-dimethyl-2-buten-1-yl radical) in the same flame and compared it to the first hydrogen abstraction reaction in other alkane- and alkene-doped H_2 flames. In our study, more than 30 combustion species were identified in the TME-doped H_2 flame, and their mole fraction profiles determined. All mole fraction profiles and the temperature profile are available for download as supplementary material. General uncertainty of the mole fractions is 15–20% for main species,

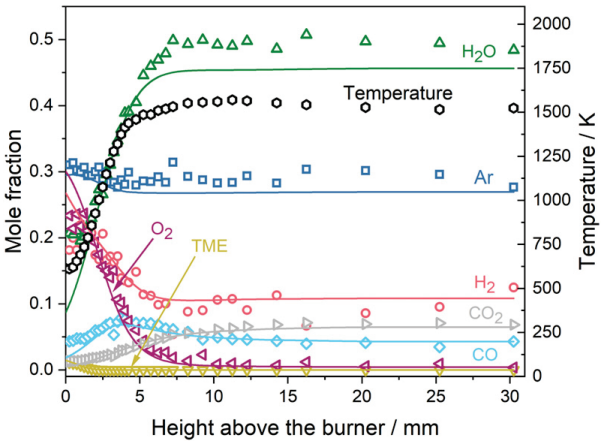

Fig. 1. Mole fraction profiles of the main combustion species and the diluent gas (symbols: experiment; solid lines: simulation) as well as the temperature profile (black hexagons).

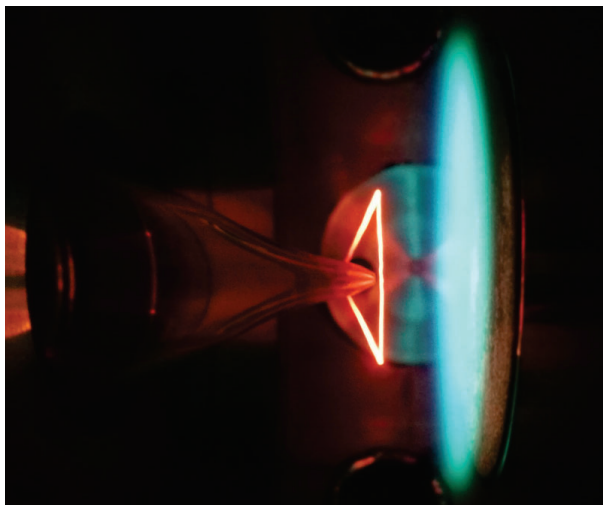

Fig. 2. Flame temperature measurement by a thermocouple in presence of the sampling nozzle.

30–50% for combustion intermediates with known photoionization cross section (PICS), and a factor of 2–4 for species with unknown, i.e., estimated, PICS [19,20]. The uncertainty of the flame temperature determination using thermocouples is comparable to optical methods and is estimated to be 5–10% [20].

Figure 1 shows the measured mole fraction profiles of the main species, i.e., the fuels TME and H_2, the oxidizer O_2, the diluent gas Ar, and the combustion products H_2O, CO, and H_2O, in comparison to the modeling results. Unless otherwise noted, the high-temperature version of the NUIGMech1.1 (NUIGMech1.1_HT with release date October 2nd, 2020) [12–14] was used for simulations, which were done with the software library Cantera [21] and with the Cantera flame reactor module for burner-stabilized flames within the Chemical Workbench [22]. The exhaust gas concentrations and mole fractions in the reaction zone of the flame are within the uncertainty of the experiment. However, there are larger deviations in the preheating zone, where the observed consumption of the fuels and the oxidizer is more pronounced than predicted by the model. Hence, higher concentrations of H_2O, CO, and CO_2 are already detected.

The temperature profile that was used as input for the kinetic modeling is also presented in Fig. 1. The profile was determined from the temperature dependence of the sampling rate through the quartz nozzle [23] by using the exhaust gas temperature of a propane-doped hydrogen flame with an identical C:H:O ratio to the TME/H_2 flame. It was shown by Krüger et al. [2] that the hydrocarbon-doped hydrogen flames have identical temperature profiles under the investigated conditions so that it is appropriate to use the measured exhaust temperature from the propane/H_2 flame. The used thermocouple had a small bead diameter of 130 µm and was coated by non-catalytic SiO_2. It was positioned very close to a quartz sampling nozzle as shown in Fig. 2 to consider the influence of the nozzle on the flame temperature. The radiation correction was done according to Gonchikzhapov and Kasper [24] and the entire procedure for obtaining the temperature profile is described in detail in the supplementary material.

Sensitivity of the simulation results on the temperature profile was evaluated by using profiles with increased (+10%) and decreased (−10%) temperature. Results for main species and selected intermediates that are discussed below are presented in Fig. S1 and S2, respectively. Exhaust gas concentrations of H_2, H_2O, CO, and CO_2 are still within the uncertainty range of ±20% for main species. For mole fraction profiles of intermediate species, changes in absolute concentrations are minor and mainly spatial shifts are observed. Overall, the peak positions of many intermediate species are well predicted by simulations with the original temperature profile from Fig. 1, which also best predicts the consumption of TME and O_2 in the reaction zone.

Figure 3 shows the mole fraction profiles of typical C_1-C_3 combustion intermediates (CH_3, C_2H_2, C_2H_4, CH_2O, C_3H_4, and C_3H_6) often formed during combustion of hydrocarbons and some specific species (C_4H_8, C_5H_8, and C_5H_{10}) directly related to the fuel structure. Literature photoionization cross sections exist for all species presented in Fig. 3, and the resulting maximum experimental uncertainty of 50% is indicated. Considering the experimental uncertainty and the general uncertainty of the modeling, most species are satisfactorily reproduced and the used high-temperature mechanism NUIGMech1.1_HT appears suitable to predict the decomposition of TME under the investigated conditions. Contrasting the results for the aforementioned species, formation of isobutene (C_4H_8) is substantially underestimated by this model and

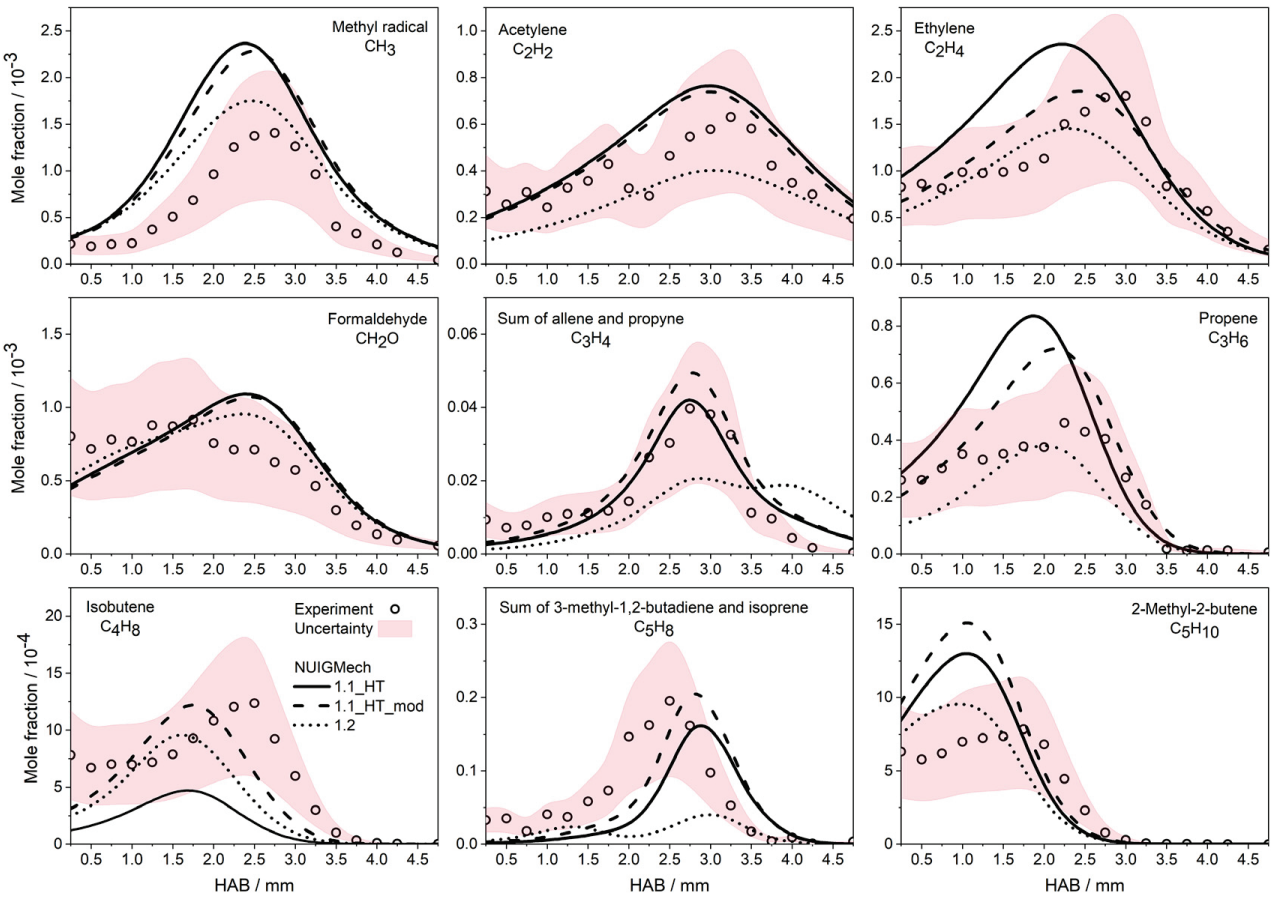

Fig. 3. Mole fraction profiles of some C_1-C_5 combustion intermediates measured in the TME/H_2 flame and comparison to the simulation results. Symbols: experimental data; shaded area: experimental uncertainty of 50%; solid lines: modeling results.

that of propene (C_3H_6) and 2-methyl-2-butene (C_5H_{10}) are overestimated. Reactions with H atoms are key reactions in alkene oxidation [4] and particularly important in the hydrogen-rich environment studied here. Updating the rate constants for reactions of H atoms with C_2-C_4 alkenes (ethylene, propene, isobutene, 1-butene, and 2-butene) and pentene isomers (2-methyl-1-butene, 2-methyl-2-butene, and 3-methyl-1-butene) from the theoretical work of Power et al. [25,26] substantially improve the prediction of the isobutene mole fraction as shown in Fig. 3, where the modified mechanism is denoted as NUIGMech1.1_HT_mod. Predictions of ethylene and propene are also improved, while the mole fraction of 2-methyl-2-butene is even more overestimated.

For most intermediates, improved agreement with the experimental mole fraction profiles can be achieved with the latest NUI Galway mechanism (NUIGMech1.2) by Sahu et al. [15]. This mechanism has also implemented the previously mentioned updates by Power et al., but also includes detailed low-temperature chemistry. As seen in Fig. 3, the three main intermediates 2-methyl-2-butene (C_5H_{10}), isobutene (C_4H_8), and propene (C_3H_6), whose formation is directly linked to the fuel decomposition over the reaction channel TME → 2-methyl-2-butene → isobutene → propene as discussed below, are now well predicted. On the other hand, predictions for the isomers C_3H_4 and C_5H_8 that have lower concentrations on the order of 10^{-5} deteriorate. Given that NUIGMech1.2 was used without modifications and was not previously validated for TME, the overall agreement between experimental mole fraction profiles and modeling results is very good.

To further investigate the fuel decay, a rate of production (ROP) analysis was done for the entire flame and is presented in Fig. 4, where the thickness of the arrows represents the carbon flux between species. Three main consumption pathways of TME (XC6D2) can be identified: (R1) Hydrogen atom addition reaction to yield the C_6H_{13} radical 2,3-dimethylbut-2-yl (XC6–2)

$$\mathrm{XC6D2} + H = \mathrm{XC6\text{–}2} \qquad \text{(R1)}$$

with a decay rate contribution of 34.9%, (R2) hydrogen atom induced substitution to yield 2-methyl-2-butene (BC5H10) and the methyl radical

$$\mathrm{XC6D2} + H = \mathrm{BC5H10} + \mathrm{CH_3} \qquad \text{(R2)}$$

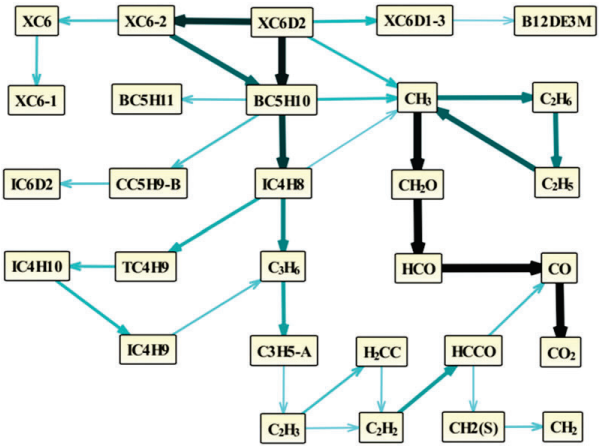

Fig. 4. Rate of production (ROP) analysis of the total carbon flux in the entire TME/H_2 flame. Only carbon fluxes higher than 8% are shown.

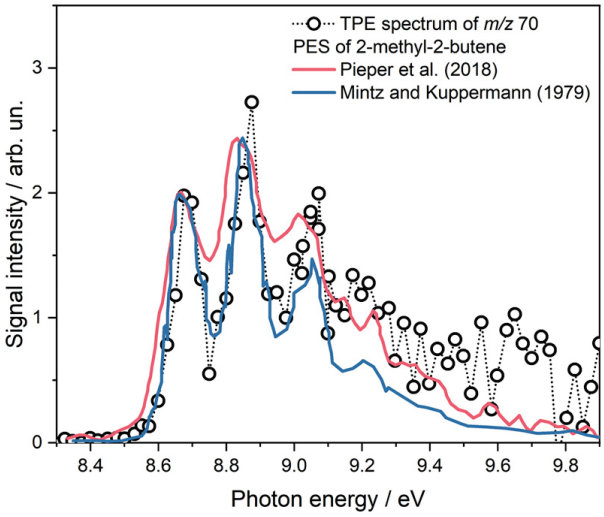

Fig. 5. Assignment of 2-methyl-2-butene to *m/z* 70 by photoelectron spectroscopy in the TME/H_2 flame.

with a contribution of 55.3%, and (R3) hydrogen atom abstraction reaction to yield the resonance-stabilized C_6H_{11} radical 2,3-dimethyl-2-buten-1-yl (XC6D1–3)

$$XC6D2 + H = XC6D1\text{–}3 + H_2 \quad (R3)$$

with a contribution of 9.6% to TME decay. Its resonance structure is the 2,3-dimethyl-1-buten-3-yl radical. The 2,3-dimethylbut-2-yl radical (XC6–2) also contributes significantly to the formation of 2-methyl-2-butene (BC5H10) by β-CC-scission

$$XC6\text{–}2 = BC5H10 + CH_3 \quad (R4)$$

making this species an important intermediate in the combustion of TME with a maximum mole fraction of about $1{\cdot}10^{-3}$ in both the experiment and simulations. Mole fraction profiles of the two fuel radicals formed by H abstraction (C_6H_{11}) and H addition (C_6H_{13}) reactions are presented in Fig. S3 in the supplementary material. Quantification is based on estimated cross sections and absolute values are therefore affected with high uncertainties, but the modeling results show that the predicted concentration of C_6H_{13} by NUIGMech1.2 is one order of magnitude smaller than the predictions of the high-temperature mechanisms and in better accordance to the experiment.

Figure 5 presents the measured photoelectron spectra at a mass-to-charge ratio (*m/z*) of 70 in the TME-doped hydrogen flame. 2-Methyl-2-butene at *m/z* 70 is unambiguously identified by its threshold photoelectron spectrum (TPES). The spectrum shows the vibrational fine structure of the first band corresponding to the C = C stretching mode with a vertical ionization energy of 8.86 eV [27] at the highest intensity transition and is well reproduced by two reference photoelectron spectra from the work of Pieper et al. [28] and Mintz and Kuppermann [27]. According to the rate of production analysis in Fig. 4, direct formation of isobutene (IC4H8) from 2-methyl-2-butene (BC5H10) by substitution reaction

$$BC5H10 + H = IC4H8 + CH_3 \quad (R5)$$

is a main pathway in the TME/H_2 flame. Isobutene formation by β-CC-scission of the tertiary 2-methylbut-2-yl radical (BC5H11), which is itself formed by H atom addition to 2-methyl-2-butene, may also be likely, but is less pronounced in the used mechanism. Ruwe et al. [29] detected isobutene and 2-butene in a rich 2-methyl-2-butene laminar premixed low-pressure flame by photoionization mass spectrometry in comparably high concentrations and concluded that their formation occurs via the C_5H_{11} radicals formed by H addition from the fuel. In the TME/H_2 flame, we have only observed the formation of isobutene as verified by the photoelectron spectrum of *m/z* 56 from this flame in comparison to the spectrum of the neat substance (see Fig. 6). A TPE spectrum of *trans*-2-butene from direct calibration is also presented in Fig. 6 and further confirms the absence of 2-butene in the TME/H_2 flame. The TPE spectrum of 2-butene looks similar in shape, but is shifted to a ca. 100 meV lower photon energy. Depending on the model, the maximum mole fraction of isobutene is 6.2–10.6 times higher than that of 2-butene and generally corroborates a dominance of isobutene.

A second decomposition product of the C_6H_{13} radical (XC6–2) is 2,3-dimethylbutane (XC6) formed by a further hydrogen atom addition

$$XC6\text{–}2 + H = XC6 \quad (R6)$$

as shown in the reaction path analysis in Fig. 4. At *m/z* 86, the hydrocarbon 2,3-dimethylbutane

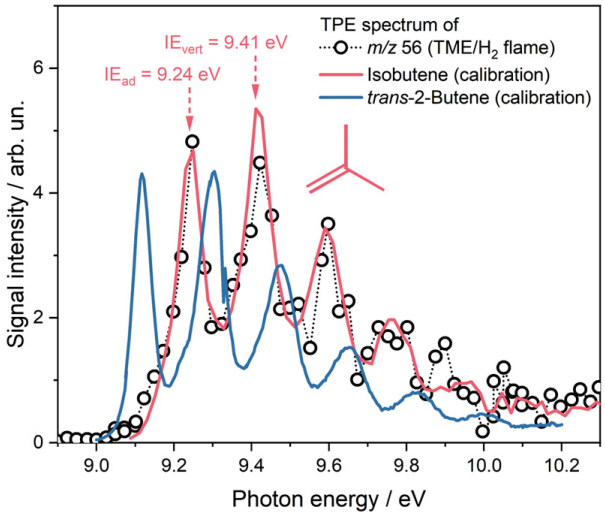

Fig. 6. Assignment of isobutene to *m/z* 56 by photoelectron spectroscopy in the TME/H_2 flame.

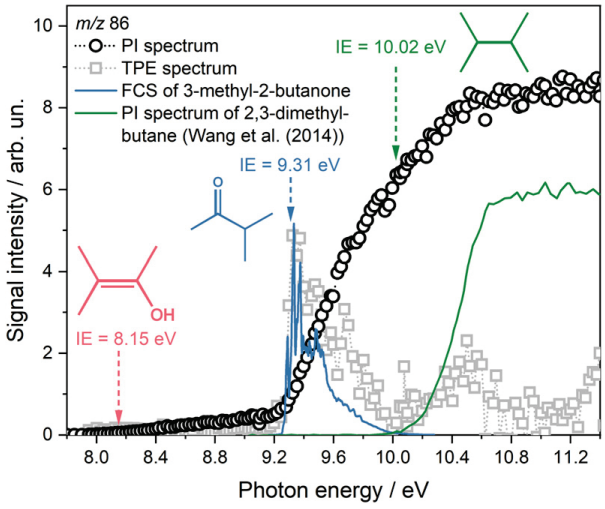

Fig. 7. Photoionization and threshold photoelectron spectra of *m/z* 86 measured in the TME/H_2 flame and comparison with a Franck-Condon simulation of 3-methyl-2-butanone and a literature spectrum of 2,3-dimethylbutane.

(C_6H_{14}), which has an ionization energy of 10.02 eV [30], cannot be identified with confidence from the PI or TPE spectrum. No increase in photoion yield is observed at the ionization energy of this species. Instead, the photoionization curve stagnates at about 10.5 eV (see Fig. 7) which is in accordance with the reference spectrum of 2,3-dimethylbutane measured by Wang et al. [31]. An onset in the PI spectrum is measured at a significantly lower photon energy of about 8.1 eV and a second increase of the signal between 9.25 and 9.3 eV is observed. Ionization energies of other C_6H_{14} isomers are in the range of 10.06 and 10.18 eV [30] so that their presence can be excluded and oxygenated species must

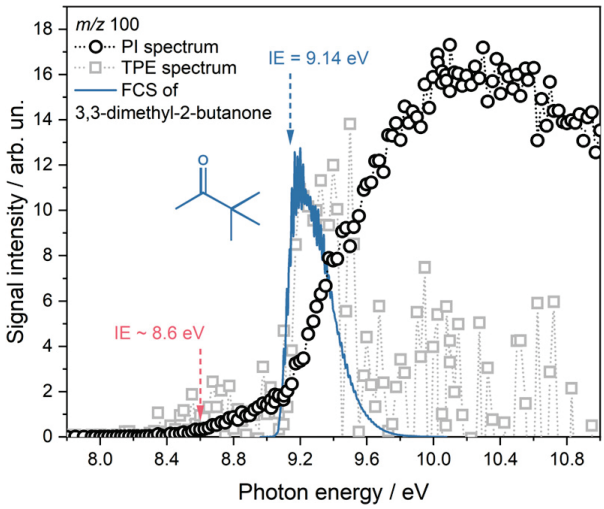

Fig. 8. Photoionization and threshold photoelectron spectra of *m/z* 100 measured in the TME/H_2 flame and comparison with a Franck-Condon simulation of 3,3-dimethyl-2-butanone.

be considered instead. One possibility is the ketone 3-methyl-2-butanone ($C_5H_{10}O$) with an ionization energy of 9.31 eV [32]. It is predicted by the high-temperature models with a maximum mole fraction of about $4.1{\cdot}10^{-5}$ and in higher concentration of $1.7{\cdot}10^{-4}$ by the NUIGMech1.2. It is formed by unimolecular decomposition of the 1,1,2-trimethylpropoxy radical ($C_6H_{13}O$). The latter radical is formed in the mechanism via reaction of the C_6H_{13} radical 2,3-dimethylbut-2-yl (indicated as XC6–2 in the ROP analysis) with HO_2 and CH_3O_2 radicals, respectively. Our calculation of the adiabatic ionization energy for 3-methyl-2-butanone at the G4 level of theory [33] with Gaussian 16 [34] gives a value of 9.29 eV close to the literature value of 9.31 eV from [32]. A Franck-Condon simulation (FCS) was performed at the B3LYP\6–311G(2d,d,p) optimized geometries. This spectrum is also presented in Fig. 7 and confirms the presence of 3-methyl-2-butanone in the investigated flame. Franck-Condon simulations were also performed for 3,3-dimethyl-2-butanone (Fig. 8) and 2,3-dimethyl-1,3-butadiene (Fig. 9) at the same level of theory.

A possible oxygenate that may explain the onset at about 8.1 eV is the enol 3-methyl-2-buten-2-ol (C_5H_9OH) with an ionization energy of 8.15 eV [35]. It is not included in the mechanism, but could be directly formed from 2-methyl-2-butene (BC5H10) by a substitution reaction:

$$\mathrm{BC5H10 + OH = C_5H_9OH + H} \qquad \text{(R7)}$$

It has to be noted that several more $C_5H_{10}O$ isomers exist, but the presence of both the enol 3-methyl-2-buten-2-ol and its keto tautomer 3-methyl-2-butanone is plausible in the investigated

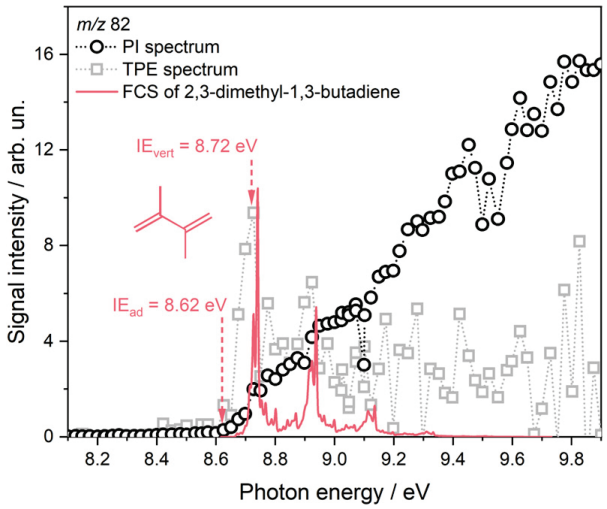

Fig. 9. Photoionization and threshold photoelectron spectra of *m/z* 82 measured in the TME/H_2 flame and comparison with a Franck-Condon simulation of 2,3-dimethyl-1,3-butadiene.

TME/H_2 flame. Formation of these oxygenates may be enhanced by low-temperature oxidation chemistry, which has already been observed in other hydrocarbon-doped hydrogen flames with the identical C:H:O ratio [36] and can be more pronounced due to probe perturbations [37]. Probe perturbations have been extensively studied [19,20,38,39] and the cooling effect of the sampling nozzle is sufficiently approximated for our 1D simulations using the perturbed temperature profile. However, there are other probe-induced effects that may affect the flame structure and can only be covered by 2D simulations. In particular, the distortion of the streamlines by the suction effect of the probe can explain deviations very close to the burner, but can be reduced by small orifice diameters [39].

Concentrations of many oxygenates are already near their maximum for the first 1.25 mm in the flame, where the measured temperature is below 740 K and falls into the low-temperature regime. They are better predicted by the NUIGMech1.2 as shown in Fig. S4 for ketene (C_2H_2O), acetaldehyde (CH_3CHO), acetone (C_3H_6O), and 3-methyl-2-butanone ($C_5H_{10}O$). Figure S5 shows two mass spectra recorded at a HAB of 1 mm for photon energies of 10.6 and 9.6 eV. This position corresponds to a flame temperature of about 690 K. The presence of methyl hydroperoxide (CH_3OOH) in the TME/H_2 flame can be clearly demonstrated by the measured photoionization spectrum at *m/z* 48 in comparison to a reference spectrum of the methyl hydroperoxide measured by Moshammer et al. [40] as shown in Fig. S6 in the supplementary material, which hints at the participation of the low-temperature oxidation chemistry in this flame. Formation of alkyl hydroperoxides was also observed in other alkane- and alkene-doped hydrogen flames in [36]. Other larger oxygenated species could be detected in the TME/H_2 flame, e.g., butanone at *m/z* 72 is clearly identified by comparison of the measured TPE spectrum with the reference spectrum of the neat substance by Kercher et al. [41] as presented in Fig. S7 in the supplementary material. The calculated maximum mole fraction of this oxygenated species, based on the PICS of butanal [42], is $3.1 \cdot 10^{-4}$ and all used mechanisms strongly underestimate the concentration.

A species with a significant higher mass than the hydrocarbon fuel TME was observed at *m/z* 100 as presented in Fig. 8 (see also the mass spectrum in Fig. S5). The onset of the PI spectrum is found at 8.6 eV. The signal slope increases at 9.1 eV, which may be caused by the oxygenate 3,3-dimethyl-2-butanone (also known as pinacolone), as suggested by the comparison of the measured photoelectron spectrum with a Franck-Condon simulation. The adiabatic ionization energy of 9.14 eV from the literature [32] closely matches our calculated value of 9.09 eV. A possible formation pathway can be found in the low-temperature chemistry according to Fish and Wilson [43], i.e., the oxidation of the 2,3-dimethylbut-2-yl radical by molecular oxygen to yield the 2-hydroperoxy-2,3-dimethylbut-3-yl radical ($C_6H_{13}O_2$), which then decomposes to 3,3-dimethyl-2-butanone ($C_6H_{12}O$) and OH according to R8:

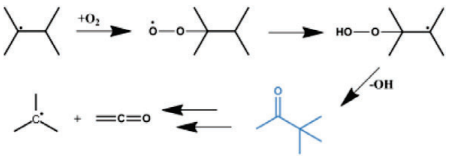

(R8)

Consumption of 3,3-dimethyl-2-butanone by H abstraction, followed by β-CC-scission would then yield ketene (C_2H_2O) and *tert*–butyl radicals (C_4H_9). *tert*–Butyl radicals have the lowest ionization energy of all butyl radicals and were clearly identified in the TME/H_2 flame by the onset at about 6.9 eV in the PI spectrum (see Fig. S8 in the supplementary material). They are also formed by hydrogen addition reaction from isobutene as presented in the ROP analysis (see Fig. 4) and their presence in the flame cannot be taken as confirmation for the formation of 3,3-dimethyl-2-butanone. In principle, the formation of O-heterocycles by decomposition of hydroperoxyalkyl radicals ($C_6H_{13}O_2$) and ring closure, e.g., 2,2,3-trimethyloxetane or 2,2,3,3-tetramethyloxirane, is also possible under low-temperature conditions as observed in the oxidation of 2,3-dimethylbutane [31,43]. Experimental ionization energies of branched heptanes (C_7H_{16}) are unknown, their formation, however, is less likely, e.g., 2,2,3-trimethylbutane may be formed by recombination of the 2,3-dimethylbut-2-yl radical with methyl radicals. However, neither 3,3-

dimethyl-2-butanone nor 2,2,3-trimethylbutane are included in the reaction mechanism.

The fuel radical, i.e., the C_6H_{11} radical (XC6D1–3 in the ROP analysis) decomposes to 3-methyl-1,2-butadiene (B12DE3M) and methyl radicals:

$$XC6D1\text{–}3 = B12DE3M + CH_3 \quad (R9)$$

In Fig. S9 (see supplementary material), the measured photoionization spectrum at *m/z* 68 is well reproduced by both reference spectra of the C_5H_8 isomers 3-methyl-1,2-butadiene [42] and isoprene [44] up to a photon energy of 9.5 eV. Although the spectrum of the former species better represents the measured PI curve at higher photon energies, the presence of isoprene cannot be excluded. Hydrogen atom assisted isomerization of 3-methyl-1,2-butadiene to isoprene is also included in the reaction mechanisms. Therefore, the presented mole fraction of C_5H_8 in Fig. 3 is the sum of both discussed isomers and was calculated with the known photoionization cross section of 3-methyl-1,2-butadiene by Yang et al. [42]. Note that a higher mole fraction of isoprene is predicted by the model than for its isomer 3-methyl-1,2-butadiene. Instead of formation of 3-methyl-1,2-butadiene (C_5H_8) by β-CC-scission from the fuel radical (C_6H_{11}), 2,3-dimethyl-1,3-butadiene (C_6H_{10}) can also be formed by β-CH-scission. Its presence can be confirmed by the onset in the PI spectrum of *m/z* 82 at about 8.6 eV (see Fig. 9) that fits to the ionization energy of 8.62 eV for 2,3-dimethyl-1,3-butadiene measured by Bieri at al. [45] and the Franck-Condon simulation also fits to the measured TPE spectrum. The measured PI spectrum of the C_6H_{11} radical is presented in Fig. S10.

Conclusion

A laminar premixed low-pressure hydrogen flame doped with tetramethylethylene (TME) was investigated by photoionization mass spectrometry and photoelectron photoion coincidence spectroscopy. TME was chosen due to its special structure (i.e., it only contains allylic C–H bonds) and its decay is described based on the experimental and modeling results. Overall, three fuel consumption pathways can be identified. At *m/z* 70, 2-methyl-2-butene (C_5H_{10}) with an ionization energy of 8.69 eV is clearly identified by its photoelectron spectrum and is found in significant concentration in the flame. The formation of this species is directly linked to fuel decay by hydrogen addition to initially form the 2,3-dimethylbut-2-yl radical (C_6H_{13}) and by subsequent β-CC-scission of this radical. The reaction mechanism also shows that this decomposition step is the most important one regarding the total carbon flux in the reaction path analysis and 2-methyl-2-butene is also formed directly from the fuel by a substitution reaction. The formation of 2-methyl-2-butene can explain the observation of isobutene in the investigated flame since it is a decomposition product of 2-methyl-2-butene. As expected, hydrogen abstraction by H and OH at one of the equivalent C–H bonds is also possible and results in the formation of the resonance-stabilized 2,3-dimethyl-2-buten-1-yl radical (C_6H_{11}) at *m/z* 83. This radical can decompose to 3-methyl-1,2-butadiene (C_5H_8) by β-CC-scission and 2,3-dimethyl-1,3-butadiene (C_6H_{10}) by β-CH-scission, respectively. Both species are identified in the investigated flame. The presence of isoprene (2-methyl-1,3-butadiene) at *m/z* 70 cannot be excluded since its ionization energy is very close to the ionization energy of 3-methyl-1,2-butadiene and rapid isomerization to isoprene by 1,2-H-shift reaction is known. The experimental results confirm the formation of a species with higher mass than the fuel at *m/z* 100. The photoionization spectrum at this mass-to-charge ratio has a distinct increase at about 9.1 eV, which agrees with 3,3-dimethyl-2-butanone ($C_6H_{12}O$). A plausible formation route proceeds via the 2-hydroperoxy-2,3-dimethylbut-3-yl radical due to low-temperature oxidation chemistry in the flame.

Declaration of Competing Interest

The authors declare that they have no known competing financial interests or personal relationships that could have appeared to influence the work reported in this paper.

Acknowledgments

The authors gratefully acknowledge Luka Debenjak and Patrick Ascher for technical assistance, Andras Bodi for experimental research support, Munko Gonchikzhapov for assistance during temperature measurements, and all other members of the SLS flame team. The authors thank the German Research Foundation (DFG) for financial support under contract KA3871/3–2 and KO4786/2–2. Patrick Hemberger additionally thanks the Swiss Federal Office of Energy for financial support under contract SI/501269–01. The experiments were performed at the Swiss Light Source of the Paul Scherrer Institute in Villigen, Switzerland.

Supplementary materials

Supplementary material associated with this article can be found, in the online version, at doi:10.1016/j.proci.2022.07.205.

References

[1] D.F. McMillen, D.M. Golden, Hydrocarbon bond dissociation energies, Ann. Rev. Phys. Chem. 33 (1982) 493–532.

[2] D. Krüger, P. Oßwald, M. Köhler, P. Hemberger, T. Bierkandt, Y. Karakaya, T. Kasper, Hydrogen abstraction ratios: a systematic iPEPICO spectroscopic investigation in laminar flames, Combust. Flame 191 (2018) 343–352.

[3] C.S. McEnally, L.D. Pfefferle, Decomposition and hydrocarbon growth processes for hexenes in nonpremixed flames, Combust. Flame 143 (2005) 246–263.

[4] C.-.W. Zhou, A. Farooq, L. Yang, A.M. Mebel, Combustion chemistry of alkenes and alkadienes, Prog. Energy Combust. Sci. 90 (2022) 100983.

[5] Y. Wu, B. Rossow, V. Modica, X. Yu, L. Wu, F. Grisch, Laminar flame speed of lignocellulosic biomass-derived oxygenates and blends of gasoline/oxygenates, Fuel 202 (2017) 572–582.

[6] R.R. Baldwin, D.R. Stout, R.W. Walker, Relative rate study of the addition of HO_2 radicals to ethylene and to tetramethylethylene, J. Chem. Soc. Faraday Trans. 80 (1984) 3481–3489.

[7] H. Biehl, J. Bittner, B. Bohn, R. Geers-Müller, F. Stuhl, Temperature dependence of the rate constants of the reactions of oxygen atoms with trans-2-butene, cis-2-butene, 2-methylpropene, 2-methyl-2-butene, and 2,3-dimethyl-2-butene, Int. J. Chem. Kinet. 27 (1995) 277–285.

[8] R.W. Murray, W. Kong, S.N. Rajadhyaksha, The ozonolysis of tetramethylethylene. Concentration and temperature effects, J. Org. Chem. 58 (1993) 315–321.

[9] M. Barton, J.R. Ebdon, A.B. Foster, S. Rimmer, Ozonolysis of tetramethylethylene: Characterization of cyclic and open-chain oligoperoxidic products, J. Org. Chem. 69 (2004) 6967–6973.

[10] X. Yang, J. Deng, D. Li, J. Chen, Y. Xu, K. Zhang, X. Shang, Q. Cao, Transient species in the ozonolysis of tetramethylethene, J. Environ. Sci. 95 (2020) 210–216.

[11] G.T Drozd, J. Kroll, N.M Donahue, 2,3-Dimethyl-2-butene (TME) ozonolysis: pressure dependence of stabilized Criegee intermediates and evidence of stabilized vinyl hydroperoxides, J. Phys. Chem A 115 (2011) 161–166.

[12] Y. Wu, S. Panigrahy, A.B. Sahu, et al., Understanding the antagonistic effect of methanol as a component in surrogate fuel models: a case study of methanol/n-heptane mixtures, Combust. Flame 226 (2021) 229–242.

[13] S.S. Nagaraja, J. Liang, S. Dong, S. Panigrahy, A. Sahu, G. Kukkadapu, S.W. Wagnon, W.J. Pitz, H.J. Curran, A hierarchical single-pulse shock tube pyrolysis study of C2–C6 1-alkenes, Combust. Flame 219 (2020) 456–466.

[14] S. Dong, K. Zhang, P.K. Senecal, G. Kukkadapu, S.W. Wagnon, S. Barrett, N. Lokachari, S. Panigaphy, W.J. Pitz, H.J. Curran, A comparative reactivity study of 1-alkene fuels from ethylene to 1-heptene, Proc. Combust. Inst. 38 (2021) 611–619.

[15] A.B. Sahu, A.A.E.-S. Mohamed, S. Panigrahy, C. Saggese, V. Patel, G. Bourque, W.J. Pitz, H.J. Curran, An experimental and kinetic modeling study of NO_x sensitization on methane autoignition and oxidation, Combust. Flame 238 (2022) 111746.

[16] B. Sztáray, K. Voronova, K.G. Torma, K.J. Covert, A. Bodi, P. Hemberger, T. Gerber, D.L. Osborn, CRF-PEPICO: double velocity map imaging photoelectron photoion coincidence spectroscopy for reaction kinetics studies, J. Chem. Phys. 147 (2017) 013944.

[17] P. Oßwald, P. Hemberger, T. Bierkandt, E. Akyildiz, M. Köhler, A. Bodi, T. Gerber, T. Kasper, *In situ* flame chemistry tracing by imaging photoelectron photoion coincidence spectroscopy, Rev. Sci. Instrum. 85 (2014) 025101.

[18] P. Hemberger, A. Bodi, T. Bierkandt, M. Köhler, D. Kaczmarek, T. Kasper, Photoelectron photoion coincidence spectroscopy provides mechanistic insights in fuel synthesis and conversion, Energy Fuels 35 (2021) 16265–16302.

[19] N. Hansen, T.A. Cool, P.R. Westmoreland, K. Kohse-Höinghaus, Recent contributions of flame-sampling molecular-beam mass spectrometry to a fundamental understanding of combustion chemistry, Prog. Energy Combust. Sci. 35 (2009) 168–191.

[20] F.N. Egolfopoulos, N. Hansen, Y. Ju, K. Kohse-Höinghaus, C.K. Law, F. Qi, Advances and challenges in laminar flame experiments and implications for combustion chemistry, Prog. Energy Combust. Sci. 43 (2014) 36–67.

[21] D.G. Goodwin, R.L. Speth, H.K. Moffat, B.W. Weber, Cantera: an object-oriented software toolkit for chemical kinetics, thermodynamics, and transport processes, http://www.cantera.org, Version 2.5.1, 2021.

[22] Chemical Workbench, http://www.kintechlab.com/, Version 4.1.19528, 2017.

[23] M. Schenk, L. Leon, K. Moshammer, P. Oßwald, T. Zeuch, L. Seidel, F. Mauss, K. Kohse-Höinghaus, Detailed mass spectrometric and modeling study of isomeric butene flames, Combust. Flame 160 (2013) 487–503.

[24] M. Gonchikzhapov, T. Kasper, Decomposition reactions of $Fe(CO)_5$, $Fe(C_5H_5)_2$, and TTIP as precursors for the spray-flame synthesis of nanoparticles in partial spray evaporation at low temperatures, Ind. Eng. Chem. Res. 59 (2020) 8551–8561.

[25] J. Power, K.P. Somers, S.S. Nagaraja, W. Wyrebak, H.J. Curran, Theoretical study of the reaction of hydrogen atoms with three pentene isomers: 2-methyl-1-butene, 2-methyl-2-butene, and 3-methyl-1-butene, J. Phys. Chem. A 124 (2020) 10649–10666.

[26] J. Power, K.P. Somers, S.S. Nagaraja, H.J. Curran, Hierarchical study of the reactions of hydrogen atoms with alkenes: a theoretical study of the reactions of hydrogen atoms with C_2–C_4 alkenes, J. Phys. Chem. A 125 (2021) 5124–5145.

[27] D.M. Mintz, A. Kuppermann, Photoelectron spectroscopy of ethylene, isobutylene, trimethylethylene, and tetramethylethylene at variable angle, J. Chem. Phys. 71 (1979) 3499–3513.

[28] J. Pieper, S. Schmitt, C. Hemken, et al., Isomer identification in flames with double-imaging photoelectron/photoion coincidence spectroscopy (i^2PEPICO) using measured and calculated reference photoelectron spectra, Z. Phys. Chem. 232 (2018) 153–187.

[29] L. Ruwe, K. Moshammer, N. Hansen, K. Kohse-Höinghaus, Consumption and hydrocarbon growth processes in a 2-methyl-2-butene flame, Combust. Flame 175 (2017) 34–46.
[30] K. Watanabe, T. Nakayama, J. Mottl, Ionization potentials of some molecules, J. Quant. Spectrosc. Radiat. Transf. 2 (1962) 369–382.
[31] Z. Wang, O. Herbinet, Z. Cheng, B. Husson, R. Fournet, F. Qi, F. Battin-Leclerc, Experimental investigation of the low temperature oxidation of the five isomers of hexane, J. Phys. Chem. A 118 (2014) 5573–5594.
[32] P.J. Linstrom, W.G. Mallard, in, National Institute of Standards and Technology, Gaithersburg MD, 20899, https://doi.org/10.18434/T4D303, (retrieved December 3, 2021).
[33] L.A. Curtiss, P.C. Redfern, K. Raghavachari, Gaussian-4 theory, J. Chem. Phys. 126 (2007) 084108.
[34] M.J. Frisch, G.W. Trucks, H.B. Schlegel, et al., Gaussian 16, Revision A.03, Gaussian, Inc, Wallingford, CT, 2016.
[35] F. Turecek, L. Brabec, J. Korvola, Unstable enols in the gas phase. Preparation ionization, energies, and heats of formation of (E)- and (Z)-2-buten-2-ol, 2-methyl-1-propen-1-ol, and 3-methyl-2-buten-2-ol, J. Am. Chem. Soc. 110 (1988) 7984–7990.
[36] T. Bierkandt, P. Oßwald, N. Gaiser, et al., Observation of low-temperature chemistry products in laminar premixed low-pressure flames by molecular-beam mass spectrometry, Int. J. Chem. Kinet. 53 (2021) 1063–1081.
[37] X. Zhang, Y. Zhang, T. Li, et al., Low-temperature chemistry triggered by probe cooling in a low-pressure premixed flame, Combust. Flame 204 (2019) 260–267.
[38] N. Hansen, R.S. Tranter, J.B. Randazzo, J.P.A. Lockhart, A.L. Kastengren, Investigation of sampling-probe distorted temperature fields with X-ray fluorescence spectroscopy, Proc. Combust. Inst. 37 (2019) 1401–1408.
[39] Y. Karakaya, J. Sellmann, I. Wlokas, T. Kasper, Influence of the sampling probe on flame temperature, species, residence times and on the interpretation of ion signals of methane/oxygen flames in molecular beam mass spectrometry measurements, Combust. Flame 229 (2021) 111388.
[40] K. Moshammer, A.W. Jasper, D.M. Popolan-Vaida, et al., Detection and identification of the keto-hydroperoxide ($HOOCH_2OCHO$) and other intermediates during low-temperature oxidation of dimethyl ether, J. Phys. Chem. A 119 (2015) 7361–7374.
[41] J.P. Kercher, E.A. Fogleman, H. Koizumi, B. Sztáray, T. Baer, Heats of formation of the propionyl ion and radical and 2,3-pentanedione by threshold photoelectron photoion coincidence spectroscopy, J. Phys. Chem. A 109 (2005) 939–946.
[42] B. Yang, J. Wang, T.A. Cool, N. Hansen, S. Skeen, D.L. Osborn, Absolute photoionization cross-sections of some combustion intermediates, Int. J. Mass Spectrom. 309 (2012) 118–128.
[43] A. Fish, J.P. Wilson, The nonisothermal oxidation of 2,3-dimethylbutane, Symp. (Int.) Combust. 13 (1971) 229–238.
[44] X. Liu, W. Zhang, Z. Wang, et al., Dissociative photoionization of isoprene: experiments and calculations, J. Mass Spectrom. 44 (2009) 404–409.
[45] G. Bieri, F. Burger, E. Heilbronner, J.P. Maier, Valence ionization energies of hydrocarbons, Helv. Chim. Acta 60 (1977) 2213–2233.

Activation effect of ozone and DME on the partial oxidation of natural gas surrogates and validation of pressure-dependent ozone decomposition

Kaczmarek, D., Bierkandt, T., Rudolph, C., Grimm, S., Shaqiri, S., Höner, M., Gaiser, N., Atakan, B., Köhler, M., Hemberger, P., Kasper, T.
Applications in Energy and Combustion Science, 2023, 13, 100107
DOI: 10.1016/j.jaecs.2022.100107

My contribution to this work was the development of the reactor interface to the CRF-PEPICO endstation, manufacturing supervision of the design, the commissioning of the experiment, support in the measurement of data.

Applications in Energy and Combustion Science 13 (2023) 100107

Contents lists available at ScienceDirect

Applications in Energy and Combustion Science

journal homepage: www.sciencedirect.com/journal/applications-in-energy-and-combustion-science

Activation effect of ozone and DME on the partial oxidation of natural gas surrogates and validation of pressure-dependent ozone decomposition

D. Kaczmarek [a,*], T. Bierkandt [b], C. Rudolph [c], S. Grimm [c], S. Shaqiri [a], M. Höner [a], N. Gaiser [b], B. Atakan [c], M. Köhler [b], P. Hemberger [d], T. Kasper [a,e]

[a] Institute for Combustion and Gas Dynamics, Mass spectrometry in reactive flows, University of Duisburg-Essen, Duisburg, Germany
[b] Institute of Combustion Technology, German Aerospace Center (DLR), Pfaffenwaldring 38-40, Stuttgart 70569, Germany
[c] Institute for Combustion and Gas Dynamics, Thermodynamics, University of Duisburg-Essen, Duisburg, Germany
[d] Laboratory for Synchrotron Radiation and Femtochemistry, Paul Scherrer Institute, Villigen, Switzerland
[e] Technical Thermodynamics, University of Paderborn, Paderborn, Germany

ARTICLE INFO

Keywords:
Polygeneration
Plug-flow reactor
Partial oxidation
Natural gas
Dimethyl ether
Ozone

ABSTRACT

To address current challenges related to climate change, novel concepts, such as engine-based polygeneration under fuel-rich conditions, have recently been developed. In this context, understanding and validation of the associated chemical kinetics are a key factor for prediction and optimizations. In this work, the combined effect of ozone and DME as additives on the partial oxidation of natural gas mixtures is investigated in a plug-flow reactor at a pressure of 4 bar and at temperatures ranging from 373 to 973 K. Double-imaging photoelectron photoion coincidence (i^2PEPICO) spectroscopy measurements are presented to study the conversion of the reactants and the formation of main products, and to identify important intermediates responsible for the low temperature chemistry phenomena and ignition characteristics of the natural gas/dimethyl ether/ozone mixture. Among the activation effect of ozone, the temperature-variant ozone dissociation at elevated pressures up to 20 bar is studied for the first time, revealing the start of ozone decomposition at 423 K in the investigated pressure range. In addition, the ozone decomposition is shown to be slightly pressure-dependent in the pressure range between 1 and 20 bar with lower ozone conversions at higher pressures. The experimental results are compared with model predictions using literature reaction mechanisms for validation and further analysis. The ozone decomposition initiates fuel conversion and the formation of oxygenates and hydroperoxides at very low temperatures, i.e., 423 K, resulting in an overall three-stage oxidation process at ~450 K (1. stage), ~550 K (2. stage), and ~750 K (3. stage). Also, the overall fuel conversion is enhanced in the intermediate temperature range (between 550 K and 750 K) by up to 40%-points. The hydroperoxides, among other species, are clearly identified by mass-selected threshold photoelectron spectra from the literature. Excellent agreement between experiments and simulations is found, while deviations are observed for some oxygenates at very low temperatures showing the need for further model improvements.

1. Introduction

Overcoming the climate crisis is currently one of the biggest challenges facing the world. To limit the consequences, emissions should be avoided or recycled, renewable energies must be integrated into the energy system, and primary fossil energy sources should be used efficiently. The use of internal combustion engines allows the flexible provision of various forms of secondary energy, such as work, heat, and chemical energy, combined with small exergy losses by partial oxidation of low-order hydrocarbons, like methane and natural gas [1,2]. High equivalence ratios and high temperatures and pressures are needed to convert methane or natural gas to synthesis gas or oxygenates. During the compression stroke in the internal combustion engine, medium to high temperatures and pressures prevail, but these alone do not lead to ignition or conversion of the fuel [3]. The addition of small amounts of more reactive additives is required to improve the conversion and ignition characteristics of the base fuel under these conditions. In this context, carbon-based, hydrogen-based, or oxygenated additives, such

* Corresponding author.
E-mail address: dennis.kaczmarek@uni-due.de (D. Kaczmarek).

https://doi.org/10.1016/j.jaecs.2022.100107
Received 22 June 2022; Received in revised form 30 October 2022; Accepted 9 December 2022
Available online 10 December 2022

as dimethyl ether [4] or diethyl ether [5], and their effect on the partial oxidation of methane or natural gas were recently studied. These additives already consume the existing oxygen, so the oxygen is not available for the oxidation of the base fuel, and consequently, the conversion of the base fuel decreases [6].

In more conventional combustion systems, such as lean driven homogeneous charge compression ignition (HCCI) engines, the addition of ozone instead of common additives helps to control stable operation and to reduce emissions [7–11]. The effect of ozone on carbon-based fuels is based on the formation of highly reactive O-atoms through dissociation. Also, rapid exothermic ozonolysis occurs when olefins are present in the mixture (in gasoline up to 20%), as also recently investigated for ethylene/oxygen/ozone mixtures in a jet-stirred reactor at temperatures between 300 and 1000 K by Smith Lewin et al. [12]. The overall effect is that ozone promotes chain branching reactions and radical formation, even at low temperatures [13]. A current overview on the effect of ozone addition on combustion was given by Sun et al. [13].

The dissociation of ozone in bath gases was kinetically investigated by only a few groups. In 1962, Jones and Davidson [14] studied the ozone decomposition behind reflected shock waves at temperatures between 689 and 910 K and a wide range of ozone mole fractions (0.0438–1.87 mole-%) in a diluent, argon and nitrogen, respectively. They obtained rate coefficients for $M+O_3 \rightleftharpoons M+O_2+O$ and $O+O_3 \rightleftharpoons O_2+O_2$ at their low-pressure-limit. The data set on ozone dissociation, available in the literature, was extended by Michael [15] in 1971 and by Peukert et al. [16] in 2013. Michael [15] performed shock-tube experiments combined with time-of-flight mass spectrometer measurements to obtain ozone time histories behind reflected shock waves at temperatures between 988 and 1400 K. The initial mixtures consisted of ozone with mole fractions of 4.20–5.10 mole-% in krypton. From the ozone time histories, Michael [15] derived rate coefficients of the reactions $M+O_3 \rightleftharpoons M+O_2+O$ and $O+O_3 \rightleftharpoons O_2+O_2$ with krypton as collision partner. Similarly, Peukert et al. [16] performed shock-tube experiments of ozone/krypton mixtures and measured the associated O-atom formation via atomic resonance absorption spectrometry (ARAS) at temperatures between 819 and 1166 K and pressures between 0.13 and 0.6 bar. In contrast to the work of Michael [15] or Jones and Davidson [14], Peukert et al. [16] evaluated highly diluted mixtures with ozone mole fractions of 0.007177 and 0.0167 mole-% in krypton. Jian et al. [17] performed plug-flow reactor experiments with ozone/oxygen and ozone/oxygen/hydrogen mixtures, diluted in nitrogen at atmospheric pressure and temperatures between 400 K and 575 K. They found the conversion onset of ozone at temperatures of 425 K for mixtures containing 0.245 mole-% ozone and 2.1 mole-% oxygen, and that ozone is completely decomposed at 550 K. Using these experiments, they updated kinetic models on the ozone dissociation and ozone-oxygen-hydrogen interactions, which is fundamental for combustion processes using hydrogen-containing fuels.

Unlike ozone dissociation, molecular recombination reactions do not occur without external influences. Sehested et al. [18] and De Cobos and Troe [19] studied, among other groups, the recombination reaction ($O_2+O \rightleftharpoons O_3$) to form ozone from molecular and atomic oxygen, diluted in argon, using pulsed radiolysis or laser flash photolysis, however, this is not of interest for this study.

With increasing interest in the effect of ozone on the breaking of C-C or C-H bonds of hydrocarbons, the fundamentals of the ozone-assisted conversion of, e.g., methane and natural gas surrogates has been frequently studied. Gesser et al. [20] studied the fuel-rich oxidation of methane and ethane in a plug-flow reactor at equivalence ratios of 23 and 40 and atmospheric pressure, aiming at the formation of alcohols. An ozone/oxygen mixture containing 0.24 mole-% ozone in the total mixture was used as an oxidizer. They observed that ozone is completely consumed at 533 K. The addition of ozone initiated the conversion of methane and ethane at low temperatures between 573 and 673 K, while without ozone no conversion was observed in this temperature range. The conversion of methane and ethane was found to be 2% and 4%, respectively. Also, the ozone addition led to methanol and ethanol selectivities of 20% and 30%, respectively. Beside methanol, other oxygenated products or intermediates, such as formaldehyde or methyl hydroperoxide, were identified by Rotzoll [21], who presented plug-flow reactor experiments with methane/ozone/oxygen mixtures at equivalence ratios of 1, 2, and 4 with up to 3 mole-% ozone in the total mixture. In contrast to Gesser et al. [20], Rotzoll [21] studied the ozone-assisted conversion of methane at low pressures of 360 – 470 mbar and temperatures between 480 and 830 K and found an early reaction onset at around 500 K. The complete conversion of ozone was finally observed at around 700 K. In the context of ignition characteristics and combustion performance, Ji et al. [22] studied the ignition delay times of lean methane/ozone/air mixtures ($\Phi = 0.6$) with varying ozone mole fractions between 0 and 0.1 mole-%. They found that the increased reactivity of ozone leads to a significantly reduced ignition delay time, however, peak pressure and pressure rise rates are increased. More recently, Herzler et al. also observed reduced ignition delay times at temperatures below 1100 K determined in a high-pressure shock-tube at fuel-rich conditions ($\Phi = 2, 10$) and a pressure of 30 bar [23]. In spite of the negative side effects found by Ji et al. [22], the addition of ozone to natural gas enables a reduction of the intake temperature in HCCI or PCCI (premixed charged compression ignition) engines, as described by Salahi and Gharehghani [24], and helps to reduce emissions and to save fuel due to overall lower temperatures and leaner fuel-air mixtures. Oxidation of alternative fuels, such as biogas (that are mainly methane/CO_2 mixtures), also benefits from ozone addition, as recently pointed out by Paulauskas et al. [25] because the addition of ozone can counteract the effects of higher heat capacities and, e.g., lower flame speeds and temperatures of CO_2-containing mixtures.

Studies on the oxidation of dimethyl ether (DME) in the presence of ozone [26–28] recommend its usage in cool flames or low temperature oxidation applications because DME conversion at low temperatures is enabled as reactive intermediates such as H_2O_2, CH_3OCHO, CH_3OCH_2, and $CH_3OCH_2O_2$ are increasingly formed. Zhao et al. [28] performed atmospheric pressure experiments at temperatures between 400 and 750 K to investigate the oxidation of lean DME/ozone/oxygen mixtures ($\Phi = 0.3$) with up to 0.146 mole-% ozone and developed a kinetic model. They found that ozone starts to decompose at temperatures around 450 K and that ozone decomposition is coupled to CH_2O and H_2O_2 formation.

Ozone-assisted combustion of other fuels, such as ethanol, methyl ester, or iso-octane, has also been investigated in other studies that can be found in the literature [11,29,30].

But, experimental studies on ozone-assisted combustion/oxidation at elevated pressure under well-known boundary conditions such as in flow or jet-stirred reactors are scarce in the literature. Such studies can help to identify key reactions during the oxidation process and contribute to the validation of kinetic models that are capable of correctly predicting ignition timing, intermediates, and interesting species or emissions in engine simulations. This gap is addressed here by investigating the effect of ozone and DME on the homogeneous partial oxidation of a natural gas surrogate with respect to fuel conversion and the formation of useful products like methanol or acetaldehyde in a flow reactor at a pressure of 4 bar. The experimental results are compared to simulation results using a widely validated reaction mechanism combined with an ozone submechanism. The choice of the ozone submechanism is based on the comparison of ozone dissociation in experiments with corresponding simulations. To our knowledge, these are the first high-pressure ozone dissociation experiments in a flow reactor at pressures of up to 20 bar, thus making an unprecedented contribution to the experimental database available in the literature. The obtained knowledge about ozone dissociation helps to explore the homogeneous partial oxidation of the natural gas/DME/ozone mixture. Key reactions are identified by the determination of the complete product composition, using the isomer-selective detection technique of double-imaging photoelectron photoion coincidence spectroscopy as

well as reaction path analyses.

2. Experimental methods

In this section, the experimental setups used for the ozone decomposition and partial oxidation measurements are described. Both measurement series are performed in the same flow reactor described elsewhere [4,31] so only a brief description is given here. Details of the individual measurement series are given in the respective subchapters.

The reactor consists of a 650 mm long quartz tube with an inner diameter of 6 mm enclosed by an Inconel® 601 tube with an inner diameter of 12 mm coated with Silcolloy® 1000 (SilcoTek) to minimize heterogenous reactions. Due to the wall thickness of 1 mm, there is a small gap between the outer wall of the quartz tube and the inner wall of the Inconel® tube. This gap is sealed on both sides with Teflon® tape so that the flow is directed through the quartz tube. Still, the gas can diffuse into this gap so that the pressure inside and outside the quartz tube is equalized. A 500 mm long copper shell, wrapped by heating wires, provides an extended isothermal zone inside the reactor. During operation, the wall temperature of the Inconel® tube is measured by two type-K thermocouples. This temperature is used to regulate the heaters. For each wall temperature, the centerline temperature profiles inside the reactor were measured prior to the experiments under experimental conditions. The reactants are metered and controlled by Coriolis mass flow controllers and mixed before entering the reactor. An ozone generator (TG-40, Ozone Solutions) is used to convert a part of the oxygen stream to ozone upstream of the Coriolis mass flow controller, while the ozone concentration in the gas mixture is measured online by UV/VIS spectroscopy. The pressure is measured and regulated by a heated needle valve upstream and downstream of the reactor, respectively.

2.1. Ozone decomposition measurements

The ozone decomposition measurements were performed at (absolute) pressures of p = 1, 10, and 20 bar, temperatures between 298 and 598 K, and varying volume flow rates to maintain nearly the same residence time in the isothermal zone of the reactor. The volume flow rate is given by V = 50 sccm • p[bar] • 523.15 K / T[K]. To systematically investigate the ozone dissociation, two different ozone amounts were considered, i.e., 100 ppm ozone in oxygen and 5000 ppm ozone in oxygen. It must be noted that the 100 ppm ozone measurements are chosen according to the predicted ozone amount needed in test engines [32]. Accordingly, the 100 ppm ozone measurements were made at the temperatures and pressures described above. In addition, the 5000 ppm ozone measurements were performed at 1 bar to quantify the effect of ozone amount on its dissociation.

Because of the pressure limit of the ozone generator of 4 bar, the ozone mixtures were prepared prior to the experiments in a stainless-steel tank coated with SilcoNert® 2000 (SilcoTek). The stainless-steel tank was first filled with the ozone/oxygen mixture, generated by the ozone generator, up to a pressure of 4 bar. In a second step, the pressure in the tank was increased up to 35 bar by adding oxygen. To obtain homogeneity, the high-pressure ozone/oxygen mixtures were prepared at least one hour prior to the experiments. Hence, the test gas consists of the ozone/oxygen mixture from the stainless-steel tank and neat oxygen each supplied to the reactor by the Coriolis mass flow controller in a ratio that yields the above-mentioned ozone mole fractions. The inertness of the SilcoNert® 2000 coating was demonstrated by sampling the ozone/oxygen mixture from the tank at specified intervals over a 48-hour period, and no ozone was depleted. To measure the ozone concentrations, the reactor was coupled to two UV/VIS spectrometers up- and downstream of the reactor. Although the absorption spectrum of ozone shows a maximum near 254 nm, this wavelength (exact: 253.74 nm) was only used for the 1 bar measurements to calculate the ozone concentration using the Beer-Lambert law and the extinction coefficients from [33]. For measurements at higher pressures, the absorbance spectrum became "fringy" near 254 nm due to saturation effects so that another wavelength, i.e., 289.44 nm, was used for the evaluation. The optical path length of the gas cells is 54 mm.

The measured temperature profiles for each combination of temperature and pressure are shown in Fig. 1, which shows that the length of the isothermal zone decreases with increasing pressure from 450 mm (1 bar) to approx. 300 mm (20 bar). It should be noted that it is not the pressure but the higher volume flow that is responsible for this effect.

2.2. Partial oxidation measurements of natural gas/dimethyl ether/ozone at the Swiss Light Source

The partial oxidation measurements were performed at temperatures between 373 and 973 K in steps of 25 K and a pressure of 4 bar. To obtain plug-flow conditions according to the model of Levenspiel [34], a constant volumetric flow rate of 265 sccm (standard cubic centimeters per minute at 273.15 K and 1013.25 hPa) was used in the partial oxidation measurements. Consequently, the residence times along the complete reactor length vary between 16.5 s (at 373 K) and 8.9 s (at 973 K). The measured temperature profiles, depicted in Fig. 2, show an isothermal zone of approx. 450 mm, and proof that the varying residence times and temperatures do not affect the length of the isothermal zone.

The natural gas surrogate consists of 90% methane (CH_4), 9% ethane (C_2H_6), and 1% propane (C_3H_8). The dimethyl ether (CH_3OCH_3, further abbreviated as DME) amount related to the base fuel is 10%. The oxidation of the natural gas/DME mixture is performed at an equivalence ratio of 2; the oxidizer is an ozone/oxygen mixture resulting in an ozone mole fraction of 245 ppm in the total gas mixture. To minimize the temperature rise from the heat release of exothermal reactions, the test gas is diluted with 95% argon. The mole fractions of the test gas mixture are given in Table 1.

In contrast to the ozone decomposition measurements, ozone was continuously produced by the ozone generator so that no ozone/oxygen mixture preparation was needed. The inlet ozone concentration was measured by a UV/VIS spectrometer upstream of the reactor. The reactor is coupled to the vacuum ultraviolet (VUV) beamline at the Swiss Light Source storage ring (Paul Scherrer Institute) and the product gas is analyzed via double-imaging photoelectron photoion coincidence (i^2PEPICO) spectroscopy following single-photon ionization by VUV light. Because of the chamber-in-chamber design, a longer transfer line is necessary downstream of the needle valve at the reactor outlet as described in [31], where also a detailed description of the SLS reactor

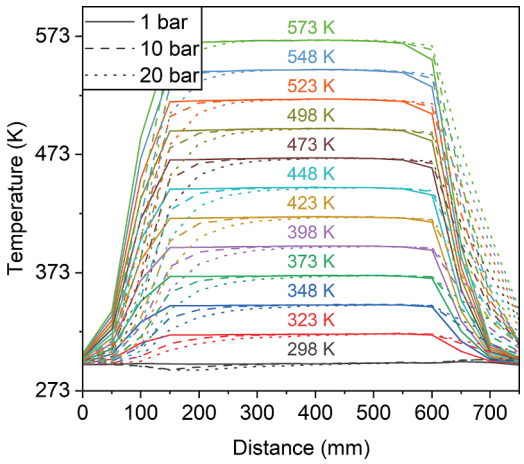

Fig. 1. Measured temperature profiles for reactor temperatures between 298 and 573 K and pressures of 1, 10, and 20 bar. The volume flow rate varies between 34 and 1755 sccm to obtain a constant residence time of approx. 15.3 ± 2 s for the whole reactor length and 7 ± 0.5 s for the reactor distance between 15 and 55 cm.

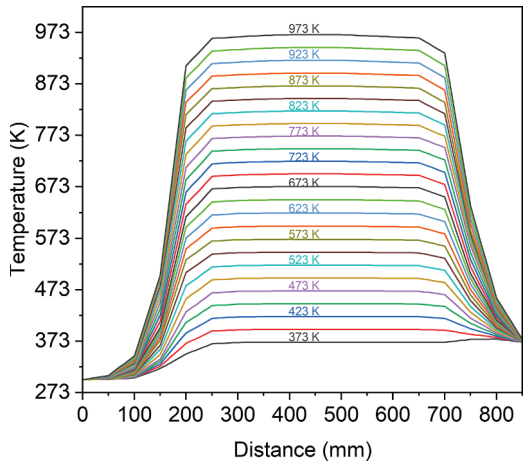

Fig. 2. Measured temperature profiles for reactor temperatures between 373 and 973 K and a pressure of 4 bar. The volume flow rate is 265 sccm resulting in residence times between 16.5 and 8.9 s.

Table. 1
Mole fractions of the test gas mixture used in the partial oxidation measurements.

Ar	CH_4	C_2H_6	C_3H_8	CH_3OCH_3	O_2	O_3
0.948	0.02	0.002	0.00022	0.0025	0.0275	0.000245

experiment can be found. Here, only a brief description is given. At the end of the heated transfer line (373 K), a gas sample is drawn by a quartz nozzle with a small orifice. Residual gases are pumped by a first pumping stage operated at a pressure of 120 mbar. The sampled gas expands into the second pumping stage with a pressure of about $9{\cdot}10^{-6}$ mbar to form a molecular beam. The centerline of this molecular beam expands through a skimmer into the spectrometer chamber where the molecular beam intersects with the photon beam. A gas filter (filled with neat neon or a gas mixture of neon, argon, and krypton) eliminates radiation of higher harmonics. For photon energies smaller than 10.5 eV, a magnesium fluoride window is used. The photon energy can be tuned between 5 and 21 eV. Ionized species are analyzed by time-of-flight mass spectrometry with a mass resolution of $m/\Delta m \approx 300$ and electrons and ions are velocity map imaged (i^2PEPICO setup [35,36]). Each electron can be assigned to a cation from the same ionization event, which permits the measurement of photoion mass-selected threshold photoelectron spectra (ms-TPES). The threshold photoelectrons were selected in a window of 0.005–0.01 eV kinetic energy release.

For each temperature step, photoionization (PI) mass spectra at several photon energies are obtained to allow for the separation of isomeric species. The selected photon energies are 9.7, 10.0, 10.3, 10.6, 11.2, 12.0, 12.8, 13.2, 14.2, 15.0, and 16.0 eV. Secondly, an energy scan was performed at a constant temperature of 573 K in a photon energy range between 9.3 and 12.0 eV in 0.025 eV steps to identify several intermediate species by their photoionization efficiency (PIE) curves, i.e, the photoion yield spectra, or their mass-selected threshold photoelectron spectra. Uncertainties in mole fractions, obtained by direct calibrations and the calibration method described elsewhere [31,37], are typically estimated to be 15–20% for the main species and 30–50% for intermediates with known photoionization cross sections. Mole fractions of species with less well-known or unknown photoionization cross sections exhibit higher uncertainties up to a factor of 2–4 [38]. The used photoionization cross sections are given in the supplemental material. The uncertainties of the mole fractions determined in the UV/VIS experiments were estimated to be 5% based on repeatability measurements.

3. Modeling

Simulations were performed using the plug-flow-reactor model in Chemkin Pro [39]. The plug-flow assumption is justified by the dispersion model of Levenspiel [34] and two-dimensional shear-flow simulations, provided in the supplementary material. The chemical reactions were simulated along the full length of the reactor using the measured temperature profiles presented in sections 2.1 and 2.2. As catalytic reactions and wall interactions are assumed to be negligible, only homogeneous gas-phase reactions included in the respective reaction mechanisms were considered.

For the ozone decomposition, the reaction mechanisms of Zhao et al. [28], Halter et al. [40], and Jian et al. [17] were tested and validated, respectively. It should be noted that only the reaction mechanism of Zhao et al. [28] contains pressure-dependent reactions in the O_3-subset, highlighting the interest in comparing and validating the three mechanisms for elevated pressures. Also, each mechanism was developed for different approaches: While the kinetic models of Halter et al. [40] and Zhao et al. [28] were developed for the ozone-assisted oxidation of methane and DME, respectively, the mechanism of Jian et al. [17] was developed to describe H_2-O_2-O_3 interactions.

The simulations of the partial oxidation of natural gas/DME/ozone mixtures were performed using the Aramco3.0 mechanism, developed by Zhou et al. [41], because previous studies already demonstrated that the Aramco3.0 model can reliably predict the conversion and formation of key species and intermediates [42]. Since the Aramco3.0 does not contain ozone chemistry, the O_3-subset of Jian et al. [17] was added to the Aramco3.0 model. The reason for choosing the model of Jian et al. [17] is discussed in section 4.1. Note, that direct reactions of hydrocarbons with ozone, e.g., ozonolysis reactions, are not contained.

4. Results and discussion

In this section, the experimental results of the ozone dissociation and partial oxidation experiments are presented and discussed. To validate the used reaction mechanisms, simulations based on the respective kinetic models were compared to experiments. Reaction path and sensitivity analyses were performed to unravel the formation of some products during the partial oxidation. Also, oxygenated intermediates, important for the partial oxidation process including ozone, were identified by PIE curves and ms-TPES.

4.1. Ozone decomposition

Fig. 3 shows the ozone mole fraction at the end of the reactor as a function of temperature and pressure for oxygen/ozone mixtures with ozone inlet mole fractions of 100 ppm and 5000 ppm (only at 1 bar).

As can be seen from Fig. 3, the decomposition of ozone starts at 423 K at 1 bar and is shifted towards 448 K with increasing pressure in the 100 ppm O_3 experiments. At these temperatures, 2-4% O_3 is decomposed. With increasing temperature, ozone mole fractions decrease in an S-shaped manner. No ozone is detected at temperatures above 598 K (100 ppm, 1 bar) and 623 K (100 ppm, 20 bar), which shows similar pressure dependence, as mentioned before. Note that residence times were kept constant. For better comparability, the O_3 mole fractions obtained in the 100 ppm O_3 measurements are shown again in a common diagram (see Fig. 4), from which it becomes clear that less ozone is converted with increasing pressure at the respective temperature (especially visible between 523 and 623 K). In particular, the O_3 mole fraction at 1 bar is 13% (at 523 K) to 168% (at 573 K) lower compared to the mole fraction at 10 and 20 bar. This amounts to ~5 ppm in the temperature range between 523 K and 573 K. It can also be seen that the results obtained for the 10 and 20 bar measurements are closer together than the results obtained at 1 and 10 bar. This observation suggests that the high-pressure limit of the ozone decomposition reaction may be in the investigated pressure region. In this area, the deviation between the

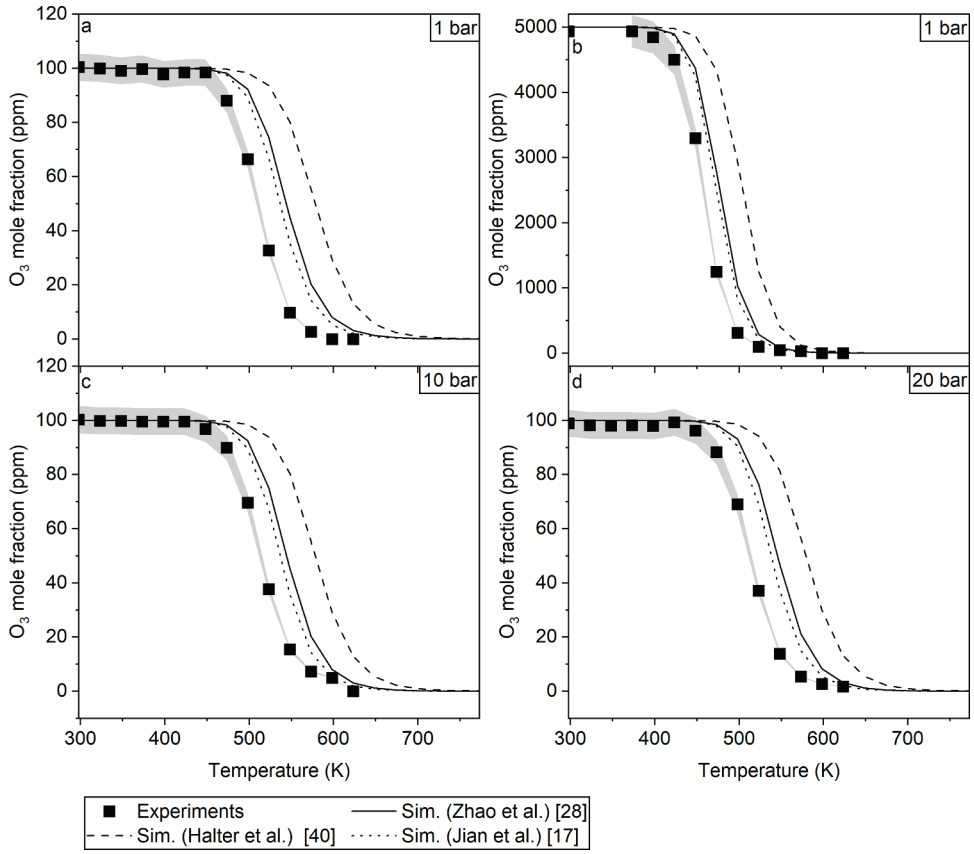

Fig. 3. Ozone dissociation of 100 ppm O_3 in the O_3/O_2 mixture (a, c, d) as a function of the temperature for pressures of 1, 10, and 20 bar, respectively. Ozone dissociation of 5000 ppm O_3 in the O_3/O_2 mixture (b) as a function of the temperature for a pressure of 1 bar. Symbols mirror experiments, lines reflect simulations using the models of Zhao et al. [28], Halter et al. [40], and Jian et al. [17]. Uncertainties are indicated by the shaded areas.

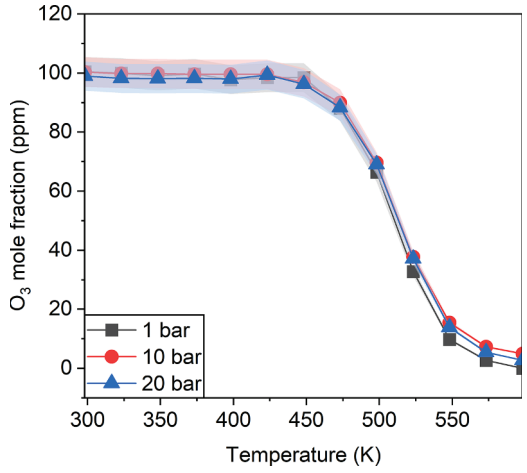

Fig. 4. Pressure dependence of ozone dissociation of the 100 ppm O_3 in O_3/O_2 mixture. Presented are experimental results of 1 bar (black), 10 bar (red), and 20 bar (blue), respectively. It must be noted that lines do not represent simulations but rather linking lines between symbols. Uncertainties are indicated as shaded areas.

data points approaches the uncertainty of the data and so the occurrence of the high-pressure limit can only be confirmed by further experiments with higher accuracy in ozone detection.

At an ozone inlet mole fraction of 5000 ppm, the decomposition already starts at 398 K, so that an increasing inlet mole fraction of O_3 results in a shift of the decomposition onset towards lower temperatures (see Fig. 3b). In addition, the ozone depletion not only shifts towards lower temperatures, but it also becomes steeper. As a result, ozone is almost completely depleted at 548 K.

Comparing the experimental results of the 100 ppm O_3 measurements with model predictions, the best agreement is obtained with the model of Jian et al. [17] followed by the model of Zhao et al. [28] and finally Halter et al. [40]. It can also be noted that the model predictions using the mechanisms of Jian et al. [17] and Zhao et al. [28] are comparable and shifted towards higher temperatures by less than 50 K compared to the experiments. In contrast, the predictions using the mechanism of Halter et al. [40] are shifted by 100 K towards higher temperatures. For the experiment with 5000 ppm O_3, the agreement between experiment and model predictions becomes better, evident from the smaller shifts of less than 25 K (Jian et al. [17] and Zhao et al. [28]) and 50 K (Halter et al. [40]) towards higher temperatures, respectively.

Reaction path analyses show that for all O_3 mechanisms, reaction R1 ($O_3+M \rightleftharpoons O_2+O+M$) is the most important reaction with respect to the initialization of O_3 decomposition. In the mechanisms of Jian et al. [17] and Zhao et al. [28], reaction R1 is formulated as a three-body reaction, while in the mechanism of Halter et al. [40] three separate reactions (O_3+N_2, O_3+O_2, O_3+O_3) are included. In the model of Jian et al. [17], also a separate reaction for O_3+O_3 is included and a collision efficiency of 0 is given for O_3 in reaction R1 as their calculated third body efficiencies for O_3 showed a significant temperature dependence [17]. In addition, only in the mechanism of Zhao et al. [28], reaction R1 is included as pressure-dependent leading to higher reaction rates at higher pressure. But even the simulations using the model of Zhao et al. [28] show the same pressure influence as observed for the other models and in the experiments, that is, higher pressures lead to slightly lower O_3 conversions at specific temperatures. The reason for this observation

could be the generally weak pressure dependence of R1 combined with a high oxygen amount in the mixture and the higher pressure that both lead to a shift of the equilibrium towards O_3.

Once O radicals are formed via reaction R1, a second reaction, i.e., the reaction of O_3 with the O radical yielding two O_2 molecules (reaction R2 ($O_3+O \rightleftharpoons O_2+O_2$)), becomes important. Only in the 5000-ppm experiment at 1 bar, the decomposition of O_3 with O_3 as a collision partner starts to play a role (reaction R1 with M = O_3 or reaction R3 ($O_3+O_3 \rightleftharpoons O_2+O+O_3$) in case of the Halter et al. [40] and Jian et al. [17] mechanisms), accelerating the ozone decomposition as also observed in the experiments.

Comparing the agreement between simulations and the experiments performed in this study with the agreement observed in the study of Jian et al. [17], a slightly worse agreement is found. One possible reason for the larger disagreement is the large amount of oxygen and the absence of an inert gas. Both have a great influence on the chemical kinetics and affect the O_3 mole fraction at the end of the reactor. The kinetic model of Jian et al. [17] is validated for mixtures containing a N_2 dilution of ~95% and an O_2 mole fraction of 2.1%. So, the deviation may occur because of uncertainties in the third-body efficiencies for O_2, O_3, and/or N_2 and uncertainties of the thermodynamic data that are used to calculate the reverse reaction rates of the equilibrium reactions mentioned above.

Because of the best agreement between experiment and simulation, the model of Jian et al. [17] was selected for further simulations.

4.2. *Effect of ozone on the partial oxidation of natural gas/dimethyl ether mixtures*

Fig. 5 shows experimentally obtained mole fractions of all reactants as a function of temperature compared to model predictions using the Aramco3.0 [41] and the O_3-subset from Jian et al. [17]. Particularly for C_2H_6 and DME, the reactants start to be converted at very low temperatures around 400 K. In general, a three-stage oxidation process is observed with increasing temperature, starting at very low temperatures between 373 and 523 K, followed by a low-temperature range up to a temperature of 773 K, and ending in the high-temperature range at higher temperatures. Such an oxidation scheme was already observed in an earlier NG/O_3 study [42,43]. In short, the decomposition of O_3 releases O radicals that react with the fuel to form mainly oxygenated species including hydroperoxides, which in turn contribute to the formation of OH radicals when they decompose at higher temperatures. At these temperatures (523 – 773 K), the reactivity is still too low to initiate complete conversion of the reactants, which does not occur until the H_2O_2, formed in the two previous oxidation steps, begins to decompose at temperatures higher than 800 K initiating effective chain branching.

The conversion of C_2H_6 and DME reaches 25% in the very low temperature regime and 50% in the low temperature regime. In contrast, considering the experimental uncertainties, the conversion of CH_4 and C_3H_8 cannot be confirmed up to temperatures higher than 800 K and 500 K, respectively. Nevertheless, it is expected that small amounts of CH_4 and C_3H_8 are also converted at these temperatures and contribute to the formation of methyl and propyl hydroperoxides.

The experimental results agree well with the model predictions with a slight underestimation of the conversion of O_3, C_2H_6, and DME at temperatures between 423 K and 523 K.

To better assess the influence of O_3 and DME on the conversion process, the mole fractions of DME and C_2H_6 obtained in this study are compared to the mole fractions of the two species obtained in neat natural gas, natural gas/DME, and natural gas/O_3 mixtures in Fig. 6. It shows that the combined addition of O_3 and DME is much more effective in initiating fuel conversion than O_3 or DME alone, since the conversion of DME and C_2H_6 is much higher at temperatures up to 800 K than the conversion of these reactants in the other mixtures. The aforementioned three-stage oxidation process is also more pronounced. To underline this observation, it should be noted that, compared to the experiments presented here, the NG/10% DME experiment was performed at a slightly higher pressure of 6 bar and that more ozone was introduced into the mixture in the NG/O_3 experiments, specifically 380 ppm instead of 245 ppm. Consequently, the combined addition of ozone and low-temperature oxidation species such as DME can be interesting in terms of polygeneration processes in HCCI engines, as already pointed out by Schröder et al. [32].

Figs. 7 and 8 show the experimental and simulated mole fractions of some observed products that could be interesting as target products in polygeneration processes, namely synthesis gas (H_2/CO, see Fig. 7a), unsaturated hydrocarbons (Fig. 7b), and oxygenated species (Figs. 8a and 8b). In addition, the mole fractions of hydroperoxides are shown in Fig. 10 since these species are buffer molecules [43] and can therefore act as ignition enhancer in auto-ignition based combustion processes due to the release of OH radicals during their decomposition. It must be noted that an accurate prediction of hydrogen peroxide and hydroperoxides are also important for an accurate prediction of the ignition timing in engines using similar mixtures, since both species act as buffer molecules for the formation of OH radicals at higher temperatures. This means that the desired influence of ozone, i.e., an increased reactivity of the mixture, is shifted to higher temperatures. Mole fractions of all detected species are shown in the supplementary material. All species were identified by their mass-to-charge (m/z) ratio, PIE curve, and/or ms-TPES, as also detailed in section 4.3 for some species typical for ozone-assisted fuel conversions.

Synthesis gas and CO_2 are mainly formed at temperatures above 800

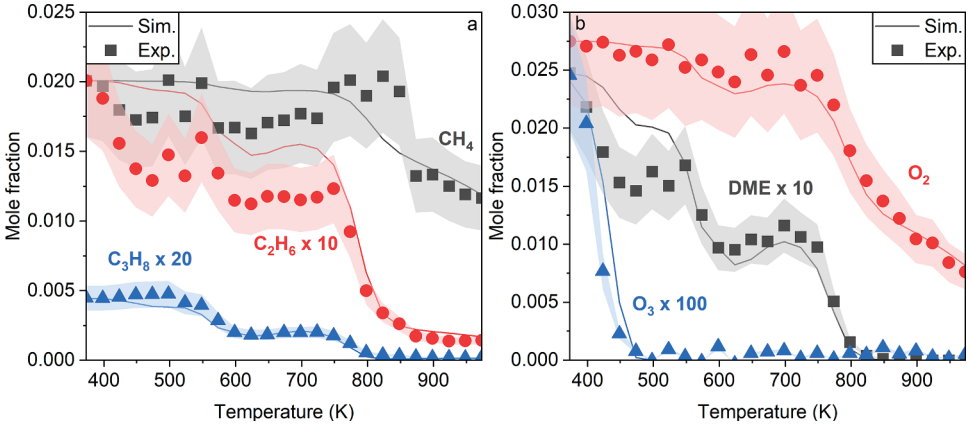

Fig. 5. (a): Mole fractions of CH_4 (black), C_2H_6 (red, note factor of 10), and C_3H_8 (blue, note factor of 20) as a function of temperature. (b): Mole fractions of DME (black, note factor of 10), O_2 (red), and O_3 (blue, note factor of 100) as a function of temperature. Symbols represent experiments, lines represent simulations, performed with the combined Aramco3.0 model. Uncertainties are indicated as shaded areas.

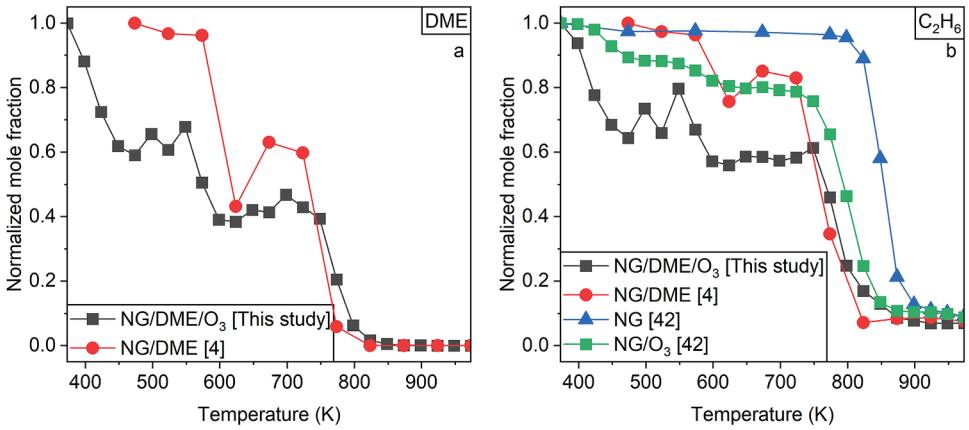

Fig. 6. (a): Comparison of DME mole fractions of natural gas/DME/ozone mixtures (10% DME in natural gas, 245 ppm O_3), presented in this study (black) and natural gas/DME mixtures (10% DME in natural gas) without ozone (red), published in Kaczmarek et al. [4]. (b): Comparison of C_2H_6 mole fractions of natural gas/DME/ozone mixtures (10% DME in natural gas, 245 ppm O_3) (black), presented in this study, natural gas/DME mixtures (10% DME in natural gas) without ozone (red), published in Kaczmarek et al. [4], natural gas mixtures (blue) and natural gas/ozone mixtures (natural gas, 360 ppm O_3) (green), published in Kaczmarek et al. [42]. It must be noted that lines do not represent simulations but rather linking lines between symbols.

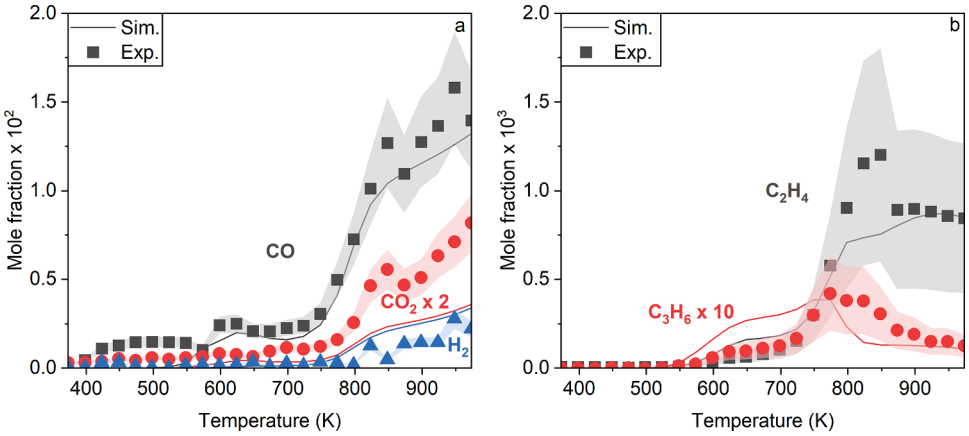

Fig. 7. (a): Mole fractions of CO (black), CO_2 (red, note factor of 2), and H_2 (blue) as a function of temperature. (b): Mole fractions of C_2H_4 (black) and C_3H_6 (red, note factor of 10) as a function of temperature. Symbols represent experiments, lines represent simulations, performed with the combined Aramco3.0 model. Uncertainties are shown as shaded areas.

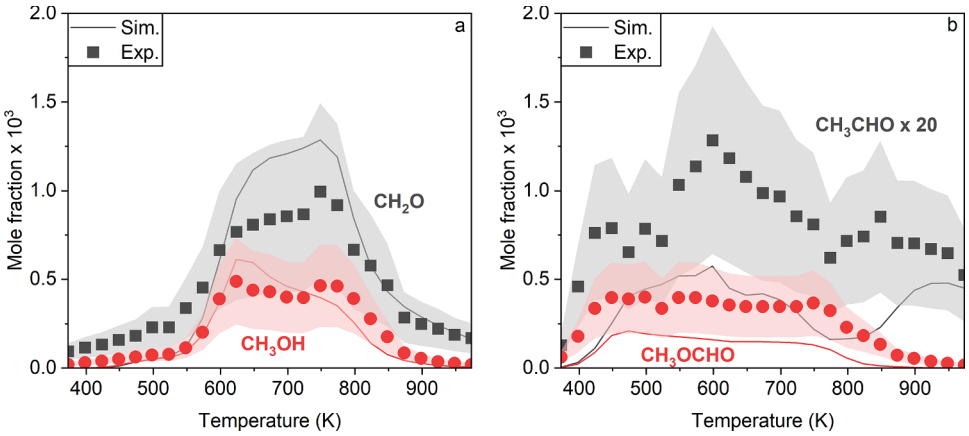

Fig. 8. (a): Mole fractions of CH_2O (black) and CH_3OH (red) as a function of temperature. (b): Mole fractions of CH_3CHO (black, note factor of 20) and CH_3OCHO (red) as a function of temperature. Symbols represent experiments, lines represent simulations, performed with the combined Aramco3.0 model. Uncertainties are shown as shaded areas.

K, while their formation (especially visible for CO) in very low mole fractions can be observed also in the very low temperature region. This is attributed to the small conversion of the reactants and too low reactivity of the mixture to promote fully oxidized products at these temperatures. The model predictions show a reasonable agreement to the experiments with a slight underprediction of the CO and CO_2 mole fractions at very low and high temperatures, respectively. In contrast to CO, unsaturated species are not formed in the very low temperature region, as seen in Fig. 7b. Instead, the production of C_2H_4 and C_3H_6, mainly formed by C_2H_6 and C_3H_8 starts around 600 K, corresponding to the second oxidation stage. Thus, it can be concluded that the main reaction pathways in the very low temperature region lead from C_2H_6 and C_3H_8

via the alkyl radicals + O_2 to the alkyl peroxy radicals. These species finally react with HO_2 radicals to form the hydroperoxides, while the temperature is too low to promote the reaction of alkyl radicals with O_2 or the decomposition of the alkyl peroxy radical to alkenes. This reaction pathway is confirmed by the low conversion of C_2H_6 and C_3H_8, the production of the hydroperoxides shown in Fig. 10, as well as the production of methanol and formaldehyde, which both are follow-up products of this reaction sequence as already shown for the NG/DME experiments in [4].

The maximum mole fractions of C_2H_4 and C_3H_6 are observed at temperatures around 800 K, followed by a slow decrease at higher temperatures. This behavior is also represented by the simulations, whereas the C_3H_6 mole fractions are overpredicted at temperatures between 550 and 700 K.

The mole fractions of synthesis gas and unsaturated species are comparable to those obtained in the NG/DME experiments published earlier [4] taking into account the higher dilution. The same applies to the mole fractions of CH_2O and CH_3OH, shown in Fig. 8a with the difference that the formation already starts in the very low temperature region at around 400 K compared to 600 K in the aforementioned NG/DME experiments. It should be noted that in the experiments presented here, only a pressure of 4 bar was required to obtain results similar to those obtained in the 6 bar experiments referred to above, again demonstrating the increased reactivity of the mixture due to the addition of O_3.

The mole fractions of CH_2O and CH_3OH agree very well with the model predictions with a slight underprediction of the mole fractions of CH_2O in the very low temperature region. This underprediction, corresponding to the low conversion of C_2H_6 and DME (see Figs. 5a and 5b), is also evident for the oxygenates methyl formate (CH_3OCHO) and acetaldehyde (CH_3CHO). It can be assumed that reactions from C_2H_6 and DME towards CH_3CHO and CH_3OCHO, respectively, are responsible for this observation. To test this assumption, a reaction path analysis was performed at 573 K at a reactor position at which 50% of DME has been converted related to the maximum DME conversion at this temperature (at 185 mm). The reaction pathway in Fig. 9 shows that CH_3CHO is mainly produced by C_3H_8 oxidation in the simulations, either directly by the reaction sequence via the iso-propyl (i-C_3H_7) radical or indirectly via the decomposition of n-C_3H_7O contributing to the formation of ethyl (C_2H_5) radicals. The second formation pathway proceeds via C_2H_6 oxidation, more specifically $C_2H_5 \rightarrow CH_3CH_2O \rightarrow CH_3CHO$ indicating an interaction between the C_2 and C_3 reaction pathway. It must be noted that a similar interaction, including the C_1 reaction pathway, can also be observed in the formation pathway of i-C_3H_7O that finally decomposes to acetaldehyde and methyl radicals, as it is formed by the reaction of i-$C_3H_7O_2$ and CH_3O_2 and $C_2H_5O_2$, originating from the CH_4 and C_2H_6 oxidation pathway, respectively. Given the experimental results, it is suggested that the mentioned pathways involving species formed by C_2H_6 oxidation are underestimated by the model since more C_2H_6 is converted and more CH_3CHO is formed in the experiments than in the simulations. Nevertheless, four of the most sensitive reactions regarding CH_3CHO formation are CH_4, C_2H_6, and C_3H_8 + OH as well as i-C_3H_7O + $C_2H_5O_2$ which shows that the correct descriptions of the C_1 – C_3 pathways are equally important for an accurate prediction of the CH_3CHO mole fractions.

CH_3OCHO is mainly produced via the low-temperature chemistry pathway of DME also evident from Fig. 9. In addition, the reaction of CH_3OOH and CH_2OCHO, an intermediate of DME oxidation, contributes to the formation of CH_3OCHO. As CH_3OOH is produced in the C_1 pathway via $CH_3 \rightarrow CH_3O_2 \rightarrow CH_3OOH$ and the oxidation pathways of all fuels contribute to the formation of CH_3, all fuels indirectly contribute to the formation of CH_3OCHO. This interaction also shown for the formation of CH_3CHO indicates the importance of the investigation of more complex natural gas surrogates in order to develop and

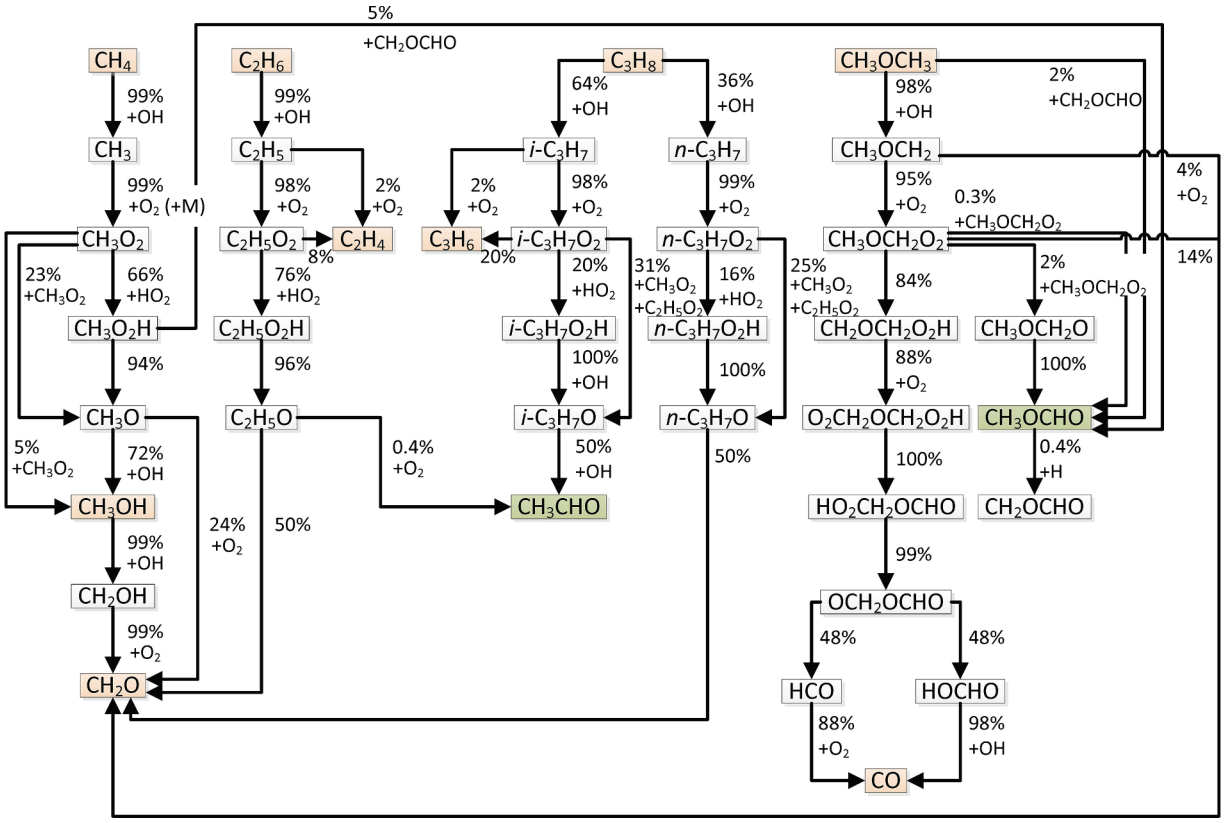

Fig. 9. Reaction path analysis at 573 K and 50% DME conversion related to the maximum conversion at the respective temperature (at 185 mm) using the Aramco3.0 mechanism extended by the O_3-submechanism of Jian et al. [17].

improve comprehensive models with the aim to accurately predict the formation of useful products in polygeneration-based applications. The most sensitive reactions with respect to CH_3OCHO formation are the decomposition of O_3, followed by DME + OH and further reactions of DME intermediates. However, the reaction of two methyl peroxy radicals (CH_3O_2) yielding O_2 and two methoxy radicals (CH_3O) as well as O_3 + HO_2 and O_3 + H are also included in the ten most sensitive reactions again showing that a correct description of the C_1 reaction pathway, but also of the ozone submechanism, are important for accurate model predictions.

As a result, the rate coefficients of the most sensitive reactions mentioned above should be reassessed to improve the prediction of the formation of CH_3CHO and CH_3OCHO at low temperatures. It must be noted that this underprediction is observed almost throughout the whole temperature range studied, while the trends are predicted with good agreement. But the reactions responsible for the formation and consumption of both products remain largely the same, so changing the rate coefficients to achieve a better agreement at very low temperatures should have a comparable positive effect on the prediction at higher temperatures.

For the quantification of hydroperoxides, limited information regarding photoionization cross sections is available in the literature. Here, the signals at 10.3 eV (m/z 48: CH_3OOH, methyl hydroperoxide), 10.6 eV (m/z 62: C_2H_5OOH, ethyl hydroperoxide and m/z 76: C_3H_7OOH, propyl hydroperoxide), and 11.2 eV (m/z 34: hydrogen peroxide) were considered. The estimated photoionization cross sections were taken from Moshammer et al. [44] (CH_3OOH), Rodriguez et al. [45] and Wang et al. [46] (C_2H_5OOH, C_3H_7OOH), and Dodson et al. [47] (H_2O_2).

Fig. 10 shows a surprisingly good agreement between the experimental and simulated mole fractions of all three detected alkyl hydroperoxides, considering the high uncertainties of the photoionization cross sections. Nevertheless, the maximum mole fractions obtained for methyl and ethyl hydroperoxide at a temperature around 550 K in the simulations are not reached in the experiments. This could be explained by the narrow temperature range at which these high mole fractions are observed in the simulations, as it is ~ 25 K, which matches the temperature steps in the experiment. Finally, a higher temperature resolution could help to solve this issue and improve the agreement between experiment and simulation. However, just as surprising as the good agreement for alkyl hydroperoxides is the poor agreement for the smallest peroxide, hydrogen peroxide, especially considering the better-known photoionization cross section. Most probably, heterogeneous wall reactions that are not considered in this study are responsible for this observation. Such wall reactions were already discussed by Porter et al. [48] and, more recently, by Bahrini et al. [49], who observed these reactions in a quartz jet-stirred reactor. To account for this effect and improve the agreement between simulations and experiments, a temperature-dependent wall loss reaction of H_2O_2 with higher loss-rates at higher temperatures was included in their kinetic model. Taking into account a higher residence time in the experiments presented here compared to the JSR experiments in [49], reinforced by the longer transfer line mentioned in Section 2.2, a significant influence of H_2O_2 wall reactions on the H_2O_2 mole fractions can be expected.

4.3. Identification of oxygenated intermediates

Alkyl hydroperoxides (ROOH) are formed in the low-temperature chemistry (LTC) regime at temperatures lower than 850 K from the reaction of alkylperoxy radicals (ROO) with HO_2. They originate from the first oxygen addition on alkyl radicals. Since first detected in 2010, they are routinely identified by photoionization mass spectrometry during the oxidation of alkanes in jet-stirred reactors [46], but also in flow reactors and recently in low-pressure flames [50,51]. In our flow reactor study with DME and ozone as additive, formation of C_1-C_3 alkyl hydroperoxides directly starts at 373 K just below the LTC regime (below 400 K), named as extreme low-temperature (ELTC) zone by Rousso et al. [30]. As shown in Fig. 11a-c, methyl hydroperoxide (CH_3OOH) at m/z 48, ethyl hydroperoxide (C_2H_5OOH) at m/z 62, and propyl hydroperoxide (C_3H_7OOH) at m/z 76 were clearly identified by their respective threshold photoelectron spectrum measured at a reactor temperature of 573 K.

The used reference spectra are from Bierkandt et al. [50], who measured alkyl hydroperoxides in a 2-butene/H_2 flame with the same PEPICO spectrometer used in our work. The second smaller band in the spectrum of m/z 48 at 11.6 eV might be attributed to methyl hydroperoxide. However, the Franck-Condon simulation (FCS) of methanediol [50] is indeed well-structured and agrees only to a limited extend with our experimental spectrum. The threshold photoelectron spectra of the two larger alkyl hydroperoxides are characterized by dissociative photoionization resulting in a sharp signal drop at higher photon energies.

Specific species that are formed in the ozonolysis, i.e., the reaction of unsaturated hydrocarbons with ozone, are the Criegee intermediates, which are zwitterions and of relevance in tropospheric chemistry [52]. Direct reaction of alkanes with ozone is very slow compared to alkenes and is typically not considered in combustion processes [13]. The smallest Criegee intermediate is formaldehyde oxide (CH_2OO) and results from C_2H_4 + O_3 over decomposition of a primary ozonide. The first direct kinetic measurement of this elusive species was reported by Welz

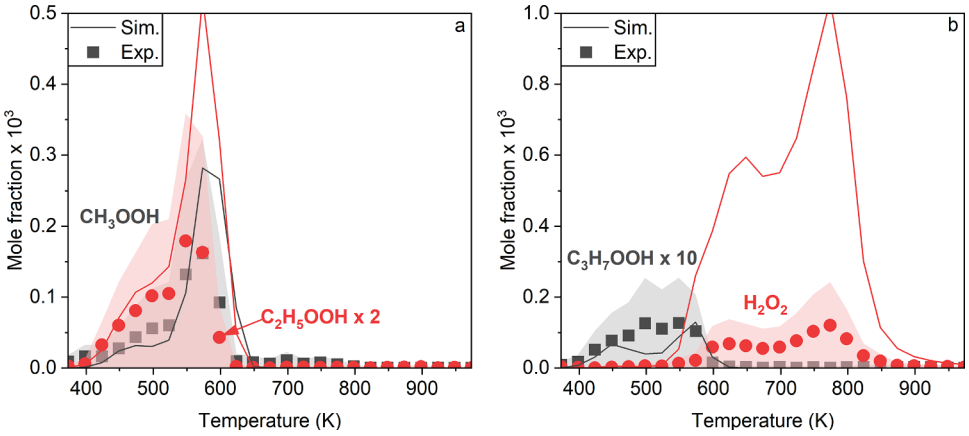

Fig. 10. (a): Mole fractions of CH_3OOH (black) and C_2H_5OOH (red, note a factor of 2) as a function of temperature. (b): Mole fractions of C_3H_7OOH (black, note factor of 10) and H_2O_2 (red) as a function of temperature. Symbols represent experiments, lines represent simulations, performed with the combined Aramco3.0 model. Uncertainties are shown as shaded areas.

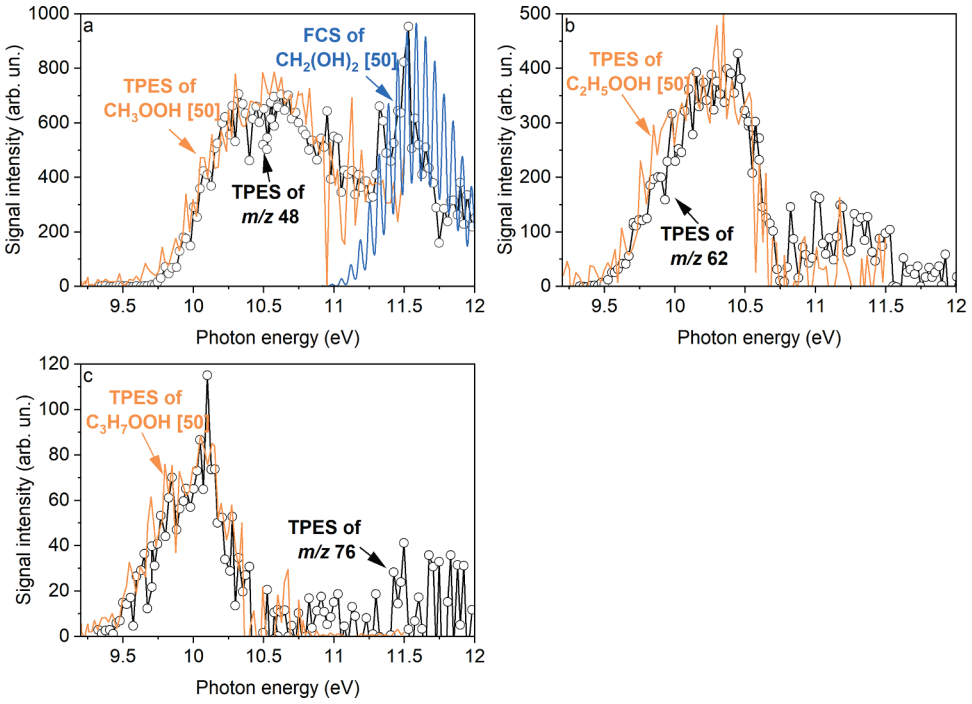

Fig. 11. Identification of C_1-C_3 alkyl hydroperoxides by their threshold photoelectron spectra. Reference spectra of methyl, ethyl, and propyl hydroperoxides are from the work of Bierkandt et al. [50].

et al. [53] as a product from the reaction of the iodomethyl radical (CH_2I) with molecular oxygen (O_2). Fig. 12a shows the measured photoionization spectrum of m/z 46 at a reactor temperature of 573 K. At this temperature, 50% of the fuel DME (CH_3OCH_3) is still present and its adiabatic ionization energy of 10.025 eV [54] reasonably matches the observed onset at about 9.9 eV. However, the literature spectrum of DME [55] does not mirror the measured spectrum alone and deviates at photon energies higher than 10.3 eV. Due to the low mass resolution of the PEPICO spectrometer, isobaric species must be considered besides isomeric species. For m/z 46, ethanol (C_2H_5OH), dioxirane (c-CH_2OO), and formic acid (HCOOH) have significantly higher ionization energies of 10.48 eV [54], 10.82 eV [56], and 11.33 eV [54], respectively, and cannot account for the observed deviation at least up to the photon energy of 10.5 eV, which corresponds to the ionization energy of ethanol.

The Criegee intermediate CH_2OO might contribute to the overall signal at m/z 46 since its ionization energy of 9.991 eV [57] is quite similar to that of DME. In Fig. 12a, the experimental photoionization spectrum of CH_2OO from the work of Welz et al. [53] is also presented, but an unambiguous statement on the presence of CH_2OO with a weighted sum is difficult due to its noisy spectrum. Compared to the PI spectrum, the threshold photoelectron spectrum at m/z 46 shown in Fig. 12b is satisfactorily represented by dimethyl ether alone. The DME photoelectron spectrum [57] shows a broad band between 9.8 and 10.5 eV, while the TPE spectrum of CH_2OO measured by Chicharro et al. [58] has a narrow band at 9.99 eV as the main feature. The structured bands above 11.3 eV in Fig. 12b can be assigned to formic acid (HCOOH), which is a main oxygenate under the investigated conditions. Due to the high concentration of DME, which was used as an additive in our study, it cannot be ruled out that the CH_2OO signal is overlapped by the broad DME spectrum. Note that CH_2OO is not included in the reaction mechanism and similarity in ionization energies of DME and CH_2OO prevents species separation with the realized temperature scans. Therefore, no information on its concentration can be given for the investigated conditions.

Formation of ethylene (C_2H_4) starts at reactor temperatures of about 550 K. At this temperature, ozone is already degraded and formation of the Criegee intermediate from the above-mentioned reaction, i.e., C_2H_4 + O_3, should be unlikely. Rousso et al. have not directly identified CH_2OO by photoionization mass spectrometry in a jet-stirred reactor during ethylene + O_3 reaction and suggested rapid degradation, instead [60]. Formation of CH_2OO was also theoretically proposed by Andersen

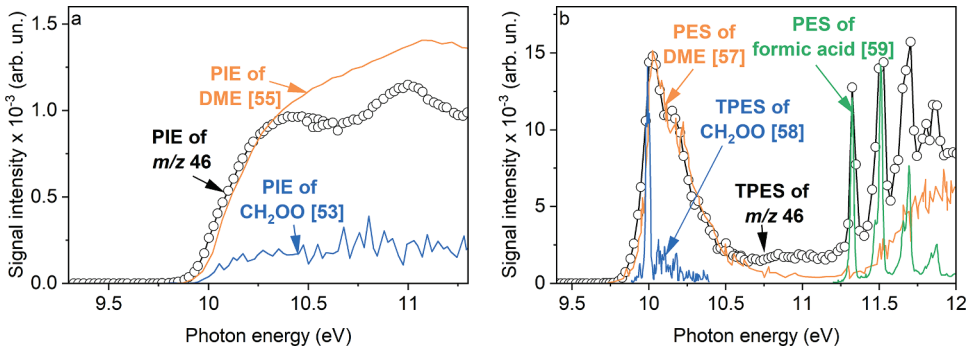

Fig. 12. (a): Photoionization spectrum of m/z 46 in comparison with literature spectra of CH_2OO and dimethyl ether (DME) [53,55]. (b): Threshold photoelectron spectrum of m/z 46 in comparison with literature spectra of DME [57], CH_2OO [58], and formic acid [59].

and Carter in the low-temperature combustion of DME by decomposition of the hydroperoxymethyl formate (HPMF) [61,62]. HPMF ($HOOCH_2OCHO$) is a keto-hydroperoxide and was previously identified during oxidation of DME with an ionization threshold of 9.85 eV [63]. In our experiment, the mass spectrum shows a weak signal at m/z 92, but the signal-to-noise ratio is too low to obtain a threshold photoelectron spectrum. The ion signal in the PI spectrum increases linearly from about 9.4 eV so that the observed ionization threshold is smaller than the reported ionization energy of HPMF in the work of Moshammer et al. [63] as shown in Fig. 13. The presence of isobaric hydrocarbon species, i.e., C_7H_8 isomers, can be excluded, but other oxygenated species may be present. The cyclic $C_2H_4O_4$ species c-$CH_2OOCH(OH)O$ has a calculated ionization energy of 9.59-9.65 eV [63], which is also higher than the measured onset in our spectrum of m/z 92. Most likely is the presence of the $C_3H_8O_3$ species ethoxymethyl hydroperoxide ($C_2H_5OCH_2OOH$), which has a calculated ionization energy of 9.44 eV for the lowest energy conformer [64]. The onset in the JSR-sampled photoionization spectrum of $C_3H_8O_3$ from the work of Rousso et al. [64], who investigated the ozonolysis of ethylene and concluded that ethoxymethyl hydroperoxide (EMHP) is formed by reaction of ethanol with CH_2OO, fits not perfectly to our spectrum. However, presence of EMHP under the investigated conditions could be possible while formation of HPMF is unlikely or its concentration is very low. EMHP ($C_2H_5OCH_2OOH$) is not included in the mechanism used here, but HPMF ($HOOCH_2OCHO$) is included and has a predicted maximum mole fraction of 289.25 ppm at 548.15 K. $HOOCH_2OCHO$ is formed by LTC reactions starting with addition of O_2 to the methoxymethyl radical ($CH_3OCH_2 + O_2 \rightleftharpoons CH_3OCH_2OO$) followed by intramolecular hydrogen shift ($CH_3OCH_2OO \rightleftharpoons CH_2OCH_2OOH$), a second O_2 addition reaction ($CH_2OCH_2OOH + O_2 \rightleftharpoons OOCH_2OCH_2OOH$), and finally by OH elimination ($OOCH_2OCH_2OOH \rightleftharpoons HOOCH_2OCHO + OH$).

At m/z 64 (see Fig. 14), a strong signal rise is observed in the measured photoionization spectrum at a photon energy of 10.4 eV. Rousso et al. [64] have investigated the ozonolysis of ethylene in a jet-stirred reactor using a high-resolution time-of-flight mass-spectrometer at the Advanced Light Source and assigned the onset at 9.85 eV in their PI spectrum of CH_4O_3 (m/z 64.016) to hydroxymethyl hydroperoxide ($HOCH_2OOH$) formed by reaction of formaldehyde oxide with water ($CH_2OO + H_2O \rightleftharpoons HOCH_2OOH$). At higher photon energies, their spectrum was affected by a fragment of HPMF (loss of CO) as also observed in the work of Moshammer et al. [63] during the oxidation of DME, where hydroxymethyl hydroperoxide (HMHP) was not detected. Note that the reaction of formaldehyde oxide with water is significantly slower than reactions with alcohols and carboxylic acids [65] and can explain the absence of HMHP. In our spectrum, the onset near 10.4 eV may also result from HPMF fragmentation and would be a prove for the formation of hydroperoxymethyl formate under the investigated

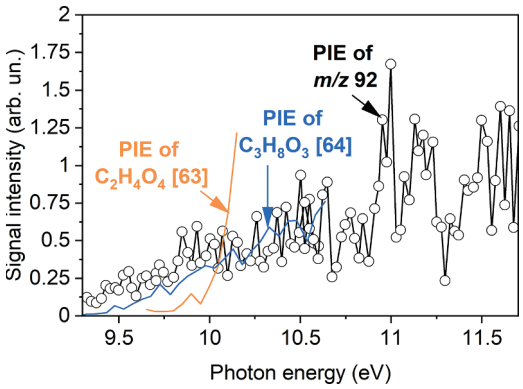

Fig. 13. Photoionization spectrum of m/z 92 in comparison with JSR-sampled photoionization spectra of $C_2H_4O_4$ from oxidation of DME [63] and $C_3H_8O_3$ from ozonolysis of ethylene [64].

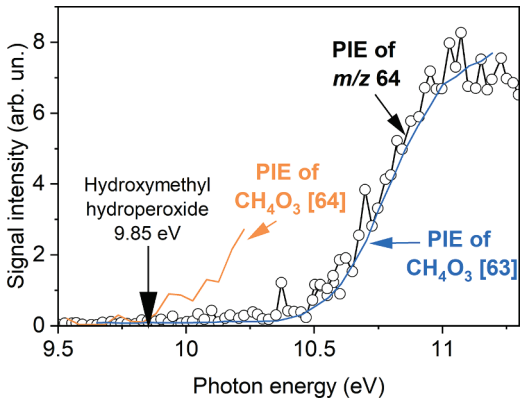

Fig. 14. Photoionization spectrum of m/z 64 in comparison with spectra of CH_4O_3 from ethylene ozonolysis [64] and oxidation of DME [63].

conditions, however, clear identification of HPMF at m/z 92 was not possible as discussed above.

Other oxygenated intermediates, which were clearly identified by the synchrotron experiment, are formaldehyde (CH_2O) at m/z 30, methanol (CH_3OH) at m/z 32, hydrogen peroxide (H_2O_2) at m/z 34, ketene (C_2H_2O) at m/z 42, ethenol (C_2H_3OH) and acetaldehyde (CH_3CHO) at m/z 44, and methyl formate (CH_3OCHO) at m/z 60.

5. Conclusions

The temperature-dependent ozone decomposition was measured for the first time at high pressures up to 20 bar to provide validation data for future improvements of the ozone submechanisms. A small pressure dependence was found with slightly lower ozone conversions at a specific temperature with increasing pressure. Comparisons between model predictions using ozone submechanisms available in the literature and experiments reveal discrepancies. The most recent submechanism by Jian et al. [17] shows the best agreement. Based on this mechanism, the ozone-assisted partial oxidation of a natural gas/DME mixture was investigated in a plug-flow reactor at elevated pressure to evaluate the effect of ozone on the consumption and formation of reactants and products, respectively. It was shown that the released O radicals due to ozone decomposition at very low temperatures (starting around 400 K) initiate fuel conversion and the formation of oxygenated species such as methyl formate and acetaldehyde but also several hydroperoxides acting as buffer molecules for OH radicals. Only this formation of the hydroperoxides which survive to higher temperatures leads to the formation of OH at high temperatures in engines with ozone addition, and this buffers the effect of the additive. This is nicely seen in the temperature regimes of the disappearance of ozone, the hydroperoxides, and of hydrogen peroxide / formaldehyde [43]. Due to the successive decomposition of ozone, alkyl hydroperoxides, and hydrogen peroxide, a three-stage oxidation process was observed. C_1-C_3 alkyl hydroperoxides, among other oxygenates, were clearly identified by photoion mass-selected threshold photoelectron spectra from the literature. However, the discussed uncertainties regarding the identification of the smallest Criegee intermediate CH_2OO at m/z 46 and the hydroperoxymethyl formate (HPMF) at m/z 92 leave room for future investigations. Identification of these species would benefit from a higher mass resolution to determine the exact elemental composition. The comparison of the presented results with results obtained in previous studies of the partial oxidation of natural gas/DME and natural gas/ozone mixtures showed that the combined addition of ozone and DME is much more effective in lowering the reaction onset temperature (start of fuel conversion) compared to the addition of ozone or DME alone, which can be of particular interest for HCCI-based polygeneration processes. Simulations performed with literature reaction mechanisms revealed strengths and weaknesses in predicting the mole fractions of the

reactants and products. Subsequent reaction path and sensitivity analyses helped to discuss key reaction pathways towards species of interest and suggest reactions that require further re-evaluation to improve model predictions for ozone-assisted fuel conversions.

Declaration of Competing Interests

The authors declare that they have no known competing financial interests or personal relationships that could have appeared to influence the work reported in this paper.

Data availability

Data will be made available on request.

Acknowledgments

Financial support by the Deutsche Forschungsgemeinschaft within the framework of the DFG research unit FOR 1993 “Multifunctional conversion of chemical species and energy” (Project number 229243862) is gratefully acknowledged. The manuscript summarizes the results of the subproject GV1. The authors also thank the Deutsche Forschungsgemeinschaft for financial support under contract KA3871/3-2 and KO4786/2-2. Patrick Hemberger additionally thanks the Swiss Federal Office of Energy for financial support under contract SI/501269-01. We further acknowledge the Paul Scherrer Institute, Villigen, Switzerland for provision of synchrotron radiation beamtime at the VUV beamline (X04DB) of the SLS and would like to thank Andras Bodi, Luka Debenjak, and Patrick Ascher for assistance.

Supplementary materials

Supplementary material associated with this article can be found, in the online version, at doi:10.1016/j.jaecs.2022.100107.

References

[1] Atakan B. Gas turbines for polygeneration? A thermodynamic investigation of a fuel rich gas turbine cycle. Int J Thermodyn 2011;14. https://www.researchgate.net/publication/272990485_Gas_turbines_for_polygeneration_A_thermodynamic_investigation_of_a_fuel_rich_gas_turbine_cycle.
[2] Atakan B, Kaiser SA, Herzler J, Porras S, Banke K, Deutschmann O, Kasper T, Fikri M, Schießl R, Schröder D, Rudolph C, Kaczmarek D, Gossler H, Drost S, Bykov V, Maas U, Schulz C. Flexible energy conversion and storage via high-temperature gas-phase reactions: the piston engine as a polygeneration reactor. Renew Sustain Energy Rev 2020;133:110264.
[3] Wiemann S, Hegner R, Atakan B, Schulz C, Kaiser SA. Combined production of power and syngas in an internal combustion engine—experiments and simulations in SI and HCCI mode. Fuel 2018;215:40–5.
[4] Kaczmarek D, Herzler J, Porras S, Shaqiri S, Fikri M, Schulz C, et al. Plug-flow reactor and shock-tube study of the oxidation of very fuel-rich natural gas/DME/O_2 mixtures. Combust Flame 2021;225:86–103.
[5] Drost S, Kaczmarek D, Eckart S, Herzler J, Schießl R, Fritsche C, Fikri M, Atakan B, Kasper T, Krause H, Schulz C, Maas U. Experimental investigation of ethanol oxidation and development of a reduced reaction mechanism for a wide temperature range. Energy Fuels 2021;35:14780–92.
[6] Kaczmarek D, Atakan B, Kasper T. Plug-flow reactor study of the partial oxidation of methane and natural gas at ultra-rich conditions. Combust Sci Technol 2019;191:1571–84.
[7] Kobashi Y, Wang Y, Shibata G, Ogawa H, Naganuma K. Ignition control in a gasoline compression ignition engine with ozone addition combined with a two-stage direct-injection strategy. Fuel 2019;249:154–60.
[8] Schönborn A, Hellier P, Aliev AE, Ladommatos N. Ignition control of homogeneous-charge compression ignition (HCCI) combustion through adaptation of the fuel molecular structure by reaction with ozone. Fuel 2010;89:3178–84.
[9] Pinazzi PM, Foucher F. Influence of injection parameters, ozone seeding and residual NO on a Gasoline Compression Ignition (GCI) engine at low load. Proc Combust Inst 2017;36:3659–68.
[10] Masurier J-B, Foucher F, Dayma G, Dagaut P. Investigation of iso-octane combustion in a homogeneous charge compression ignition engine seeded by ozone, nitric oxide and nitrogen dioxide. Proc Combust Inst 2015;35:3125–32.
[11] Contino F, Masurier J-B, Foucher F, Lucchini T, D’Errico G, Dagaut P. CFD simulations using the TDAC method to model iso-octane combustion for a large range of ozone seeding and temperature conditions in a single cylinder HCCI engine. Fuel 2014;137:179–84.
[12] Smith Lewin C, Herbinet O, Battin-Leclerc F, Bourgalais J. Ozone-assisted oxidation of ethylene in a jet-stirred reactor: an experimental and modeling study. Chem Phys Lett 2022;806:139986.
[13] Sun W, Gao X, Wu B, Ombrello T. The effect of ozone addition on combustion: kinetics and dynamics. Prog Energy Combust Sci 2019;73:1–25.
[14] Jones WM, Davidson N. The thermal decomposition of ozone in a shock tube. J Am Chem Soc 1962;84:2868–78.
[15] Michael JV. Thermal decomposition of ozone. J Chem Phys 1971;54:4455–9.
[16] Peukert SL, Sivaramakrishnan R, Michael JV. High temperature shock tube studies on the thermal decomposition of O_3 and the reaction of dimethyl carbonate with O-atoms. J Phys Chem A 2013;117:3729–38.
[17] Jian J, Hashemi H, Wu H, Jasper AW, Glarborg P. A reaction mechanism for ozone dissociation and reaction with hydrogen at elevated temperature. Fuel 2022;322:124138.
[18] Sehested J, Nielsen OJ, Egsgaard H, Larsen NW, Andersen TS, Pedersen T. Kinetic study of the formation of isotopically substituted ozone in argon. J Geophys Res 1998;103:3545–52.
[19] de Cobos AEC, Troe J. High-pressure range of the recombination $O + O_2 \rightarrow O_3$. Int J Chem Kinet 1984;16:1519–29.
[20] Gesser HD, Hunter NR, Das PA. The ozone sensitized oxidative conversion of methane to methanol and ethane to ethanol. Catal Lett 1992;16:217–21.
[21] Rotzoll G. Mass spectrometric investigation and computer modeling of the methane-oxygen-ozone reaction from 480 to 830 K. J Phys Chem 1986;90:677–83.
[22] Ji S, Li Y, Tian G, Shu M, Jia G, He S, Lan X, Cheng Y. Investigation of laminar combustion characteristics of ozonized methane-air mixture in a constant volume combustion bomb. Energy 2021;226:120349.
[23] Herzler J, Fikri M, Schulz C. Shock-tube study of the ignition and product formation of fuel-rich CH4/ozone/air and natural gas/ozone/air mixtures at high pressure. Appl Energy Combust Sci 2022;12:100082.
[24] Salahi MM, Gharehghani A. Control of combustion phasing and operating range extension of natural gas PCCI engines using ozone species. Energy Convers Manag 2019;199:112000.
[25] Paulauskas R, Skvorčinskienė R, Zakarauskas K, Striūgas N. Combustion performance of low calorific gas enriched by oxygen and ozone. Fuel 2022;324:124761.
[26] Hajilou M, Ombrello T, Won SH, Belmont E. Experimental and numerical characterization of freely propagating ozone-activated dimethyl ether cool flames. Combust Flame 2017;176:326–33.
[27] Liao H, Kang S, Hansen N, Zhang F, Yang B. Influence of ozone addition on the low-temperature oxidation of dimethyl ether in a jet-stirred reactor. Combust Flame 2020;214:277–86.
[28] Zhao H, Yang X, Ju Y. Kinetic studies of ozone assisted low temperature oxidation of dimethyl ether in a flow reactor using molecular-beam mass spectrometry. Combust Flame 2016;173:187–94.
[29] Liao W, Kang S, Chu Z, Liu Z, Wang Y, Yang B. Exploring the low-temperature oxidation chemistry with ozone addition in an RCM: a case study on ethanol. Combust Flame 2022;237:111727.
[30] Rousso AC, Jasper AW, Ju Y, Hansen N. Extreme low-temperature combustion chemistry: ozone-initiated oxidation of methyl hexanoate. J Phys Chem A 2020;124:9897–914.
[31] Hoener M, Kaczmarek D, Bierkandt T, Bodi A, Hemberger P, Kasper T. A pressurized flow reactor combustion experiment interfaced with synchrotron double imaging photoelectron photoion coincidence spectroscopy. Rev Sci Instrum 2020;91:45115.
[32] Schröder D, Banke K, Kaiser SA, Atakan B. The kinetics of methane ignition in fuel-rich HCCI engines: DME replacement by ozone. Proc Combust Inst 2021;38:5567–74.
[33] Gorshelev V, Serdyuchenko A, Weber M, Chehade W, Burrows JP. High spectral resolution ozone absorption cross-sections – Part 1: measurements, data analysis and comparison with previous measurements around 293 K. Atmos Meas Tech 2014;7:609–24.
[34] Levenspiel O. Chemical reaction engineering. 3rd. New York: John Wiley & Sons; 1999.
[35] Sztáray B, Voronova K, Torma KG, Covert KJ, Bodi A, Hemberger P, Gerber T, Osborn DL. CRF-PEPICO: double velocity map imaging photoelectron photoion coincidence spectroscopy for reaction kinetics studies. J Chem Phys 2017;147:13944.
[36] Bodi A, Hemberger P, Gerber T, Sztáray B. A new double imaging velocity focusing coincidence experiment: i^2PEPICO. Rev Sci Instrum 2012;83:83105.
[37] Osswald P, Hemberger P, Bierkandt T, Akyildiz E, Köhler M, Bodi A, Gerber T, Kasper T. In situ flame chemistry tracing by imaging photoelectron photoion coincidence spectroscopy. Rev Sci Instrum 2014;85:25101.
[38] Hansen N, Cool TA, Westmoreland PR, Kohse-Höinghaus K. Recent contributions of flame-sampling molecular-beam mass spectrometry to a fundamental understanding of combustion chemistry. Prog Energy Combust Sci 2009;35:168–91.
[39] Ansys, Chemkin-Pro 2021 R2. San Diego: Reaction Design; 2017.
[40] Halter F, Higelin P, Dagaut P. Experimental and detailed kinetic modeling study of the effect of ozone on the combustion of methane. Energy Fuels 2011;25:2909–16.
[41] Zhou C-W, Li Y, Burke U, Banyon C, Somers KP, Ding S, Khan S, Hargis JW, Sikes T, Mathieu O, Petersen EL, AlAbbad M, Farooq A, Pan Y, Zhang Y, Huang Z, Lopez J, Loparo Z, Vasu SS, Curran HJ. An experimental and chemical kinetic modeling study of 1,3-butadiene combustion: ignition delay time and laminar flame speed measurements. Combust Flame 2018;197:423–38.

[42] Kaczmarek D, Rudolph C, Atakan B, Kasper T. Kinetic investigation of the ozone-assisted partial oxidation of fuel-rich natural gas mixtures at elevated pressure. Proc Combust Inst 2022;14:185.
[43] Freund D, Horn C, Atakan B, King R, Peitsch D. Active flow and combustion control 2021 (Eds.). Cham: Springer International Publishing; 2022. p. 47–65.
[44] Moshammer K, Jasper AW, Popolan-Vaida DM, Wang Z, Bhavani Shankar VS, Ruwe L, et al. Quantification of the keto-hydroperoxide ($HOOCH_2OCHO$) and other elusive intermediates during low-temperature oxidation of dimethyl ether. J Phys Chem A 2016;120:7890–901.
[45] Rodriguez A, Herbinet O, Meng X, Fittschen C, Wang Z, Xing L, Zhang L, Battin-Leclerc F. Hydroperoxide measurements during low-temperature gas-phase oxidation of n-heptane and n-decane. J Phys Chem A 2017;121:1861–76.
[46] Wang Z, Herbinet O, Hansen N, Battin-Leclerc F. Exploring hydroperoxides in combustion: history, recent advances and perspectives. Prog Energy Combust Sci 2019;73:132–81.
[47] Dodson LG, Shen L, Savee JD, Eddingsaas NC, Welz O, Taatjes CA, et al. VUV photoionization cross sections of HO_2, H_2O_2, and H_2CO. J Phys Chem A 2015;119:1279–91.
[48] Porter R, Glaude P-A, Buda F, Battin-Leclerc F. A tentative modeling study of the effect of wall reactions on oxidation phenomena. Energy Fuels 2008;22:3736–43.
[49] Bahrini C, Morajkar P, Schoemaecker C, Frottier O, Herbinet O, Glaude P-A, et al. Experimental and modeling study of the oxidation of n-butane in a jet stirred reactor using cw-CRDS measurements. Phys Chem Chem Phys 2013;15:19686–98.
[50] Bierkandt T, Oßwald P, Gaiser N, Krüger D, Köhler M, Hoener M, Shaqiri S, Kaczmarek D, Karakaya Y, Hemberger P, Kasper T. Observation of low-temperature chemistry products in laminar premixed low-pressure flames by molecular-beam mass spectrometry. Int J Chem Kinet 2021;53:1063–81.
[51] Zhang X, Zhang Y, Li T, Li Y, Zou J, Dagaut P, Yang J, Li W, Zeng M, Jin H, Yuan W, Qi F. Low-temperature chemistry triggered by probe cooling in a low-pressure premixed flame. Combust Flame 2019;204:260–7.
[52] Taatjes CA, Shallcross DE, Percival CJ. Research frontiers in the chemistry of Criegee intermediates and tropospheric ozonolysis. Phys Chem Chem Phys 2014;16:1704–18.
[53] Welz O, Savee JD, Osborn DL, Vasu SS, Percival CJ, Shallcross DE, Taatjes CA. Direct kinetic measurements of Criegee intermediate (CH_2OO) formed by reaction of CH_2I with O_2. Science (New York, N.Y.) 2012;335:204–7.
[54] P. Linstrom, NIST Chemistry WebBook, NIST Standard Reference Database 69, 1997.
[55] Cool TA, Wang J, Nakajima K, Taatjes CA, Mcllroy A. Photoionization cross sections for reaction intermediates in hydrocarbon combustion. Int J Mass spectrom 2005;247:18–27.
[56] Nguyen MT, Nguyen TL, Ngan VT, Nguyen HMT. Heats of formation of the Criegee formaldehyde oxide and dioxirane. Chem Phys Lett 2007;448:183–8.
[57] Bock H, Kimura K, Katsumata S, Achiba Y, Yamazaki T, Iwata S. Handbook of He photoelectron spectra of fundamental organic molecules. Ionization energies, ab initio assignments, and valence electronic structure for 200 molecules. Jpn Sci Soc Ber Bunsenges Phys Chem 1982;86:266.
[58] Chicharro DV, Poullain SM, Bañares L, Hrodmarsson HR, García GA, Loison J-C. Threshold photoelectron spectrum of the CH_2OO Criegee intermediate. Phys Chem Chem Phys 2019;21:12763–6.
[59] Schwell M, Leach S, Hottmann K, Jochims H-W, Baumgärtel H. He I photoelectron spectroscopy of formic acid isotopomers HCOOH and DCOOD. Chem Phys 2001;272:77–90.
[60] Rousso AC, Hansen N, Jasper AW, Ju Y. Low-temperature oxidation of ethylene by ozone in a jet-stirred reactor. J Phys Chem 2018;A 122:8674–85.
[61] Andersen A, Carter EA. Insight into selected reactions in low-temperature dimethyl ether combustion from Born-Oppenheimer molecular dynamics. J Phys Chem A 2006;110:1393–407.
[62] Andersen A, Carter EA. Hybrid density functional theory predictions of low-temperature dimethyl ether combustion pathways. II. Chain-branching energetics and possible role of the Criegee intermediate. J Phys Chem A 2003;107:9463–78.
[63] Moshammer K, Jasper AW, Popolan-Vaida DM, Lucassen A, Diévart P, Selim H, et al. Detection and identification of the keto-hydroperoxide ($HOOCH_2OCHO$) and other intermediates during low-temperature oxidation of dimethyl ether. J Phys Chem A 2015;119:7361–74.
[64] Rousso AC, Hansen N, Jasper AW, Ju Y. Identification of the Criegee intermediate reaction network in ethylene ozonolysis: impact on energy conversion strategies and atmospheric chemistry. Phys Chem Chem Phys 2019;21:7341–57.
[65] Tadayon SV, Foreman ES, Murray C. Kinetics of the reactions between the Criegee intermediate CH_2OO and alcohols. J Phys Chem A 2018;122:258–68.

Bibliography

Ahmed, M., Shuai, C. and Ahmed, M. (2023) 'Analysis of energy consumption and greenhouse gas emissions trend in China, India, the USA, and Russia', *International Journal of Environmental Science and Technology*, 20(3), pp. 2683–2698.

Asatryan, R., Bozelli, J.W. and Simmie, J.M. (2007) 'Thermochemistry for Enthalpies and Reaction Paths of Nitrous Acid Isomers', *International Journal of Chemical Kinetics*, 39(7), pp. 378–398.

Baer, T. and Tuckett, R.P. (2017) 'Advances in threshold photoelectron spectroscopy (TPES) and threshold photoelectron photoion coincidence (TPEPICO)', *Physical Chemistry Chemical Physics*, 19(15), pp. 9698–9723.

Berman, M.R., Tsuchiya, T., Gregušová, A., Perera, S.A. and Bartlett, R.J. (2007) 'HNNC radical and its role in the CH + N2 reaction', *Journal of Physical Chemistry A*, 111(29), pp. 6894–6899.

Berman, M.R. and Lin, M.C. (1983) 'Kinetics and Mechanism of the CH + N2 Reaction. Temperature- and Pressure-Dependence Studies and Transition-State-Theory Analysis', *Journal of Physical Chemsitry*, 87, pp. 3933–3942.

Bierkandt, T. (2018) *Systematische Untersuchung flacher Niederdruckflammen mittels Photoionisationsmassenspektrometrie und Spektroskopie*. Duisburg: Universität Duisburg-Essen.

Bierkandt, T., Hoener, M., Gaiser, N., Hansen, N., Köhler, M. and Kasper, T. (2021) 'Experimental flat flame study of monoterpenes: Insights into the combustion kinetics of α-pinene, β-pinene, and myrcene', *Proceedings of the Combustion Institute*, 38(2), pp. 2431–2440.

Bierkandt, T., Oßwald, P., Gaiser, N., Krüger, D., Köhler, M., Hoener, M., Shaqiri, S., Kaczmarek, D., Karakaya, Y., Hemberger, P. and Kasper, T. (2021) 'Observation of low-temperature chemistry products in laminar premixed low-pressure flames by molecular-beam mass spectrometry', *International Journal of Chemical Kinetics*, 53(10), pp. 1063–1081.

Bierkandt, T., Hemberger, P., Oßwald, P., Gaiser, N., Hoener, M., Krüger, D., Kasper, T. and Köhler, M. (2023) 'A combustion chemistry study of tetramethylethylene in a laminar premixed low-pressure hydrogen flame', *Proceedings of the Combustion Institute*, 39(2), pp. 1699–1708.

Bodi, A., Hemberger, P., Gerber, T. and Sztáray, B. (2012) 'A new double imaging velocity focusing coincidence experiment: I2PEPICO', *Review of Scientific Instruments*, 83(8), p. 083105.

Bodi, A., Hemberger, P., Osborn, D.L. and Sztáray, B. (2013) 'Mass-resolved isomer-selective chemical analysis with imaging photoelectron photoion coincidence spectroscopy', *Journal of Physical Chemistry Letters*, 4(17), pp. 2948–2952.

Bodi, A. and Hemberger, P. (2014) 'Imaging breakdown diagrams for bromobutyne isomers with photoelectron-photoion coincidence', *Physical Chemistry Chemical Physics*, 16(2), pp. 505–515.

British Petroleum (2023) *bp Energy Outlook 2023*.

Chai, J. and Goldsmith, C.F. (2017) 'Rate coefficients for fuel + NO2: Predictive kinetics for HONO and HNO2 formation', *Proceedings of the Combustion Institute*, 36(1), pp. 617–626.

Chen, X., Fuller, M.E. and Goldsmith, C.F. (2019) 'Decomposition Kinetics for HONO and HNO2', *Reaction Chemistry & Engineering*, 4, pp. 323–333.

Cool, T.A., McIlroy, A., Qi, F., Westmoreland, P.R., Poisson, L., Peterka, D.S. and Ahmed, M. (2005) 'Photoionization mass spectrometer for studies of flame chemistry with a synchrotron light source', *Review of Scientific Instruments*, 76(9), p. 094102.

Curtiss, L.A., Redfern, P.C. and Raghavachari, K. (2007) 'Gaussian-4 theory', *Journal of Chemical Physics*, 126(8), p. 084108.

Ellis, A., Feher, M. and Wright, T. (2005) *Electronic and photoelectron spectroscopy - Fundamentals and Case Studies*. 1st edn. Cambridge, New York, Melbourne, Madrid, Cape Town, Singapore, São Paulo: Cambridge University Press.

Felsmann, D., Lucassen, A., Krüger, J., Hemken, C., Tran, L.S., Pieper, J., Garcia, G.A., Brockhinke, A., Nahon, L. and Kohse-Höinghaus, K. (2016) 'Progress in Fixed-Photon-Energy Time-Efficient Double Imaging Photoelectron/Photoion Coincidence Measurements in Quantitative Flame Analysis', *Zeitschrift fur Physikalische Chemie*, 230(8), pp. 1067–1097.

Frisch, M.J., Trucks, G.W., Schlegel, H.B., Scuseria, G.E., Robb, M. a., Fox, D.J., *et al.* (2016) 'Gaussian 16, Revision C.01'.

Fuller, M.E. and Goldsmith, C.F. (2019) 'On the relative importance of HONO versus HNO2 in low-temperature combustion', *Proceedings of the Combustion Institute*, 37(1), pp. 695–702.

Glarborg, P., Miller, J.A., Ruscic, B. and Klippenstein, S.J. (2018) 'Modeling nitrogen chemistry in combustion', *Progress in Energy and Combustion Science*, 67, pp. 31–68.

Gossler, S., Ruwe, L., Yuan, W., Yang, J., Chen, X., Schmitt, S., Maier, L., Kohse-Höinghaus, K., Qi, F. and Deutschmann, O. (2021) 'Exploring the interaction kinetics of butene isomers and NOx at low temperatures and diluted conditions', *Combustion and Flame*, 233, p. 111557.

Hansen, N., Cool, T.A., Westmoreland, P.R. and Kohse-Höinghaus, K. (2009) 'Recent contributions of flame-sampling molecular-beam mass spectrometry to a fundamental understanding of combustion chemistry', *Progress in Energy and Combustion Science*, 35(2), pp. 168–191.

Harvey, J.N. (2007) 'Understanding the kinetics of spin-forbidden chemical reactions', *Physical Chemistry Chemical Physics*, 9(3), pp. 331–343.

Hemberger, P., Van Bokhoven, J.A., Pérez-Ramírez, J. and Bodi, A. (2020) 'New analytical tools for advanced mechanistic studies in catalysis: Photoionization and photoelectron photoion coincidence spectroscopy', *Catalysis Science and Technology*, 10(7), pp. 1975–1990.

Hoener, M., Kaczmarek, D., Bierkandt, T., Bodi, A., Hemberger, P. and Kasper, T. (2020) 'A pressurized flow reactor combustion experiment interfaced with synchrotron double imaging photoelectron photoion coincidence spectroscopy', *Review of Scientific Instruments*, 91(4), p. 045115.

Hoener, M., Bodi, A., Hemberger, P., Endres, T. and Kasper, T. (2021) 'Threshold photoionization shows no sign of nitryl hydride in methane oxidation with nitric oxide', *Physical Chemistry Chemical Physics*, 23(2), pp. 1265–1272.

Hoener, M. and Kasper, T. (2022) 'Nitrous acid in high-pressure oxidation of CH4 doped with nitric oxide: Challenges in the isomer-selective detection and quantification of an elusive intermediate', *Combustion and Flame*, 243, p. 112096.

Ickes, A.M., Bohac, S. V. and Assanis, D.N. (2009) 'Effect of 2-ethylhexyl nitrate cetane improver on NOx emissions from premixed low- temperature diesel combustion', *Energy and Fuels*, 23(10), pp. 4943–4948.

Janzer, C., Richter, S., Naumann, C. and Methling, T. (2022) '"Green propellants" as a hydrazine substitute: experimental investigations of ethane/ethene-nitrous oxide mixtures and validation of detailed reaction mechanism', *CEAS Space Journal*, 14, pp. 151–159.

Johnson, M., Bodi, A., Schulz, L. and Gerber, T. (2009) 'Vacuum ultraviolet beamline at the Swiss Light Source for chemical dynamics studies', *Nuclear Instruments and Methods in Physics Research, Section A: Accelerators, Spectrometers, Detectors and Associated Equipment*, 610(2), pp. 597–603.

Kaczmarek, D., Bierkandt, T., Rudolph, C., Grimm, S., Shaqiri, S., Höner, M., Gaiser, N., Atakan, B., Köhler, M., Hemberger, P. and Kasper, T. (2023) 'Activation effect of ozone and DME on the partial oxidation of natural gas surrogates and validation of pressure-dependent ozone decomposition', *Applications in Energy and Combustion Science*, 13, p. 100107.

Kaczmarek, D., Atakan, B. and Kasper, T. (2019) 'Investigation of the partial oxidation of methane/n-heptane-mixtures and the interaction of methane and n-heptane under ultra-rich conditions', *Combustion and Flame*, 205, pp. 345–357.

Karabeyoglu, A., Dyer, J., Stevens, J. and Cantwell, B. (2008) 'Modeling of N2O decomposition events', in *44th AIAA/ASME/SAE/ASEE Joint Propulsion Conference and Exhibit*.

Kasper, T., Oßwald, P., Struckmeier, U., Kohse-Höinghaus, K., Taatjes, C.A., Wang, J., Cool, T.A., Law, M.E., Morel, A. and Westmoreland, P.R. (2009) 'Combustion chemistry of the propanol isomers - investigated by electron ionization and VUV-photoionization molecular-beam mass spectrometry', *Combustion and Flame*, 156(6), pp. 1181–1201.

Klippenstein, S.J., Pfeifle, M., Jasper, A.W. and Glarborg, P. (2018) 'Theory and modeling of relevance to prompt-NO formation at high pressure', *Combustion and Flame*, 195, pp. 3–17.

Knyazkov, D.A., Shmakov, A.G., Dyakov, I. V., Korobeinichev, O.P., De Ruyck, J. and Konnov, A.A. (2009) 'Formation and destruction of nitric oxide in methane flames doped with NO at atmospheric pressure', *Proceedings of the Combustion Institute*, 32(1), pp. 327–334.

Kohse-Höinghaus, K., Oßwald, P., Cool, T.A., Kasper, T., Hansen, N., Qi, F., Westbrook, C.K. and Westmoreland, P.R. (2010) 'Biofuel combustion chemistry: From ethanol to biodiesel', *Angewandte Chemie - International Edition*, 49(21), pp. 3572–3597.

Kohse-Höinghaus, K. (2023) 'Combustion, Chemistry, and Carbon Neutrality', *Chemical Reviews*, 123(8), pp. 5139–5219.

Krüger, D., Oßwald, P., Köhler, M., Hemberger, P., Bierkandt, T. and Kasper, T. (2019) 'The fate of the OH radical in molecular beam sampling experiments', *Proceedings of the Combustion Institute*, 37(2), pp. 1563–1570.

Krüger, J., Garcia, G.A., Felsmann, D., Moshammer, K., Lackner, A., Brockhinke, A., Nahon, L. and Kohse-Höinghaus, K. (2014) 'Photoelectron-photoion coincidence spectroscopy for multiplexed detection of intermediate species in a flame', *Physical Chemistry Chemical Physics*, 16(41), pp. 22791–22804.

Levenspiel, O. (1999) *Chemical Reaction Engineering*. 3rd edn. John Wiley and Sons.

Lewars, E.G. (2016) *Computational Chemistry: Introduction to the Theory and Applications of Molecular and Quantum Mechanics*. 3rd edn. Dordrecht: Springer.

Li, Z.Z., Su, C.-W., Moldovan, N.-C. and Umar, M. (2023) 'Energy consumption within policy uncertainty: Considering the climate and economic factors', *Renewable Energy*, 208, pp. 567–576.

Liaw, J.-C., Höner, M. and Kasper, T. (2019) 'Optimiertes Design eines Plug-Flow Reaktors zur Durchführung von Verbrennungsexperimenten', in *Thermodynamik-Kolloquium 2019*. Duisburg.

Lissianski, V. V., Zamansky, V.M. and Gardiner, W.C. (2000) *Gas-Phase Combustion Chemistry*, *Gas-Phase Combustion Chemistry*. Edited by W.C. Gardiner. New York: Springer-Science + Business Media, LLC.

Liu, Y., Sun, X., Sethi, V., Nalianda, D., Li, Y.G. and Wang, L. (2017) 'Review of modern low emissions combustion technologies for aero gas turbine engines', *Progress in Aerospace Sciences*, 94, pp. 12–45.

Lucassen, A., Oßwald, P., Struckmeier, U., Kohse-Höinghaus, K., Kasper, T., Hansen, N., Cool, T.A. and Westmoreland, P.R. (2009) 'Species identification in a laminar premixed low-pressure flame of morpholine as a model substance for oxygenated nitrogen-containing fuels', *Proceedings of the Combustion Institute*, 32(1), pp. 1269–1276.

Lucassen, A., Labbe, N., Westmoreland, P.R. and Kohse-Höinghaus, K. (2011) 'Combustion chemistry and fuel-nitrogen conversion in a laminar premixed flame of morpholine as a model biofuel', *Combustion and Flame*, 158(9), pp. 1647–1666.

Lucassen, A. (2011) *Systematische Analyse von Flammen stickstoffhaltiger Modellsubstanzen mittels Molekularstrahlmassenspektrometrie*. Bielefeld: Fakultät für Chemie Universität Bielefeld.

Maligne, D., Cessou, A. and Stepowski, D. (2009) 'Chemiluminescence of BO2 to map the creation of thermal NO in flames', *Combustion and Flame*, 156(2), pp. 348–361.

Marrodán, L., Arnal, Á.J., Millera, Á., Bilbao, R. and Alzueta, M.U. (2018) 'The inhibiting effect of NO addition on dimethyl ether high-pressure oxidation', *Combustion and Flame*, 197(2), pp. 1–10.

Marrodán, L., Song, Y., Herbinet, O., Alzueta, M.U., Fittschen, C., Ju, Y. and Battin-Leclerc, F. (2019) 'First detection of a key intermediate in the oxidation of fuel + NO systems: HONO', *Chemical Physics Letters*, 719, pp. 22–26.

Mayer, P.M. and Baer, T. (1996) 'A photoionization study of vibrational cooling in molecular beams', *International Journal of Mass Spectrometry and Ion Processes*, 156(3), pp. 133–139.

McBride, B.J., Zehe, M.J. and Gordon, S. (2002) *NASA Glenn coefficients for calculating thermodynamic properties of individual species: National Aeronautics and Space Administration*, *John H. Glenn Research Center at Lewis Field*.

Mišík, M. and Nosko, A. (2023) 'Post-pandemic lessons for EU energy and climate policy after the Russian invasion of Ukraine: Introduction to a special issue on EU green recovery in the post-Covid-19 period', *Energy Policy*, 177, p. 113546.

Missen, R.W., Mims, C.A. and Saville, B.A. (1999) *Introduction to Chemical Reaction Engineering*. New York: John Wiley & Sons, Inc.

Moskaleva, L. V. and Lin, M.C. (2000) 'The spin-conserved reaction CH + n2 → H + NCN: A major pathway to prompt no studied by quantum/statistical theory calculations and kinetic modeling of rate constant', *Proceedings of the Combustion Institute*, 28(2), pp. 2393–2401.

Okafor, E.C., Somarathne, K.D.K.A., Hayakawa, A., Kudo, T., Kurata, O., Iki, N. and Kobayashi, H. (2019) 'Towards the development of an efficient low-NOx ammonia combustor for a micro gas turbine', *Proceedings of the Combustion Institute*, 37(4), pp. 4597–4606.

Oßwald, P., Hemberger, P., Bierkandt, T., Akyildiz, E., Köhler, M., Bodi, A., Gerber, T. and Kasper, T. (2014) 'In situ flame chemistry tracing by imaging photoelectron photoion coincidence spectroscopy', *Review of Scientific Instruments*, 85(2), p. 025101.

Qi, F. (2013) 'Combustion chemistry probed by synchrotron VUV photoionization mass spectrometry', *Proceedings of the Combustion Institute*, 34(1), pp. 33–63.

Rasmussen, C.L., Rasmussen, A.E. and Glarborg, P. (2008) 'Sensitizing effects of NOx on CH4 oxidation at high pressure', *Combustion and Flame*, 154(3), pp. 529–545.

Sengupta, D., Sumathi, R. and Peyerimhoff, S.D. (1999) 'Unimolecular decomposition of the isomers of [HNO2]+ and [HNO2]- systems: A DFT study', *Chemical Physics*, 248(2–3), pp. 147–159.

Song, Y., Marrodán, L., Vin, N., Herbinet, O., Assaf, E., Fittschen, C., Stagni, A., Faravelli, T., Alzueta, M.U. and Battin-Leclerc, F. (2019) 'The sensitizing effects of NO2 and NO on methane low temperature oxidation in a jet stirred reactor', *Proceedings of the Combustion Institute*, 37(1), pp. 667–675.

Sztáray, B., Voronova, K., Torma, K.G., Covert, K.J., Bodi, A., Hemberger, P., Gerber, T. and Osborn, D.L. (2017) 'CRF-PEPICO: Double velocity map imaging photoelectron photoion coincidence spectroscopy for reaction kinetics studies', *Journal of Chemical Physics*, 147(1), p. 013944.

Taatjes, C.A., Hansen, N., Osborn, D.L., Kohse-Höinghaus, K., Cool, T.A. and Westmoreland, P.R. (2008) '"Imaging" combustion chemistry via multiplexed synchrotron-photoionization mass spectrometry', *Physical Chemistry Chemical Physics*, 10(1), pp. 20–34.

Theodore, L. (2012) *Chemical Reactor Engineering*. Hoboken: John Wiley & Sons, Inc.

Tomeczek, J. and Gradoń, B. (2003) 'The role of N2O and NNH in the formation of NO via HCN in hydrocarbon flames', *Combustion and Flame*, 133(3), pp. 311–322.

Valera-Medina, A., Xiao, H., Owen-Jones, M., David, W.I.F. and Bowen, P.J. (2018) 'Ammonia for power', *Progress in Energy and Combustion Science*, 69, pp. 63–102.

Verbiezen, K., Donkerbroek, A.J., Klein-Douwel, R.J.H., van Vliet, A.P., Frijters, P.J.M., Seykens, X.L.J., Baert, R.S.G., Meerts, W.L., Dam, N.J. and ter Meulen, J.J. (2007) 'Diesel combustion: In-cylinder NO concentrations in relation to injection timing', *Combustion and Flame*, 151(1–2), pp. 333–346.

Wang, J., Fan, W., Li, Y., Xiao, M., Wang, K. and Ren, P. (2012) 'The effect of air staged combustion on NOx emissions in dried lignite combustion', *Energy*, 37(1), pp. 725–736.

Warnatz, J., Maas, U. and Dibble, R.W. (2006) *Combustion - Physical and Chemical Fundamentals, Modeling and Simulation, Experiments, Pollutant Formation*. 4th edn. Berlin, Heidelberg: Springer-Verlag.

Willmott, P. (2011) *An Introduction to Synchrotron Radiation - Techniques and Applications*. 1st edn. Hoboken: John Wiley & Sons Ltd.

Young, D.C. (2001) *Computational Chemistry: A Practical Guide for Apllying Techniques to Real-World Problems*. New York: John Wiley & Sons, Inc.

Yuan, W., Ruwe, L., Schwarz, S., Cao, C., Yang, J., Deutschmann, O., Kohse-Höinghaus, K. and Qi, F. (2021) 'Insights into the interaction kinetics between propene and NOx at moderate temperatures with experimental and modeling methods', *Proceedings of the Combustion Institute*, 38(1), pp. 795–803.

Zeldovich, Y.B. (1946) 'The Oxidation of Nitrogen in Combustion Explosions', *Acta Physicochimica U.S.S.R.*, 21, pp. 577–628.

Zhang, H., Schmitt, S., Ruwe, L. and Kohse-Höinghaus, K. (2021) 'Inhibiting and promoting effects of NO on dimethyl ether and dimethoxymethane oxidation in a plug-flow reactor', *Combustion and Flame*, 224, pp. 94–107.

Anlage in der Dissertation:
Zitation von studentischen Arbeiten

Erklärung zur Zitation von Inhalten aus studentischen Arbeiten

In Ergänzung zu meinem Antrag auf Zulassung zur Promotion in der Fakultät für Maschinenbau der Universität Paderborn erkläre ich gemäß §11 der Promotionsordnung und unter Beachtung der Regelung zur Zitation studentischer Arbeiten:

Die von mir vorgelegte Dissertation habe ich selbstständig verfasst, **und ich habe keine anderen** als die dort angegebenen Quellen und Hilfsmittel benutzt. Es sind **Inhalte** / **keine Inhalte** studentischen Ursprungs (studentische Arbeiten) in dieser Dissertation enthalten.

Ich habe die verwendeten Arbeiten entsprechend der Regelung „Zitation aus studentischen Arbeiten in Dissertationen“ zitiert.

Ort, Datum:

Unterschrift